

GALERKIN BOUNDARY ELEMENT MODELING OF
THREE-DIMENSIONAL FUNCTIONALLY GRADED MATERIAL SYSTEMS

BY

ALOK SUTRADHAR

BSCE., Bangladesh University of Engineering & Technology, 1995
MSCE., Bangladesh University of Engineering & Technology, 1999

DISSERTATION

Submitted in partial fulfillment of the requirements
for the degree of Doctor of Philosophy in Civil and Environmental Engineering
in the Graduate College of the
University of Illinois at Urbana-Champaign, 2005

Urbana, Illinois

UMI Number: 3182388

INFORMATION TO USERS

The quality of this reproduction is dependent upon the quality of the copy submitted. Broken or indistinct print, colored or poor quality illustrations and photographs, print bleed-through, substandard margins, and improper alignment can adversely affect reproduction.

In the unlikely event that the author did not send a complete manuscript and there are missing pages, these will be noted. Also, if unauthorized copyright material had to be removed, a note will indicate the deletion.

UMI[®]

UMI Microform 3182388

Copyright 2005 by ProQuest Information and Learning Company.

All rights reserved. This microform edition is protected against unauthorized copying under Title 17, United States Code.

ProQuest Information and Learning Company
300 North Zeeb Road
P.O. Box 1346
Ann Arbor, MI 48106-1346

© Copyright by Alok Sutradhar, 2005

CERTIFICATE OF COMMITTEE APPROVAL

*University of Illinois at Urbana-Champaign
Graduate College*

April 14, 2005

We hereby recommend that the thesis by:

ALOK SUTRADHAR

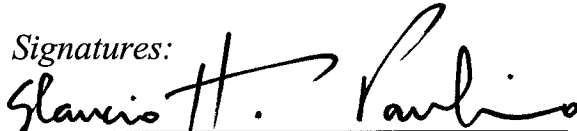
Entitled:


**GALERKIN BOUNDARY ELEMENT MODELING OF
THREE-DIMENSIONAL FUNCTIONALLY GRADED MATERIAL SYSTEMS**

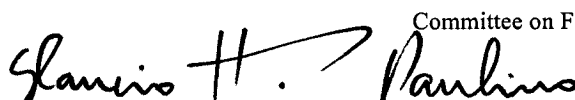
Be accepted in partial fulfillment of the requirements for the degree of:

Doctor of Philosophy


Signatures:


Director of Research - Glauco H. Paulino



Head of Department - Robert H. Dodds Jr.


Chairperson - Glauco H. Paulino

Committee on Final Examination*


Committee Member - Narayana R. Aluru


Committee Member - C. Armando Duarte


Committee Member - B. David Semceraro

Committee Member -

Committee Member -

* Required for doctoral degree but not for master's degree

Abstract

Recent advances in material processing technology have enabled the design and manufacture of new functionally graded material systems that can withstand very high temperature and large thermal gradient. Galerkin boundary element method is a powerful numerical method with good efficiency and accuracy which uses C^0 elements for hypersingular integrals which are essential for solving fracture problem. In the boundary element formulation, treatment of the singular and hypersingular integrals is one of the main challenges. A direct treatment of the hypersingular integral using a hybrid analytical/numerical approach is presented. Symmetric Galerkin formulation for exponentially graded material using the Green's function approach is developed. In the Green's function approach, each material variation requires different fundamental solution to be derived and consequently, new computer codes to be developed. In order to alleviate this constraint a "simple" Galerkin boundary element method is proposed where the nonhomogeneous problems can be transformed to known homogeneous problems for a class of variations (quadratic, exponential and trigonometric) of thermal conductivity. The material property can have a functional variation in one, two and three dimensions. Recycling existing codes for homogeneous media, the problems in nonhomogeneous media can be solved maintaining a pure boundary only formulation. This method can be used for any problem governed by potential theory. Within this scope, novel Galerkin boundary element method formulations for steady state and transient heat conduction, and fracture problems involving multiple interacting cracks in three-dimensional graded material systems are developed. The transient heat conduction is carried out using a Laplace transform Galerkin formulation whereas the crack problem is formulated using the dual boundary element method approach. The implementations of all the techniques involved in this work are discussed and several numerical examples are presented to demonstrate the accuracy and efficiency of the methods. Finally, new techniques of scientific visualization, which is an integral part of computational science research, are explored in the context of boundary element method. This investigation includes developing new modules for viewing the boundary and the domain data using modern visualization tools, developing virtual reality based visualization and concluding with web based interactive visualization.

To my parents

Acknowledgments

I would like to take this opportunity to express my sincere gratitude to my advisor, Professor Glaucio H. Paulino for his invaluable guidance, encouragement and support. Working with him was an enlightening and truly edifying experience.

I would like to thank Dr. Leonard Gray for his research suggestions and for being such a great mentor during my stay at the Oak Ridge National Laboratory. I am also grateful to Dr. Dave Semeraro who gave the opportunity to work in the exciting field of visualization and also supported me for the last couple of years. I would also like to thank the members of my Dissertation Committee, Professor Narayana R Aluru, Professor C. Armando Duarte and Dr. Dave Semeraro for their kind and constructive remarks and suggestions. Special thanks to Professor Taher Saif for all his advice and suggestions over the years.

I have immense gratitude for my parents, for their unflagging dedication and absolute confidence in me and for their prayers from this world and beyond. This achievement is but their blessings. It is through their encouragement and care that I have made it through all the steps to reach this point in life, and I couldn't have done it without them. My father has always been and will be my source of motivation and constant inspiration. They would be the happiest to see me graduate. My beliefs and values have been shape by their influence.

I feel particularly indebted to my wife Jaya for her unwavering patience through seemingly endless hours of work and sporadic episodes of frustration and anxiety. She has always been there supporting me, and is an important part of my life and keeps me normal. I cherish dearly all the joy she and her gift our daughter Ankita brings into my life everyday. Also, I acknowledge my wonderful sister Rita, her husband Dipu and my brother Utpal for their perpetual care and support over the years. Thanks also go to my close relatives Sheba, Hasan and Amber for their inspiration and affection.

I would also like to thank my wonderful friends and office mates who, over the years, have become like family to me: my good friends Matt Walters and Zhengyu Zhang. The stimulating and vibrant discussions that we had ranged from physics, mechanics to religion and philosophy, I would definitely miss those. Also thanks go to all my lab mates from past to present - Dr. Youn-sha Chan, Dr. Jeong-ho Kim, Seong Hyeok Song, Bin Shen,

Kyoungsoo Park, Eshan Dave, Levent Ozturk, Masha Romadina, Mariana Silva, Zhaoxu Dong, Ran Li and Christina Eng for their kind company.

Special thanks to all of my friends here for their warm friendship and support. During my first few years at UIUC, I became good friends with Dr. Aman Haque, I enjoyed the conversations that we had together. Many thanks to Munawar Hafiz, who has been like my younger brother, for a special friendship and for all the thrill we had scouting around. Finally, I would like to mention all my close friends, Tim Khalid, Tamara Iqbal, Rumi Shammin, Tabassum Haque, Tahmina Akhter, and Sharif Russell for making life in Champaign enjoyable and entertaining.

Table of Contents

Chapter 1	Introduction	1
1.1	Boundary Element Method (BEM)	1
1.1.1	Collocation	2
1.1.2	Galerkin	2
1.1.3	Symmetric Galerkin (SG)	3
1.1.4	Boundary-based meshfree methods	4
1.2	Functionally Graded Materials (FGMs)	5
1.3	Approaches for solving problems in nonhomogeneous media using BEM	5
1.4	Thesis Organization	6
Chapter 2	Evaluation of Singular and hypersingular integrals in GBEM for FGMs	8
2.1	Introduction	9
2.2	Singular and hypersingular boundary integrals	10
2.3	Evaluation of singular double integrals	13
2.3.1	Coincident Integration	14
2.3.2	Edge Adjacent Integration	22
2.3.3	Vertex Adjacent Integration	27
2.4	Concluding Remarks	29
Chapter 3	Green's function approach for heat conduction in graded materials	30
3.1	Introduction	30
3.2	On the FGM Green's function	31
3.3	Symmetric Galerkin Formulation	32
3.4	Numerical Implementation	35
3.4.1	FGM Cube with material gradation in z -direction	36
3.4.2	FGM Cube with material gradation in 45° with the z -axis	38
3.4.3	Interior Neumann FGM-sphere problem	41
3.4.4	FGM compressor blade	43
3.5	Concluding Remarks	44
Chapter 4	Green's function approach for transient heat conduction in graded materials	48
4.1	Introduction	49
4.2	Basic Equations	50
4.3	Green's Function	52
4.4	Laplace Transform BEM (LTBEM) Formulation	52

4.5	Numerical Implementation of the 3D Galerkin BEM	55
4.6	Numerical Inversion of the Laplace Transform	57
4.7	Numerical Examples	58
4.7.1	Transient two-dimensional heat conduction in a homogeneous cube .	59
4.7.2	Cylinder of homogeneous material with constant surface temperature	60
4.7.3	Constant temperature on two planes of an FGM cube	63
4.7.4	Linear heat flux on a face of an FGM cube	66
4.7.5	Time-dependent boundary condition	68
4.8	Concludin Remarks	69
Chapter 5	Simple BEM for nonhomogeneous media: Problems of potential	72
5.1	Introduction	73
5.2	Related Work	74
5.3	Governing Equations considering variable conductivity	76
5.3.1	Reduction to the Laplace equation	77
5.3.2	Reduction to the modified Helmholtz equation	77
5.3.3	Reduction to the standard Helmholtz equation	78
5.3.4	Remarks	79
5.3.5	Boundary Conditions	79
5.4	Green's function versus reduction to parent equation: A comparison of ap- proaches	81
5.4.1	Green's function approach for three dimensional (3D) problems . . .	81
5.4.2	Reduction to the modified Helmholtz equation	82
5.5	Numerical Implementation	83
5.5.1	Galerkin Boundary Integral Equation.	83
5.5.2	Simple Kernel functions	84
5.5.3	Treatment of boundary conditions	85
5.5.4	Boundary Elements	86
5.5.5	Corners	87
5.6	ABAQUS User Subroutine	87
5.7	Numerical Examples	88
5.7.1	Cube with material gradation with z -axis	88
5.7.2	Cube with a 3D material gradation	93
5.7.3	Cylindrical cavity in a parallelepiped	95
5.7.4	FGM Rotor problem	96
5.8	Concluding Remarks	99
Chapter 6	Simple BEM for Transient heat conduction in FGMs	104
6.1	Introduction	104
6.2	Basic equations and the simple BEM concept	107
6.2.1	Material variations	109
6.2.2	Multi-dimensional material variation	110
6.3	Green's function (GF)	110
6.4	Laplace transform BEM (LTBEM) formulation	113

6.4.1	Approach 1: Formulation based on One-step Transformation	113
6.4.2	Approach 2: Formulation Based on Two-step Transformation	115
6.4.3	Remarks	117
6.5	Numerical implementation of the Galerkin LTBE	117
6.5.1	Galerkin boundary integral equation.	117
6.5.2	Treatment of boundary conditions	118
6.5.3	Boundary elements	120
6.5.4	Singular integrals	121
6.5.5	Corners	121
6.5.6	Numerical inversion of the Laplace transform	122
6.6	Examples	123
6.6.1	Cube problem	124
6.6.2	Rotor problem	129
6.7	Concluding Remarks	138
Chapter 7 Simple BEM for multiple cracks in FGMs		141
7.1	Introduction	142
7.2	On the simple BEM concept	143
7.2.1	Governing Equation	143
7.2.2	Variable Transformation Approach	144
7.2.3	Boundary conditions	145
7.3	Crack Analysis	146
7.3.1	Displacement discontinuity approach	146
7.3.2	The Dual BEM approach	148
7.4	Numerical Implementation	149
7.4.1	Galerkin Boundary Integral Equation.	149
7.4.2	Galerkin Hypersingular Boundary Integral Equation.	149
7.4.3	Interpolation of physical variables	151
7.4.4	Boundary elements	151
7.4.5	Treatment of boundary conditions	152
7.4.6	Singular integrals	153
7.4.7	Corners	155
7.5	Numerical Examples	155
7.5.1	Penny shaped crack inside a cylinder	156
7.5.2	Three parallel penny shaped cracks inside a cylinder	157
7.5.3	Multiple random cracks inside a cube	160
7.6	Concluding Remarks	161
Chapter 8 Scientific Visualization with BEM		171
8.1	Introduction	171
8.2	Visualization process and techniques	173
8.3	Visualization: Softwares and frameworks	174
8.4	Visualization of BEM Data	175
8.4.1	Basic Data representation	175

8.4.2	Visualizing the boundary results	177
8.4.3	Visualizing BEM Interior Data	179
8.5	MechVR: A Virtual Reality-Based Scientific Visualization Tool	186
8.5.1	CAVE: <u>C</u> ave <u>A</u> utomatic <u>V</u> irtual <u>E</u> nvironment	186
8.5.2	The MechVR	188
8.6	Web Visualization using VRML	193
8.6.1	Virtual Reality Modeling Language (VRML) visualization	194
8.6.2	Creating and viewing VRML models	195
8.7	Remarks	195
Chapter 9	Conclusions and Future Work	197
9.1	Concluding Remarks	197
9.2	Suggestions for Future Works	199
Appendix A	201
A.1	Maple codes for analytical integration	201
A.1.1	Analytical integration for coincident case	201
A.1.2	Analytical integration for edge adjacent case	205
A.2	Analytical solution of the FGM cube problem (Example 3 of Section 4.7)	207
A.3	ABAQUS user subroutine	210
References	212
Author's Biography	230

List of Tables

3.1	Global error (\mathcal{E}) estimates on the boundary for FGM cube ($\beta = 1.0$).	39
5.1	Problems governed by Eq. (5.1)	73
5.2	Table of Green's function for various forms of $k(z)$ given by Eq. (5.1)	80
5.3	Global error (\mathcal{E}) for FGM cube ($\beta = 1.0$).	92
5.4	Rate of Convergence of temperature solution for the Green's function and the simple BEM methods.	92
5.5	CPU times for the BEM simulations	92
6.1	Variable transformation approach	112
6.2	Mesh discretization by means of BEM and FEM for the rotor problem.	129
7.1	Family of material variations: transformation approach	145

List of Figures

1.1	Illustration of a generic body with boundary Σ and domain Ω . The source point is P (normal \mathbf{N}) and the field point is Q (normal \mathbf{n}).	2
1.2	Local support for the Galerkin BEM.	3
2.1	Illustration of a generic body with boundary Σ and domain Ω . The present SGBEM relies on a boundary-only formulation for FGMs. The source point is P (normal \mathbf{N}) and the field point is Q (normal \mathbf{n}).	10
2.2	Isoparametric equilateral triangular linear element in $\{\eta, \xi\}$ space, where $-1 \leq \eta \leq 1, 0 \leq \xi \leq \sqrt{3}(1 - \eta)$	13
2.3	Four different cases considered for integration: (a) non-singular; (b) coincident; (c) edge adjacent; and (d) vertex adjacent.	14
2.4	First polar coordinate transformation, $\{\eta^*, \xi^*\} \rightarrow \{\rho, \theta\}$, for the coincident integration. The variable t eventually replaces θ . Note that $P = P(\eta, \xi)$. . .	15
2.5	The source P is moved off the surface boundary in the direction of \mathbf{N} at a distance of ϵ	17
2.6	Geometry of the second polar coordinate transformation, $\{t, \xi\} \rightarrow \{\Lambda, \Psi\}$, for the coincident integration.	20
2.7	(a) Polar coordinate transformation employed in the Q element, $\{\eta^*, \xi^*\} \rightarrow \{\rho, \theta\}$; (b) Second polar coordinate transformation $\{\rho, \xi\} \rightarrow \{\Lambda, \Psi\}$ for the edge-adjacent integration.	23
2.8	(a) Initial polar coordinate transformation employed in both P and Q elements; (b) Final polar coordinate transformation $\{\rho_p, \rho_q\} \rightarrow \{\Lambda, \Psi\}$ for the vertex adjacent integration.	28
3.1	Illustration of a generic body with boundary Σ and domain Ω . The present SGBEM relies on a boundary-only formulation for FGMs. The source point is P (normal \mathbf{N}) and the field point is Q (normal \mathbf{n}).	33
3.2	Geometry and boundary conditions of the FGM unit cube problem with constant temperature on two planes. The faces with prescribed temperature are shaded.	37
3.3	The four meshes used for the convergence study of the FGM cube problem. .	38
3.4	Temperature profile in z direction for the FGM cube discretized with 432 elements and 294 nodes.	38
3.5	Variation of flux on the face $z = 0$ for different values of the material nonhomogeneity parameter β	39

3.6	The convergence of the temperature and the flux	40
3.7	Geometry and boundary conditions of the FGM cube problem with material gradation in 45° with the z -axis. The faces with prescribed temperature are shaded.	40
3.8	Continuous (used in BEM) and discrete (used in the FEM) representation of the conductivity k considering $\beta = 0.75$	41
3.9	Temperature profile along edge AA' (in z direction) for the FGM cube problem.	41
3.10	Flux distribution along BB' (in x direction) for the FGM cube problem.	42
3.11	The mesh of the FGM unit sphere graded along the z -direction.	42
3.12	Temperature variation with θ (degrees) in $X = 0$ plane.	43
3.13	Top view of the compressor.	44
3.14	The geometry and the boundary conditions of the analysis region.	45
3.15	The boundary element mesh for the analysis region of the compressor.	45
3.16	Temperature distribution in z -direction at edge of the blade.	46
3.17	Flux distribution along segment GF of the blade.	46
3.18	BEM contour plot of the temperature of the blade.	47
4.1	Isoparametric quadratic triangular element of 6 nodes. The intrinsic coordinate space is the right triangle in (ξ, η) space with $\xi \geq 0, \eta \geq 0$ and $\xi + \eta \leq 1$	56
4.2	Geometry and BCs for the cube problem. (a) Original 2D problem. (b) Equivalent 3D problem. The faces with prescribed temperature (Temp=1.0) are shaded (Example 1).	61
4.3	Temperature variation at edge ($y=0, z=1$) (shown with a dark solid line in Figure 4.2(b)) considering time $t = 0.75$ for the cube problem with homogeneous material (Example 1).	62
4.4	Temperature variation with distance (x coordinate) (shown with a dark solid line in Figure 4.2(b)) at different time levels for the cube problem with homogeneous material (Example 1).	62
4.5	Flux distribution along x direction at $y=1$ face for the cube problem with homogeneous material (Example 1).	63
4.6	Geometry and mesh of the cylinder problem (Example 2).	63
4.7	Variation of temperature along the radial coordinate (r) for the cylinder problem (Example 2).	64
4.8	Geometry and boundary conditions of the FGM cube problem with constant temperature on two planes. The faces with prescribed temperature are shaded (Example 3).	65
4.9	Temperature profile in z direction at different time levels for the FGM cube problem with constant temperature on two planes (Example 3).	66
4.10	Change of flux with time for the FGM cube with constant temperature on two planes (Example 3).	67
4.11	Color Contour plot of temperature at time $t = 0.5$ for the FGM cube with constant temperature on two planes (Example 3).	67
4.12	Geometry and boundary conditions of the FGM cube problem with linear heat flux. The face with prescribed temperature ($\phi = 1000x$) is shaded (Example 4).	68

4.13	Flux distribution along edge $[y=0, z=1]$ considering various times for the FGM cube problem with linear heat flux in one face (Example 4).	69
4.14	Temperature distribution along edge $[x=1, y=1]$ considering various times for the FGM cube with linear heat flux in one face (Example 4).	70
4.15	Color Contour plot of temperature at steady state for the FGM cube with linear heat flux in one face (Example 4).	70
4.16	Geometry and boundary conditions of the FGM cube problem with time-dependent boundary conditions. The face with prescribed time-dependent boundary condition is shaded (Example 5).	71
4.17	Temperature profile in z direction at $t = 1$ for the FGM cube problem with time-dependent boundary condition (Example 5).	71
5.1	Definition of the boundary value problem with boundary Σ and domain Ω . The source point is P (normal \mathbf{N}) and the field point is Q (normal \mathbf{n}). . . .	74
5.2	The local support of the Galerkin formulation at point P	84
5.3	Corner treatment in the Galerkin BEM	87
5.4	Thermal conductivity variation along the z direction. The quadratic variation is $k(z) = 5(1 + 2z)^2$, the trigonometric is $k(z) = 5(\cos(z) + 2\sin(z))^2$, and the exponential variation is $k(z) = 5e^{2z}$. The insert shows the geometry, mesh and the boundary conditions of the unit cube. The BEM mesh consists of 294 nodes and 108 quadratic triangular elements.	89
5.5	(a) Temperature profile in the z direction for different material variations, (b) Variation of flux at $z = 1$ surface with different values of nonhomogeneity parameter β	91
5.6	Convergence plots of temperature for the Green's function approach and the simple BEM approaches.	93
5.7	Convergence plots of flux for the Green's function approach and the simple BEM approach (Modified Helmholtz).	93
5.8	Representation of iso-surfaces for the three dimensional variation of thermal conductivity $k(x, y, z)$	94
5.9	(a) Contour plot of temperature for the cube with 3D material variation. (b) Contour plot of flux for the cube with 3D material variation.	95
5.10	The mesh and the geometry of the parallelepiped. For the sake of clarity meshes in four faces of the parallelepiped have been omitted in the figure in the top. The XY and YZ views are provided which shows the mesh in those faces.	97
5.11	(a) Thermal conductivity for the parallelepiped with cylindrical cavity. (b) Flux along z in $y = 0$ plane at edge $[x = 1, y = 0]$ of the parallelepiped. . . .	98
5.12	Contour plot of flux for cylindrical cavity in parallelepiped.	99
5.13	Geometry of the functionally graded rotor with 8-fold symmetry.	99
5.14	Profile of thermal conductivity in z direction. The quadratic variation of the conductivity is $k(z) = 20(1 + 420.7z)^2$	100
5.15	Thermal boundary conditions and the BEM mesh with 1584 elements and 3492 nodes.	100

5.16	The FEM mesh with 7600 elements and 35514 nodes.	101
5.17	Temperature distribution along the right top edge (indicated by the arrow). .	101
5.18	Temperature distribution along the circular contour on the top face.	102
5.19	BEM contour plot of the temperature of the rotor.	102
5.20	Radial heat flux along the interior edge (indicated by the arrow).	103
6.1	The local support of the Galerkin formulation at the source point P	119
6.2	A triangle in the 3D space is mapped to an equilateral triangular quadratic element in $\{\eta, \xi\}$ space, where $-1 \leq \eta \leq 1$, $0 \leq \xi \leq \sqrt{3}(1 - \eta)$	120
6.3	Four different cases considered for integration: (a) non-singular; (b) coincident; (c) edge adjacent; and (d) vertex adjacent.	122
6.4	Corner treatment in the Galerkin BEM.	123
6.5	Geometry and boundary conditions of the FGM unit cube problem with constant temperature on two planes. The BEM mesh consists of 294 nodes and 108 quadratic triangular elements.	125
6.6	Thermal conductivity variation along the z direction. The quadratic variation is $k(z) = 5(1 + 2z)^2$, the exponential variation is $k(z) = 5e^{2z}$ and the trigonometric variation is $k(z) = 5[\cos(0.2z) + 2\sin(0.2z)]^2$	131
6.7	Temperature profile in the z direction for different time levels for the FGM cube problem with quadratic material variation.	131
6.8	Temperature profile in the z direction for different time levels for the FGM cube problem with exponential material variation.	132
6.9	Temperature profile in the z direction for different time levels for the FGM cube problem with trigonometric material variation.	132
6.10	Variation of flux at $z = 0$ surface with time for the three variations.	133
6.11	Variation of flux at $z = 1$ surface with time for three types of material gradation.	133
6.12	Representation of iso-surfaces for the three dimensional variation of thermal conductivity $k \equiv k(x, y, z)$	134
6.13	The geometry, boundary conditions and the BEM mesh of the FGM unit cube problem with 3D material variation.	134
6.14	Variation of temperature with time at $(1, 1, 1)$ and $(0.5, 1, 0.5)$	135
6.15	Variation of flux with time at $(0.5, 0, 0.5)$	135
6.16	Geometry of the functionally graded rotor with 8-fold symmetry.	136
6.17	Profile of thermal conductivity and specific heat along z direction. The quadratic variation of the thermal conductivity and specific heat are $k(z) = 20(1 + 420.7z)^2$ and $c(z) = 5(1 + 420.7z)^2$, respectively.	136
6.18	Thermal boundary conditions and the BEM mesh on the rotor.	137
6.19	The FEM mesh with 7600 20-noded brick elements and 35514 nodes.	137
6.20	Temperature distribution along the right top edge (indicated by the arrow). .	138
6.21	Temperature distribution along the circular contour around the hole on the top face.	138
6.22	BEM contour plot of the temperature of the rotor at different time levels. . .	139
6.23	Radial heat flux along the interior edge (indicated by the arrow).	140

7.1	Definition of the boundary value problem with boundary Γ (including crack surfaces and outer boundary) and interior domain Ω	144
7.2	Fracture scheme using the dual BEM approach.	147
7.3	Local support for the Galerkin BEM.	150
7.4	A triangle in the 3D space is mapped to an equilateral triangular quadratic element in $\{\eta, \xi\}$ space.	150
7.5	Four different cases considered for integration: (a) non-singular; (b) coincident; (c) edge adjacent; and (d) vertex adjacent.	154
7.6	Corner treatment in the Galerkin BEM. Notice that the 6 normal vectors in the figure define the 6 planes that compose the semi-cylindrical geometry (with axis along the y-direction).	156
7.7	Geometry and boundary condition for penny shaped crack inside a cylinder.	157
7.8	Illustration of the BEM mesh for penny shaped crack inside a cylinder (1752 elements and 3502 nodes). The cylinder is clipped for visualization purpose.	158
7.9	Illustration of FEM mesh for penny shaped crack inside a cylinder (6,680 elements and 27,310 nodes); (a) half mesh; (b) surface-only display.	158
7.10	Temperature along radial distance from the center of the crack for $\beta = 0.0$ (homogeneous media).	159
7.11	Temperature along radial distance from the center of the crack for $\beta = 0.5$ (graded medium).	159
7.12	Temperature along radial distance from the center of the crack for $\beta = 1.0$ (graded medium).	161
7.13	Comparison of contour plots of temperature for the FEM and BEM results for the lower crack surface for $\beta = 1.0$	161
7.14	A contour plot showing the temperature distribution obtained from BEM on the wall and on the crack surface for $\beta = 0.5$	162
7.15	Geometry and boundary condition of three penny shaped cracks inside a cylinder.	162
7.16	BEM mesh for three penny shaped crack inside a cylinder with 5,180 elements and 7,752 nodes. The cylinder is clipped for visualization purpose.	163
7.17	The FEM mesh for three penny shaped cracks inside a cylinder (16,080 elements and 28,732 nodes); (a) mesh discretization; (b) Section through the middle of the FEM mesh only showing the surface of the elements; (c) Section through the crack plane showing the mesh around the crack front.	164
7.18	Temperature distribution along radial distance from the center for $\beta = 0.0$ on the three cracks inside a cylinder.	165
7.19	Temperature distribution along radial distance from the center for $\beta = 0.5$ on the three cracks inside a cylinder.	165
7.20	Temperature distribution along radial distance from the center for $\beta = 1.0$ on the three cracks inside a cylinder.	166
7.21	BEM temperature distribution on the upper (left) and lower (right) crack surfaces for the top, middle and bottom crack. The material nonhomogeneity parameter $\beta = 1.0$	167

7.22	Multiple cracks inside a cube. The complete BEM mesh consists of 900 elements and 2,033 nodes.	168
7.23	(a) Temperature distribution on the wall with a clip plane applied. (b) Clipped cube. (c) Clipped cube showing the temperature distribution of the upper crack surfaces and walls. is shown.	169
7.24	BEM flux distribution on the $z = 1$ (left) and $z = 0$ (right) plane of the cube.	170
8.1	Visualization pipeline: Steps of the visualization process.	174
8.2	Different types of dataset	176
8.3	ParaView : Flux results of a parallelepiped with a cylindrical cavity (from Chapter 5)	178
8.4	Contours: A scalar range and number of contours are specified for temperature profile.	179
8.5	Glyphs representing the flux for the parallelepiped with cavity.	180
8.6	Flux results of: (a) Model without using the clipper. (b) Model after clipping with a plane through the cavity.	181
8.7	Clippers	182
8.8	Visualizing the results on the crack surfaces using the two clippers.	182
8.9	ParaView : Shranked surfaces of the tetrahedrons created using Delaunay 3D.	184
8.10	Slices of the interior of the cube	186
8.11	Clipper to show that interior results are obtained for the FGM rotor.	187
8.12	Isosurface generated for the temperature for the FGM rotor problem.	188
8.13	Thresholding the temperature from 100 to 160 units for the FGM rotor problem.	189
8.14	NCSA CAVE: (a)Schematic Illustration (b) A cartoon model showing the projectors and the overall assembly.	190
8.15	The simplified flowchart of MechVR.	191
8.16	MechVR on the CAVE: (a) Isosurface (b) Slices and (c) hyperstreamlines.	192
8.17	Preliminary user interface of MechVR	193
8.18	Demonstration of MechVR inside CAVE	194
8.19	Screen shots of the VRML option in ParaView	196
8.20	VRML model showing the mesh of the three crack problem (Chapter 7)	196

Chapter 1

Introduction

Boundary element method (BEM) has been used mostly for problems in homogeneous media. For problems in three dimensions (3D) especially moving boundary problems BEM is highly efficient and suitable. Recently, graded material systems have been an important topic of research because of its superior properties. In this work, the main focus is to solve steady state as well as transient heat conduction and crack problems in 3D graded material systems using Galerkin (symmetric and non-symmetric) BEM. This chapter gives an introduction to the boundary element method and the graded material system. Several approaches that can be used to solve problems of potential in nonhomogeneous media are discussed. Finally the organization of the thesis is given.

1.1 Boundary Element Method (BEM)

The BEM has emerged as a powerful numerical method in computational mechanics in recent years. In this technique, the boundary of the domain is discretized, thereby reducing the dimension of the problem by one. For example, in three dimensions the discretization is performed on the bounding surface only; and in two dimensions, the discretization is on the boundary contour only. This leads to smaller linear systems, less computer memory requirements, and more efficient computation. For problems with unbounded domain this effect is more pronounced. In domain based methods, unbounded domains are truncated and approximated. BEM can automatically model the behaviour at infinity without setting up a mesh to approximate it. For moving boundary problems like crack propagation, remeshing an evolving geometry is much simpler with boundary element analysis than with a domain-based analysis such as the finite element method (FEM), especially if multiple interacting cracks are involved. In large scale numerical modeling using finite element methods, the mesh preparation is the most labour intensive and costly portion. Without the need of

dealing with the interior mesh, the BEM is more cost effective in mesh preparation. With these advantages, the BEM is indeed an essential part in today's computational techniques. Examples can be drawn from the fields of elasticity, geomechanics, structural mechanics, electromagnetism, acoustics, hydraulics, hydrodynamics and biomechanics among many.

1.1.1 Collocation

In collocation, the boundary integral equations (BIE) are enforced at specified points. In its simplest form, these collocation points are chosen to be the nodes used to discretize the boundary. Collocation BEM leads to non-symmetric matrices. Coupling with finite element method is not straight-forward. A typical collocation BIE can be defined as

$$\mathcal{B}(P) \equiv \phi(P) + \int_{\Sigma} \left(\frac{\partial}{\partial \mathbf{n}} G(P, Q) \right) \phi(Q) dQ - \int_{\Sigma} G(P, Q) \frac{\partial \phi}{\partial \mathbf{n}}(Q) dQ \quad (1.1)$$

where ϕ is the potential, $G(P, Q)$ is the Green's function, and P and Q are the source point and the field point, respectively. For an exact solution $\mathcal{B}(P) \equiv 0$.

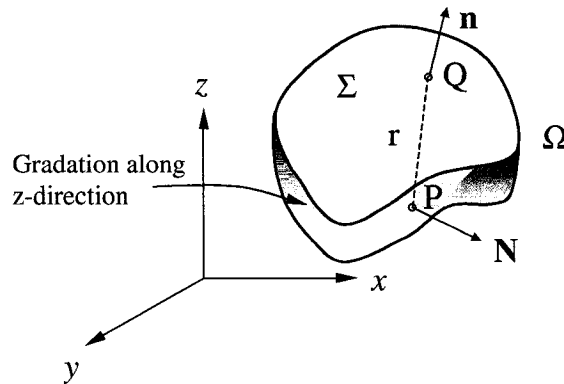


Figure 1.1: Illustration of a generic body with boundary Σ and domain Ω . The source point is P (normal \mathbf{N}) and the field point is Q (normal \mathbf{n}).

1.1.2 Galerkin

In contrast to collocation, the Galerkin approach does not require that the BIEs be satisfied at any point. Instead the equations are enforced in a weighted sense. Thus

$$\int_{\Sigma} \psi_k(P) \mathcal{B}(P) dP = 0 \quad (1.2)$$

In mathematical terminology, the ‘strong’ requirement of satisfying the BIEs at any given point is exchanged by a ‘weak’ solution in which the equations hold in integrated sense. This requirement has excellent geometric interpretation, the approximate Galerkin solution is the exact solution projected onto the subspace consisting of all functions which are a linear combination of the shape functions. The Galerkin solution therefore is the linear combination which is the ‘closest’ to the exact solution. In standard Galerkin procedure, the weight functions are composed of the shape functions that are non-zero at a node, as a result it gives the local support as illustrated in Figure 1.2.

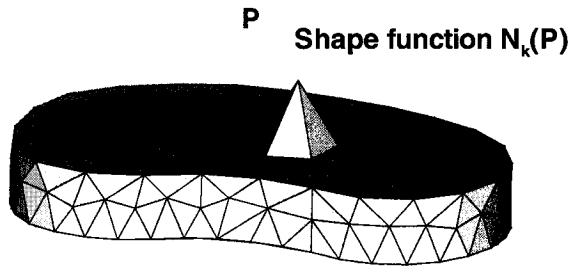


Figure 1.2: Local support for the Galerkin BEM.

In addition to this, in Galerkin BEM handling the hypersingular integrals are simpler than collocation. The Galerkin approximation allows standard continuous C^0 elements to be used for evaluation of hypersingular integrals. Galerkin BEM is in general more accurate and provides more elegant schemes for dealing with boundary corners and edges.

1.1.3 Symmetric Galerkin (SG)

The symmetric Galerkin boundary element method (SGBEM) possesses the attractive feature of producing a symmetric coefficient matrix [85, 88, 161]. The SGBEM is suitable for coupling with the popular finite element method (FEM) [13].

The hypersingular boundary integral equation (HBIE) for the derivative $\partial\phi/\partial\mathbf{n} = \nabla\phi \cdot \mathbf{n}$,

is usually written in the form

$$\mathcal{F}(P) \equiv \frac{\partial \phi}{\partial \mathbf{N}}(P) + \int_{\Sigma} \phi(Q) \frac{\partial^2 G}{\partial \mathbf{N} \partial \mathbf{n}}(P, Q) dQ - \int_{\Sigma} \frac{\partial G}{\partial \mathbf{N}}(P, Q) \frac{\partial \phi}{\partial \mathbf{n}}(Q) dQ = 0. \quad (1.3)$$

Eq. (1.3) is formally obtained by differentiating the standard BIE for potential, and then interchanging the derivative with the integral. Following the Galerkin approximation, the HBIE, Eq. (1.3), takes the form

$$\int_{\Sigma} \psi_k(P) \mathcal{F}(P) dP = 0, \quad (1.4)$$

If the kernels of the BIE and HBIE holds the symmetry properties, a SG formulation can be obtained. Symmetry of the coefficient matrix for a general mixed boundary value problem is achieved by the following simple arrangement. The BIE is employed on the Dirichlet surface, and the HBIE equation is used on the Neumann surface.

1.1.4 Boundary-based meshfree methods

Meshfree (or meshless) method has attracted a lot of attention from researchers in recent years, and it is regarded as a potential new generation of numerical methods in computational mechanics. A meshfree method does not require a mesh to discretize the problem domain or boundary, and the approximate solution is constructed entirely based on a set of scattered nodes.

Mukherjee and his research collaborators, have proposed one of the earliest boundary-based meshfree method called the Boundary Node Method (BNM) [126, 102, 26, 28, 27, 29, 30]. Other examples of boundary-based meshfree methods are the local Boundary Integral Equation (LBIE) approach [193, 165], the Boundary Cloud Method (BCM) [111], Hp cloud method [103, 104] and the Boundary Point Interpolation Method (BPIM) [114]. The LBIE, however, is not strictly a boundary method since it requires evaluation of integrals over certain surfaces that can be regarded as closure surfaces of boundary elements. Li and Aluru [111] have recently proposed a boundary only method called the BCM. This method is very similar to the BNM in that scattered boundary points are used for constructing approximating functions and these approximations are used with the appropriate BIEs for the problem. However, a key attractive feature of this work is that, unlike the BNM where boundary curvilinear co-ordinates must be employed, the usual Cartesian co-ordinates can be used in the BCM.

1.2 Functionally Graded Materials (FGMs)

Functionally graded materials or FGMs are a new generation of composites where the volume fraction of the FGM constituents vary gradually, giving a non-uniform microstructure with continuously graded macroproperties such as heat conductivity, specific heat, density, etc. Typically, in an FGM, one face of a structural component is an engineering ceramic that can resist severe thermal loading and the other face is a metal which has excellent structural strength. FGMs consisting of heat-resisting ceramic and fracture-resisting metal can improve the properties of thermal barrier systems because cracking and delamination, which are often observed in conventional layered systems, are reduced by proper smooth transition of material properties. Ceramic based FGMs have also been used for thermal protection – see Carrillo-Heian *et al.*[23]. FGMs are being developed as thermal barrier materials for combustion chambers, gas vanes, air vanes, nose cones, fuel valve sheets and piston crowns which undergo high-temperature gradient and high-thermal cycles in addition to wear. A comprehensive treatment of the science and technology of FGMs can be found, for example, in the books by Miyamoto *et al.*[122], Suresh and Mortensen [171], and the review article by Paulino *et al.*[138].

1.3 Approaches for solving problems in nonhomogeneous media using BEM

Approaches to treat problems of potential theory in nonhomogeneous media include the following:

- *Green's function* [34, 35]
- *Domain integral evaluation* [125, 2, 135, 133, 142]
- *Variable transformation.* [172, 173]

In the *Green's function approach*, the Green's function has to be derived and a boundary-only formulation can be obtained [34, 35]. A drawback of this approach is that each different material variation requires a different fundamental solution, and thus the kernels for the BEM implementation are different from the standard kernels usually employed for homogeneous problems. As a result, each time a new computer code has to be developed. Moreover, if the treatment of singularity involves analytical integration, then the process becomes much involved [176]. Several approaches have been developed to evaluate *domain integrals*

associated with boundary element formulations including approximate particular solution methods [125, 2], dual reciprocity methods [135], and multiple reciprocity methods [133, 142].

The particular solution methods and dual reciprocity methods can be considered more or less to be equivalent in nature [92]. These methods have been widely used on the axiom that the domain integral in the boundary integral formulation is eliminated. In these methods the inhomogeneous term of the governing differential equation is approximated by a simple function such as $(1+r)$ [127] or radial basis functions (RBFs) [67, 178]. The mathematical properties and the convergence rates of the RBF approximations have been studied extensively [67, 66]. In these techniques, the boundary-only nature of the BEM is lost.

In this thesis a *transformation approach*, called the “simple BEM,” for potential theory problems in nonhomogeneous media is proposed, where nonhomogeneous problems are transformed into known problems in homogeneous media. The method leads to a pure boundary-only formulation.

1.4 Thesis Organization

In Chapter 2, the evaluation of the hypersingular (and singular) integrals in GBEM is explained. A hybrid analytical/numerical approach based on ‘limit to the boundary approach’ is adopted. Hypersingular integrals that arise in the SGBEM formulation for heat conduction in an exponentially graded material is evaluated.

In Chapter 3, the numerical implementation of the SGBEM for heat conduction in exponential graded material is described.

Transient heat conduction in exponentially graded materials using a Laplace transform BEM is presented in Chapter 4. The Green’s function is derived first. The problem is formulated in the Laplace space and numerical inversion of the Laplace transform was carried out to get back to the time domain.

A novel simple boundary element technique to address problems of potential flow for nonhomogeneous media is presented in Chapter 5. By using a transformation approach this method can handle material variation that are quadratic, exponential, and trigonometric in nature, and also the functional variation can be in one, two or three dimensions. By simple modification of the boundary conditions, standard codes for homogeneous material problems are used.

Chapter 6 develops the ‘simple’ BEM for transient heat conduction problems. By simple variable transformation, transient heat conduction problems in functionally graded materials for three different classes of material variation (quadratic, exponential, trigonometric) can

be transformed into the homogeneous diffusion problem. FGM transient heat conduction problem with constant diffusivity are solved. A Laplace transform Galerkin BEM formulation has been presented here in order to implement the methodology.

Chapter 7 describes the 'simple BEM' for solving multiple cracks in problems governed by potential theory. Steady state heat conduction problems with functionally graded thermal conductivity are investigated.

Chapter 8 investigates the scientific visualization including virtual reality and web based visualization. State of art visualization techniques and how they can be used for visualizing BEM results has been studied and explored.

Finally, the thesis ends with some closing remarks and comments on future research in Chapter 9.

Chapter 2

Evaluation of Singular and hypersingular integrals in GBEM for FGMs

This chapter discusses the evaluation of hypersingular integrals that arises in the Galerkin boundary element method (GBEM) (e.g. symmetric and non-symmetric) formulation for FGMs. The procedure for treating the hypersingular integral are applicable to other less singular integrals. The methods are first described in the simplest possible continuous approximation, a linear element. The two key features of the singular integration are first, the definition of the integrals as limits from the exterior of the domain, and second, the combination of analytical and numerical evaluation procedures. The boundary limit provides a consistent scheme for defining all singular integrals, weakly singular, strongly singular, and hypersingular, resulting in direct evaluation algorithms. The key task for the direct evaluation will be to isolate the divergent terms and to show that they cancel. Symbolic computation is exploited to simplify the work involved in carrying out the limit process and analytic integration, and example Maple codes are provided.

This chapter is organized as follows. Section 2.1 gives an introduction to the singular integrals in GBEM and techniques that are found in the literature to evaluate them. The singular and hypersingular integrals that arise in the BEM formulation for heat conduction in exponentially graded materials are presented in Section 2.2. In Section 2.3 the details of the treatment of hypersingular integrals are presented. Finally the chapter ends with some concluding remarks in Section 2.4

2.1 Introduction

One of the challenges in a Galerkin (and symmetric Galerkin) BEM formulation is the evaluation of singular double surface integrals (four dimensional integrals in parametric space). In a Galerkin approximation, the integration is carried out with respect to both the field point and the source point. For a numerical implementation, this means that the integrals are evaluated for every pair of elements. Singular integrals occur as the Green's function and its derivatives diverge when the field point approaches the source point. An integral is therefore singular if the elements are *coincident*, or are *adjacent*, sharing either an edge or a vertex. The required double integrations of hypersingular kernel functions have in a way limited the implementations of the SGBEM.

In a broad sense, the strategies proposed to address such class of problems can be classified as regularization, finite part, and direct approach. The regularization techniques employ many procedures such as use of simple solutions, and application of Stokes theorem [112, 57, 59]. The finite part approach is based on extracting the principal value of the singular integral, and direct evaluation based on multiple analytic integration [81, 3, 22, 146]. A direct approach [74, 73], using neither Stokes theorem nor finite-part integral, is revisited and adopted herein. As previous works [74, 73] only considered the simple Laplace equation, one of the goals of this work is to demonstrate that the direct “limit to the boundary” approach works very well for evaluating the singular and hypersingular integrals for the special FGM Green's function. This approach is also helpful to treat other complicated Green's functions.

A direct treatment of the hypersingular double integrals using a hybrid analytical/numerical approach applied to the hypersingular integrals that arise in the SGBEM formulation for heat conduction in an exponentially graded material is presented in this chapter. The details of the SGBEM formulation and the numerical implementation are presented in the next chapter. The implementation is a pure boundary-only formulation without any domain integral. It relies on the Green's function (GF) for the partial differential equation incorporating the material gradation. In order to handle the complexity of the FGM Green's function, the direct limit approach of reference [73] needs to be modified. This direct limit approach is shown to be suitable for dealing with complicated Green's functions, which appear in applications such as those involving FGMs.

2.2 Singular and hypersingular boundary integrals

Let the FGM be defined by the thermal conductivity that varies exponentially in one Cartesian coordinate, i.e.

$$k(x, y, z) = k(z) = k_0 e^{2\beta z} , \quad (2.1)$$

where β denotes the material nonhomogeneity parameter. Steady state isotropic heat conduction in a solid is governed by the equation

$$\nabla \cdot (k(x, y, z) \nabla \phi) = 0 . \quad (2.2)$$

where \cdot denotes the inner product, $\phi = \phi(x, y, z)$ is the temperature function, $k(x, y, z)$ is the thermal conductivity which can be a function of the Cartesian coordinates. The fundamental solution or the Green's function is derived [75, 110] as

$$G(P, Q) = \frac{e^{\beta(-r+R_z)}}{4\pi r} \quad (2.3)$$

where

$$R_z = z_Q - z_P \quad \text{and} \quad r = \|\mathbf{R}\| = \|\mathbf{Q} - \mathbf{P}\|, \quad (2.4)$$

P and Q are the source point and the field point, respectively.

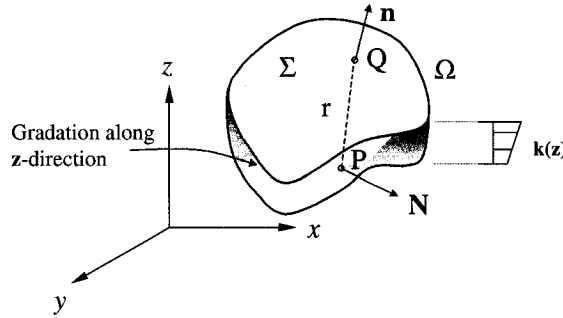


Figure 2.1: Illustration of a generic body with boundary Σ and domain Ω . The present SGBEM relies on a boundary-only formulation for FGMs. The source point is P (normal \mathbf{N}) and the field point is Q (normal \mathbf{n}).

The singular boundary integral equation (BIE) for surface temperature $\phi(P)$ on the boundary Σ (see Figure 2.1) is

$$\phi(P) + \int_{\Sigma} F(P, Q) \phi(Q) dQ = \int_{\Sigma} G_S(P, Q) \mathcal{F}(Q) dQ , \quad (2.5)$$

and the kernel functions are

$$\begin{aligned}
G_S(P, Q) &= \frac{G(P, Q)}{k(z_Q)} = -\frac{1}{4k_0\pi} \frac{e^{\beta(-r-z_Q-z_P)}}{r} \\
F(P, Q) &= \frac{\partial}{\partial n} G(P, Q) - 2\beta n_z G(P, Q) \\
&= -\frac{e^{\beta(-r+R_z)}}{4\pi} \left(\frac{\mathbf{n} \cdot \mathbf{R}}{r^3} + \beta \frac{\mathbf{n} \cdot \mathbf{R}}{r^2} + \beta \frac{n_z}{r} \right).
\end{aligned} \tag{2.6}$$

where the surface flux,

$$\mathcal{F}(Q) = -k(z_Q) \frac{\partial}{\partial n} \phi(Q). \tag{2.7}$$

The hypersingular boundary integral equation (HBIE) for surface temperature $\mathcal{F}(P)$ on the boundary Σ is defined by,

$$\mathcal{F}(P) + \int_{\Sigma} W(P, Q) \phi(Q) dQ = \int_{\Sigma} S(P, Q) \mathcal{F}(Q) dQ. \tag{2.8}$$

The kernel functions are computed as

$$\begin{aligned}
S(P, Q) &= -k(z_P) \frac{\partial}{\partial N} G_S(P, Q) \\
&= \frac{e^{\beta(-r-R_z)}}{4\pi} \left(\frac{\mathbf{N} \cdot \mathbf{R}}{r^3} + \beta \frac{\mathbf{N} \cdot \mathbf{R}}{r^2} - \beta \frac{N_z}{r} \right)
\end{aligned} \tag{2.9}$$

and

$$\begin{aligned}
W(P, Q) &= -k(z_P) \frac{\partial}{\partial N} F(P, Q) \\
&= \frac{k_0}{4\pi} e^{\beta(-r+z_Q+z_P)} \left(3 \frac{(\mathbf{n} \cdot \mathbf{R})(\mathbf{N} \cdot \mathbf{R})}{r^5} + 3\beta \frac{(\mathbf{n} \cdot \mathbf{R})(\mathbf{N} \cdot \mathbf{R})}{r^4} \right. \\
&\quad + \frac{\beta^2 (\mathbf{n} \cdot \mathbf{R})(\mathbf{N} \cdot \mathbf{R}) - \beta (N_z \mathbf{n} - n_z \mathbf{N}) \cdot \mathbf{R} - \mathbf{n} \cdot \mathbf{N}}{r^3} \\
&\quad \left. - \beta \frac{\beta (N_z \mathbf{n} - n_z \mathbf{N}) \cdot \mathbf{R} + \mathbf{n} \cdot \mathbf{N}}{r^2} - \beta^2 \frac{N_z n_z}{r} \right).
\end{aligned} \tag{2.10}$$

In this work, the direct limit procedure is employed to define and evaluate the singular integrals. If the limit is taken with the source point P approaching the boundary from *outside* the domain, then the “free terms” $\phi(P)$ in the BIE (Eq. (2.5)) and $\mathcal{F}(P)$ in the

HBIE (Eq. (2.8)) are not present. Thus, the exterior limit BIE and HBIE take the form

$$\begin{aligned}\mathcal{P}_s(P) &\equiv \int_{\Sigma} F(P, Q)\phi(Q) dQ - \int_{\Sigma} G_S(P, Q)\mathcal{F}(Q) dQ = 0, \\ \mathcal{F}_s(P) &\equiv \int_{\Sigma} W(P, Q)\phi(Q) dQ - \int_{\Sigma} S(P, Q)\mathcal{F}(Q) dQ = 0,\end{aligned}\quad (2.11)$$

where \mathcal{P}_s denotes the equation for the surface temperature (potential) and \mathcal{F}_s denotes the equation for the surface flux. The free terms are automatically incorporated in the “*exterior limit*” evaluation of the $F(P, Q)$ and $S(P, Q)$ integrals. Thus, a separate computation of these free terms is avoided, and they are obtained as a natural outcome of the direct limit procedure [116].

The surface temperature and surface flux are approximated in terms of values at element nodes Q_j and shape functions $\psi_j(Q)$, *i.e.*,

$$\phi(Q) = \sum_j \phi(Q_j)\psi_j(Q), \quad \mathcal{F}(Q) = \sum_j \mathcal{F}(Q_j)\psi_j(Q). \quad (2.12)$$

In a Galerkin approximation, Eq. (2.11) is enforced in an average sense, with the shape functions employed as the weighting functions. Therefore, the Galerkin boundary integral equations take the form

$$\int_{\Sigma} \psi_k(P)\mathcal{P}_s(P) dP = 0 \quad (2.13)$$

$$\int_{\Sigma} \psi_k(P)\mathcal{F}_s(P) dP = 0. \quad (2.14)$$

In this chapter, the analysis for a linear element will be considered in detail, as this forms the basis for handling higher order interpolations. An equilateral triangle parameter space $\{\eta, \xi\}$, where

$$-1 \leq \eta \leq 1, \quad 0 \leq \xi \leq \sqrt{3}(1 - |\eta|) \quad (2.15)$$

will be employed (see Figure 2.2). This choice of parameter space is convenient for executing the coincident integration, as will be explained in the next section. The three linear shape functions are

$$\psi_1(\eta, \xi) = \frac{\sqrt{3}(1 - \eta) - \xi}{2\sqrt{3}}, \quad \psi_2(\eta, \xi) = \frac{\sqrt{3}(1 + \eta) - \xi}{2\sqrt{3}}, \quad \psi_3(\eta, \xi) = \frac{\xi}{\sqrt{3}}. \quad (2.16)$$

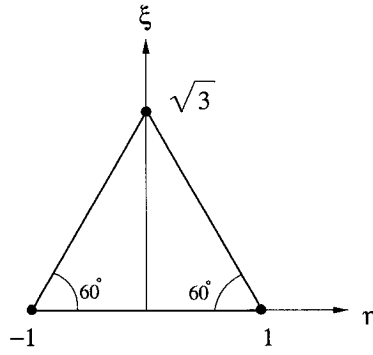


Figure 2.2: Isoparametric equilateral triangular linear element in $\{\eta, \xi\}$ space, where $-1 \leq \eta \leq 1$, $0 \leq \xi \leq \sqrt{3}(1 - |\eta|)$.

2.3 Evaluation of singular double integrals

For three dimensional problems, there are four typical configurations for the two elements containing source point P and field point Q (see Figure 2.3). Thus the following four distinct situations regarding the singularity must be considered:

- *Non-singular case*, when the source point P and the field point Q lie on distinct elements, that do not share a common vertex or edge.
- *Coincident case*, when the source point P and the field point Q lie in the same element;
- *Edge adjacent case*, when two elements share a common edge; and
- *Vertex adjacent case*, when a vertex is the only common node between the two elements.

The non-singular integrals can be evaluated using standard Gaussian quadrature formulas. In the direct limit approach for evaluating the singular integrals, the integrals for the coincident and the edge-adjacent cases are forced to be finite by moving the source P off the boundary in the direction \mathbf{N} at a distance of ϵ . The next step is to employ polar coordinate transformations and then integrate analytically with a *fixed distance from the singularity*. After the exact integration, the limit $\epsilon \rightarrow 0$ is considered. It will be demonstrated that the coincident and the edge-adjacent hypersingular integrals are separately divergent, producing terms of the form $\log(\epsilon)$. However, the divergent terms from the coincident case can be shown to cancel out with the divergent terms from the edge-adjacent case, and therefore the divergent terms are removed exactly in this approach. Taking the limit $\epsilon \rightarrow 0$ back to the boundary results in finite expressions, thus giving a well behaved integral. Once the divergent terms have been identified and removed, the remaining terms of the integral can be

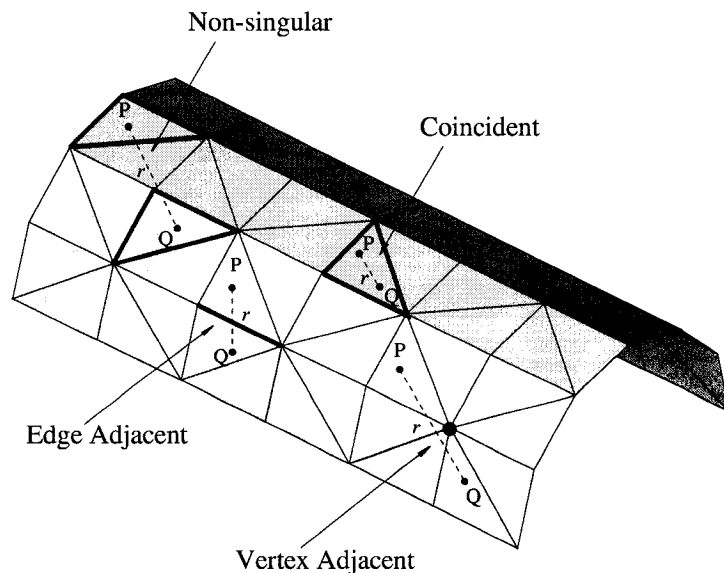


Figure 2.3: Four different cases considered for integration: (a) non-singular; (b) coincident; (c) edge adjacent; and (d) vertex adjacent.

evaluated using standard numerical quadrature. The discussion here about $\log(\epsilon)$ singularity, etc. applies only to the hypersingular equation. The direct approach has been designed to handle this worst case, but apply equally to the less-singular integrals.

Compared to the simple Laplace equation treated in [73], the challenge here is to work with the complicated hypersingular kernel function $W(P, Q)$, Eq. (2.10). In particular, the exponential in this function precludes a complete analytic integration as in [73], and thus additional procedures are required.

2.3.1 Coincident Integration

The details of the procedure to evaluate the hypersingular integrals involving the kernel $W(P, Q)$ are described in this section. However, the integration of the kernels G_S , $S(P, Q)$ or $F(P, Q)$ can be handled in exactly the same manner, with the added simplification that no divergent terms appear in the limit $\epsilon \rightarrow 0$. When the source point P and the field point Q lie within the same element E (see Figure 2.3), $E_P = E_Q = E$, and the coincident integral to be evaluated is

$$\int_E \psi_k(P) \int_E \phi(Q) W(P, Q) dQ dP = \sum_{j=1}^3 \phi(Q_j) \int_E \psi_k(P) \int_E \psi_j(Q) W(P, Q) dQ dP, \quad (2.17)$$

where E is defined by nodes P_k , $1 \leq k \leq 3$. Let the parametric variables for the outer P integration be denoted by (η, ξ) , and that for Q by (η^*, ξ^*) . Transferring the integral to the parametric space ($dQ \rightarrow J_Q d\xi^* d\eta^*$ and $dP \rightarrow J_P d\xi d\eta$) introduces the Jacobians J_Q and J_P . For coincident integration considering linear elements, the J_Q and J_P are equal and constant. The Jacobians can be conveniently incorporated into the hypersingular kernels, i.e.

$$J_P^2 W(P, Q) = \frac{k_0}{4\pi} e^{\beta(-r+z_Q+z_P)} \left(3 \frac{(J_P \mathbf{N} \cdot \mathbf{R})^2}{r^5} + 3\beta \frac{(J_P \mathbf{N} \cdot \mathbf{R})^2}{r^4} + \frac{\beta^2 (J_P \mathbf{N} \cdot \mathbf{R})^2 - J_P^2}{r^3} - \beta \frac{J_P^2}{r^2} - \beta^2 \frac{(J_P N_z)^2}{r} \right). \quad (2.18)$$

- *First Polar Coordinate transformation* $\{\eta^*, \xi^*\} \rightarrow \{\rho, \theta\}$: For the inner Q integration, the first step is to define a polar coordinate system centered at $P = (\eta, \xi)$,

$$\eta^* - \eta = \rho \cos(\theta), \quad \xi^* - \xi = \rho \sin(\theta) \quad (2.19)$$

as shown in Figure 2.4. Polar coordinate transformations centered at the singularity are particularly effective, as the Jacobian of the transformation, $\rho d\rho$, reduces the order of the singularity. This aspect will be used in all the singular integrations.

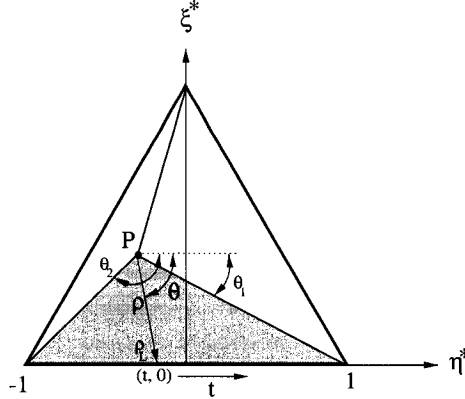


Figure 2.4: First polar coordinate transformation, $\{\eta^*, \xi^*\} \rightarrow \{\rho, \theta\}$, for the coincident integration. The variable t eventually replaces θ . Note that $P = P(\eta, \xi)$.

The upper limit of ρ ($0 < \rho < \rho_L(\theta)$) is different for the three edges of the triangle and consequently, the (ρ, θ) integration is split into three sub-triangles (see Figure 2.4). It suffices to consider the calculation for the lower sub-triangle (shaded portion of the triangle in Figure 2.4). By exploiting the symmetry of the equilateral parametric

space, the remaining sub-triangles are handled by rotating the element and employing the formulas for the lower sub-triangle associated with the edge $\xi^* = 0$.

For the lower sub-triangle, the integration limits are

$$0 \leq \rho \leq \rho_L \quad \text{and} \quad \Theta_1 \leq \theta \leq \Theta_2 \quad (2.20)$$

where

$$\rho_L = -\frac{\xi}{\sin(\theta)}, \quad \Theta_1 = -\frac{\pi}{2} - \tan^{-1}\left(\frac{1+\eta}{\xi}\right), \quad \Theta_2 = -\frac{\pi}{2} + \tan^{-1}\left(\frac{1-\eta}{\xi}\right). \quad (2.21)$$

In the limit to the boundary approach as P is moved off the boundary in the direction of the source normal \mathbf{N} at distance of ϵ , P is replaced by $P + \epsilon\mathbf{N}$ for the exterior boundary limit (see Figure 2.5), therefore, the distance $r = \|\mathbf{Q} - \mathbf{P}\|$ takes the simple form

$$r^2(\rho, \theta) = \epsilon^2 + a^2(\theta)\rho^2, \quad (2.22)$$

where

$$a^2(\theta) = a_{cc} \cos^2(\theta) + a_{cs} \cos(\theta) \sin(\theta) + a_{ss} \sin^2(\theta) \quad (2.23)$$

The three coefficients a_{cc} , a_{cs} , a_{ss} , depend solely upon the coordinates of the element nodes (a^2 is a positive quantity), i.e.

$$\begin{aligned} a_{cc} &= 1/4[(x_2 - x_1)^2 + (y_2 - y_1)^2 + (z_2 - z_1)^2], \\ a_{cs} &= 1/(2\sqrt{3})[(x_2 - x_1)(x_1 + x_2 - 2x_3) + (y_2 - y_1)(y_1 + y_2 - 2y_3) \\ &\quad + (z_2 - z_1)(z_1 + z_2 - 2z_3)], \\ a_{ss} &= 1/12[(y_1 + y_2 - 2y_3)^2 + (x_1 + x_2 - 2x_3)^2 + (z_1 + z_2 - 2z_3)^2]. \end{aligned} \quad (2.24)$$

Here $P_k = (x_k, y_k, z_k)$, ($k = 1, 2, 3$) are the (x, y, z) coordinates of the element nodes.

The term $J_P \mathbf{N} \cdot \mathbf{R}$ in the kernel (see expression (2.18)) becomes $-\epsilon J_P$ as P is moved to $P + \epsilon\mathbf{N}$. The shape function of P , $\psi_j(P)$ is a function of η and ξ . With the polar coordinate transformation centered on P (Eq. (2.19)), the shape function $\psi_j(Q)$ is a

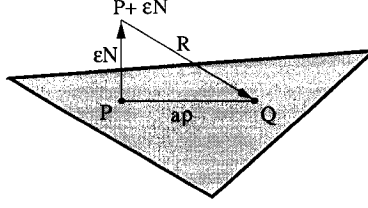


Figure 2.5: The source P is moved off the surface boundary in the direction of \mathbf{N} at a distance of ϵ .

linear function of ρ , i.e.

$$\psi_j(Q) = c_{j,0}(\eta, \xi) + c_{j,1}(\eta, \xi, \theta)\rho = \sum_{m=0}^1 c_{j,m}\rho^m \quad (2.25)$$

$$\psi_j(P) = c_{j,0}(\eta, \xi). \quad (2.26)$$

As a result of the polar transformation, $(z_Q - z_P)$ can be written as $\alpha\rho$ where α is a function of θ and z coordinates of the element vertices, i.e.,

$$\alpha = \frac{1}{2} \cos(\theta) + \frac{1}{2\sqrt{3}}(2z_3 - z_1 - z_2) \sin(\theta) \quad (2.27)$$

Since $e^{2\beta z_P}$ is independent of ρ , it is taken outside of the ρ integral, and the exponential term in Eq. (2.18) can be written as

$$\begin{aligned} e^{\beta(-r+z_Q+z_P)} &= e^{\beta(-r+z_Q-z_P+2z_P)} \\ &= e^{2\beta z_P} e^{\beta(-\sqrt{\epsilon^2+a^2\rho^2}+\alpha\rho)}. \end{aligned} \quad (2.28)$$

Employing the boundary limit procedure and expressing the kernel function in polar coordinates, one obtains Eq. (2.17) as

$$\begin{aligned} &\frac{1}{4\pi} \sum_{m=0}^1 \int_{-1}^1 d\eta \int_0^{\sqrt{3}(1-|\eta|)} \psi_k(\eta, \xi) d\xi \int_{\Theta_1}^{\Theta_2} c_{j,m} d\theta \int_0^{\rho_L} \rho^{m+1} \\ &e^{\beta(-\sqrt{\epsilon^2+a^2\rho^2}+\alpha\rho)} \left(\frac{3c^2 J_P^2}{(\epsilon^2 + a^2\rho^2)^{5/2}} - \frac{J_P^2}{(\epsilon^2 + a^2\rho^2)^{3/2}} + \frac{3\beta \epsilon^2 J_P^2}{(\epsilon^2 + a^2\rho^2)^2} \right. \\ &\left. + \frac{\beta^2 \epsilon^2 J_P^2}{(\epsilon^2 + a^2\rho^2)^{3/2}} - \frac{\beta J_P^2}{\epsilon^2 + a^2\rho^2} - \frac{\beta^2 J_P^2}{\sqrt{\epsilon^2 + a^2\rho^2}} \right) d\rho. \end{aligned} \quad (2.29)$$

Here J_P^z denotes $J_P N_z$, which is the Jacobian J_P multiplied by the z component of the normal at P , i.e. N_z .

- *First Taylor expansion of the exponential function:* Due to the exponential term in the kernel, it is not possible to integrate the entire expression analytically. Our goal for analytic integration is to explicitly identify the divergent terms in the integral. This can be done by employing a Taylor expansion of the exponential term. Expanding up to the first two terms is sufficient to identify the divergent terms, i.e.

$$e^{\beta(-\sqrt{\epsilon^2+a^2\rho^2}+\alpha\rho)} = 1 + \beta \left(-\sqrt{\epsilon^2 + a^2\rho^2} + \alpha\rho \right) + \mathcal{O}(\rho^2). \quad (2.30)$$

As the remainder of the expansion is of order ρ^2 , this expansion leads to a sufficiently well behaved expression for the remainder of the integral so that numerical quadrature can be safely used.

- *First analytical integration (on ρ):* Incorporating the Taylor expansion, the integral to be evaluated analytically is

$$\begin{aligned} & \sum_{m=0}^1 \int_0^{\rho_L} \rho^{m+1} \left(1 + \beta \left(-\sqrt{\epsilon^2 + a^2\rho^2} + \alpha\rho \right) \right) \left(\frac{3\epsilon^2 J_P^2}{(\epsilon^2 + a^2\rho^2)^{5/2}} \right. \\ & \left. - \frac{J_P^2}{(\epsilon^2 + a^2\rho^2)^{3/2}} + \frac{3\beta\epsilon^2 J_P^2}{(\epsilon^2 + a^2\rho^2)^2} + \frac{\beta^2\epsilon^2 J_P^2}{(\epsilon^2 + a^2\rho^2)^{3/2}} - \frac{\beta J_P^2}{\epsilon^2 + a^2\rho^2} - \frac{\beta^2(J_P^z)^2}{\sqrt{\epsilon^2 + a^2\rho^2}} \right) d\rho. \end{aligned} \quad (2.31)$$

For $m = 0$ (see Eq. (2.25)), the exact analytical integration results in

$$\begin{aligned} F_0 = & \frac{\beta^3}{2}(J_P^z)^2 \left(1 - \frac{\alpha}{a} \right) \rho_L^2 + \frac{\beta^2}{a} \left[\left(1 - \frac{\alpha}{a} \right) J_P^2 - (J_P^z)^2 \right] \rho_L \\ & + 2\beta J_P^2 \frac{\alpha}{a^3} + \beta J_P^2 \frac{\alpha}{a^3} \log(\epsilon) + \frac{J_P^2}{a^3 \rho_L}. \end{aligned} \quad (2.32)$$

All terms are well behaved at $\epsilon = 0$ except for the last two. However the expression

$$\frac{\alpha\beta J_P^2 \log(\epsilon)}{a^3} \quad (2.33)$$

is *not* the divergent term that is being sought. It is easily seen that this term cancels out in the subsequent integration over θ . As the term does not contain ρ_L , a complete integration over $0 \leq \theta \leq 2\pi$ can be considered. Note that α is a linear function of $\cos(\theta)$

and $\sin(\theta)$, and thus satisfies $\alpha(\pi + \theta) = -\alpha(\theta)$. From Eq. (2.23), $a(\pi + \theta) = a(\theta)$, and from Eq. (2.25), $c_{j,m}$ is independent of θ for $m = 0$. Hence, the subsequent integration of the $\log(\epsilon)$ term on expression (2.33) results in zero, i.e.

$$-\log(\epsilon)c_{j,0}(\eta, \xi)J_P^2 \int_0^{2\pi} \frac{\alpha\beta}{a^3} d\theta = 0 . \quad (2.34)$$

For $m = 1$, the analytical integration becomes,

$$F_1 = \frac{\beta^3}{2}(J_P^z)^2 \left(1 - \frac{\alpha}{a}\right) \rho_L^3 + \frac{\beta^2}{2a} \left[\left(1 - \frac{\alpha}{a}\right) J_P^2 - (J_P^z)^2 \right] \rho_L^2 + 2 \frac{J_P^2}{a^3} + \frac{J_P^2}{a^3} \log(\epsilon) - J_P^2 \frac{\log(a\rho_L)}{a^3}. \quad (2.35)$$

A divergent term similar to expression (2.33) also appears in this case. This term is also seen to cancel out in the subsequent integration over θ . The coefficient $c_{j,1}(\eta, \xi, \theta)$ is linear in $\cos(\theta)$ and $\sin(\theta)$, and therefore satisfies $c_{j,1}(\eta, \xi, \pi + \theta) = -c_{j,1}(\eta, \xi, \theta)$. Thus

$$-\log(\epsilon)J_P^2 \int_0^{2\pi} \frac{c_{j,1}(\eta, \xi, \theta)}{a^3} d\theta = 0 . \quad (2.36)$$

This first analytic integration is not sufficient to display the divergent term, and the subsequent integration on θ will not pose any problem. It is the next integration on ξ , (cf. Eq. (2.29)) which has to be dealt with analytically. The analytic integration over ρ produces results that behave as $1/\rho_L$ (see the last term in Eq. (2.32)) and, from Eq. (2.21), $\rho_L = -\xi/\sin(\theta)$. This term is capable of producing a $\log(\epsilon)$ contribution upon ξ integration with the lower limit of $\xi = 0$. Therefore it is necessary to interchange the order of the integration on θ and ξ in order to identify the divergent term through analytical integration.

- *Variable Transformation* $\{\theta\} \rightarrow \{t\}$: As the limits of the θ integration (i.e. Θ_1 and Θ_2) depend on ξ and η , the integration on the variable θ and ξ is not interchangeable. To circumvent this problem, a new variable t ($-1 \leq t \leq 1$) is introduced via

$$\theta = -\frac{\pi}{2} + \tan^{-1} \left(\frac{t - \eta}{\xi} \right), \quad \frac{d\theta}{dt} = \frac{\xi}{\xi^2 + (t - \eta)^2}, \quad (2.37)$$

which also results in $\rho_L = (\xi^2 + (t - \eta)^2)^{1/2}$. As depicted in Figure 2.4, t is the ‘end-point’ $(t, 0)$ of ρ on the ξ^* -axis.

Interchanging the order of integration and transforming the variable from $\theta \rightarrow t$, the

integral (cf. Eq. (2.31)) for $m = 0$ can be written as,

$$\frac{J_P^2}{4\pi} \int_{-1}^1 d\eta \int_{-1}^1 dt \int_0^{\sqrt{3}(1-|\eta|)} \psi_k(\eta, \xi) c_{j,0} F_0(\rho_L) d\xi . \quad (2.38)$$

- *Second Polar Coordinate transformation* $\{t, \xi\} \rightarrow \{\Lambda, \Psi\}$: From Eq. (2.37), the singularity is now at $t = \eta$, $\xi = 0$, and another polar coordinate transformation $\{\Lambda, \Psi\}$, replacing $\{t, \xi\}$, is employed (see Figure 6),

$$t = \Lambda \cos(\Psi) + \eta, \quad \xi = \Lambda \sin(\Psi) . \quad (2.39)$$

The goal is to integrate Λ analytically. With the two changes of variables, $\theta \rightarrow t$ and $\{t, \xi\} \rightarrow \{\Lambda, \Psi\}$, $\cos(\theta)$ becomes $\cos(\Psi)$ and $\sin(\theta)$ becomes $-\sin(\Psi)$. Thus, $a(\theta)$, Eq. (2.23), becomes simply $a(\Psi)$ and is a constant as far as the Λ integration is concerned. As shown in Figure 2.6, the $\{t, \xi\}$ domain is a rectangle, and integrating over $\{\Lambda, \Psi\}$ will necessitate a decomposition into three subdomains

$$0 \leq \Psi \leq \Psi_1, \Psi_1 \leq \Psi \leq \pi - \Psi_2, \text{ and } \pi - \Psi_2 \leq \Psi \leq \pi, \quad (2.40)$$

where

$$\Psi_1 = \tan^{-1} \left(\frac{\sqrt{3}(1-|\eta|)}{1-\eta} \right), \quad \Psi_2 = \tan^{-1} \left(\frac{\sqrt{3}(1-|\eta|)}{1+\eta} \right) \quad (2.41)$$

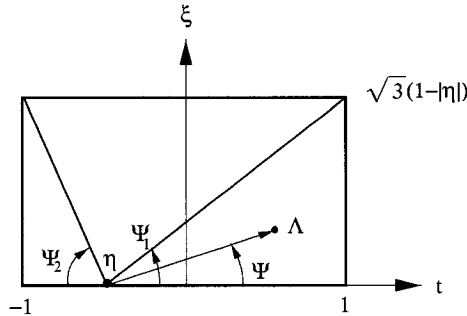


Figure 2.6: Geometry of the second polar coordinate transformation, $\{t, \xi\} \rightarrow \{\Lambda, \Psi\}$, for the coincident integration.

- *Second Taylor expansion of the exponential function*: With this final coordinate transformation, the P shape functions are linear in Λ , as are the coefficients $c_{j,m}$ from the Q shape functions. Part of the exponential term, $e^{2\beta z_P}$, which was previously kept outside of the ρ integral (cf. Eq. (2.28)), is a linear function of Λ , and this term has

to be included in the integration on Λ . In order to integrate analytically, a Taylor expansion of the exponential term is once again necessary. Note that z_P has a constant part which is independent of Λ ,

$$z_P = z_P^0 + \Lambda z_P^1. \quad (2.42)$$

Thus the term $e^{2\beta z_P^0}$ can be kept out of the Λ integration. The rest can be expanded up to three terms in order to obtain the necessary divergent term,

$$e^{2\beta\Lambda z_P^1} = 1 + 2\beta\Lambda z_P^1 + 2\beta^2\Lambda^2(z_P^1)^2 + \mathcal{O}(\Lambda^3). \quad (2.43)$$

Theoretically, two terms in the above expansion are sufficient, however, an additional term was considered for convergence of numerical results. A discussion on additional terms in the Taylor expansion employed in HBIEs has been presented by Gray and Paulino [78].

- *Second analytical integration (on Λ):* The product of the shape functions of P and Q produces terms of Λ up to order 2. The integrals (cf. Eq. (2.38)) to be evaluated are therefore of the form

$$-\frac{J_P^2}{4\pi} \int_{-1}^1 d\eta \int \sin(\Psi) d\Psi \int_0^1 \Lambda^s f(\Lambda) d\Lambda \quad (2.44)$$

for $s = 0, 1, 2$ where $f(\Lambda)$ is a function of Λ . The missing limits of the Λ and Ψ integrals depend upon the particular sub-triangle in Figure 2.6 being considered. The Λ integrations for $s = 1$ and $s = 2$ are straightforward. For $s = 0$, a finite contribution plus a divergent term of the form

$$L_{kj}^c = \log(\epsilon) \frac{J_P^2}{4\pi} \int_{-1}^1 \hat{\psi}_k^0 \hat{\psi}_j^0 d\eta \int_0^\pi \frac{\sin(\Psi)}{a^3} d\Psi, \quad (2.45)$$

is found. Here, $\hat{\psi}_i^0$ are the shape functions evaluated at $\Lambda = \rho = 0$, as

$$\hat{\psi}_1^0 = \frac{1-\eta}{2}, \quad \hat{\psi}_2^0 = \frac{1+\eta}{2}, \quad \hat{\psi}_3^0 = 0. \quad (2.46)$$

Note that as $a = a(\Psi)$ is independent of η , Eq. (2.45) simplifies to

$$L_{kj}^c = \log(\epsilon) \frac{J_P^2}{4\pi} \frac{1 + \delta_{kj}}{3} \int_0^\pi \frac{\sin(\Psi)}{a^3} d\Psi, \quad (2.47)$$

where δ_{kj} is the usual Kronecker delta function and $1 \leq k, j \leq 2$. For $m = 1$, following the same procedure as above does not produce any divergent terms.

The divergent term L_{kj}^c is precisely the same as that obtained from the hypersingular *homogeneous* Laplace equation [73]. This comes as no surprise because the new feature in the FGM kernels is the exponential term. In the Taylor expansion,

$$e^{\beta r} = 1 + (\beta r) + \frac{(\beta r)^2}{2} + \frac{(\beta r)^3}{6} + \dots, \quad (2.48)$$

the leading constant is the most singular, the subsequent terms actually help to kill off the singularity. Thus the divergence comes from the first term of the expansion, which is exactly the same term for the Laplace equation. The important consequence of this observation is that it will not be necessary to prove that Eq. (2.47) cancels with the corresponding divergence from the adjacent edge integration (obtained below). The proof in reference [73] suffices to demonstrate this point, which is presented later in this chapter.

2.3.2 Edge Adjacent Integration

In this case an edge is shared between the two elements as shown in Figure 2.3. Orient the elements so that the shared edge is defined by $\xi = 0$ in E_P , and $\xi^* = 0$ for E_Q , and the singularity occurs when $\eta = -\eta^*$.

- *First Polar Coordinate transformation* $\{\eta^*, \xi^*\} \rightarrow \{\rho, \theta\}$: The first step is to employ polar coordinates for the Q integration [73],

$$\eta^* = \rho \cos(\theta) - \eta, \quad \xi^* = \rho \sin(\theta) \quad (2.49)$$

As shown in Figure 2.7(a), the θ integration must be split into two pieces (for simplicity the integrands are omitted, but it will be useful to retain the Jacobians of the transformations)

$$\int_{-1}^1 d\eta \int_0^{\sqrt{3}(1-|\eta|)} d\xi \left[\int_0^{\Theta_1(\eta)} d\theta \int_0^{L_1(\theta)} \rho d\rho + \int_{\Theta_1(\eta)}^{\pi} d\theta \int_0^{L_2(\theta)} \rho d\rho \right], \quad (2.50)$$

where

$$L_1(\theta) = \frac{\sqrt{3}(1+\eta)}{\sin(\theta) + \sqrt{3}\cos(\theta)}, \quad L_2(\theta) = \frac{\sqrt{3}(1-\eta)}{\sin(\theta) - \sqrt{3}\cos(\theta)}. \quad (2.51)$$

The break-point in θ ,

$$\theta_1(\eta) = \frac{\pi}{2} - \tan^{-1} \left(\frac{\eta}{\sqrt{3}} \right) \quad (2.52)$$

is only a function of η . The integrations can therefore be rearranged as follows,

$$\begin{aligned} & \int_{-1}^1 d\eta \int_0^{\theta_1(\eta)} d\theta \int_0^{\sqrt{3}(1-|\eta|)} d\xi \int_0^{L_1(\theta)} \rho d\rho \\ & + \int_{-1}^1 d\eta \int_{\theta_1(\eta)}^{\pi} d\theta \int_0^{\sqrt{3}(1-|\eta|)} d\xi \int_0^{L_2(\theta)} \rho d\rho . \end{aligned} \quad (2.53)$$

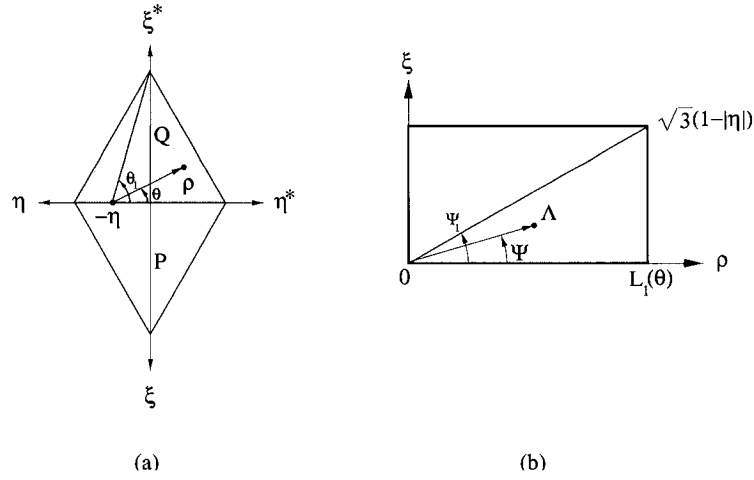


Figure 2.7: (a) Polar coordinate transformation employed in the Q element, $\{\eta^*, \xi^*\} \rightarrow \{\rho, \theta\}$; (b) Second polar coordinate transformation $\{\rho, \xi\} \rightarrow \{\Lambda, \Psi\}$ for the edge-adjacent integration.

- *Second Polar Coordinate transformation $\{\rho, \xi\} \rightarrow \{\Lambda, \Psi\}$* : As the singularity occurs at $\rho = \xi = 0$, a second polar coordinate transformation is introduced

$$\rho = \Lambda \cos(\Psi), \quad \xi = \Lambda \sin(\Psi). \quad (2.54)$$

The Ψ integration must also be taken in two parts (Figure 2.7(b)), resulting in the four integrals

$$\begin{aligned} & \int_{-1}^1 d\eta \int_0^{\Theta_1(\eta)} d\theta \left[\int_0^{\Psi_1} d\Psi \int_0^{\lambda_{11}} \cos(\Psi) \Lambda^2 d\Lambda + \int_{\Psi_1}^{\pi/2} d\Psi \int_0^{\lambda_{12}} \cos(\Psi) \Lambda^2 d\Lambda \right] + \\ & \int_{-1}^1 d\eta \int_{\Theta_1(\eta)}^{\pi} d\theta \left[\int_0^{\Psi_2} d\Psi \int_0^{\lambda_{21}} \cos(\Psi) \Lambda^2 d\Lambda + \int_{\Psi_2}^{\pi/2} d\Psi \int_0^{\lambda_{22}} \cos(\Psi) \Lambda^2 d\Lambda \right]. \end{aligned} \quad (2.55)$$

The formulas for the Λ limits are simply

$$\lambda_{n1} = L_n(\theta)/\cos(\Psi), \quad \lambda_{n2} = L_n(\theta)/\sin(\Psi), \quad (2.56)$$

for $n = 1, 2$. The distance function takes the form

$$r^2 = \epsilon^2 + \epsilon a_1 \Lambda + a_2 \Lambda^2, \quad (2.57)$$

but this quadratic expression (in the denominators) can be integrated exactly. The Λ^2 factor from the two polar transformations sufficiently reduces the order of the singularity such that one analytic integration (over Λ) will produce the $\log(\epsilon)$ term.

- *Taylor Expansion of the exponential function:* The Λ integral can not be evaluated analytically unless a Taylor expansion is once again utilized for the exponential term. To extract the divergent terms from this integral, a one term expansion will be enough (same arguments as for the coincident integration). Similarly to Eq. (2.28) and Eq. (2.43), the exponential term for this case can be written as,

$$\begin{aligned} e^{\beta(-r+z_Q+z_P)} &= e^{\beta(-r+z_Q-z_P+2z_P)} \\ &= e^{\beta(-\sqrt{\epsilon^2+a^2\Lambda^2}+\alpha\Lambda+2(z_P^0+\Lambda z_P^1))} \\ &= e^{2\beta z_P^0} e^{\beta(-\sqrt{\epsilon^2+a^2\Lambda^2}+\alpha\Lambda+2\Lambda z_P^1)}. \end{aligned} \quad (2.58)$$

The term $e^{2\beta z_P^0}$ is taken outside of the Λ integration since it is independent of Λ . A one term Taylor expansion is employed in the remaining exponential term, i.e.

$$e^{\beta(-\sqrt{\epsilon^2+a^2\Lambda^2}+\alpha\Lambda+2\Lambda z_P^1)} = 1 + \mathcal{O}(\Lambda). \quad (2.59)$$

The rest of the expansion is of the order of Λ . This expansion along with the Λ^2 from the Jacobian of the polar transformation will be sufficient to provide a smooth function for numerical integration. This follows from the observation that $\Lambda = 0$ encapsulates all three conditions for $r = 0$, namely $\xi = \xi^* = 0$, and $\eta = -\eta^*$. Thus, as in the coincident algorithm, the exact integration is with respect “to the distance from the singularity”.

- *Analytical Integration on Λ :* The Λ integration results in a finite quantity plus a

divergent contribution, which is given by

$$L_{kj}^e = \log(\epsilon) \frac{1}{4\pi} \int_{-1}^1 \hat{\psi}_k^0 \hat{\psi}_j^0 d\eta \int_0^\pi d\theta \int_0^{\pi/2} \cos(\Psi) \left(\frac{3J_{PN}^1 J_{Qn}^1}{a_2^{5/2}} - \frac{J_{Qn} \cdot J_{PN}}{a_2^{3/2}} \right) d\Psi, \quad (2.60)$$

where J_{Qn}^1 and J_{PN}^1 are the coefficients of Λ in $J_{Qn} \cdot \mathbf{R}$ and $J_{PN} \cdot \mathbf{R}$ respectively,

$$J_{PN} \cdot \mathbf{R} = J_{PN}^1 \Lambda - J_P \epsilon, \quad J_{Qn} \cdot \mathbf{R} = J_{Qn}^1 \Lambda - J_{Qn} \cdot \mathbf{N}. \quad (2.61)$$

As in Eq. (2.46), $\hat{\psi}_k^0$ and $\hat{\psi}_j^0$ denote the shape functions evaluated at $\Lambda = 0$. This expression, Eq. (2.60), and the expression for L_{kj}^c , Eq. (2.47), cancel one another. As noted above (Section 2.3.1), the proof of such cancellation [73] is precisely the same as that for Laplace equation, which is given next for completeness.

Proof of Cancellation

Recapitulating the above results, the coincident and edge adjacent integrations give rise to divergent $\log(\epsilon)$ terms of the form

$$\begin{aligned} L_{kj}^c &= \frac{J_P^2}{4\pi} \frac{1 + \delta_{kj}}{3} \int_0^\pi \frac{\sin(\Psi)}{a^3} d\Psi \\ L_{kj}^e &= \frac{1}{4\pi} \frac{1 + \delta_{kj}}{3} \int_0^\pi d\theta \int_0^{\pi/2} \cos(\Psi) \left(\frac{3J_{PN}^1 J_{Qn}^1}{a_2^{5/2}} - \frac{J_{Qn} \cdot J_{PN}}{a_2^{3/2}} \right) d\Psi, \end{aligned} \quad (2.62)$$

where $k, j = 1, 2$ refer to the two nodes P_1 and P_2 along the common edge. It is therefore necessary to establish that

$$J_P^2 \int_0^\pi \frac{\sin(\Psi)}{a^3} d\Psi = - \int_0^\pi d\theta \int_0^{\pi/2} \cos(\Psi) \left(\frac{3J_{PN}^1 J_{Qn}^1}{a_2^{5/2}} - \frac{J_{Qn} \cdot J_{PN}}{a_2^{3/2}} \right) d\Psi, \quad (2.63)$$

and this will be accomplished by brute force, evaluating the integrals. This is most easily carried out using a symbolic computation program.

To simplify matters, it is convenient (and permissible) to shift and rotate the elements so that $P_1 = (0, 0, 0)$, $P_2 = (x_2, 0, 0)$ and $P_3 = (x_3, y_3, 0)$, and thus $\mathbf{N} = (0, 0, 1)$ and $J_P = x_2 y_3 / 2\sqrt{3}$. Note that for the edge adjacent Q -element, the convention is that $Q_1 = P_2$ and $Q_2 = P_1$. Setting $Q_3 = (x_3^*, y_3^*, z_3^*)$, $J_{Qn} = (0, z_3^* x_2, -y_3^* x_2)$.

From Eq. (2.22) and the comment below Eq. (2.38), the coincident integral takes the

form

$$J_P^2 \int_0^\pi \frac{\sin(\Psi)}{(a_{cc} \cos(\Psi)^2 - a_{cs} \cos(\Psi) \sin(\Psi) + a_{ss} \sin(\Psi)^2)^{3/2}} d\Psi, \quad (2.64)$$

and for the shifted geometry

$$a_{cc} = \frac{1}{4} x_2^2$$

$$a_{cs} = \sqrt{3} x_2 (2 x_3 - x_2) / 6 \quad (2.65)$$

$$a_{ss} = (x_2^2 + 4 x_3^2 + 4 y_3^2 - 4 x_3 x_2) / 12 \quad (2.66)$$

After substituting $q = \cotan(\Psi)$, Eq. (2.64) becomes

$$-J_P^2 \int_{-\infty}^{\infty} \frac{1}{(a_{cc} q^2 - a_{cs} q + a_{ss})^{3/2}} dq, \quad (2.67)$$

and carrying out the integration we find that the coincident divergent term becomes simply

$$J_P^2 \int_0^\pi \frac{\sin(\Psi)}{a^3} d\Psi = x_2. \quad (2.68)$$

Thus, as expected, the divergent term does not depend upon P_3 .

As a consequence of the double integration, the evaluation of the edge integral is considerably more involved. Although symbolic computation will eventually execute all of the required calculus and algebra, manipulation is required to modify the forms of the expressions, and care is required to keep the size of the expressions from exceeding the available memory. The discussion below will therefore only outline the procedure. As a function of Ψ , the coefficient a_2 defined in Eq. (2.56) takes the form

$$a_2 = c_2 \cos^2(\Psi) + c_1 \cos(\Psi) \sin(\Psi) + c_0 \sin^2(\Psi) \quad (2.69)$$

where the c_j are functions of $\cos(\theta)$ and $\sin(\theta)$. Thus, as with L_{kj}^c , substituting $q = \cotan(\Psi)$ is convenient, resulting in an integral of the form

$$\int_0^\infty \left[\alpha_1 \frac{q^2}{(c_2 q^2 + c_1 q + c_0)^{5/2}} + \alpha_2 \frac{q}{(c_2 q^2 + c_1 q + c_0)^{3/2}} \right] dq. \quad (2.70)$$

The function of θ that results from this integration once again benefits from the sub-

stitution $p = \cotan(\theta)$, and the θ integral becomes

$$\int_{-\infty}^{\infty} \frac{h_1(p)}{(s_2 p^2 + s_1 p + s_0)^2} dp + \int_{-\infty}^{\infty} \frac{h_2(p)}{\sqrt{(t_2 p^2 + t_1 p + t_0)} (s_2 p^2 + s_1 p + s_0)^2} dp, \quad (2.71)$$

where $h_1(p)$ and $h_2(p)$ are quadratic and cubic polynomials, respectively. The coefficients $\{s_j\}$ and $\{t_j\}$ are now just functions of the nodal coordinates. The first integral is found to be 0, while the second is, as desired, $-x_2$.

2.3.3 Vertex Adjacent Integration

In this case the singularity is limited to a single point in the four dimensional integration (see Figure 2.3). Orient the P and Q elements so that the singular point is $\eta = -1$ and $\eta^* = -1$.

- *Two Polar Coordinate transformations* ($\{\eta^*, \xi^*\} \rightarrow \{\rho_q, \theta_q\}$, $\{\eta, \xi\} \rightarrow \{\rho_p, \theta_p\}$): Two separate polar coordinates are first introduced in each element (see Figure 2.8(a)),

$$\begin{aligned} \eta^* &= \rho_q \cos(\theta_q) - 1, & \xi^* &= \rho_q \sin(\theta_q) \\ \eta &= \rho_p \cos(\theta_p) - 1, & \xi &= \rho_p \sin(\theta_p). \end{aligned} \quad (2.72)$$

This results in an integral of the form

$$\int_0^{\pi/3} d\theta_p \int_0^{L_p(\theta_p)} \rho_p d\rho_p \int_0^{\pi/3} d\theta_q \int_0^{L_q(\theta_q)} \rho_q d\rho_q, \quad (2.73)$$

where

$$L_p(\theta_p) = 2\sqrt{3}/[\sin(\theta_p) + \sqrt{3}\cos(\theta_p)], \quad L_q(\theta_q) = 2\sqrt{3}/[\sin(\theta_q) + \sqrt{3}\cos(\theta_q)]. \quad (2.74)$$

As the vertex adjacent integration will not produce a divergent term, we omit the kernel function and just keep track of the Jacobians in the subsequent expressions. Now interchanging the order of the integration between ρ_p and θ_q , one obtains

$$\int_0^{\pi/3} d\theta_p \int_0^{\pi/3} d\theta_q \int_0^{L_p(\theta_p)} \rho_p d\rho_p \int_0^{L_q(\theta_q)} \rho_q d\rho_q.$$

- *Third Polar Coordinate transformations* $\{\rho_p, \rho_q\} \rightarrow \{\Lambda, \Psi\}$: The only singularity is at the common vertex $\rho_p = \rho_q = 0$, and thus a third polar coordinate transformation is

performed

$$\rho_p = \Lambda \cos(\Psi), \quad \rho_q = \Lambda \sin(\Psi).$$

As illustrated in Figure 2.8(b), the $\{\rho_p, \rho_q\}$ domain is a rectangle, and thus the Ψ integration must be taken in two pieces. The combined Jacobian in this case is $\cos(\Psi) \sin(\Psi) \Lambda^3$, and thus Eq. (2.73) becomes

$$\int_0^{\pi/3} d\theta_p \int_0^{\pi/3} d\theta_q \left[\int_0^{\Psi_1} \cos(\Psi) \sin(\Psi) d\Psi \int_0^{L_1(\Psi)} \Lambda^3 d\Lambda + \int_{\Psi_1}^{\pi/2} \cos(\Psi) \sin(\Psi) d\Psi \int_0^{L_2(\Psi)} \Lambda^3 d\Lambda \right], \quad (2.75)$$

where

$$L_1(\Psi) = L_P(\theta_p) / \cos(\Psi) \quad \text{and} \quad L_2(\Psi) = L_Q(\theta_q) / \sin(\Psi). \quad (2.76)$$

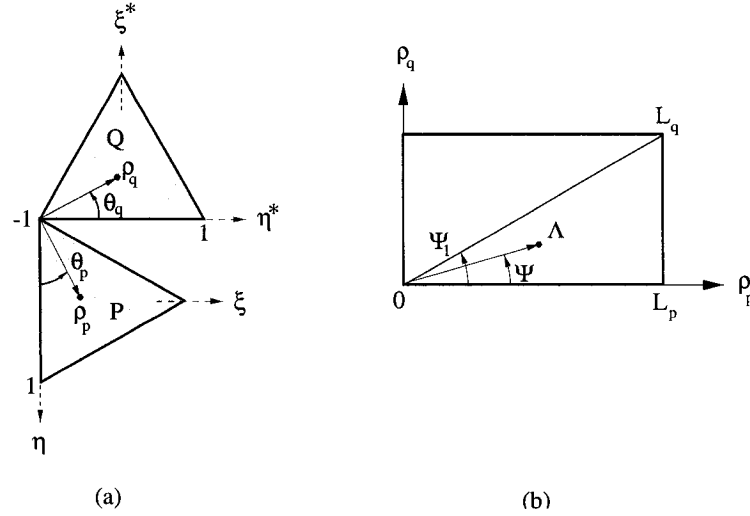


Figure 2.8: (a) Initial polar coordinate transformation employed in both P and Q elements; (b) Final polar coordinate transformation $\{\rho_p, \rho_q\} \rightarrow \{\Lambda, \Psi\}$ for the vertex adjacent integration.

With the Λ^3 factor multiplying the kernel function, it is possible to immediately set $\epsilon = 0$, and the distance function is then $r^2 = a^2 \Lambda^2$ (the coefficient being a function of all three angles and nodal coordinates). It is then immediately apparent that this integral is finite. Although numerical evaluation with Gaussian quadrature could be employed for the entire integration we prefer to execute the Λ integral semi-analytically in order to achieve better accuracy.

2.4 Concluding Remarks

The direct “limit to the boundary” approach for evaluation of the singular integrals, can be successfully applied to FGMs. Procedures for directly evaluating Galerkin hypersingular and singular integrals have been presented. For the coincident and edge adjacent cases the key is to explicitly identify the divergent terms that appear in the limit to the boundary. To this end, multiple polar coordinate transformations and analytic integration were employed. This results in an efficient scheme as the remaining are of reduced dimension of smooth functions which can be evaluated using numerical integration.

Chapter 3

Green's function approach for heat conduction in graded materials

A symmetric Galerkin formulation and implementation for heat conduction in a three dimensional functionally graded material is presented in this chapter. The Green's function of the actual problem is used to develop a boundary-only formulation without any domain discretization, in which the thermal conductivity varies exponentially in one coordinate. Several test examples are provided to verify the numerical implementation. The results of test calculations are in good agreement with exact solutions and corresponding finite element method simulations.

3.1 Introduction

The symmetric Galerkin boundary element method (SGBEM) formulation possesses the attractive feature of producing a symmetric coefficient matrix [85, 88, 161] and, in addition, the Galerkin approximation allows standard continuous C^0 elements to be used for evaluation of hypersingular integrals. These properties make the SGBEM suitable for coupling with the popular finite element method (FEM) [13]. The Galerkin technique has the important property of "local support" that is especially suitable for treating corners, including the Dirichlet corners [137].

Although the development of the SGBEM started in the last decade, most of the computational implementations have concentrated in two dimensional (2D) problems [21, 61, 89, 147], however, recently a number of three dimensional (3D) implementations have also been reported [112, 62, 60, 118], mostly limited to homogeneous media. A review of various applications of the SGBEM can be found in the paper by Bonnet *et al.* [13], among others. The present work emphasizes nonhomogeneous media as described below.

The Galerkin (non-symmetric) formulation for FGMs using the singular boundary integral equation has been examined by Gray *et al.* [75] for steady state problems, and by Sutradhar *et al.* [174, 175] for transient problems. A dual reciprocity boundary element method applied to heat conduction for FGMs has been reported by Tanaka *et al.* [178]. Chen [34, 35] has developed a collocation-based BEM for Darcy's flow with spatial variation of permeability and has presented closed-form Green's functions for various permeability functions.

In this chapter, a SGBEM for heat conduction for FGMs is formulated. The implementation is a pure boundary-only formulation without any domain integral. It relies on the Green's function (GF) for the partial differential equation incorporating the material gradation. In this chapter, first the Green's function and the governing equation for the FGM problem are presented. Second, the symmetric Galerkin formulation is shown. Next, numerical examples are provided that verify the formulation. Finally, the chapter concludes with a few remarks.

3.2 On the FGM Green's function

Steady state isotropic heat conduction in a solid is governed by the equation

$$\nabla \cdot (k(x, y, z) \nabla \phi) = 0 . \quad (3.1)$$

where \cdot denotes the inner product, $\phi = \phi(x, y, z)$ is the temperature function, $k(x, y, z)$ is the thermal conductivity which can be a function of the Cartesian coordinates. Let the FGM be defined by the thermal conductivity that varies exponentially in one Cartesian coordinate, i.e.

$$k(x, y, z) = k(z) = k_0 e^{2\beta z} , \quad (3.2)$$

where β denotes the material nonhomogeneity parameter. Substituting this material expression into Eq. (3.1), one obtains

$$\nabla^2 \phi + 2\beta \phi_z = 0, \quad (3.3)$$

where ϕ_z is the derivative of ϕ with respect to z , i.e.

$$\phi_z \equiv \partial \phi / \partial z. \quad (3.4)$$

The Green's function is the solution to the adjoint equation with a delta function force, namely

$$\nabla^2 G(P, Q) - 2\beta G_z(P, Q) = -\delta(Q - P) , \quad (3.5)$$

where δ denotes the Dirac delta function, P and Q denote the source point and the field point, respectively, and G_z is the derivative of G with respect to z . The solution of this equation is derived [75, 110] as

$$G(P, Q) = \frac{e^{\beta(-r+R_z)}}{4\pi r} \quad (3.6)$$

where

$$R_z = z_Q - z_P \quad \text{and} \quad r = \|\mathbf{R}\| = \|\mathbf{Q} - \mathbf{P}\|. \quad (3.7)$$

The Green's function for the nonhomogeneous problem is essential for developing a boundary-only integral equation formulation. Note that the Green's function for an FGM can be rewritten as [140]

$$G(P, Q) = \frac{1}{4\pi r} + \frac{e^{\beta(-r+R_z)} - 1}{4\pi r}. \quad (3.8)$$

The first term of Eq. (3.8) is the Green's function for the Laplace equation in homogeneous media. The second term is bounded in the limit as $r \rightarrow 0$ and is a consequence of the grading; when β tends to zero (material is homogeneous), this graded term vanishes. This form shows that the singularity for the FGM Green's function is precisely the same as for the homogeneous. It will therefore not be surprising that the divergent terms in the hypersingular integral are the same as for the Laplace equation [73].

3.3 Symmetric Galerkin Formulation

The governing boundary integral equation corresponding to Eq. (3.3) is

$$\phi(P) + \int_{\Sigma} \phi(Q) \left(\frac{\partial}{\partial n} G(P, Q) - 2\beta n_z G(P, Q) \right) dQ = \int_{\Sigma} G(P, Q) \frac{\partial}{\partial n} \phi(Q) dQ , \quad (3.9)$$

which differs in form from the usual integral statements by the presence of the additional term multiplying $\phi(Q)$, i.e. $[-2\beta n_z G(P, Q)]$, due to the material gradation.

In the SGBEM, the symmetry comes from the symmetry properties of the kernel functions [13, 12]. For the homogeneous Laplace equation, the fundamental solution is symmetric, but the FGM Green's function, Eq. (3.6), is not. In order to get symmetric kernels, the FGM boundary integral equations are re-formulated in terms of physical variables (flux instead of normal derivative), as described below. Thus, to obtain a symmetric matrix, the equations

are written in terms of the surface flux,

$$\mathcal{F}(Q) = -k(z_Q) \frac{\partial}{\partial n} \phi(Q). \quad (3.10)$$

The boundary integral equation (BIE) for surface temperature $\phi(P)$ on the boundary Σ (see Figure 3.1) is therefore

$$\phi(P) + \int_{\Sigma} F(P, Q) \phi(Q) dQ = \int_{\Sigma} G_S(P, Q) \mathcal{F}(Q) dQ, \quad (3.11)$$

and the kernel functions are

$$\begin{aligned} G_S(P, Q) &= -\frac{G(P, Q)}{k(z_Q)} = -\frac{1}{4k_0\pi} \frac{e^{\beta(-r-z_Q-z_P)}}{r} \\ F(P, Q) &= \frac{\partial}{\partial n} G(P, Q) - 2\beta n_z G(P, Q) \\ &= -\frac{e^{\beta(-r+R_z)}}{4\pi} \left(\frac{\mathbf{n} \cdot \mathbf{R}}{r^3} + \beta \frac{\mathbf{n} \cdot \mathbf{R}}{r^2} + \beta \frac{n_z}{r} \right). \end{aligned} \quad (3.12)$$

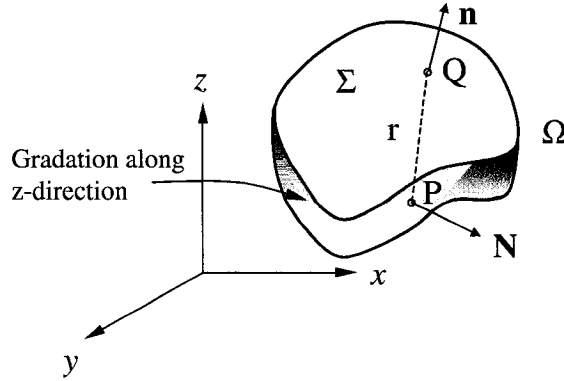


Figure 3.1: Illustration of a generic body with boundary Σ and domain Ω . The present SGBEM relies on a boundary-only formulation for FGMs. The source point is P (normal \mathbf{N}) and the field point is Q (normal \mathbf{n}).

Notice that $G_S(P, Q)$, unlike $G(P, Q)$, is symmetric with respect to P and Q . This is one of the conditions needed for symmetry. The hypersingular boundary integral equation (HBIE) is obtained by differentiating Eq. (3.11) with respect to the source P in the direction \mathbf{N} , which is normal to the boundary at P . In this case, however, it needs to be multiplied by $-k(z_P)$ to obtain the corresponding equation for surface flux, i.e.

$$\mathcal{F}(P) + \int_{\Sigma} W(P, Q) \phi(Q) dQ = \int_{\Sigma} S(P, Q) \mathcal{F}(Q) dQ. \quad (3.13)$$

The kernel functions are computed as

$$\begin{aligned}
S(P, Q) &= -k(z_P) \frac{\partial}{\partial N} G_S(P, Q) \\
&= \frac{e^{\beta(-r-R_z)}}{4\pi} \left(\frac{\mathbf{N} \cdot \mathbf{R}}{r^3} + \beta \frac{\mathbf{N} \cdot \mathbf{R}}{r^2} - \beta \frac{N_z}{r} \right)
\end{aligned} \tag{3.14}$$

and

$$\begin{aligned}
W(P, Q) &= -k(z_P) \frac{\partial}{\partial N} F(P, Q) \\
&= \frac{k_0}{4\pi} e^{\beta(-r+z_Q+z_P)} \left(3 \frac{(\mathbf{n} \cdot \mathbf{R})(\mathbf{N} \cdot \mathbf{R})}{r^5} + 3\beta \frac{(\mathbf{n} \cdot \mathbf{R})(\mathbf{N} \cdot \mathbf{R})}{r^4} \right. \\
&\quad + \frac{\beta^2 (\mathbf{n} \cdot \mathbf{R})(\mathbf{N} \cdot \mathbf{R}) - \beta (N_z \mathbf{n} - n_z \mathbf{N}) \cdot \mathbf{R} - \mathbf{n} \cdot \mathbf{N}}{r^3} \\
&\quad \left. - \beta \frac{\beta (N_z \mathbf{n} - n_z \mathbf{N}) \cdot \mathbf{R} + \mathbf{n} \cdot \mathbf{N}}{r^2} - \beta^2 \frac{N_z n_z}{r} \right).
\end{aligned} \tag{3.15}$$

The three symmetry requirements for the kernel functions are now fulfilled, i.e.

$$G_S(P, Q) = G_S(Q, P), \quad W(P, Q) = W(Q, P), \quad S(P, Q) = F(Q, P) \tag{3.16}$$

Interchanging Q and P implies replacing $\mathbf{N}(P)$ with $\mathbf{n}(Q)$ and changing the sign of \mathbf{R} , and thus all the conditions necessary for symmetry are seen to hold.

In this work, the direct limit procedure is employed to define and evaluate the singular integrals. If the limit is taken with the source point P approaching the boundary from *outside* the domain, then the “free terms” $\phi(P)$ in the BIE (Eq. (3.11)) and $\mathcal{F}(P)$ in the HBIE (Eq. (3.13)) are not present. Thus, the exterior limit BIE and HBIE take the form

$$\begin{aligned}
\mathcal{P}_s(P) &\equiv \int_{\Sigma} F(P, Q) \phi(Q) \, dQ - \int_{\Sigma} G_S(P, Q) \mathcal{F}(Q) \, dQ = 0, \\
\mathcal{F}_s(P) &\equiv \int_{\Sigma} W(P, Q) \phi(Q) \, dQ - \int_{\Sigma} S(P, Q) \mathcal{F}(Q) \, dQ = 0,
\end{aligned} \tag{3.17}$$

where \mathcal{P}_s denotes the equation for the surface temperature (potential) and \mathcal{F}_s denotes the equation for the surface flux. The free terms are automatically incorporated in the “*exterior limit*” evaluation of the $F(P, Q)$ and $S(P, Q)$ integrals. Thus, a separate computation of these free terms is avoided, and they are obtained as a natural outcome of the direct limit procedure [116].

The surface temperature and surface flux are approximated in terms of values at element nodes Q_j and shape functions $\psi_j(Q)$, *i.e.*,

$$\phi(Q) = \sum_j \phi(Q_j)\psi_j(Q), \quad \mathcal{F}(Q) = \sum_j \mathcal{F}(Q_j)\psi_j(Q). \quad (3.18)$$

In a Galerkin approximation, Eq. (3.17) is enforced in an average sense, with the shape functions employed as the weighting functions. Therefore, the Galerkin boundary integral equations take the form

$$\int_{\Sigma} \psi_k(P)\mathcal{P}_s(P) dP = 0 \quad (3.19)$$

$$\int_{\Sigma} \psi_k(P)\mathcal{F}_s(P) dP = 0. \quad (3.20)$$

After discretization, the set of equations can be written in block-matrix form as $[H]\{\phi\} = [G]\{\mathcal{F}\}$, and in block-matrix these equations become

$$\begin{bmatrix} H_{11} & H_{12} \\ H_{21} & H_{22} \end{bmatrix} \begin{Bmatrix} \phi_{bv} \\ \phi_u \end{Bmatrix} = \begin{bmatrix} G_{11} & G_{12} \\ G_{21} & G_{22} \end{bmatrix} \begin{Bmatrix} \mathcal{F}_u \\ \mathcal{F}_{bv} \end{Bmatrix}. \quad (3.21)$$

Symmetry of the coefficient matrix for a general mixed boundary value problem is achieved by the following simple arrangement. The BIE is employed on the Dirichlet surface, and the HBIE equation is used on the Neumann surface. The first row represents the BIE written on the Dirichlet surface, and the second row represents the HBIE written on the Neumann surface. Similarly, the first and the second columns arise from integrating over Dirichlet and Neumann surfaces, respectively. The subscripts in the matrix therefore denote known boundary values (bv) and unknown (u) quantities. Rearranging Eq. (3.21) into the form $[\mathbf{A}]\{x\} = \{b\}$, one obtains

$$\begin{bmatrix} -G_{11} & H_{12} \\ G_{21} & -H_{22} \end{bmatrix} \begin{Bmatrix} \mathcal{F}_u \\ \phi_u \end{Bmatrix} = \begin{Bmatrix} -H_{11}\phi_{bv} + G_{12}\mathcal{F}_{bv} \\ H_{21}\phi_{bv} - G_{22}\mathcal{F}_{bv} \end{Bmatrix}. \quad (3.22)$$

The symmetry of the coefficient matrix, $G_{11} = G_{11}^T$, $H_{22} = H_{22}^T$, and $H_{12} = G_{21}$, now follows from the properties of the kernel functions (see Eq. (3.16)).

3.4 Numerical Implementation

In this section, results for four test cases are reported, demonstrating the implementation of the above techniques. The evaluation of the singular integrals was carried out using the hybrid analytical/numerical integration integration explained in chapter 2. To verify the

numerical implementation, the following FGM examples are presented:

- (1) Cube with material gradation in z -direction,
- (2) Cube with material gradation in 45° with the z -axis,
- (3) Sphere (interior Neumann),
- (4) Compressor blade.

This set of examples comprise a rigorous test of the SGBEM code. The first example has analytical solution and is suitable for a mesh convergence study. The second example differs from the previous one by considering a different direction of material gradation, which is not aligned with any of the reference Cartesian axes. The third example consists of a Neumann problem and it is used to test the hypersingular BIE in the SGBEM implementation. Finally, the last example is a complicated engineering problem. All the above FGM problems can be verified for the homogeneous material case (constant conductivity) when the material nonhomogeneity parameter vanishes ($\beta = 0$).

3.4.1 FGM Cube with material gradation in z -direction

A simple FGM cube with constant temperature on two planes is considered first. As the analytical solution of this problem can be obtained, this problem is suitable for a convergence study. The problem of interest is shown in Figure 3.2. The top surface of the cube at $[z = 1]$ is maintained at a temperature of $T = 100$ while the bottom face at $[z = 0]$ is zero. The remaining four faces are insulated (zero normal flux). The thermal conductivity is

$$k(x, y, z) = k_0 e^{2\beta z} = 5e^{2\beta z}, \quad (3.23)$$

and various values of β will be considered. The analytical solution for the temperature is

$$\phi(x, y, z) = T \frac{1 - e^{-2\beta z}}{1 - e^{-2\beta L}}, \quad (3.24)$$

where L is the dimension of the cube (in the z -direction), and the analytical solution for the flux (on $z = 1$) is

$$q(x, y, z) = -k(x, y, z) \frac{2\beta T e^{-2\beta z}}{1 - e^{-2\beta L}} = -k_0 \frac{2\beta T}{1 - e^{-2\beta L}} \quad (3.25)$$

The cube is discretized with 432 boundary elements and 294 nodes as shown in Figure 3.3(d). The computed temperature variation in the z direction is plotted with different values of β

(material nonhomogeneity parameter) and compared with the analytical solution in Figure 3.4. For this problem the flux on each face of the unit cube is constant. Figure 3.5 shows the variation of the flux on the face $z = 0$ with respect to the change of the material nonhomogeneity parameter β , and compares the results with the analytical flux solution. For the face $z = 1$, the flux has the same variation as on the face $z = 0$, but with opposite sign (cf. Eq. (3.25)).

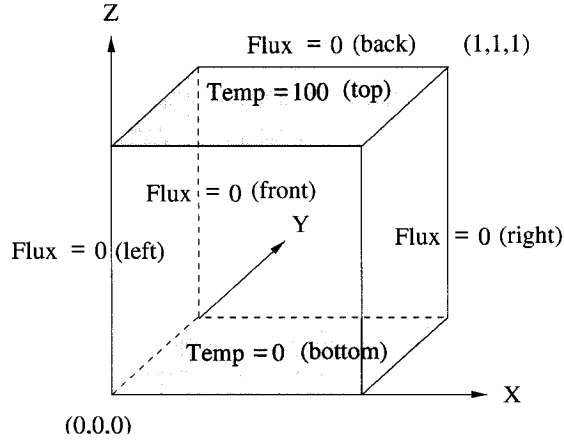


Figure 3.2: Geometry and boundary conditions of the FGM unit cube problem with constant temperature on two planes. The faces with prescribed temperature are shaded.

The error in the temperature solution and the flux is computed considering various mesh discretizations (Figure 3.3) and employing a global error measure,

$$\mathcal{E} = \frac{1}{|u^{(e)}|_{max}} \sqrt{\frac{1}{NP} \sum_{I=1}^{NP} [u_I^{(e)} - u_I^{(c)}]^2} \quad (3.26)$$

where \mathcal{E} is the error in the solution, the superscripts (e) and (c) denote, respectively, the exact and the computed solutions, and NP is the total number of nodes. The four meshes illustrated in the Figure 3.3 were considered for this study. The computed global error with increasing number of elements is given in Table 3.1, which shows that the global error reduces with mesh refinement (cf. Table 3.1 and Figure 3.3). The convergence of the solution is plotted in Figure 3.6. The rate of convergence for the temperature is 1.135 while for the flux is 1.132. It is interesting to notice that both the temperature and flux exhibit similar rates of convergence.

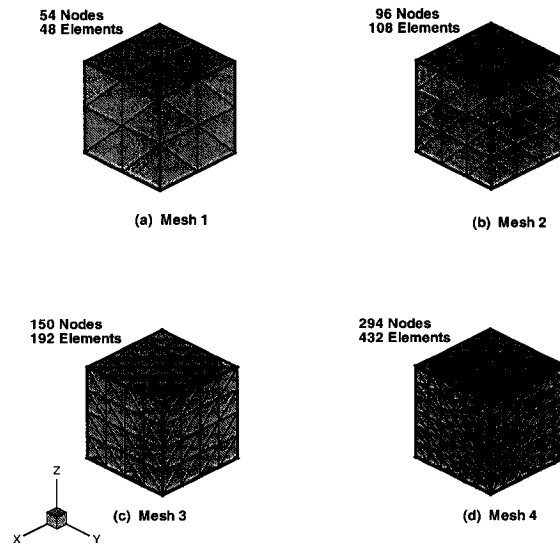


Figure 3.3: The four meshes used for the convergence study of the FGM cube problem.

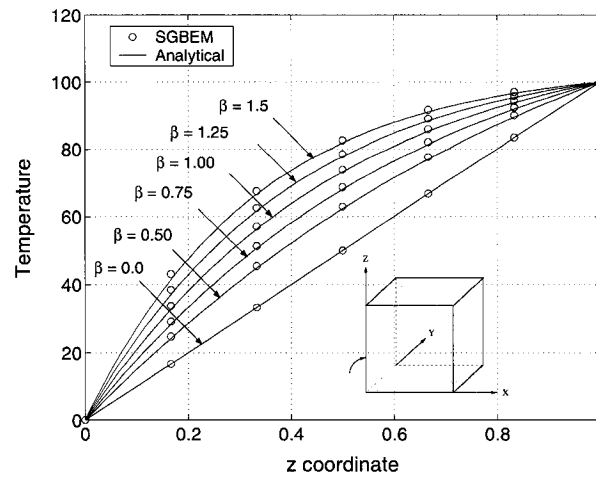


Figure 3.4: Temperature profile in z direction for the FGM cube discretized with 432 elements and 294 nodes.

3.4.2 FGM Cube with material gradation in 45° with the z -axis

The geometry and the boundary conditions for this example are the same as those in the previous example, except for the direction of the variation of the thermal conductivity. Here the variation of the thermal conductivity is in a direction 45° off the z -axis, as shown in Figure

Table 3.1: Global error (\mathcal{E}) estimates on the boundary for FGM cube ($\beta = 1.0$).

Mesh	No. of nodes	No. of elements	Global Error \mathcal{E}	
			Potential	Flux
1	54	48	0.0155	0.0303
2	96	108	0.0091	0.0165
3	150	192	0.0063	0.0123
4	294	432	0.0041	0.0101

3.7. With this change, the problem becomes more interesting than the previous example because the heat flux is no longer constant on the two faces. The thermal conductivity is

$$k(x, y, z') = k_0 e^{2\beta z'} = 5e^{1.5z'}, \quad (3.27)$$

where z' is an axis 45° off the z -axis (see Figure 3.7). The SGBEM solution is compared with an FEM solution obtained from a commercial package ABAQUS [1] using 20 node quadratic brick elements. In the FEM simulation, 10 homogeneous layers (see Figure 3.8) were used to approximate the continuous grading and the conductivity of each layer was computed using Eq. (3.27), where z' was taken as the z' -coordinate of the layer centroid. It should be mentioned that FEM is not restricted to using the discontinuous piece-wise constant approximation available in existing commercial packages. It is possible to incorporate continuous grading within individual elements, and codes with this capability have been

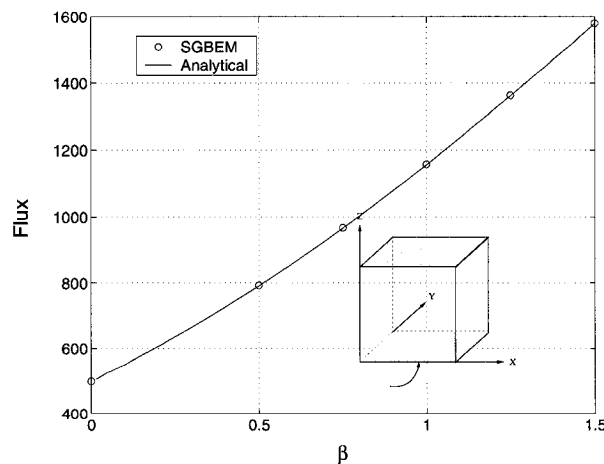


Figure 3.5: Variation of flux on the face $z = 0$ for different values of the material nonhomogeneity parameter β .

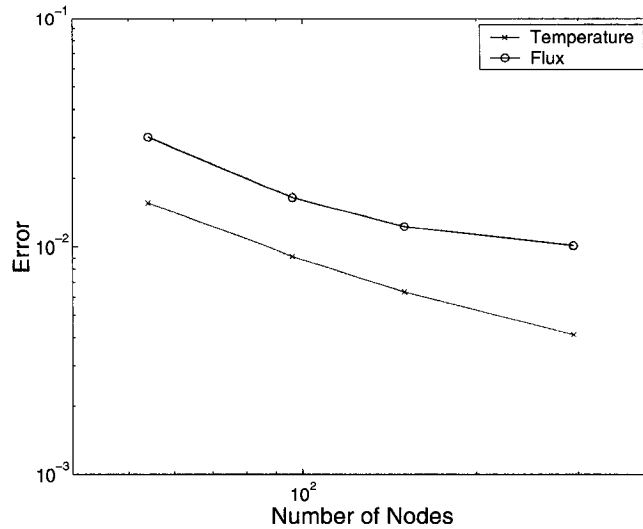


Figure 3.6: The convergence of the temperature and the flux

developed [138, 99], including a 3D public domain code WARP3D [180, 80]. The FEM mesh for the problem, shown in Figure 3.7, consists of 4961 nodes and 1000 elements. The temperature distribution along AA' in the $Y = 0$ plane (see Figure 3.7) with different values of β is plotted against the corresponding FEM solution in Figure 3.9. Also the flux distribution at the edge of the top face (along BB') is plotted with different values of β and compared with the FEM solution in Figure 3.10. Both of the SGBEM solutions agree with the FEM results within plotting accuracy.

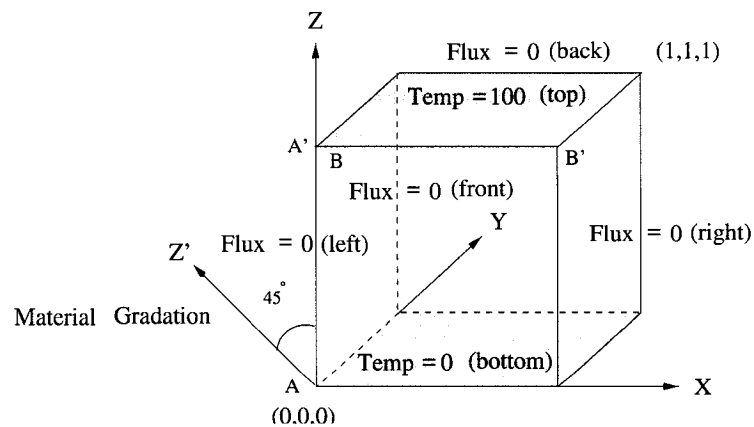


Figure 3.7: Geometry and boundary conditions of the FGM cube problem with material gradation in 45° with the z -axis. The faces with prescribed temperature are shaded.

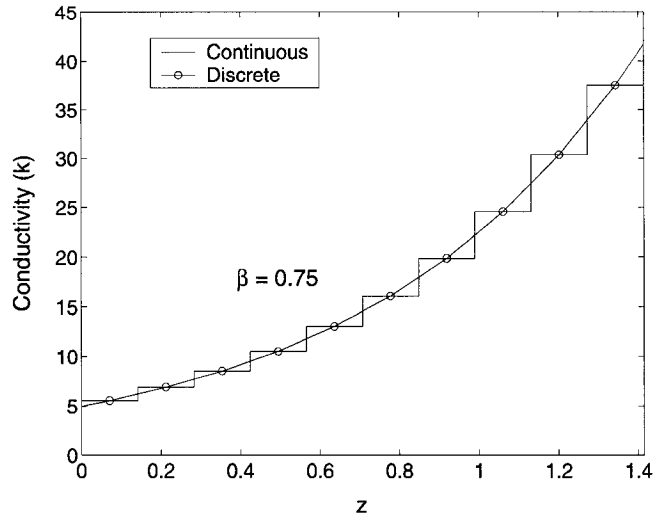


Figure 3.8: Continuous (used in BEM) and discrete (used in the FEM) representation of the conductivity k considering $\beta = 0.75$.

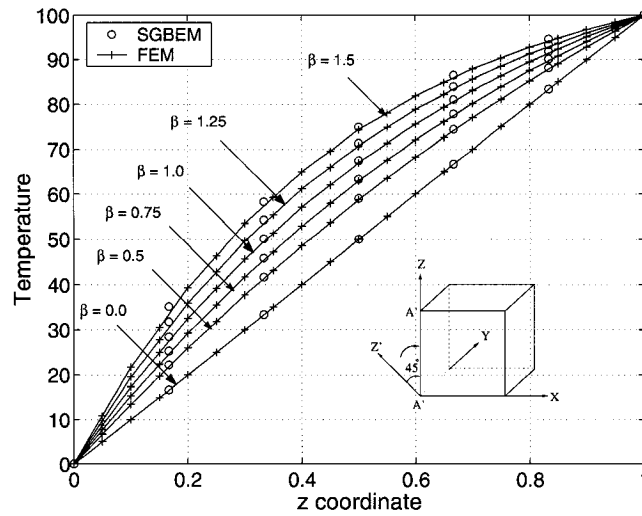


Figure 3.9: Temperature profile along edge AA' (in z direction) for the FGM cube problem.

3.4.3 Interior Neumann FGM-sphere problem

This example is an interior Neumann problem with prescribed boundary flux on the surface of the unit FGM sphere illustrated by Figure 3.11. The thermal conductivity is defined as

$$k(x, y, z) = k_0 e^{2\beta z} = 5e^{2\beta z}, \quad (3.28)$$

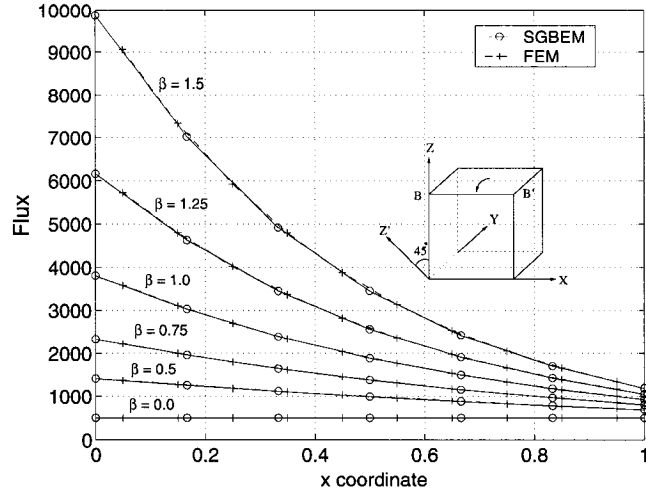


Figure 3.10: Flux distribution along BB' (in x direction) for the FGM cube problem.

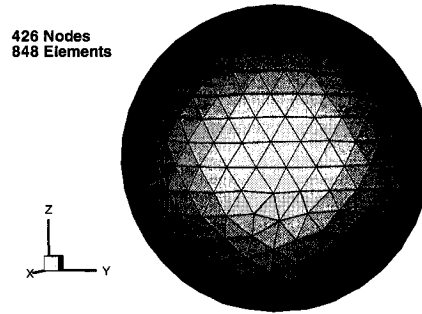


Figure 3.11: The mesh of the FGM unit sphere graded along the z -direction.

and the prescribed flux is

$$q(x, y, z) = -2k_0 e^{2\beta z} (\beta(x^2 + y^2) - z). \quad (3.29)$$

The exact solution for the surface temperature is

$$\phi(x, y, z) = \beta(x^2 + y^2) - 2z. \quad (3.30)$$

As this is an interior Neumann problem, the solution is not unique, and an arbitrary constant can be added to the temperature. To enforce a unique solution, the temperature at

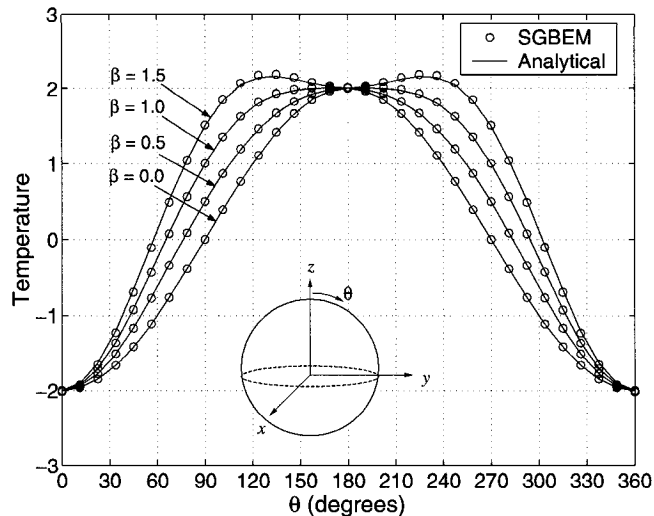


Figure 3.12: Temperature variation with θ (degrees) in $X = 0$ plane.

$(x, y, z) = (0, 0, 1)$ was specified to be the value given by the analytical solution. The sphere is discretized using 426 nodes and 848 elements (see Figure 3.11). The accuracy of the results obtained serve to verify the hypersingular BIE formulation as this equation is employed for the Neumann problem. It is also a good check if the limit to the boundary is correctly picking up on the surface orientation. The surface temperature is plotted against θ along the boundary where the $X = 0$ plane intersects the sphere and compared with analytical solution in Figure 3.12 for different values of β . The symmetry of the solution is captured by the SGBEM (cf. temperature variation from 0° to 180° and from 180° to 360°). Moreover, the numerical results agree with the analytical ones within plotting accuracy.

3.4.4 FGM compressor blade

A 3D analysis is performed on a one stage compressor where blades are attached to the main rotating components as shown in Figure 3.13. The transient response of a rotor made of homogeneous material with similar geometry has been investigated by Benz and Rencis [8] by coupling two-dimensional and axisymmetric boundary zones. The compressor consists of a cylinder with 24 equally spaced blades attached to it. A 15° segment is used for the three-dimensional analysis due to symmetry. The grading direction is the z axis and the thermal conductivity varies according to

$$k(z) = 20e^{0.46z}. \quad (3.31)$$

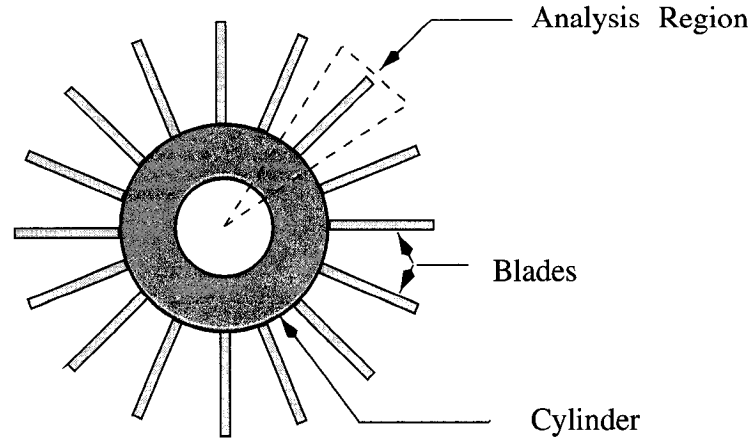


Figure 3.13: Top view of the compressor.

The geometry, boundary condition and the BEM mesh are shown in Figure 3.14 and Figure 3.15.

The BEM mesh consists of 5180 linear elements and 3501 nodes. The BEM solution is compared with an FEM solution obtained from the commercial package ABAQUS [1] using 20 node quadratic brick elements. In the FEM simulation 10 homogeneous layers were used to approximate the continuous grading, the conductivity of each layer was computed using Eq. (3.31), where z was taken as the z -coordinate of the layers centroid (see previous section for comments about FEM modeling of FGMs). The FEM mesh employed 903 nodes and 130 elements. The temperature distribution along the corner edge (which includes Point A) is plotted in Figure 3.16. The flux distribution along edge GF is plotted in Figure 3.17 and compared with the corresponding FEM solution. The minimal discrepancy can be attributed to the relatively coarse mesh of the FEM solution. Finally a contour plot of the temperature distribution is shown in Figure 3.18.

3.5 Concluding Remarks

Symmetric Galerkin boundary element analysis can be successfully applied to FGMs. For exponentially graded (nonhomogeneous) materials, the FGM Green's function is determined and a boundary-only formulation is obtained. The numerical results presented in this chapter indicate that it is feasible to implement the complicated FGM Green's function (and its derivatives) in a standard boundary integral (symmetric Galerkin) approximation, and accurate results are obtained. In particular, the present SGBEM for FGMs can also handle crack geometries [13] as the hypersingular equation has been successfully implemented.

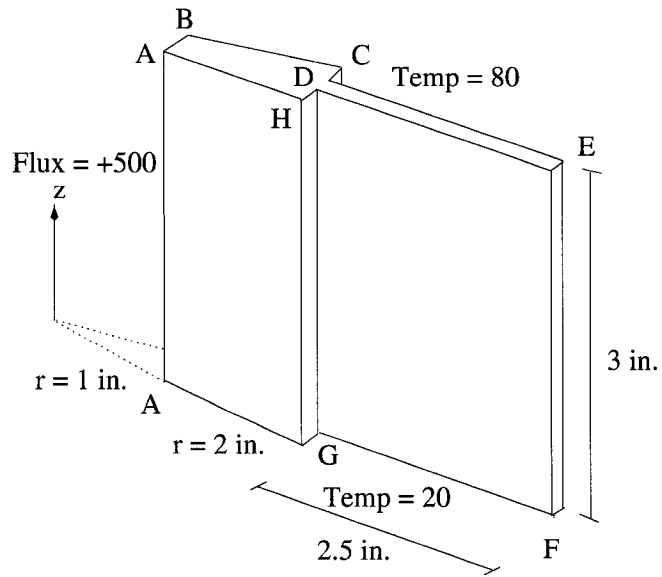


Figure 3.14: The geometry and the boundary conditions of the analysis region.

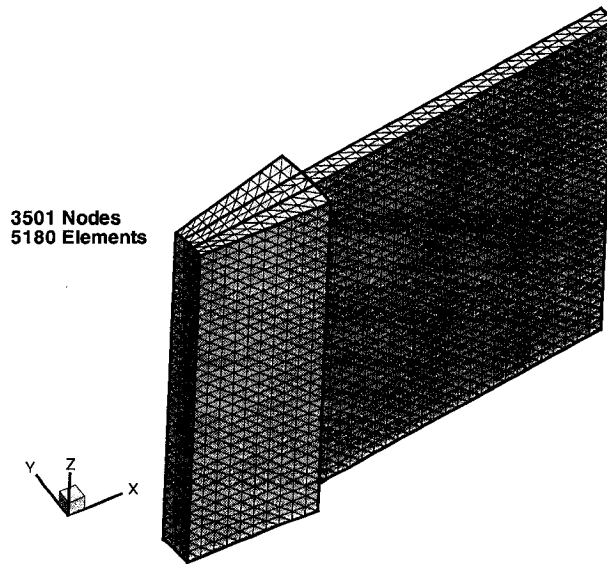


Figure 3.15: The boundary element mesh for the analysis region of the compressor.

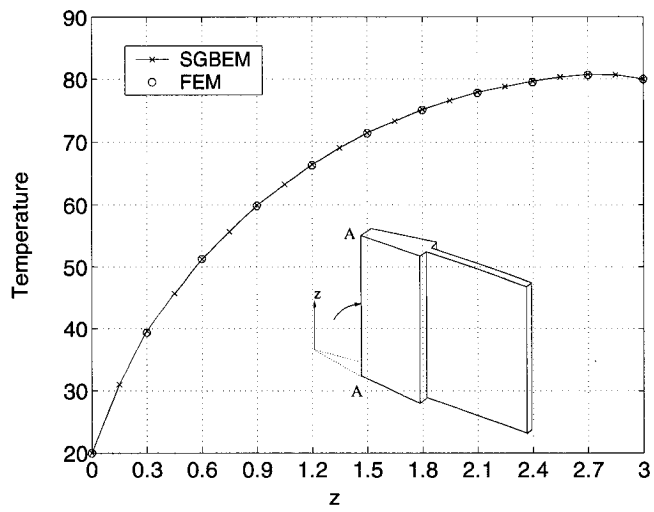


Figure 3.16: Temperature distribution in z -direction at edge of the blade.

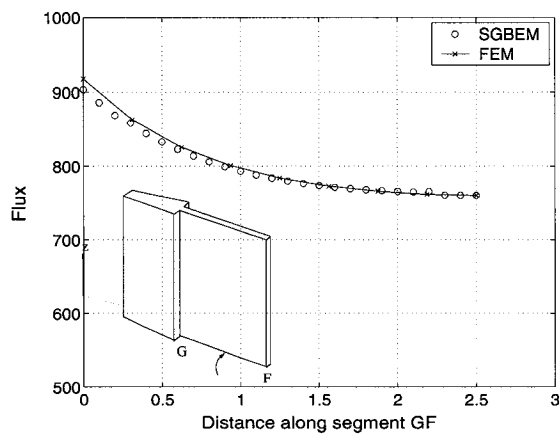


Figure 3.17: Flux distribution along segment GF of the blade.

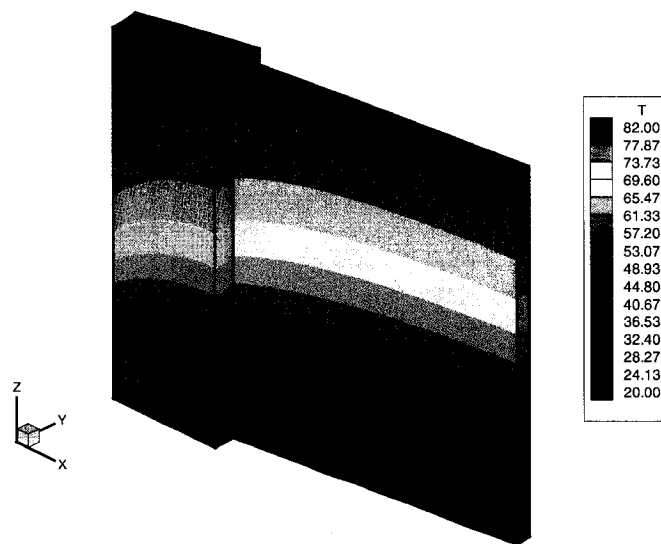


Figure 3.18: BEM contour plot of the temperature of the blade.

Chapter 4

Green's function approach for transient heat conduction in graded materials

In this chapter, the Green's function for three-dimensional transient heat conduction (diffusion equation) for functionally graded materials (FGMs) is derived. The thermal conductivity and heat capacitance both vary exponentially in one coordinate. In the process of solving this diffusion problem numerically, a Laplace transform approach is used to eliminate the dependence on time. The fundamental solution in Laplace space is derived and the boundary integral equation formulation for the Laplace Transform Boundary Element Method (LTBEM) is obtained. The numerical implementation is performed using a Galerkin approximation, and the time-dependence is restored by numerical inversion of the Laplace transform. Two numerical inversion techniques have been investigated: a Fourier series method and Stehfest's algorithm, the latter being preferred. A number of test problems have been examined and the results are compared with available analytical solutions.

This chapter is organized as follows. Section 4.1 gives an introduction to the problem at hand and does an extensive literature review. The basic equations of the diffusion problem are described in Section 4.2. The Green's function for the FGM diffusion equation is derived in Section 4.3. In Section 4.4 the Laplace Transform BEM formulation is presented. Section 4.5 discusses several aspects of the numerical implementation of the boundary integral analysis and Section 4.6 does the same for the numerical inversion of the Laplace transform. Some numerical examples are presented in Section 4.7. Finally concluding remarks are discussed in Section 4.8.

4.1 Introduction

Transient heat conduction problems can be efficiently solved with the boundary element method (BEM). The various procedures reported in the literature can essentially be classified into two broad categories: (1) the time domain approach and (2) the transform space approach.

In the *time domain approach*, a time marching scheme associated with the BEM solution at each time step is used, and solutions are found directly in the time domain. The time dependent fundamental solution is used to transform the differential system into a boundary integral equation. The numerical solution of the boundary integral requires both space and time discretization. Early works using the time-domain approach include those by Chang *et al.* [25], Shaw [153], Curran *et al.* [44], Wrobel and Brebbia [185], and many others. Recent works involve that of Lesnic *et al.* [109], Coda and Venturini [38, 37], Pasquetti and Caruso [143], Wrobel *et al.* [136], Divo and Kassab [49], etc.

By employing a time-dependent fundamental solution together with recent developments in techniques for converting volume integrals into a (series of) boundary integrals, the diffusion problem can be solved by means of finite-differencing in time and BEM discretization for the spatial variables. The volume integral can be converted through either a set of local interpolation functions – known as the dual reciprocity method, as presented by Brebbia and Wrobel [186] – or a hierarchy of higher order fundamental solutions – known as the multiple reciprocity method, as presented by Nowak [132].

A drawback of time-marching schemes is that they can be numerically inefficient. An alternative is to employ a *transform space* approach, wherein the time dependent derivative is eliminated in favor of an (algebraic) transform variable. However, once the differential system is solved in transform space, reconstituting the solution in the time domain requires an inverse transform. Although this approach is simple and attractive, the accuracy depends upon an efficient and accurate numerical inverse transform. For diffusion problems, Laplace transform (LT) seems to be the best choice. The first such formulation utilizing the Laplace transform approach was proposed by Rizzo and Shippy [145] for solution of heat conduction problems in solids. Later Liggett and Liu [113] extended the method to unsteady flows in confined aquifers. Early Laplace inversion methods were not efficient, as they employed a type of curve fitting process for which the behavior of the solution had to be known a priori. However, with the advancement of techniques for inverse LT, this approach has received renewed attention. Moridis and Reddell [124] successfully used their Laplace transform boundary element method (LTBEM) for diffusion type problems. Cheng *et al.* [33] also used the BEM to solve axisymmetric diffusion problems in the LT space. Zhu *et al.* [192], Zhu and Satravaha

[191], and Zhu [190] extended the work to the Laplace transform dual reciprocity method (LTDRM) for solving nonlinear diffusion equations with a source term and temperature-dependent diffusivity. Goldberg and Chen [67] used the Method of fundamental solutions (MFS) in Laplace space for both diffusion and Helmholtz equations. Maillet *et al.* [119] recently used this approach to solve heat transfer problems by the quadrupole method. Some details of both approaches (i.e. time domain and transformed space) in transient problems can be found in Reference [190]. Similar problems for different applications have been presented by Cheng [34] for ground water flow in heterogeneous media, and by Wu and Lee [189] and Lacerda *et al.* [105] for acoustic propagation with a mean flow.

As is usual in boundary element applications, all of the above work assumes a homogeneous medium. The present work is concerned with transient heat transfer in functionally graded materials (FGMs); the steady state FGM problem has been examined in [75]. The composition and the volume fraction of FGM constituents vary gradually, giving a non-uniform microstructure with continuously graded macroproperties (e.g. specific heat, conductivity, density). For instance, one face of a structural component (plate or cylinder) may be an engineering ceramic that can resist severe thermal loading, and the other face may be a metal to maintain structural rigidity and toughness. Example applications include pressure vessels and pipes in nuclear reactors or chemical plants, and other examples can be found in the review papers by Tanigawa [179] and Noda [129]. A comprehensive treatment of the science and technology of FGMs can be found in the book by Suresh and Mortensen [171] or the book by Miyamoto *et al.* [122].

In this work, the Green's function for the three-dimensional (3D) FGM transient diffusion equation is derived using an exponential variation transform; the boundary integral equation based upon this Green's function is then solved numerically using a Galerkin (as opposed to collocation) approximation [12]. The exponential transform technique has been previously used by Carslaw and Jaeger [24] to obtain analytical solutions for various problems. Moreover, Li and Evans [110], Onishi and Ikeuchi [90], Ramachandran [144] and, more recently, Singh and Tanaka [117] have used this transform to solve advection-diffusion problems.

4.2 Basic Equations

The transient diffusion equation is given by

$$\nabla \cdot (k \nabla \phi) = c\rho \frac{\partial \phi}{\partial t} \quad (4.1)$$

where $\phi = \phi(x, y, z; t)$ is the temperature function, c is the specific heat, ρ is the density, and k is the thermal conductivity. We assume that the thermal conductivity varies exponentially in one cartesian coordinate, i.e.

$$k(x, y, z) = k_0 e^{2\beta z} \quad (4.2)$$

in which β is the nonhomogeneity parameter. The specific heat is also graded with the same functional variation as the conductivity,

$$c(x, y, z) = c_0 e^{2\beta z} \quad (4.3)$$

Substituting these material expressions into Eq. (4.1), one obtains

$$\nabla^2 \phi + 2\beta \phi_z = \frac{1}{\alpha} \frac{\partial \phi}{\partial t} \quad (4.4)$$

where $\alpha = k_0/(c_0 \rho)$ and ϕ_z denotes the derivative of ϕ with respect to z (i.e. $\phi_z \equiv \partial \phi / \partial z$).

Two types of boundary conditions are prescribed. The Dirichlet condition for the unknown potential ϕ is

$$\phi(x, y, z; t) = \bar{\phi}(x, y, z; t) \quad (4.5)$$

on boundary Σ_1 and the Neumann condition for its flux is

$$q(x, y, z; t) = -k(\cdot) \frac{\partial \phi(x, y, z; t)}{\partial n} = \bar{q}(x, y, z; t) \quad (4.6)$$

on boundary Σ_2 , where \mathbf{n} is the unit outward normal to Σ_2 . Here a bar over the quantity of interest means that it assumes a prescribed value. For a well-posed problem $\Sigma_1 \cup \Sigma_2 = \Sigma$ with Σ being the entire boundary. As the problem is time dependent, in addition to these boundary conditions, an initial condition at a specific time t_0 must also be prescribed. A zero initial temperature distribution has been considered in all the examples in this chapter, i.e.

$$\phi(x, y, z; t_0) = \phi_0(x, y, z) = 0 \quad (4.7)$$

A nonzero initial temperature distribution may be solved with the dual reciprocity method [135].

4.3 Green's Function

The Green's function for Eq. (4.4) can be derived by employing the substitution

$$\phi = e^{-\beta z - \beta^2 \alpha t} u. \quad (4.8)$$

Thus, the derivatives in Eq. (4.4) can be expressed in terms of u , as follows:

$$\frac{\partial \phi}{\partial z} = -\beta e^{-\beta z - \beta^2 \alpha t} u + e^{-\beta z - \beta^2 \alpha t} \frac{\partial u}{\partial z} \quad (4.9)$$

$$\frac{\partial^2 \phi}{\partial z^2} = \beta^2 e^{-\beta z - \beta^2 \alpha t} u - 2\beta e^{-\beta z - \beta^2 \alpha t} \frac{\partial u}{\partial z} + e^{-\beta z - \beta^2 \alpha t} \frac{\partial^2 u}{\partial z^2} \quad (4.10)$$

$$\frac{1}{\alpha} \frac{\partial \phi}{\partial t} = \frac{1}{\alpha} (-\beta^2 \alpha e^{-\beta z - \beta^2 \alpha t}) u + \frac{e^{-\beta z - \beta^2 \alpha t}}{\alpha} \frac{\partial u}{\partial t} \quad (4.11)$$

Substituting Eqs. (4.9), (4.10) and (4.11) into Eq. (4.4), one obtains

$$\nabla^2 u = \frac{1}{\alpha} \frac{\partial u}{\partial t} \quad (4.12)$$

which is the standard diffusion equation for a homogeneous material problem. The time dependent fundamental solution for this equation is known [18], and is given by

$$u^* = \frac{1}{(4\pi\alpha\tau)^{\frac{3}{2}}} e^{-\frac{r^2}{4\alpha\tau}} \quad (4.13)$$

where $\tau = t_F - t$. Note that the function u^* represents the temperature field at time t_F produced by an instantaneous source of heat at point $P(x_p, y_p, z_p)$ and time t . The 3D fundamental solution to the FGM diffusion equation can be written by backsubstitution (using Eq. (4.8)) as

$$\phi^* = \frac{1}{(4\pi\alpha\tau)^{\frac{3}{2}}} e^{-\beta(z-z_p) - \beta^2\alpha\tau - \frac{r^2}{4\alpha\tau}} \quad (4.14)$$

4.4 Laplace Transform BEM (LTBEM) Formulation

Let the Laplace transform (LT) of ϕ be denoted by

$$\tilde{\phi}(Q, s) = \int_{\mathcal{R}} \phi(Q, t) e^{-st} dt \quad (4.15)$$

Thus, in LT space, the differential equation (4) becomes

$$\nabla^2 \tilde{\phi} + 2\beta \tilde{\phi}_z - \frac{s}{\alpha} \tilde{\phi} = 0 \quad (4.16)$$

where $\phi_0 = 0$ (at $t = 0$) is considered (see Eq. (4.7)).

Following the usual practice, the corresponding boundary integral statement can be obtained by ‘orthogonalizing’ this equation against an arbitrary (for now) function $f(x, y, z) = f(Q)$, *i.e.*, integrating over a bounded volume V

$$\int_V f(Q) (\nabla^2 \tilde{\phi} + 2\beta \tilde{\phi}_z - \frac{s}{\alpha} \tilde{\phi}) dV_Q = 0 \quad (4.17)$$

According to Green’s second identity, if the two functions ϕ and λ have continuous first and second derivatives in V , then

$$\int_V (\phi \nabla^2 \lambda - \lambda \nabla^2 \phi) dV = \int_\Sigma \left(\phi \frac{\partial \lambda}{\partial n} - \lambda \frac{\partial \phi}{\partial n} \right) dS \quad (4.18)$$

Using this relation and denoting the boundary of V by Σ , the first term of Eq. (4.17) becomes,

$$\int_V f(Q) \nabla^2 \tilde{\phi} dV_Q = \int_V \tilde{\phi}(Q) \nabla^2 f(Q) dV_Q + \int_\Sigma \left(f(Q) \frac{\partial}{\partial n} \tilde{\phi}(Q) - \tilde{\phi}(Q) \frac{\partial}{\partial n} f(Q) \right) dS_Q. \quad (4.19)$$

Integrating by parts the second term of Eq. (4.17) we obtain,

$$\int_V 2\beta f(Q) \tilde{\phi}_z dV_Q = \int_\Sigma 2\beta f(Q) n_z \tilde{\phi}(Q) dS_Q - \int_V 2\beta \frac{\partial f}{\partial z} \tilde{\phi}(Q) dV_Q \quad (4.20)$$

and using Eq. (4.19) and Eq. (4.20) in Eq. (4.17), we get after simplification,

$$\begin{aligned} 0 = & \int_\Sigma \left(f(Q) \frac{\partial}{\partial n} \tilde{\phi}(Q) - \tilde{\phi}(Q) \frac{\partial}{\partial n} f(Q) + 2\beta n_z(Q) \tilde{\phi}(Q) f(Q) \right) dS_Q \\ & + \int_V \tilde{\phi}(Q) \left(\nabla^2 f(Q) - 2\beta f_z(Q) - \frac{s}{\alpha} f(Q) \right) dV_Q \end{aligned} \quad (4.21)$$

where $f_z = \partial f / \partial z$, and $\mathbf{n}(Q) = (n_x, n_y, n_z)$ is the unit outward normal on Σ .

If we select $f(Q) = G(P, Q)$ as a Green’s function, then the Green’s function equation is (cf. Eq. (4.4))

$$\nabla^2 G(P, Q) - 2\beta G_z(Q) - \frac{s}{\alpha} G(P, Q) = -\delta(Q - P), \quad (4.22)$$

where δ is the Dirac Delta function. Thus the source point volume integral in Eq. (4.21) becomes $-\tilde{\phi}(P)$. By means of Eq. (4.22), Eq. (4.21) can be rewritten as

$$\tilde{\phi}(P) + \int_{\Sigma} \left(\frac{\partial}{\partial n} G(P, Q) - 2\beta n_z G(P, Q) \right) \tilde{\phi}(Q) dS_Q = \int_{\Sigma} G(P, Q) \frac{\partial}{\partial n} \tilde{\phi}(Q) dS_Q. \quad (4.23)$$

In order to obtain the Green's function in Laplace space, Eq. (4.22) is modified by using the substitution

$$G = e^{\beta z} v. \quad (4.24)$$

In this case, the differential equation for the LT space is

$$\nabla^2 v - \left(\beta^2 + \frac{s}{\alpha} \right) v = 0. \quad (4.25)$$

This equation is the modified Helmholtz equation, whose Green's function is known. Thus the Green's function in 3D LT space is

$$v = \frac{1}{4\pi r} e^{-\sqrt{\beta^2 + \frac{s}{\alpha}} r}. \quad (4.26)$$

By back substitution (see Eq. (4.24)), we obtain

$$G(P, Q, s) = \frac{1}{4\pi r} e^{\beta z} e^{-\sqrt{\beta^2 + \frac{s}{\alpha}} r}. \quad (4.27)$$

The boundary conditions, Eq. (4.5) and Eq. (4.6), must also be transformed into Laplace space, i.e.

$$\tilde{\bar{\phi}}(Q, s) = \int_{\mathcal{R}} \bar{\phi}(Q, t) e^{-st} dt, \quad \tilde{\bar{q}}(Q, s) = \int_{\mathcal{R}} \bar{q}(Q, t) e^{-st} dt \quad (4.28)$$

respectively. For constant boundary conditions the above equations reduce to (See Brebbia, Telles and Wrobel [18], p. 143)

$$\tilde{\bar{\phi}}(Q, s) = \frac{\bar{\phi}(Q, t)}{s}, \quad \tilde{\bar{q}}(Q, s) = \frac{\bar{q}(Q, t)}{s} \quad (4.29)$$

respectively.

The modified kernel functions, in terms of the Laplace variable s , are

$$G(P, Q, s) = \frac{1}{4\pi r} e^{\beta(z_Q - z_P) - \sqrt{\beta^2 + \frac{s}{\alpha}} r} \quad (4.30)$$

and

$$\begin{aligned} & \frac{\partial}{\partial n} G(P, Q, s) - 2\beta n_z G(P, Q, s) \\ &= \frac{e^{\beta R_z - \sqrt{\beta^2 + \frac{s}{\alpha}} r}}{4\pi} \left(-\frac{1}{r^2} \frac{\mathbf{n} \cdot \mathbf{R}}{r} - \frac{1}{r} \sqrt{\beta^2 + \frac{s}{\alpha}} \frac{\mathbf{n} \cdot \mathbf{R}}{r} + \frac{1}{r} \beta n_z - \frac{2\beta n_z}{r} \right) \end{aligned} \quad (4.31)$$

$$= -\frac{e^{\beta R_z - \sqrt{\beta^2 + \frac{s}{\alpha}} r}}{4\pi} \left(\frac{\mathbf{n} \cdot \mathbf{R}}{r^3} + \sqrt{\beta^2 + \frac{s}{\alpha}} \frac{\mathbf{n} \cdot \mathbf{R}}{r^2} + \frac{\beta n_z}{r} \right) \quad (4.32)$$

where \mathbf{n} is the unit outward normal at a field point Q , n_z is the z component of \mathbf{n} , $\mathbf{R} = \mathbf{Q} - \mathbf{P}$, $R_z = z_Q - z_P$, and r is the norm of \mathbf{R} , i.e. $r = \|\mathbf{R}\| = \|\mathbf{Q} - \mathbf{P}\|$

4.5 Numerical Implementation of the 3D Galerkin BEM

The numerical methods employed in this work use standard Galerkin implementation techniques [12] in conjunction with the LT method. A few aspects of the numerical methods are briefly reviewed in this section.

Division of the boundary into elements. The surface of the solution domain is divided into a number of connected elements. Over each element, the variation of the geometry and the variables (potential and flux) is approximated by simple functions. In this study, six noded isoparametric quadratic triangular elements are used (see Figure 4.1).

The geometry of an element can be defined by the coordinates of its six nodes using appropriate quadratic shape functions as follows

$$x_i(\xi, \eta) = \sum_{j=1}^6 N_j(\xi, \eta) (x_i)_j \quad (4.33)$$

In an isoparametric approximation, the same shape functions are used for the solution variables, as follows:

$$\begin{aligned} \phi_i(\xi, \eta) &= \sum_{j=1}^6 N_j(\xi, \eta) (\phi_i)_j \\ \frac{\partial \phi_i}{\partial n}(\xi, \eta) &= \sum_{j=1}^6 N_j(\xi, \eta) \left(\frac{\partial \phi_i}{\partial n} \right)_j \end{aligned} \quad (4.34)$$

The shape functions can be explicitly written in terms of intrinsic coordinates ξ and η as follows (see Figure 4.1):

$$\begin{aligned}
N_1(\xi, \eta) &= (1 - \xi - \eta)(1 - 2\xi - 2\eta) & N_4(\xi, \eta) &= 4\xi(1 - \xi - \eta) \\
N_2(\xi, \eta) &= \xi(2\xi - 1) & N_5(\xi, \eta) &= 4\xi\eta \\
N_3(\xi, \eta) &= \eta(2\eta - 1) & N_6(\xi, \eta) &= 4\eta(1 - \xi - \eta) \quad (4.35)
\end{aligned}$$

The intrinsic coordinate space is the right triangle with $\xi \geq 0$, $\eta \geq 0$ and $\xi + \eta \leq 1$.

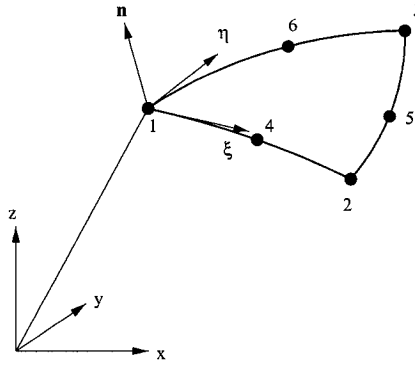


Figure 4.1: Isoparametric quadratic triangular element of 6 nodes. The intrinsic coordinate space is the right triangle in (ξ, η) space with $\xi \geq 0$, $\eta \geq 0$ and $\xi + \eta \leq 1$.

Galerkin Boundary Integral Equation. Define

$$\mathcal{B}(P) \equiv \phi(P) + \int_{\Sigma} \left(\frac{\partial}{\partial n} G(P, Q) - 2\beta n_z G(P, Q) \right) \phi(Q) dS_Q - \int_{\Sigma} G(P, Q) \frac{\partial \phi}{\partial n}(Q) dS_Q$$

and thus for an exact solution $\mathcal{B}(P) \equiv 0$.

In a Galerkin approximation, the error in the approximate solution is orthogonalized against the shape functions, *i.e.*, the shape functions are the weighting functions and $\mathcal{B}(P) = 0$ is enforced in the ‘weak sense’

$$\int_{\Sigma} N_k(P) \mathcal{B}(P) dP = 0 \quad (4.36)$$

After replacing the boundary and the boundary functions by their interpolated approximations, a set of linear algebraic equations emerges,

$$[H]\{\phi\} = [G] \left\{ \frac{\partial \phi}{\partial n} \right\}. \quad (4.37)$$

In computing the matrix elements, the singular integrals must of course be evaluated differ-

ently. The treatment of the singularity are analogous to the procedure described in Chapter 2.

4.6 Numerical Inversion of the Laplace Transform

In the LTBEEM approach, the numerical inversion of the LT is a key issue. The LT technique has been efficiently applied in conjunction with different numerical methods such as finite difference and finite element methods for the solution of ground water flow and solute transport problems (Sudicky [170], Moridis and Reddell [124]), and heat conduction problems (Chen and Chen [31], Chen and Lin [32]). In these papers different Laplace inversion algorithms such as those of Talbot [177], Dubner and Abate [53], Durbin [56], Crump [43], and Stehfest [167, 168] were used. The advantages and deficiencies of some algorithm were pointed out in Maillet *et al.* [119]. Davies and Martin [47] made a critical study of the various algorithms. Later Duffy [54] examined three popular methods for numerical inversion of the Laplace transform, i.e. direct integration [54], Week's [182] method and Talbot's method [177].

As LT inversion is an ill-posed problem, small truncation errors can be greatly magnified in the inversion process, leading to poor numerical results. In recent times, Moridis and Reddell [124] showed that Stehfest's algorithm poses no such problems and high accuracy may be achieved. Subsequently Zhu *et al.* [192], and Satravaha and Zhu [191] had similar success using numerical inversion of LT in BEM problems. Recently Maillet *et al.* [119] critically reviewed the Stehfest's algorithm and pointed out its advantages and disadvantages. For the present study, a computer code has been written following Stehfest's algorithm [167, 168].

The Stehfest's algorithm originates from Gaver [64]. If $\tilde{P}(s)$ is the Laplace Transform of $F(t)$ then an approximate value F_a of the inverse $F(t)$ for a specific time $t = T$ is given by

$$F_a = \frac{\ln 2}{T} \sum_{i=1}^N V_i \tilde{P} \left(\frac{\ln 2}{T} i \right) \quad (4.38)$$

where

$$V_i = (-1)^{N/2+1} \sum_{k=\frac{i+1}{2}}^{\min(i, N/2)} \frac{k^{N/2} (2k)!}{(N/2 - k)! k! (k - 1)! (i - k)! (2k - i)!} \quad (4.39)$$

Equations (4.38) and (4.39) correspond to the final form used in our numerical implementation.

When inverting an function from its Laplace transform, one should compare the results for different N, to verify whether the function is smooth enough, to observe the accuracy,

and to determine an optimum value of N . Originally Stehfest suggested to use $N = 10$ for single precision arithmetic, however, Moridis and Reddell [124], and Zhu *et al.* [192] found no significant change in their results for $6 \leq N \leq 10$. In the present calculations, $N = 10$ was adopted.

Most of the methods for the numerical inversion of the LT require the use of complex values of the LT parameter, and as a result the use of complex arithmetic leads to additional storage and an increase in computation time. The disadvantage of using complex arithmetic has been overcome in Stehfest's method. It uses only real arithmetic and thus produces significant reduction in storage together with an increased efficiency in computation time.

The second LT technique that has been explored is the method recently developed by Murli *et al.* [46]. This is a Fourier series method, based on the discretization of the Riemann inversion formula using trapezoidal rule with step size $h = \pi/T$:

$$F_N(t) = \frac{e^{\sigma t}}{T} \operatorname{Re} \left(\frac{F(\sigma)}{2} + \sum_{k=1}^N F\left(\sigma + \frac{ik\pi}{T}\right) e^{\frac{ik\pi t}{T}} \right) \quad (4.40)$$

Compared to Stehfest's algorithm, this method was found to require more iterations to achieve convergence, and moreover requires complex arithmetic. Thus, the results reported below employ the Stehfest's algorithm.

4.7 Numerical Examples

As noted above, the integral equation is numerically approximated via the non-symmetric Galerkin BEM Method. Standard 6-node isoparametric quadratic triangular elements are used to interpolate the boundary geometry and boundary functions for the physical variables. For all the examples, $N = 10$ is used for the Laplace inversion algorithm using the Stehfest's Method (see Section 4.6).

Five examples are considered :

1. Transient two-dimensional (2D) heat conduction in a homogeneous cube
2. Cylinder with constant surface temperature
3. Constant temperature on two planes of an FGM cube
4. Linear heat flux on a face of an FGM cube
5. Time-dependent boundary condition

The first two problems deal with homogeneous materials. These problems validate the Galerkin BEM code and ensure that the FGM implementation recovers the homogeneous case when the non-homogeneity parameter β vanishes, i.e. $\beta = 0$. The last three problems

deal with transient heat conduction in FGMs, i.e. $\beta \neq 0$. Notice that the prescribed boundary data for the first four problems is time-independent, while for the last problem it is time-dependent.

4.7.1 Transient two-dimensional heat conduction in a homogeneous cube

The original version of this problem has been proposed by Bruch and Zyzvoloski [19], consisting of a homogeneous two dimensional heat conduction in a square domain subjected to the following boundary and initial conditions (see Figure 4.2(a)):

$$\phi(L_x, y, t) = \phi(x, L_y, t) = 1.0 \quad (4.41)$$

$$\frac{\partial \phi(0, y, t)}{\partial x} = \frac{\partial \phi(x, 0, t)}{\partial y} = 0.0 \quad (4.42)$$

$$\phi(x, y, 0) = 0.0 \quad (4.43)$$

where L_x and L_y are the lengths of the solution domain in the x and y directions, respectively. k_x and k_y are the thermal conductivities in x and y directions respectively with the specific heat $c = 1.0$. The analytical solution of the 2D problem for temperature [19] is,

$$\begin{aligned} \phi(x, y, t) = & 1.0 + \sum_{n=1}^{\infty} \sum_{j=1}^{\infty} C_{nj} \cos \frac{(2n-1)\pi x}{2L_x} \cos \frac{(2j-1)\pi y}{2L_y} \times \\ & \exp \left\{ - \left(\frac{k_x(2n-1)^2\pi^2}{4L_x^2} + \frac{k_y(2j-1)^2\pi^2}{4L_y^2} \right) t \right\} \end{aligned} \quad (4.44)$$

and the analytical solution for the flux in the y direction is,

$$\begin{aligned} q(x, y, t) = & -k_y \frac{\partial \phi}{\partial y} \\ = & -k_y \sum_{n=1}^{\infty} \sum_{j=1}^{\infty} \frac{(2j-1)\pi}{2L_y} C_{nj} \cos \frac{(2n-1)\pi x}{2L_x} \sin \frac{(2j-1)\pi y}{2L_y} \times \\ & \exp \left\{ - \left(\frac{k_x(2n-1)^2\pi^2}{4L_x^2} + \frac{k_y(2j-1)^2\pi^2}{4L_y^2} \right) t \right\} \end{aligned} \quad (4.45)$$

where

$$C_{nj} = \frac{16.0(-1.0)(-1)^{n+1}(-1)^{j+1}}{\pi^2(2n-1)(2j-1)}$$

The 2D problem of Figure 4.2(a) is solved using an equivalent 3D problem as shown in Figure 4.2(b). The 3D BEM discretization consists of 200 elements on each face of the cube leading to a total of 1200 elements. The flux in the z direction is taken as zero to simulate the 2D problem. The cube is analyzed for $0 \leq x \leq 1.0$, $0 \leq y \leq 1.0$ with $k_x = k_y = 1.0$. The geometry and boundary conditions of the problem are shown in Figure 4.2(b). Figure 4.3 shows the variation of temperature at the edge of the top face (shown with a dark solid line in Figure 4.2(b)) at $t = 0.75$ considering the present BEM solution, the FEM solution [19], and the analytical solution (Eq. (4.44)). Note that the BEM solution coincides with the analytical solution within plotting accuracy. Figure 4.4 illustrates the variation of temperature at the edge of the top face (shown with a dark solid line in Figure 4.2(b)) at different time levels. Again the BEM solution agrees with the analytical solution within plotting accuracy. Figure 4.5 shows the flux distribution along x direction at the $y = 1$ face. The BEM solution and the analytical solution agree quite well.

4.7.2 Cylinder of homogeneous material with constant surface temperature

The second homogeneous test problem involves a cylindrical region, and therefore checks that curved surfaces are being handled correctly. The cylinder has zero initial temperature, the top and the bottom surfaces are insulated, and the wall temperature is kept constant. The geometry and BEM mesh for the cylinder is shown in Figure 4.6. The boundary conditions and the initial conditions are as follows,

$$\phi(r, t) = 100, \quad r = 1, \quad r = \text{radial coordinate} \quad (4.46)$$

$$\frac{\partial \phi(x, y, 2; t)}{\partial z} = \frac{\partial \phi(x, y, 0; t)}{\partial z} = 0.0, \quad (4.47)$$

$$\phi(x, y, z; 0) = 0.0 \quad (4.48)$$

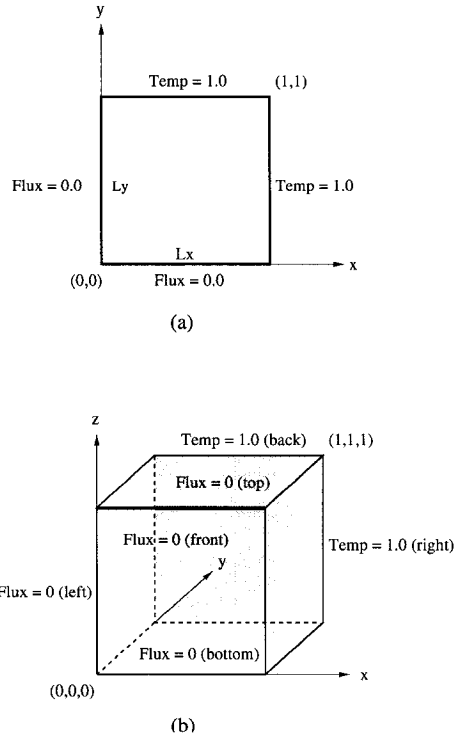


Figure 4.2: Geometry and BCs for the cube problem. **(a)** Original 2D problem. **(b)** Equivalent 3D problem. The faces with prescribed temperature (Temp=1.0) are shaded (Example 1).

The analytical solution to this problem [24] is

$$\phi = T \left(1 - \frac{2}{a} \sum_{n=1}^{\infty} e^{-k\alpha_n^2 t} \frac{J_0(r\alpha_n)}{\alpha_n J_1(a\alpha_n)} \right) \quad (4.49)$$

where T = surface temperature, a = radius of cylinder, $k = k_0/c_0$ and $\pm\alpha_n$, $n = 1, 2, \dots$ are the roots of

$$J_0(a\alpha) = 0. \quad (4.50)$$

The BEM mesh consists of 600 elements, distributed with 100 elements each for the top and bottom faces, and 400 elements for the cylindrical wall. The variation of the temperature along the radius is plotted on Figure 4.7 for various times ($t = 0.005, 0.01, 0.03, 0.05$ and 0.1). Notice that the Galerkin BEM and the analytical results agree within plotting accuracy for all time levels.

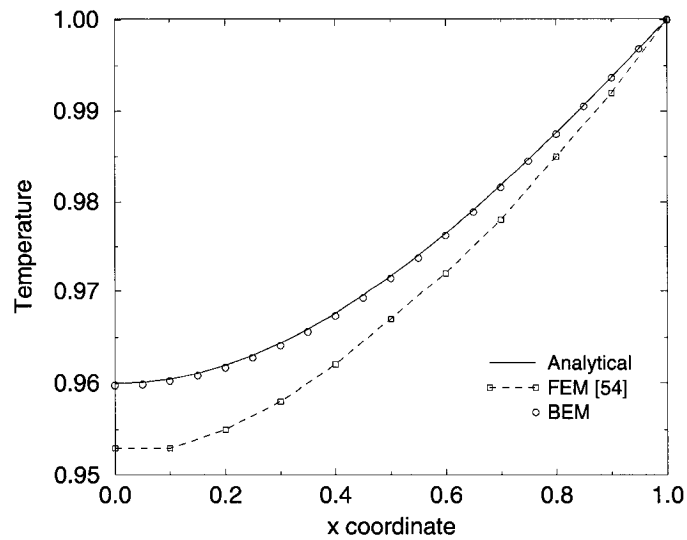


Figure 4.3: Temperature variation at edge ($y=0, z=1$) (shown with a dark solid line in Figure 4.2(b)) considering time $t = 0.75$ for the cube problem with homogeneous material (Example 1).

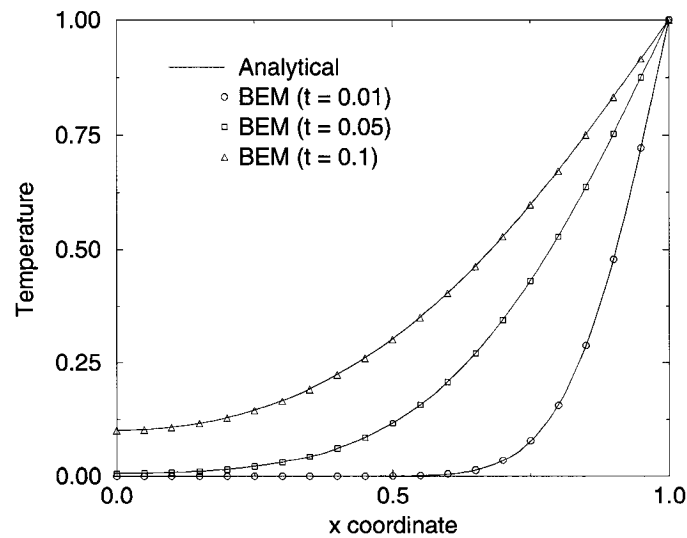


Figure 4.4: Temperature variation with distance (x coordinate) (shown with a dark solid line in Figure 4.2(b)) at different time levels for the cube problem with homogeneous material (Example 1).

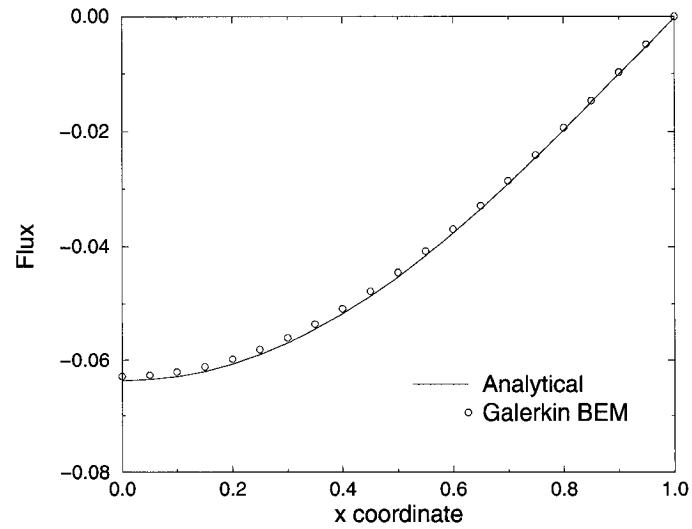


Figure 4.5: Flux distribution along x direction at $y=1$ face for the cube problem with homogeneous material (Example 1).

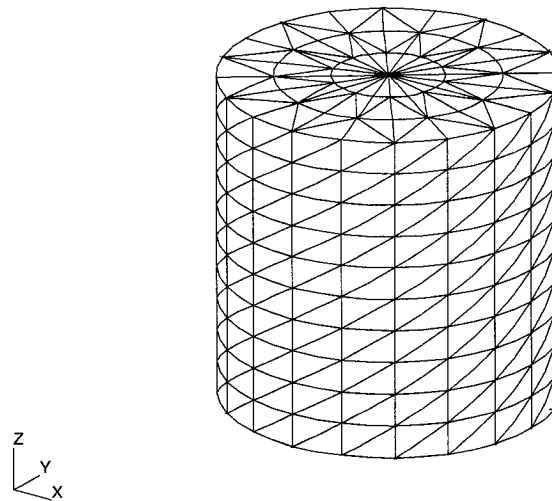


Figure 4.6: Geometry and mesh of the cylinder problem (Example 2).

4.7.3 Constant temperature on two planes of an FGM cube

The problem of interest is shown in Figure 4.8. The cube initial temperature is zero (see Eq. (4.7)). Then the top surface of the cube at $[z = 1]$ is maintained at a temperature of

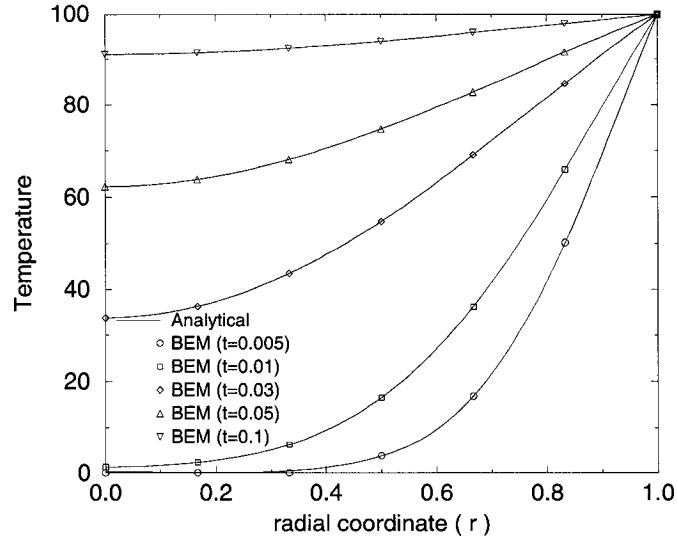


Figure 4.7: Variation of temperature along the radial coordinate (r) for the cylinder problem (Example 2).

$T = 100$ while the bottom face at $[z = 0]$ is zero. The remaining four faces are insulated (zero normal flux). The boundary conditions and the initial conditions are

$$\begin{aligned}
 \phi(x, y, 0; t) &= 0 \\
 \phi(x, y, 1; t) &= 100 \\
 \phi(x, y, z; 0) &= 0
 \end{aligned} \tag{4.51}$$

The thermal conductivity and the specific heat are taken to be

$$k(x, y, z) = k_0 e^{2\beta z} = 5e^{3z} \tag{4.52}$$

$$c(x, y, z) = c_0 e^{2\beta z} = 1e^{3z} \tag{4.53}$$

The analytical solution for temperature is (see Appendix),

$$\begin{aligned}
 \phi(x, y, z; t) &= \phi_s(x, y, z) + \phi_t(x, y, z; t) \\
 &= T \frac{1 - e^{-2\beta z}}{1 - e^{-2\beta L}} + \sum_{n=1}^{\infty} B_n \sin \frac{n\pi z}{L} e^{-\beta z} e^{-\left(\frac{n^2\pi^2}{L^2} + \beta^2\right)\alpha t}
 \end{aligned} \tag{4.54}$$

where L is the dimension of the cube (in the z -direction) and the analytical solution for flux

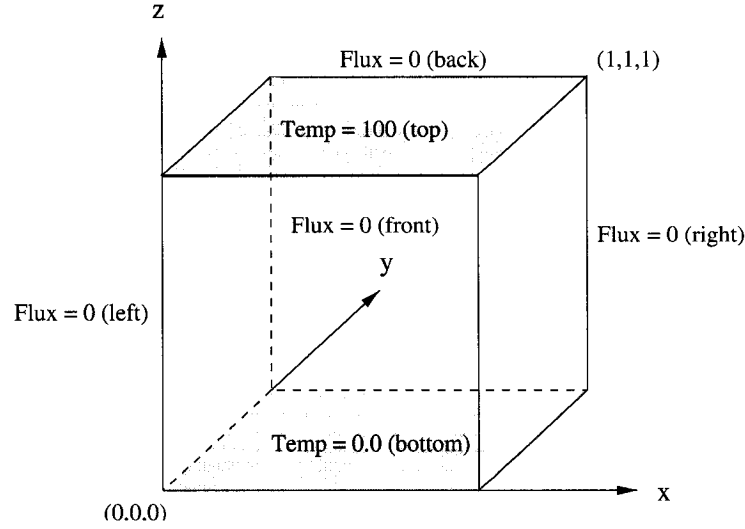


Figure 4.8: Geometry and boundary conditions of the FGM cube problem with constant temperature on two planes. The faces with prescribed temperature are shaded (Example 3).

is (see Appendix),

$$\begin{aligned}
 q(x, y, z; t) &= -k(x, y, z) \frac{\partial \phi}{\partial z} \\
 &= -k(x, y, z) \left[\frac{2\beta T e^{-2\beta z}}{1 - e^{-2\beta L}} + \sum_{n=1}^{\infty} B_n e^{-\beta z} e^{-\left(\frac{n^2 \pi^2}{L^2} + \beta^2\right) \alpha t} \left(\frac{n\pi}{L} \cos \frac{n\pi z}{L} - \beta \sin \frac{n\pi z}{L} \right) \right]
 \end{aligned} \tag{4.55}$$

where

$$B_n = -\frac{2T e^{\beta L}}{\beta^2 L^2 + n^2 \pi^2} \left[\beta L \sin n\pi \frac{1 + e^{-2\beta L}}{1 - e^{-2\beta L}} - n\pi \cos n\pi \right] \tag{4.56}$$

The Galerkin BEM mesh has 1200 elements with 200 elements on each face. Numerical solutions for the temperature profile at different times are shown in Figure 4.9. Notice that the temperature variation matches the analytical solution. Figure 4.10 shows the change of flux with time. At the top face the flux rapidly approaches the steady state flux, while on the bottom face where the temperature is zero, the flux gently approaches to the steady state flux. It is worth observing that the flux from the Galerkin BEM matches the analytical solution of Eq. (4.55) within plotting accuracy. Finally a color contour plot of temperatures at $t=0.5$ is shown in Figure 4.11. This plot confirms that the temperature field is one-dimensional and is captured by the Galerkin BEM solution.

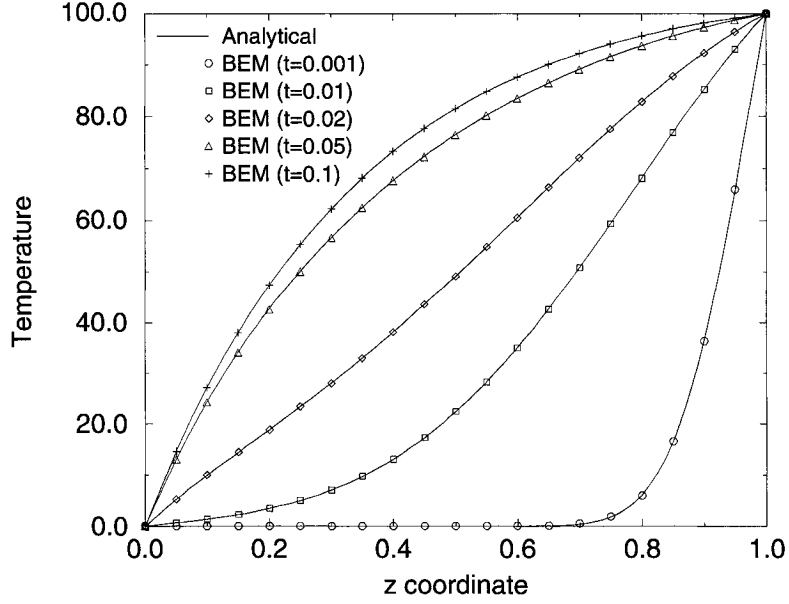


Figure 4.9: Temperature profile in z direction at different time levels for the FGM cube problem with constant temperature on two planes (Example 3).

4.7.4 Linear heat flux on a face of an FGM cube

Figure 4.12 illustrates a cube that is insulated on the faces $[y = 0]$ and $[y = 1]$, while uniform heat fluxes of 5000 units are added and removed respectively at the $[x = 1]$ and $[x = 0]$ faces. In addition the $[z = 0]$ face is specified to have an x -dependent temperature distribution $\phi = 1000x$ and at $[z = 1]$ a normal heat flux of $q = 15000x$ is removed. The initial temperature is zero (see Eq. (4.7)). The material properties are given by Eqs. (4.52) and (4.53). The boundary and the initial conditions for this problem are

$$\begin{aligned}
 \phi(x, y, 0; t) &= 1000x \\
 k(z) \frac{\partial \phi(x, 0, z; t)}{\partial y} &= k(z) \frac{\partial \phi(x, 1, z; t)}{\partial y} = 0 \\
 k(z) \frac{\partial \phi(0, y, z; t)}{\partial x} &= -5000 \\
 k(z) \frac{\partial \phi(1, y, z; t)}{\partial x} &= +5000 \\
 k(z) \frac{\partial \phi(x, y, 1; t)}{\partial z} &= 15000x \\
 \phi(x, y, z, 0) &= 0
 \end{aligned} \tag{4.57}$$

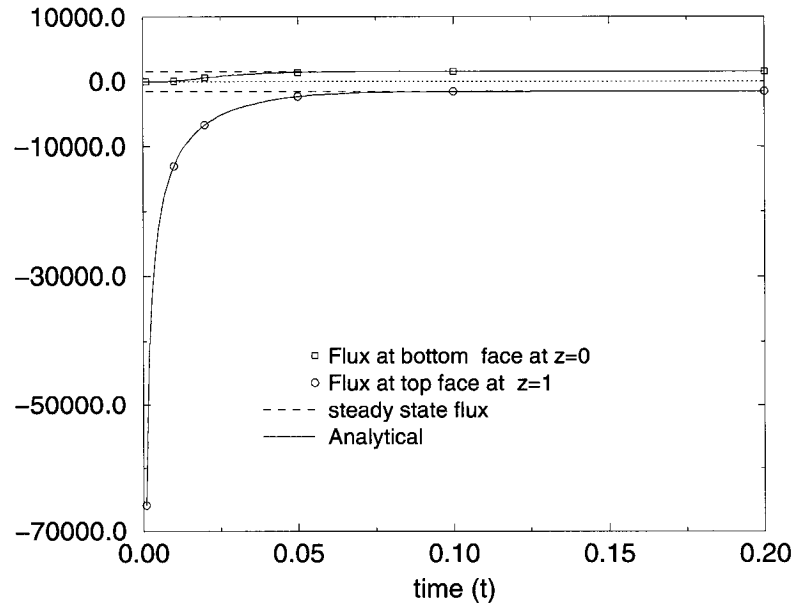


Figure 4.10: Change of flux with time for the FGM cube with constant temperature on two planes (Example 3).

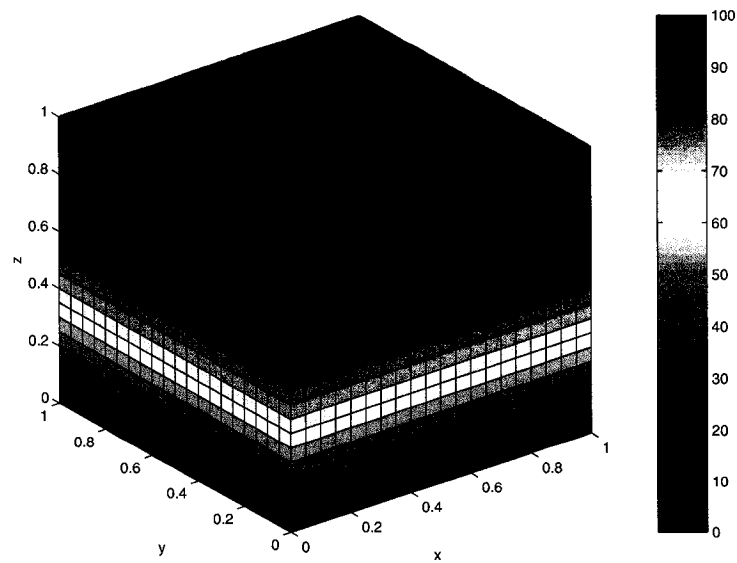


Figure 4.11: Color Contour plot of temperature at time $t = 0.5$ for the FGM cube with constant temperature on two planes (Example 3).

The results of the numerical simulations for the flux distributions along the edge $[y = 0, z = 1]$ for different times are shown in Figure 4.13. The exact steady state solution for flux is,

$$k(z) \frac{\partial \phi(x, y, 0, t)}{\partial z} = 15000x$$

As the time increases the flux converges to the steady state condition, which is expected.

The temperature distribution along edge $[x = 1, y = 1]$ with various times is plotted in Figure 4.14. Notice that as the time increases, the numerical solution approaches the steady state solution, as expected. Finally a color contour plot for temperature is shown in Figure 4.15 for the steady state condition. This plot allows one to verify the 3D surface temperature distribution obtained with the present Galerkin BEM code.

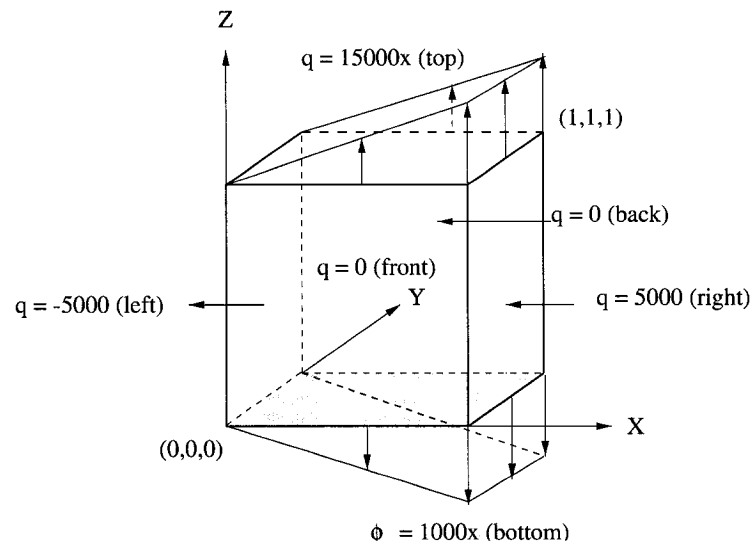


Figure 4.12: Geometry and boundary conditions of the FGM cube problem with linear heat flux. The face with prescribed temperature ($\phi = 1000x$) is shaded (Example 4).

4.7.5 Time-dependent boundary condition

This problem has prescribed time-dependent boundary condition in one face while all the other faces are insulated. The top surface of the cube at $[z = 1]$ is prescribed with a time-dependent boundary condition $\phi = 10t$. The material properties are given by expres-

sions (4.53) and (4.54). The boundary and initial conditions are

$$\begin{aligned} \frac{\partial \phi(0, y, z; t)}{\partial x} = \frac{\partial \phi(1, y, z; t)}{\partial x} = \frac{\partial \phi(x, 0, z; t)}{\partial y} = \frac{\partial \phi(x, 1, z; t)}{\partial y} = \frac{\partial \phi(x, y, 0; t)}{\partial z} = 0 \\ \phi(x, y, z; 0) = 0 \end{aligned} \quad (4.58)$$

The geometry and boundary conditions are presented in Figure 4.16. For the BEM analysis the same mesh, as in the previous example, has been used. The temperature profile in the z direction is plotted at $t = 1$ in Figure 4.17. In order to compare the results, the problem has been modeled using a commercially available FEM software. The corresponding two-dimensional finite element mesh has 100 linear quadrilateral elements and 121 nodes, the analysis was performed with a time step $\Delta t = 0.01$. From Figure 4.17 it is seen that the BEM and FEM results agree well.

4.8 Concludin Remarks

In this work it was shown that Galerkin BEM can be successfully applied to analyze transient heat conduction in functionally graded materials modeled with exponential gradation. In this

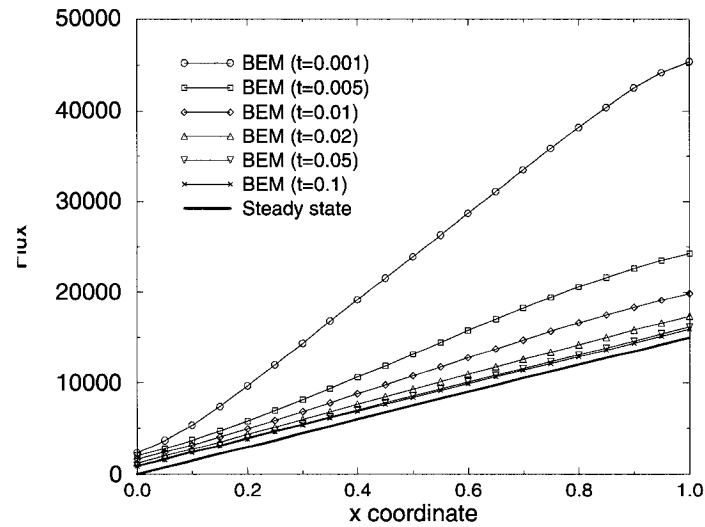


Figure 4.13: Flux distribution along edge $[y=0, z=1]$ considering various times for the FGM cube problem with linear heat flux in one face (Example 4).

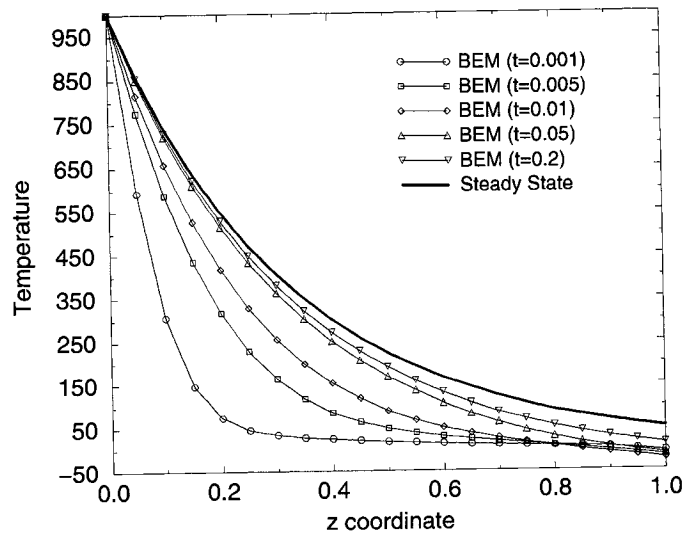


Figure 4.14: Temperature distribution along edge $[x=1, y=1]$ considering various times for the FGM cube with linear heat flux in one face (Example 4).

case the Green's function can be easily derived using a simple exponential transformation. The presented numerical results based upon this formulation, implemented in a Galerkin BEM framework, agree extremely well with available analytical solutions. The principal

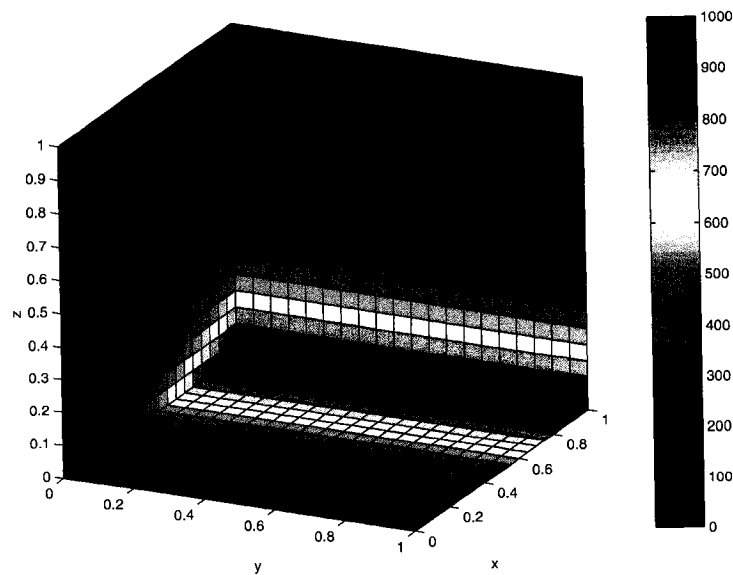


Figure 4.15: Color Contour plot of temperature at steady state for the FGM cube with linear heat flux in one face (Example 4).

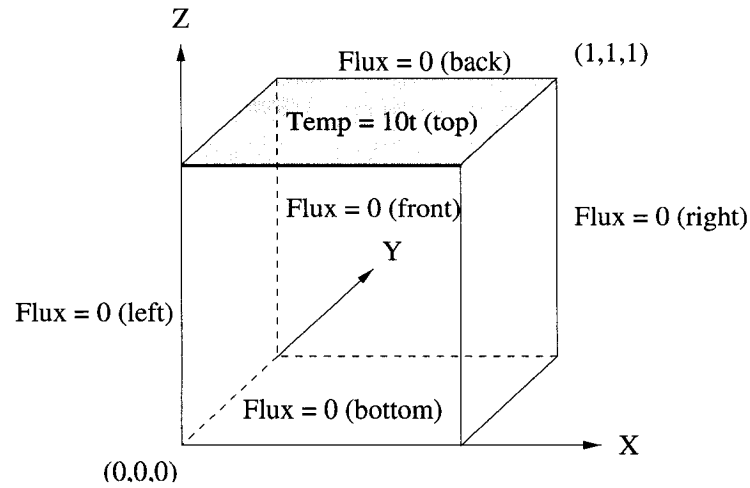


Figure 4.16: Geometry and boundary conditions of the FGM cube problem with time-dependent boundary conditions. The face with prescribed time-dependent boundary condition is shaded (Example 5).

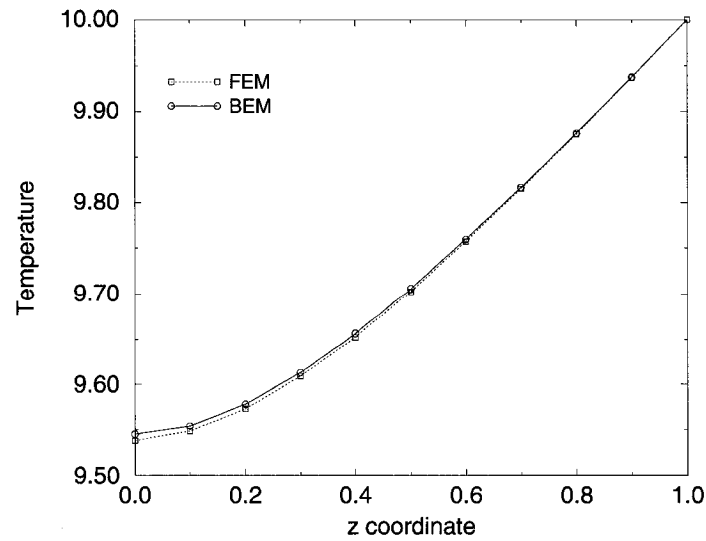


Figure 4.17: Temperature profile in z direction at $t = 1$ for the FGM cube problem with time-dependent boundary condition (Example 5).

computational difficulty with the LTBE is the numerical inversion of the transform, which was handled accurately and efficiently by Stehfest's algorithm.

Chapter 5

Simple BEM for nonhomogeneous media: Problems of potential

This chapter presents a simple boundary element method for solving potential problems in nonhomogeneous media. A physical parameter (e.g. heat conductivity, permeability, permittivity, resistivity, magnetic permeability) has a spatial distribution that varies with one or more coordinates. For certain classes of material variations the nonhomogeneous problem can be transformed to known homogeneous problems such as those governed by the Laplace, Helmholtz and modified Helmholtz equations. A three dimensional Galerkin boundary element method implementation is presented for these cases. However, the present development is not restricted to Galerkin schemes and can be readily extended to other boundary integral methods such as standard collocation. A few test examples are given to verify the proposed formulation. The results from the finite element simulations are used for comparison with the present boundary element solutions. In order to obtain results from the finite element solution using ABAQUS, an user subroutine is developed which incorporates the functional variation of the material at element level.

This chapter is organized as follows. Section 5.1 gives an introduction to the nonhomogeneous problem. Related works in the literature are discussed in Section 5.2. In Section 5.3, the governing equations considering the variable conductivity is presented. A comparison between the Green's function approach and the proposed approach is described in Section 5.4. Some aspects of the numerical implementation is given in Section 5.5. The ABAQUS user subroutine is described in Section 5.6. Finally, a number of numerical examples are presented in Section 5.7 followed by concluding remarks in Section 5.8.

5.1 Introduction

The governing differential equation for a potential function ϕ defined on a region Ω bounded by a surface Σ , with an outward normal \mathbf{n} , can be written as

$$\nabla \cdot (k(x, y, z)\nabla\phi) = 0 \quad (5.1)$$

where $k(x, y, z)$ is a position dependent material function. The general problem under consideration is presented in Figure 5.1. Equation 5.1 is the field equation for a wide range of problems in physics and engineering such as heat transfer, fluid flow motion, flow in porous media, electrostatics and magnetostatics. Table 5.1 presents a list of $k(x, y, z)$ used in different applications [134].

The boundary conditions of the problem can be of the following types:

$$\phi = \bar{\phi} \quad \text{on } \Sigma_1 \quad (\text{Dirichlet type}) \quad (5.2)$$

$$q = -k(x, y, z) \frac{\partial\phi}{\partial n} = \bar{q} \quad \text{on } \Sigma_2 \quad (\text{Neumann type}) \quad (5.3)$$

with $\Sigma = \Sigma_1 + \Sigma_2$ for a well-posed problem. The boundary value problem is a Neumann problem if the flux is known on the whole boundary, and the problem is a Dirichlet problem if the potential is known on the whole boundary. Mixed boundary conditions are also frequently encountered: flux is prescribed over some portion of the boundary and potential is prescribed over the complementary portion of the boundary.

Table 5.1: Problems governed by Eq. (5.1)

Problems	Scalar function ϕ	$k(x, y, z)$	Boundary Condition	
			Dirichlet	Neumann
Heat transfer	Temperature T	Thermal Conductivity (k)	$T = \bar{T}$	Heat flow $q = -k \frac{\partial T}{\partial n}$
Ground water flow	Hydraulic Head H	Permeability (k)	$H = \bar{H}$	Velocity flow $q = -k \frac{\partial H}{\partial n}$
Electrostatic	Field Potential V	Permittivity (ϵ)	$V = \bar{V}$	Electric flow $q = -\epsilon \frac{\partial V}{\partial n}$
Electric conduction	Electropotential E	Resistivity (k)	$E = \bar{E}$	Electric Current $q = -k \frac{\partial E}{\partial n}$
Magnetostatic	Magnetic Potential M	Magnetic permeability (μ)	$M = \bar{M}$	Magnetic Flux Density $B = -\mu \frac{\partial M}{\partial n}$

For nonhomogeneous media, $k(x, y, z)$ can assume any function of x , y and z . With recent development and research of functionally graded materials (FGMs), problems in non-

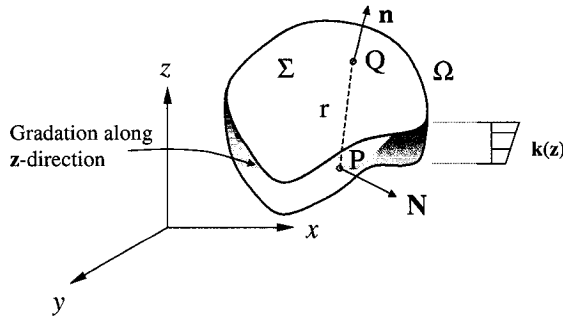


Figure 5.1: Definition of the boundary value problem with boundary Σ and domain Ω . The source point is P (normal \mathbf{N}) and the field point is Q (normal \mathbf{n}).

homogeneous media have generated new interest. In FGMs, the composition and the volume fraction of the FGM constituents vary gradually, giving a nonuniform microstructure with continuously graded macroproperties such as thermal conductivity, elasticity, hardness etc. In most engineering applications the spatial variation of $k(x, y, z)$ is in one coordinate.

There is a class of material variations, which can transform the problem equation to a Laplace or standard/modified Helmholtz equation. The present work demonstrates that by using change of variables which in turn leads to simple changes in the treatment of the boundary conditions of existing homogeneous Laplace and standard/modified Helmholtz codes, the solutions for nonhomogeneous media with quadratic, exponential and trigonometric material variations can be obtained. Numerical implementation for specific cases using these variations of $k(x, y, z)$ in one or more coordinates are presented. Heat transfer problems have been chosen for the numerical examples, although the numerical implementation can be used for any potential problem (See Table 5.1).

Another contribution of this work is the development of a user-subroutine to implement graded finite elements in the finite element method (FEM) software ABAQUS. It is used for comparison purposes with the present BEM solutions.

5.2 Related Work

In the context of BEM, problems in nonhomogeneous media has been previously studied by Cheng [34, 35], Ang *et al.*[5], Shaw [154] and recently by Gray [75] *et al.* and Dumont *et al.*[55]. The majority of these works have emphasized on obtaining the Green's function. Cheng [34] presented a direct Green's function approach for Darcy's flow with spatially variable permeability. The formulation required that the Green's function be found for each given permeability variation. He also presented the Green's function for a class of perme-

ability variations whose square root of hydraulic conductivity satisfies the Laplace and the Helmholtz equations in one to three dimensions. Shaw [155] presented a two dimensional fundamental solution involving axisymmetric material variation and also showed the inter-relationship between the fundamental solutions for different heterogeneous potential, wave and advective-diffusion problems. Lefe and Cheng [106] used a perturbation boundary element for steady state ground water flow for heterogeneous aquifers where the governing equation is decomposed into a Laplace equation and a sequence of Poisson's equations with known right-hand sides. Harrouni *et al.* [83, 84] used a global interpolation based dual reciprocity boundary element method (DRBEM) for Darcy's flow in heterogenous media where the governing equation is transformed into a Poisson-type equation with modified boundary conditions. In this technique the domain integral that arises from the nonhomogeneous part of the governing equation is interpolated by a set of complete basis functions and converted to a series of boundary integrals. Kassab and Divo [50, 48] introduced a technique for heat conduction in heterogeneous media based on a fundamental solution that is a locally radially symmetric response to a non-symmetric forcing function. Multiple techniques have been used to deal with the numerical implementation, namely the *iterative scheme* involving domain integrals and iterations, the *domain scheme* and the *direct Green's function scheme* [34]. The domain technique requires use of domain integrals or radial basis functions [83, 178]. The iterative and the domain scheme decrease the inherent efficiency of the BEM as the boundary-only nature of the method is lost. Another simple technique is the multi-zone approach [107], where the conductivity is assumed to be constant over several zones. This approach is inefficient because in order to capture the continuous variation of the material property a large number of sub-regions or zones are necessary.

Cheng [34] presented some forms of $k(x, y, z)$ for permeability in the context of Darcy's flow, for which closed form expressions of the Green's function were obtained by using a variable transformation following Georghitza [65], which allows Eq. (5.1) to be rewritten as Laplace or Helmholtz equation. In his BEM implementations, the kernels are based on the Green's function G of the heterogenous media, where G is the free-space Green's function defined as

$$\nabla \cdot (k(x, y, z) \nabla G) = -\delta(Q - P) \quad (5.4)$$

where P is the source point, Q is the field point, and the gradient ∇ is taken with respect to the field point Q ($\nabla \equiv \nabla_Q$).

5.3 Governing Equations considering variable conductivity

By defining a variable

$$v(x, y, z) = \sqrt{k(x, y, z)} \phi(x, y, z), \quad (5.5)$$

Eq. (5.1) can be rewritten as

$$\nabla^2 v + \left(\frac{\nabla k \cdot \nabla k}{4k^2} - \frac{\nabla^2 k}{2k} \right) v = 0 \quad (5.6)$$

or,

$$\nabla^2 v + k'(x, y, z)v = 0 \quad (5.7)$$

where

$$k' = \frac{\nabla k \cdot \nabla k}{4k^2} - \frac{\nabla^2 k}{2k} \quad (5.8)$$

From Eq. (5.7), three different cases can be generated. If $k'(x, y, z) = 0$, then Eq. (5.7) becomes the standard Laplace equation, i.e.

$$\nabla^2 v = 0. \quad (5.9)$$

If $k'(x, y, z) = -\beta^2$, then Eq. (5.7) converts to the modified Helmholtz equation, i.e.

$$\nabla^2 v - \beta^2 v = 0, \quad (5.10)$$

while if $k'(x, y, z) = \beta^2$, then Eq. (5.7) transforms to the standard Helmholtz equation, i.e.

$$\nabla^2 v + \beta^2 v = 0. \quad (5.11)$$

From the three cases of $k'(x, y, z)$ we can generate a family of variations of $k(x, y, z)$. Here we focus on variations which depend only on one cartesian coordinate, namely z . From an engineering point of view (for applications such as FGMs), material variation in one coordinate is of practical importance as described in [138, 101].

5.3.1 Reduction to the Laplace equation

In this case $k'(x, y, z) = 0$ and, according to Eq. (5.6), $k(x, y, z)$ can be determined by

$$\frac{\nabla k \cdot \nabla k}{4k^2} - \frac{\nabla^2 k}{2k} = 0. \quad (5.12)$$

If k varies only with z , then Eq. (5.12) becomes

$$\frac{\left(\frac{d}{dz}k(z)\right)^2}{4(k(z))^2} - \frac{\frac{d^2}{dz^2}k(z)}{2k(z)} = 0. \quad (5.13)$$

Solving Eq. (5.13), one obtains

$$k(z) = (c_1 + c_2 z)^2. \quad (5.14)$$

where c_1 and c_2 are arbitrary constants. In a more general form Eq. (5.14) can be written as

$$k(z) = k_0(c_1 + c_2 z)^2, \quad (5.15)$$

where k_0 is a reference value for k . From Eq. (5.13) and Eq. (5.14), we can infer that for quadratic variation of $k(z)$, Eq. (5.1) can be transformed to a Laplace equation. This variation can be extended to more dimensions.

5.3.2 Reduction to the modified Helmholtz equation

In this case $k'(x, y, z) = -\beta^2$ and, according to Eq. (5.6), $k(x, y, z)$ can be determined by

$$\frac{\nabla k \cdot \nabla k}{4k^2} - \frac{\nabla^2 k}{2k} = -\beta^2. \quad (5.16)$$

For k varying only with z , Eq. (5.16) becomes

$$\frac{\left(\frac{d}{dz}k(z)\right)^2}{4(k(z))^2} - \frac{\frac{d^2}{dz^2}k(z)}{2k(z)} = -\beta^2. \quad (5.17)$$

Solving Eq. (5.17), one obtains

$$k(z) = k_0(a_1 e^{\beta z} + a_2 e^{-\beta z})^2 \quad (5.18)$$

where a_1 and a_2 are arbitrary constants. Equation 5.18 can be rewritten in terms of only hyperbolic functions as

$$k(z) = k_0(b_1 \cosh \beta z + b_2 \sinh \beta z)^2 \quad (5.19)$$

where b_1 and b_2 are arbitrary constants. Alternatively Eq. (5.18) can be expressed in terms of a combination of exponential and hyperbolic functions such as

$$k(z) = k_0(b_1 e^{\beta z} + b_2 \sinh \beta z)^2 \quad (5.20)$$

or

$$k(z) = k_0(b_1 \cosh \beta z + b_2 e^{-\beta z})^2. \quad (5.21)$$

From Eq. (5.18) to Eq. (5.21) it is apparent that for a family of variations involving hyperbolic and exponential functions, Eq. (5.1) can be transformed into the modified Helmholtz equation Eq. (5.10).

5.3.3 Reduction to the standard Helmholtz equation

In this case $k'(x, y, z) = \beta^2$ and, according to Eq. (5.6), $k(x, y, z)$ can be determined by

$$\frac{\nabla k \cdot \nabla k}{4k^2} - \frac{\nabla^2 k}{2k} = \beta^2. \quad (5.22)$$

Again, for k varying only with z , we set up the following differential equation

$$\frac{\left(\frac{d}{dz}k(z)\right)^2}{4(k(z))^2} - \frac{\frac{d^2}{dz^2}k(z)}{2k(z)} = \beta^2. \quad (5.23)$$

Solving Eq. (5.23), one obtains

$$k(z) = k_0(a_1 \cos \beta z + a_2 \sin \beta z)^2. \quad (5.24)$$

where a_1 and a_2 are arbitrary constants. For a family of variations involving trigonometric sine and cosine functions, Eq. (5.1) can be transformed into the Helmholtz equation Eq. (5.11).

5.3.4 Remarks

The appeal of the transform is its generality and the fact that for all of variations of $k(x, y, z)$, the Green's function can be obtained. Table 5.2 presents a list of variations of $k(x, y, z)$ with corresponding differential equations and the closed form Green's function.

It may be mentioned that, in the present paper, we do not use these Green's functions for the boundary element method implementation. We rather use the simpler Green's function of the modified problem (Laplace equation or standard/modified Helmholtz equation).

5.3.5 Boundary Conditions

In order to solve the boundary value problem based on the modified variable v , the boundary conditions of the original problem have to be incorporated in the modified boundary value problem. Thus for the modified problem, the Dirichlet and the Neumann boundary conditions given by Eq. (5.2) and Eq. (5.3) respectively, change as follows:

$$v = \sqrt{k} \bar{\phi} \quad \text{on } \Sigma_1 \quad (5.25)$$

$$\frac{\partial v}{\partial n} = \frac{1}{2k} \frac{\partial k}{\partial n} v - \frac{\bar{q}}{\sqrt{k}} \quad \text{on } \Sigma_2 \quad (5.26)$$

Notice that the Dirichlet boundary condition of the original problem is affected by the factor \sqrt{k} . Moreover, the Neumann boundary condition of the original problem changes to a mixed boundary condition or Robin boundary condition. This later modification is the only major change on the boundary value problem.

Another common boundary condition of the original problem is a prescribed relationship between the potential and the flux (e.g. convective heat transfer problems). The boundary condition of this type is

$$q = \lambda_1 \phi + \lambda_2 \quad (\text{Robin type}) \quad (5.27)$$

The corresponding boundary condition for the modified problem would be also a Robin boundary condition similar to Eq. (5.26), i.e.

$$\frac{\partial v}{\partial n} = \left(\frac{1}{2k} \frac{\partial k}{\partial n} - \lambda_1 \right) v - \frac{\lambda_2}{\sqrt{k}} \quad (5.28)$$

Table 5.2: Table of Green's function for various forms of $k(z)$ given by Eq. (5.1)

Variation $k(z)$	Differential equation	Modified prob.	Green's function (2D)	Green's function (3D)
Parabolic: $(c_1 + c_2 z)^2$	$(c_1 + c_2 z) \nabla^2 \phi + 2c_2 \phi_z = 0$	$\nabla^2 v = 0$	$-\frac{1}{2\pi} \frac{(c_1 + c_2 z')^{-1}}{(c_1 + c_2 z)} \ln r$	$\frac{1}{4\pi r} \frac{(c_1 + c_2 z')^{-1}}{(c_1 + c_2 z)}$
Exponential: $(a_1 e^{\beta z} + a_2 e^{-\beta z})^2$	$(a_1 e^{\beta z} + a_2 e^{-\beta z})^2 \nabla^2 \phi + 2\beta \phi_z (a_1^2 e^{2\beta z} - a_2^2 e^{-2\beta z}) = 0$	$\nabla^2 v - \beta^2 v = 0$	$\frac{1}{2\pi} \frac{(a_1 e^{\beta z'} + a_2 e^{-\beta z'})^{-1}}{(a_1 e^{\beta z} + a_2 e^{-\beta z})} K_0(\beta r)$	$\frac{e^{-\beta r}}{4\pi r} \frac{(a_1 e^{\beta z'} + a_2 e^{-\beta z'})^{-1}}{(a_1 e^{\beta z} + a_2 e^{-\beta z})}$
Trigonometric: $(a_1 \cos \beta z + a_2 \sin \beta z)^2$	$(a_1 \cos \beta z + a_2 \sin \beta z)^2 \nabla^2 \phi + 2\beta \phi_z [\frac{1}{2}(a_2^2 - a_1^2) \sin 2\beta z + a_1 a_2 \cos 2\beta z] = 0$	$\nabla^2 v + \beta^2 v = 0$	$\frac{1}{2} \frac{(a_1 \cos \beta z' + a_2 \sin \beta z')^{-1}}{(a_1 \cos \beta z + a_2 \sin \beta z)} Y_0(\beta r)$	$\frac{\cos(\beta r)}{4\pi r} \frac{(a_1 \cos \beta z' + a_2 \sin \beta z')^{-1}}{(a_1 \cos \beta z + a_2 \sin \beta z)}$

5.4 Green's function versus reduction to parent equation: A comparison of approaches

The Green's function approach is not attractive because each different material variation requires a different fundamental solution, and thus the kernels for the BEM implementation are different from the standard kernels usually employed for homogeneous problems. As a result each time a new computer code has to be developed. Moreover, if the treatment of singularity involves analytical integration, then the treatment becomes more involved [176]. The differential equation for the nonhomogeneous medium is not self-adjoint. Consequently the Green's function for such cases are not symmetric also. On the contrary, the Green's functions for the modified problem (both Laplace equation and standard/modified Helmholtz equation) are symmetric. The symmetric property is of utmost importance if one wants to develop the symmetric Galerkin formulation of the problem.

To demonstrate the difference between the two approaches, the case of the exponential variation is considered and explained below.

We emphasize that with the modified problem, the class of functions of $k(x, y, z)$ can be addressed with the same code.

Let the exponential variation $k(x, y, z)$ be defined as

$$k(x, y, z) = k(z) = k_0 e^{2\beta z} \quad (5.29)$$

Below we investigate the "Green's function" approach and the "reduction to the parent equation" approach to solve the problems with the material gradation given by Eq. (5.29).

5.4.1 Green's function approach for three dimensional (3D) problems

The Green's function for the exponential case is

$$G(P, Q) = \frac{e^{\beta(-r+R_z)}}{4\pi r} \quad (5.30)$$

where

$$R_z = z_Q - z_P \quad \text{and} \quad r = \|\mathbf{R}\| = \|\mathbf{Q} - \mathbf{P}\|. \quad (5.31)$$

The boundary integral equation (BIE) for surface temperature $\phi(P)$ on the boundary Σ

(see Figure 1) is therefore

$$\phi(P) + \int_{\Sigma} \phi(Q) \left(\frac{\partial}{\partial n} G(P, Q) - 2\beta n_z G(P, Q) \right) dQ = \int_{\Sigma} G(P, Q) \frac{\partial}{\partial n} \phi(Q) dQ, \quad (5.32)$$

that differs in form from the usual integral statements by the presence of the additional term multiplying $\phi(Q)$, i.e. $[-2\beta n_z G(P, Q)]$, which are due to the material gradation.

The kernel functions for the exponential case are

$$\begin{aligned} G(P, Q) &= -\frac{1}{4\pi} \frac{e^{\beta(-r+z_Q-z_P)}}{r} \\ F(P, Q) &= \frac{\partial}{\partial n} G(P, Q) - 2\beta n_z G(P, Q) \\ &= -\frac{e^{\beta(-r+R_z)}}{4\pi} \left(\frac{\mathbf{n} \cdot \mathbf{R}}{r^3} + \beta \frac{\mathbf{n} \cdot \mathbf{R}}{r^2} + \beta \frac{n_z}{r} \right). \end{aligned} \quad (5.33)$$

5.4.2 Reduction to the modified Helmholtz equation

For the modified problem, the Green's function for the exponential case is

$$G(P, Q) = \frac{e^{-\beta r}}{4\pi r} \quad (5.34)$$

The expression of $G(P, Q)$ is simpler than that of the Green's function approach (cf. Eq. (5.30)). Moreover, Eq. (5.34) is symmetric with respect to both P and Q . A discussion on symmetric properties is presented in the next section.

The governing boundary integral equation corresponding to Eq.(5.10) is

$$\phi(P) + \int_{\Sigma} \phi(Q) \left(\frac{\partial}{\partial n} G(P, Q) \right) dQ = \int_{\Sigma} G(P, Q) \frac{\partial}{\partial n} \phi(Q) dQ, \quad (5.35)$$

The kernel functions for the exponential case in the reduction to parent equation technique are given by Eq. (5.34) and

$$\begin{aligned} F(P, Q) &= \frac{\partial}{\partial n} G(P, Q) \\ &= -\frac{e^{-\beta r}}{4\pi} \left(\frac{\mathbf{n} \cdot \mathbf{R}}{r^3} + \beta \frac{\mathbf{n} \cdot \mathbf{R}}{r^2} \right). \end{aligned} \quad (5.36)$$

The kernels in Eq. (5.33) have one more term than the kernels in Eq. (5.36). But the significant difference is the exponential term in front of the kernels. In the Green's function approach, in order to take care of the singularity using the direct limit approach [74, 73],

the power of the exponential plays an important role. The complexity of handling such exponential terms magnifies even more when applied to the hypersingular boundary integral equation. A direct treatment of singularity of the hypersingular double integrals using a hybrid analytic/numerical approach has been presented by Sutradhar *et al.*[176] for exponential variation of the thermal conductivity. The treatment is based on the direct approach [73]. The direct limit approach is shown to be suitable for dealing with complicated Green's functions, which appear in applications such as those involving FGMs.

5.5 Numerical Implementation

The numerical methods employed in the current work use standard Galerkin techniques. A discussion of these techniques in the context of the BEM is presented below.

5.5.1 Galerkin Boundary Integral Equation.

Define the collocation BIE as

$$\mathcal{B}(P) \equiv \phi(P) + \int_{\Sigma} \left(\frac{\partial}{\partial n} G(P, Q) \right) \phi(Q) dQ - \int_{\Sigma} G(P, Q) \frac{\partial \phi}{\partial n}(Q) dQ \quad (5.37)$$

and thus for an exact solution $\mathcal{B}(P) \equiv 0$.

In a Galerkin approximation, the error in the approximate solution is orthogonalized against the shape functions, *i.e.*, the shape functions are the weighting functions and $\mathcal{B}(P) = 0$ is enforced in the 'weak sense', *i.e.*

$$\int_{\Sigma} N_k(P) \mathcal{B}(P) dP = 0 \quad (5.38)$$

As a result the Galerkin technique possesses the important property of the *local support* as illustrated by Figure 5.2. This technique is especially suitable to treat corners [137]. After replacing the boundary and the boundary functions by their interpolated approximations, a set of linear algebraic equations emerges,

$$[\mathcal{H}]\{\phi\} = [\mathcal{G}] \left\{ \frac{\partial \phi}{\partial n} \right\}. \quad (5.39)$$

The matrix \mathcal{G} is symmetric because its coefficients only depend on the distance (r) between the source points (P) and the fields points (Q), but matrix \mathcal{H} is not because it depends on the normal vector of the field point point (Q). For Dirichlet problems, the Galerkin method

gives rise to symmetric system of equations. In the context of nonhomogeneous media a symmetric Galerkin boundary element method (SGBEM) has been recently presented by Sutradhar *et al.*[176]. Details of the symmetry property and numerical implementation can be found in references [85, 88, 13].

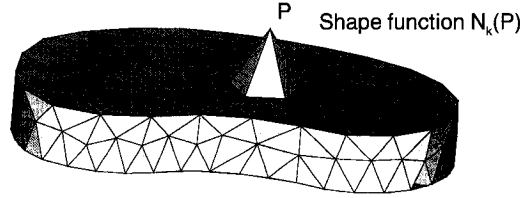


Figure 5.2: The local support of the Galerkin formulation at point P .

5.5.2 Simple Kernel functions

- *Generalized Quadratic variation of k*

For the quadratic variation of k , the problem is solved by the standard Laplace equation. The kernels corresponding to Eq. (5.37) for the Laplace equation are

$$G(P, Q) = \frac{1}{4\pi r}, \quad (5.40)$$

$$F(P, Q) = \frac{\partial}{\partial n} G(P, Q) = -\frac{1}{4\pi} \frac{\mathbf{n} \cdot \mathbf{R}}{r^3}. \quad (5.41)$$

- *Generalized Exponential variation of k*

For this variation the transformed problem is the modified Helmholtz equation. The kernel functions are

$$G(P, Q) = \frac{e^{-\beta r}}{4\pi r}, \quad (5.42)$$

$$\begin{aligned} F(P, Q) &= \frac{\partial}{\partial n} G(P, Q) \\ &= -\frac{e^{-\beta r}}{4\pi} \left(\frac{\mathbf{n} \cdot \mathbf{R}}{r^3} + \beta \frac{\mathbf{n} \cdot \mathbf{R}}{r^2} \right). \end{aligned} \quad (5.43)$$

- *Trigonometric variation of k*

For the trigonometric variation the problem is transformed into standard Helmholtz

equation. The kernel functions are

$$G(P, Q) = \frac{\cos \beta r}{4\pi r}, \quad (5.44)$$

$$F(P, Q) = \frac{\partial}{\partial n} G(P, Q) = -\frac{1}{4\pi} \left(\cos(\beta r) \frac{\mathbf{n} \cdot \mathbf{R}}{r^3} + \beta \sin(\beta r) \frac{\mathbf{n} \cdot \mathbf{R}}{r^2} \right). \quad (5.45)$$

5.5.3 Treatment of boundary conditions

As explained in Section 5.3.5, in order to solve the nonhomogeneous problem using codes for homogeneous materials (Laplace, Helmholtz and modified Helmholtz), the main modification in the implementation is to incorporate the boundary conditions for the modified problem. In this section, the necessary modifications are described.

Let us assume three nodes, of which node 1 and node 3 have prescribed Neumann boundary condition and node 2 has prescribed Dirichlet boundary condition, i.e.,

$$\begin{array}{lll} \bar{q}_1, & \bar{\phi}_2, & \bar{q}_3 \quad \text{known quantities} \\ \phi_1, & q_2, & \phi_3 \quad \text{unknown quantities} \end{array}$$

In the modified boundary value problem the variables are v and $\partial v / \partial n$. The system of algebraic equations emerges as,

$$\begin{bmatrix} H_{11} & H_{12} & H_{13} \\ H_{21} & H_{22} & H_{23} \\ H_{31} & H_{32} & H_{33} \end{bmatrix} \begin{Bmatrix} v_1 \\ v_2 \\ v_3 \end{Bmatrix} = \begin{bmatrix} G_{11} & G_{12} & G_{13} \\ G_{21} & G_{22} & G_{23} \\ G_{31} & G_{32} & G_{33} \end{bmatrix} \begin{Bmatrix} \frac{\partial v_1}{\partial n} \\ \frac{\partial v_2}{\partial n} \\ \frac{\partial v_3}{\partial n} \end{Bmatrix}.$$

By rearranging the equations so that the unknowns are passed to the left-hand side, we can rewrite the linear system

$$\begin{bmatrix} H_{11} & -G_{12} & H_{13} \\ H_{21} & -G_{22} & H_{23} \\ H_{31} & -G_{32} & H_{33} \end{bmatrix} \begin{Bmatrix} v_1 \\ \frac{\partial v_2}{\partial n} \\ v_3 \end{Bmatrix} = \begin{bmatrix} G_{11} & -H_{12} & G_{13} \\ G_{21} & -H_{22} & G_{23} \\ G_{31} & -H_{32} & G_{33} \end{bmatrix} \begin{Bmatrix} \frac{\partial v_1}{\partial n} \\ v_2 \\ \frac{\partial v_3}{\partial n} \end{Bmatrix}.$$

Using Eq. (5.25) and Eq. (5.26) we obtain, the final form of the set of equations,

$$\begin{bmatrix} \left(H_{11} - \frac{G_{11}}{2k} \frac{\partial k}{\partial n} \right) & -G_{12} & \left(H_{13} - \frac{G_{13}}{2k} \frac{\partial k}{\partial n} \right) \\ \left(H_{21} - \frac{G_{21}}{2k} \frac{\partial k}{\partial n} \right) & -G_{22} & \left(H_{23} - \frac{G_{23}}{2k} \frac{\partial k}{\partial n} \right) \\ \left(H_{31} - \frac{G_{31}}{2k} \frac{\partial k}{\partial n} \right) & -G_{32} & \left(H_{33} - \frac{G_{33}}{2k} \frac{\partial k}{\partial n} \right) \end{bmatrix} \begin{Bmatrix} v_1 \\ \frac{\partial v_2}{\partial n} \\ v_3 \end{Bmatrix} = \begin{bmatrix} G_{11} & -H_{12} & G_{13} \\ G_{21} & -H_{22} & G_{23} \\ G_{31} & -H_{32} & G_{33} \end{bmatrix} \begin{Bmatrix} \frac{\bar{q}_1}{\sqrt{k}} \\ \phi_2 \sqrt{k} \\ \frac{\bar{q}_3}{\sqrt{k}} \end{Bmatrix}.$$

We solve these equations for v_1 , $\partial v_2/\partial n$, and v_3 ; and finally, by using Eq. (5.25) and Eq. (5.26), we obtain

$$\begin{aligned}\phi_1 &= v_1/\sqrt{k}, \\ q_2 &= -\sqrt{k} \left\{ \frac{\partial v_2}{\partial n} - \frac{1}{2k} \frac{\partial k}{\partial n} v_2 \right\}, \\ \phi_3 &= v_3/\sqrt{k}.\end{aligned}$$

The extension of the current algorithm to handle multizone problems is doable but warrants careful housekeeping of the variables. A useful discussion on multizone and interface problems can be found in the paper by Gray and Paulino [77].

5.5.4 Boundary Elements

The surface of the solution domain is divided into a number of connected elements. Over each element, the variation of the geometry and the variables (potential and flux) is approximated by simple functions. Six noded isoparametric quadratic triangular elements are used. The geometry of an element can be defined by the coordinates of its six nodes using appropriate quadratic shape functions as follows

$$x_i(\xi, \eta) = \sum_{j=1}^6 N_j(\xi, \eta)(x_i)_j \quad (5.46)$$

In an isoparametric approximation, the same shape functions are used for the solution variables (both potential and flux), as follows:

$$\begin{aligned}\phi_i(\xi, \eta) &= \sum_{j=1}^6 N_j(\xi, \eta)(\phi_i)_j \\ q_i(\xi, \eta) &= \sum_{j=1}^6 N_j(\xi, \eta)(q_i)_j.\end{aligned} \quad (5.47)$$

The shape functions can be explicitly written in terms of intrinsic coordinates ξ and η as:

$$\begin{aligned}N_1(\eta, \xi) &= (\xi + \sqrt{3}\eta - \sqrt{3})(\xi + \sqrt{3}\eta)/6 & N_4(\eta, \xi) &= (\xi + \sqrt{3}\eta - \sqrt{3})(\xi - \sqrt{3}\eta - \sqrt{3})/3 \\ N_2(\eta, \xi) &= (\xi - \sqrt{3}\eta - \sqrt{3})(\xi - \sqrt{3}\eta)/6 & N_5(\eta, \xi) &= -2\xi(\xi - \sqrt{3}\eta - \sqrt{3})/3 \\ N_3(\eta, \xi) &= \xi(2\xi - \sqrt{3})/3 & N_6(\eta, \xi) &= -2\xi(\xi + \sqrt{3}\eta - \sqrt{3})/3\end{aligned} \quad (5.48)$$

The intrinsic coordinate space is the equilateral triangle with $-1 \leq \eta \leq 1$, $0 \leq \xi \leq \sqrt{3}(1 - |\eta|)$.

5.5.5 Corners

The treatment of corners in Galerkin BEM is simple and elegant due to the flexibility in choosing the weight function for the Galerkin approximation. Corners are represented by double nodes, and on each side two different weight functions are used. These weight functions are half of the usual weight. For a Neumann corner (flux specified on both sides of the corner, potential is the unknown), the weight functions are added into one. In all other cases (Dirichlet corner and mixed corner) the weight function remains separate.

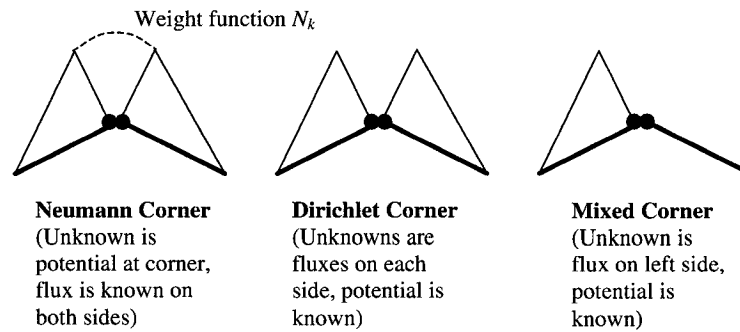


Figure 5.3: Corner treatment in the Galerkin BEM

5.6 ABAQUS User Subroutine

In general, conventional FEM software (including ABAQUS [1]) use homogeneous elements with constant material properties at the element level. In the present work, in order to incorporate the functional variation of the material at the finite element level, a user subroutine UMATHT was developed for ABAQUS [1]. By means of this subroutine, any functional variation can be included within an element by sampling the material property at each Gauss point. In general, graded elements approximate the material gradient better than conventional homogeneous elements and provide a smoother transition at element boundaries. Further investigations on graded elements can be found in the papers by Santare and Lambros [148] and Kim and Paulino [99] for 2D problems, and in the paper by Walters *et al.*[180] for 3D problems. The user subroutine UMATHT is included in the Appendix.

5.7 Numerical Examples

In this section, several test cases are reported, demonstrating the implementation of the above techniques. To validate the numerical implementation, the following four examples are presented:

- (1) Cube with material gradation along the z -axis,
- (2) Cube with a 3D material gradation,
- (3) Inclined cylindrical cavity in a parallelepiped,
- (4) Rotor problem.

The first example is a cube with constant temperatures in two sides and insulated in all the other sides. The material property varies only in the z direction. This problem has analytical solution. For this problem all the three kinds of material variation i.e. quadratic, exponential and trigonometric, are prescribed. This problem is used to verify the present formulation [100]. Also a convergence study is performed with this problem. The second example has a complicated 3D quadratic spatial material variation inside a cube with mixed boundary conditions. The third problem has a complicated geometry, an inclined cylindrical cavity in a parallelepiped. This problem is solved as a Dirichlet problem with known prescribed field. The last example is a rotor problem, which is of engineering significance in the field of functionally graded materials.

5.7.1 Cube with material gradation with z -axis

A unit cube ($L = 1$) with prescribed constant temperature on two sides is considered. The problem of interest and corresponding BEM mesh is shown in Figure 5.4. The top surface of the cube at $[z = 1]$ is maintained at a temperature of $T = 100$ while the bottom at $[z = 0]$ is zero. The remaining four faces are insulated (zero normal flux). Three different classes of variations are considered. The profiles of the thermal conductivity $k(z)$ of the three cases are illustrated in Figure 5.4.

- *Quadratic Variation of k*

The quadratic variation of the thermal conductivity $k(x, y, z)$ is defined as

$$k(x, y, z) = k(z) = k_0(a_1 + \beta z)^2 = 5(1 + 2z)^2 \quad (5.49)$$

in which β is the nonhomogeneity parameter and a_1 is a constant. The analytical

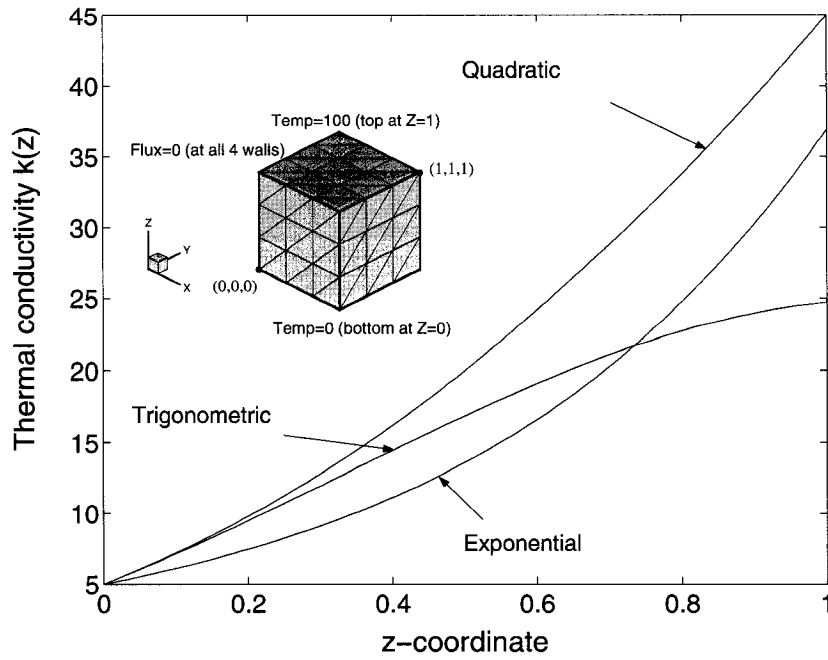


Figure 5.4: Thermal conductivity variation along the z direction. The quadratic variation is $k(z) = 5(1 + 2z)^2$, the trigonometric is $k(z) = 5(\cos(z) + 2\sin(z))^2$, and the exponential variation is $k(z) = 5e^{2z}$. The insert shows the geometry, mesh and the boundary conditions of the unit cube. The BEM mesh consists of 294 nodes and 108 quadratic triangular elements.

solution for temperature is

$$\phi(z) = 100 \frac{(a_1 + \beta L)z}{(a_1 + \beta z)L} = \frac{300z}{1 + 2z} \quad (5.50)$$

- *Exponential Variation of k* Let the exponential variation $k(x, y, z)$ be defined as

$$k(x, y, z) = k(z) = k_0 e^{2\beta z} = 5e^{2z} \quad (5.51)$$

The analytical solution for temperature for this type of material variation is

$$\phi(z) = 100 \frac{1 - e^{-2\beta z}}{1 - e^{-2\beta L}} \quad (5.52)$$

- *Trigonometric Variation of k* Let the trigonometric variation of the thermal conduc-

tivity $k(x, y, z)$ be defined as

$$k(z) = k_0(a_1 \cos \beta z + a_2 \sin \beta z)^2 = 5(\cos(z) + 2\sin(z))^2 \quad (5.53)$$

The analytical solution for temperature is

$$\phi(z) = 100 \frac{(a_1 \cot(\beta L) + a_2) \sin(\beta z)}{(a_1 \cos(\beta z) + a_2 \sin(\beta z))} \quad (5.54)$$

- Results

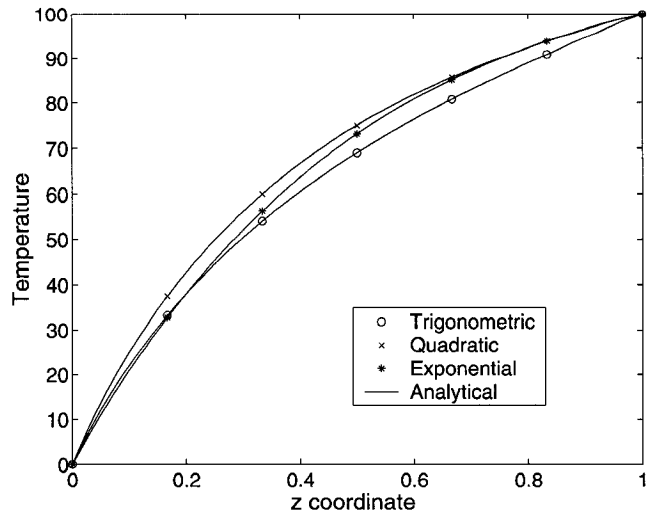
The temperature profile along the z axis is plotted for the three variations and compared with the analytical solutions in Figure 5.5(a). The variation of flux at the $z = 1$ surface with different values of the nonhomogeneity parameter β (keeping a_1 and a_2 as constants) is plotted and compared with the analytical solution in Figure 5.5(b). The numerical and analytical results are in excellent agreement.

- Convergence

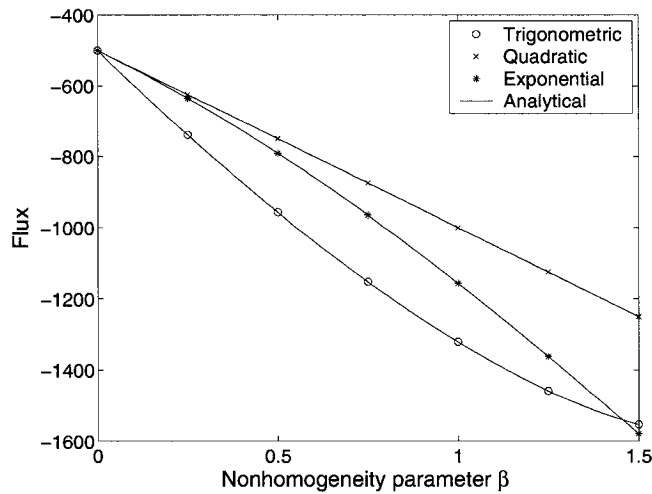
A convergence study is carried out using this example since the exact solution of this problem is known. For the exponential variation of k , the convergence for the temperature and the flux are compared with the Green's function approach and the 'simple' BEM approach (modified Helmholtz). The other 'simple' BEM techniques i.e., the reduction to Laplace and Helmholtz problem for temperature solutions are also examined. The errors in the temperature and the flux are computed considering various mesh discretizations and employing a global error measure,

$$\mathcal{E} = \frac{1}{|u^{(e)}|_{max}} \sqrt{\frac{1}{NP} \sum_{I=1}^{NP} [u_I^{(e)} - u_I^{(c)}]^2} \quad (5.55)$$

where \mathcal{E} is the error in the solution, the superscripts (e) and (c) denote, respectively, the exact and the computed solutions, and NP is the total number of nodes. The mesh properties and the errors in the temperature for different approaches are tabulated in Table 5.3. The convergence of the temperature and flux of the Green's function approach and the 'simple' BEM approach are compared in Figure 5.6 and Figure 5.7, respectively. The rates of convergence for temperature are provided in Table 5.4. The rate of convergence for the flux solution for the Green's function approach and the simple BEM (modified Helmholtz) are 1.84 and 1.0, respectively.



(a)



(b)

Figure 5.5: (a) Temperature profile in the z direction for different material variations, (b) Variation of flux at $z = 1$ surface with different values of nonhomogeneity parameter β .

- Comparison of CPU times

The CPU times required for the complete simulation for all the GBEM methods are provided in Table 5.5. The simulations were carried out in a Pentium IV, 800 MHz CPU with 512Mb of memory.

- Remarks

From Table 5.3 it is apparent that, the simple BEM technique (Modified Helmholtz) for the exponential variation has much less error than the corresponding Green's function

Table 5.3: Global error (\mathcal{E}) for FGM cube ($\beta = 1.0$).

Mesh	No. of nodes	No. of elements	Global Error \mathcal{E} for Temperature			
			GF Approach	Simple BEM Mod. Helm.	Simple BEM Laplace	Simple BEM Helm.
1	54	12	0.00714	0.003060	0.000078	0.00230
2	150	48	0.00153	0.000486	0.000065	0.00038
3	294	108	0.00044	0.000142	0.000054	0.00012
4	726	300	0.00008	0.000027	0.000043	0.00002

Table 5.4: Rate of Convergence of temperature solution for the Green's function and the simple BEM methods.

Methods	Rate of Convergence
Green's function Approach	1.85
Simple BEM (Mod. Helmholtz)	1.83
Simple BEM (Laplace)	0.27
Simple BEM (Helmholtz)	1.71

Table 5.5: CPU times for the BEM simulations

Mesh	No. of nodes	No. of elements	CPU times in sec			
			GF Approach	Simple BEM Mod. Helm.	Simple BEM Laplace	Simple BEM Helm.
1	54	12	5.33	1.53	0.70	2.36
2	150	48	27.52	9.08	3.83	13.29
3	294	108	69.64	27.46	11.03	37.28
4	726	300	256.10	129.00	50.80	163.00

approach, although both methods exhibit similar convergence rate. It is important to note that, the CPU time for the simple BEM (Modified Helmholtz) is almost half or less than the Green's function approach (See Table 5.5). Also, the CPU time for simple BEM for quadratic material variation (modified to Laplace equation) is much less than the simple BEM approaches for exponential and trigonometric material variations.

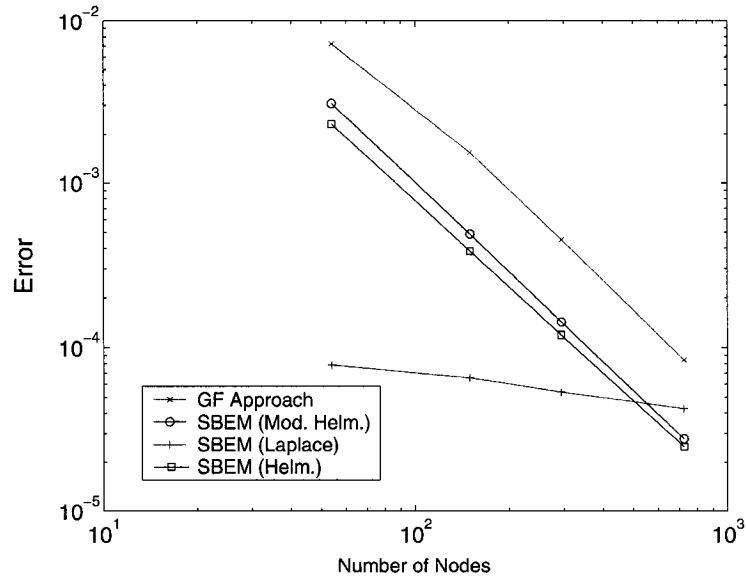


Figure 5.6: Convergence plots of temperature for the Green's function approach and the simple BEM approaches.

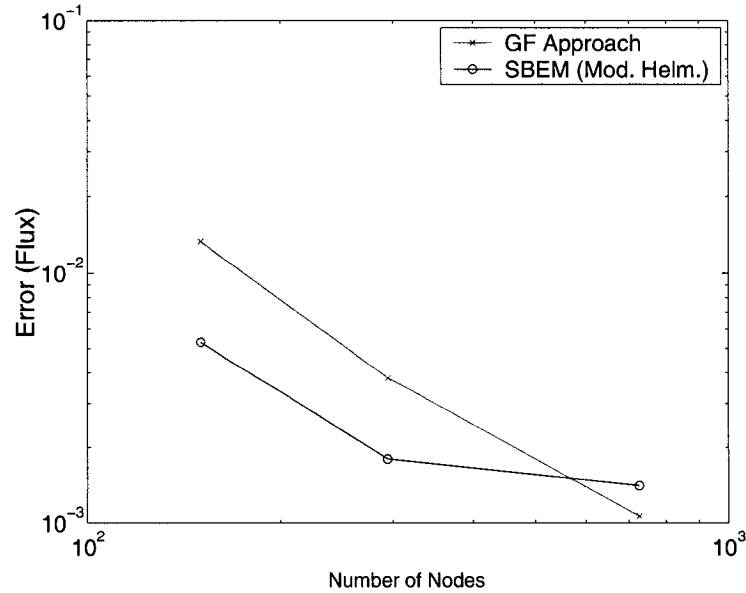


Figure 5.7: Convergence plots of flux for the Green's function approach and the simple BEM approach (Modified Helmholtz).

5.7.2 Cube with a 3D material gradation

The three dimensional thermal conductivity variation is

$$k(x, y, z) = (5 + 0.2x + 0.4y + 0.6z + 0.1xy + 0.2yz + 0.3zx + 0.7xyz)^2, \quad (5.56)$$

Figure 5.8 illustrates the iso-surfaces of the 3D variation of the thermal conductivity. It can

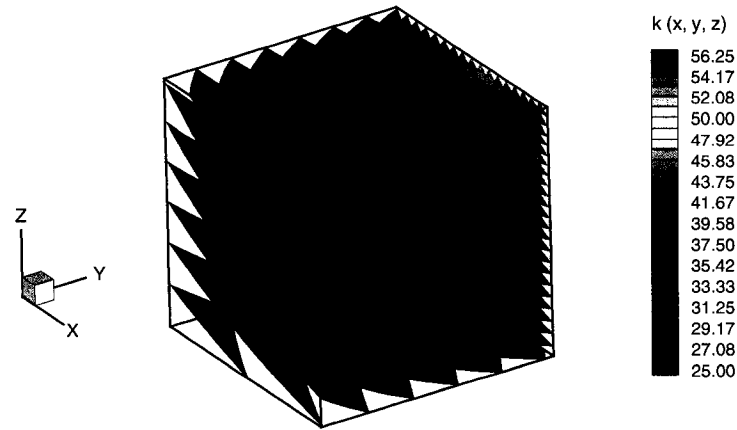


Figure 5.8: Representation of iso-surfaces for the three dimensional variation of thermal conductivity $k(x, y, z)$.

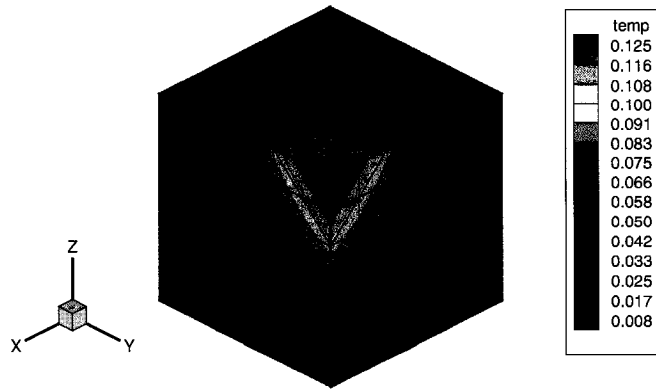
be shown that Eq. (5.56), in which $\sqrt{k(x, y, z)}$ is a linear combination of 1, x , y , z , xy , yz , zx , xyz (i.e. the most general linear function of x , y or z alone) satisfies Eq. (5.12) and thereby allows Eq. (5.1) to be reduced to a Laplace equation governing $v(x, y, z)$, by change of variables using Eq. (5.5). The following function is an admissible solution for this variation,

$$\phi(x, y, z) = \frac{xyz}{(5 + 0.2x + 0.4y + 0.6z + 0.1xy + 0.2yz + 0.3zx + 0.7xyz)}, \quad (5.57)$$

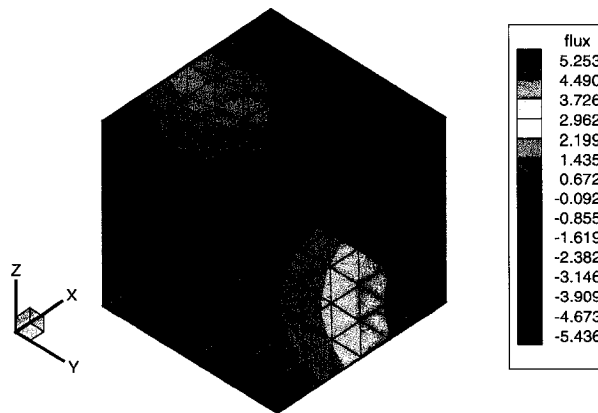
The mixed boundary conditions at the six faces of the cube are prescribed as,

$$\begin{aligned} \phi(0, y, z) &= 0 \\ \bar{q}(1, y, z) &= -k(1, y, z) \frac{\partial \phi(x, y, z)}{\partial x} = -0.2zy(25 + 2y + 3z + zy) \\ \phi(x, 0, z) &= 0 \\ \bar{q}(x, 1, z) &= -k(x, 1, z) \frac{\partial \phi(x, y, z)}{\partial y} = -0.1xz(50 + 2x + 6z + 3xz) \\ \phi(x, y, 0) &= 0 \\ \bar{q}(x, y, 1) &= -k(x, y, 1) \frac{\partial \phi(x, y, z)}{\partial z} = -0.1xy(50 + 2x + 4y + xy) \end{aligned} \quad (5.58)$$

The cube is discretized with 294 nodes and 108 quadratic triangular elements. The results for the temperature and the flux are recovered exactly up to three decimals. Contour plots of the temperature and the flux are shown in Figure 5.9.



(a)



(b)

Figure 5.9: (a) Contour plot of temperature for the cube with 3D material variation. (b) Contour plot of flux for the cube with 3D material variation.

5.7.3 Cylindrical cavity in a parallelepiped

Figure 5.10 shows the geometry of the parallelepiped with a cylindrical cavity. The inspiration for this problem comes from a paper by Ingber and Martinez [93], however the boundary conditions here are different from their paper. The thermal conductivity varies as

a trigonometrical function in one coordinate (see Figure 5.11(a)) according to

$$k(z) = 0.5(5 \cos(2z) + 7.78704 \sin(2z))^2 \quad (5.59)$$

This problem is set as a Dirichlet problem where the temperature in the surface of the body is specified as

$$u(x, y, z) = \frac{4xy \sin(2z)}{(a_1 \cos(2z) + a_2 \sin(2z))} \quad (5.60)$$

$$= \frac{4xy \sin(2z)}{(5 \cos(2z) + 7.78704 \sin(2z))} \quad (5.61)$$

The analytical solution for flux is therefore

$$\begin{aligned} q(x, y, z) = & -4k_0(a_1 \cos(2z) + a_2 \sin(2z))y \sin(2z)\mathbf{n}_1 \\ & -4k_0(a_1 \cos(2z) + a_2 \sin(2z))x \sin(2z)\mathbf{n}_2 - 8k_0xya_1\mathbf{n}_3 \end{aligned} \quad (5.62)$$

The parallelepiped including the cavity is discretized using 942 T6 elements and 2121 nodes. Flux along z in $y = 0$ plane at the intersection of $x = 1$ and $y = 0$ planes is compared with the analytical results as shown in Figure 5.11(b), which shows that the numerical and analytical solutions are in excellent agreement. The contour plot in Figure 5.12 illustrates the complex nature of the flux distribution of the problem.

5.7.4 FGM Rotor problem

The last numerical example is an FGM rotor with eight mounting holes having a eight-fold symmetry. Due to the symmetry, only one-eighth of the rotor is analysed. The top view of the rotor, the analysis region, and the geometry of the region are illustrated in Figure 5.13. The grading direction for the rotor is parallel to its line of symmetry, which is taken as the z -axis. The thermal conductivity for the rotor varies according to the following expression,

$$\text{Quadratic: } k(z) = 20(1 + 420.7z)^2. \quad (5.63)$$

The profile of the thermal conductivity $k(z)$ of the variation is illustrated in Figure 5.14. The temperature is specified along the inner radius as $T_{inner} = 20 + 1.25 \times 10^6(z - 0.01)^2$ and outer radius as $T_{outer} = 150 + 1.25 \times 10^6(z - 0.01)^2$. A uniform heat flux of 5×10^5 is added on the bottom surface where $z = 0$, and all other surfaces are insulated. The BEM mesh employs 1584 elements and 3492 nodes. A schematic for the thermal boundary

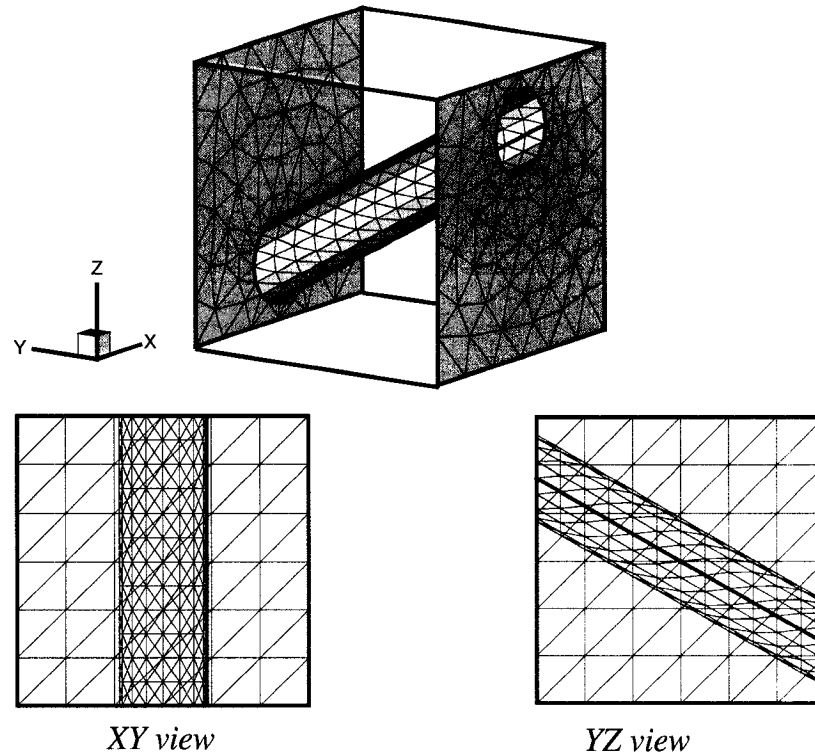
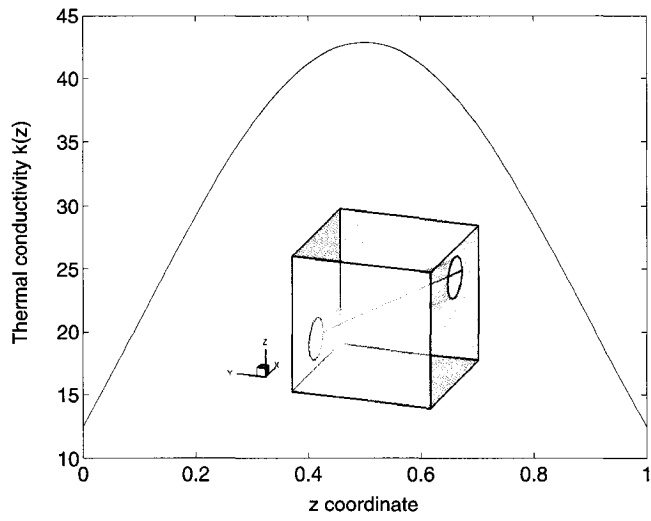
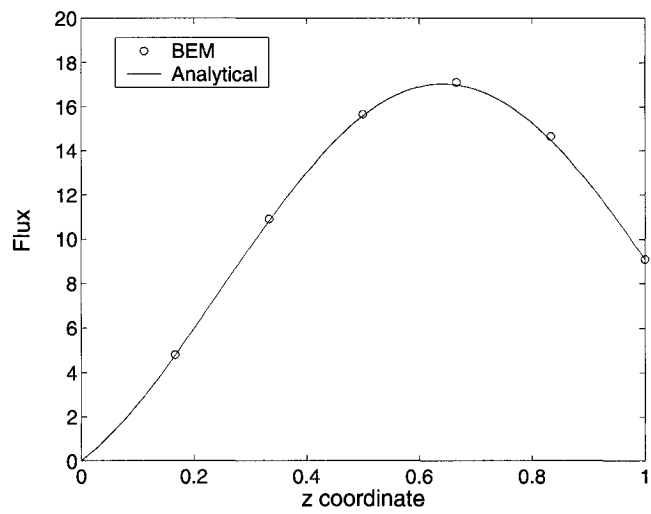


Figure 5.10: The mesh and the geometry of the parallelepiped. For the sake of clarity meshes in four faces of the parallelepiped have been omitted in the figure in the top. The XY and YZ views are provided which shows the mesh in those faces.

conditions and the BEM mesh employed is shown in Figure 5.15. This problem has been solved previously using the “Green’s function” approach by means of a Galerkin BEM (non-symmetric) by Gray *et al.*[75], who considered exponential conductivity variation. Here the solution of the problem is verified using the commercially available software ABAQUS using the user-defined subroutine UMATHT(see Appendix). The FEM mesh consists of 7600 20-noded brick elements(quadratic) and 35,514 nodes. The FEM mesh is shown in Figure 5.16, which is intended simply to provide a reference solution against which the BEM results can be compared to. The temperature along the radial direction at the edge is plotted and compared with the FEM results in Figure 5.17. Figure 5.18 shows the comparison of the BEM and FEM results for the temperature around the hole. A contour plot of the temperature distribution is shown in Figure 5.19. The radial heat flux at the right interior corner is plotted along the interior corner in Figure 5.20. All the results of the BEM and FEM solution are in very good agreement.



(a)



(b)

Figure 5.11: (a) Thermal conductivity for the parallelepiped with cylindrical cavity. (b) Flux along z in $y = 0$ plane at edge $[x = 1, y = 0]$ of the parallelepiped.

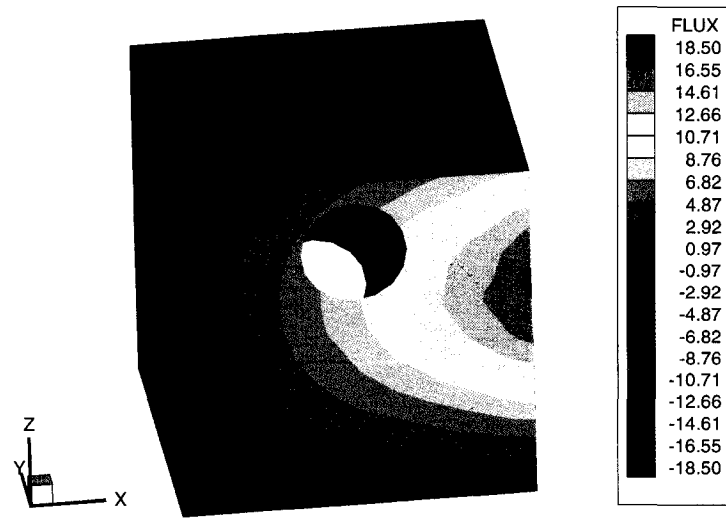


Figure 5.12: Contour plot of flux for cylindrical cavity in parallelepiped.

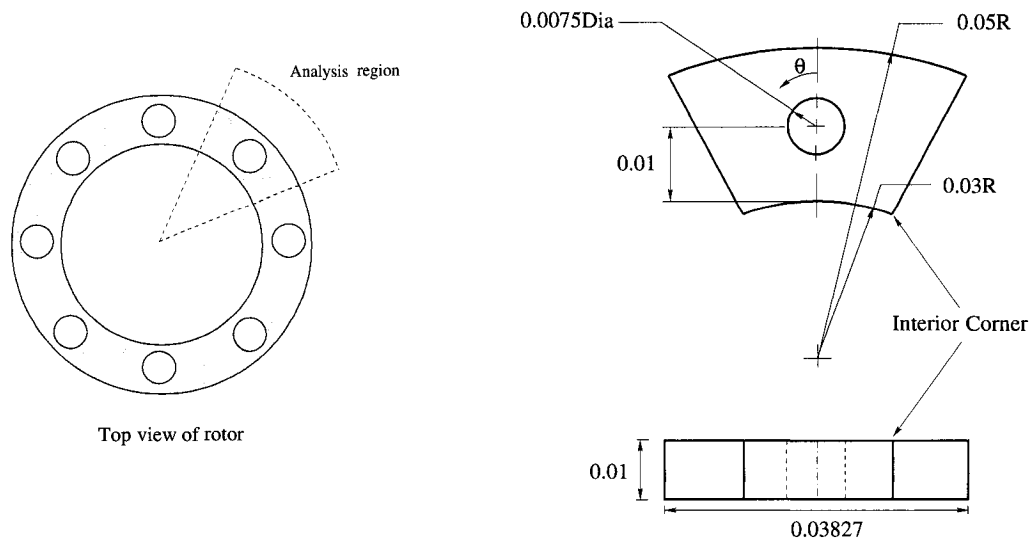


Figure 5.13: Geometry of the functionally graded rotor with 8-fold symmetry.

5.8 Concluding Remarks

A novel simple boundary element technique to address problems of potential flow for non-homogeneous media is presented. It is shown that for quadratic material variation, the nonhomogeneous problem can be transformed to a Laplace problem; for exponential vari-

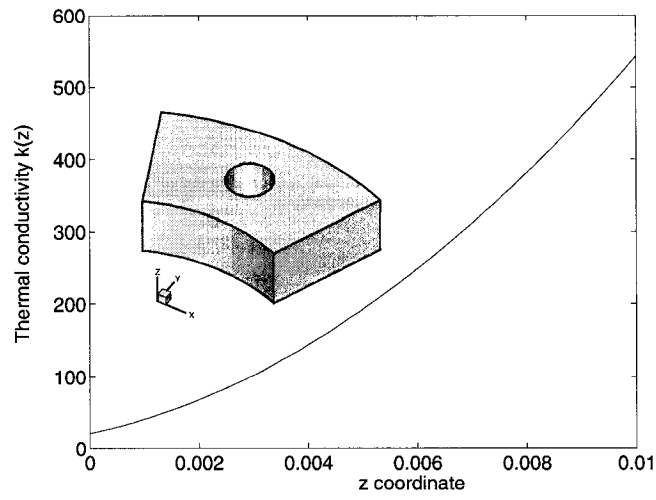


Figure 5.14: Profile of thermal conductivity in z direction. The quadratic variation of the conductivity is $k(z) = 20(1 + 420.7z)^2$.

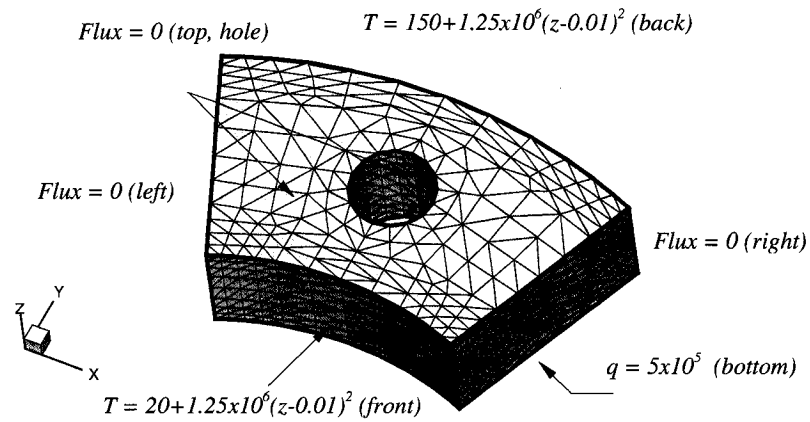


Figure 5.15: Thermal boundary conditions and the BEM mesh with 1584 elements and 3492 nodes.

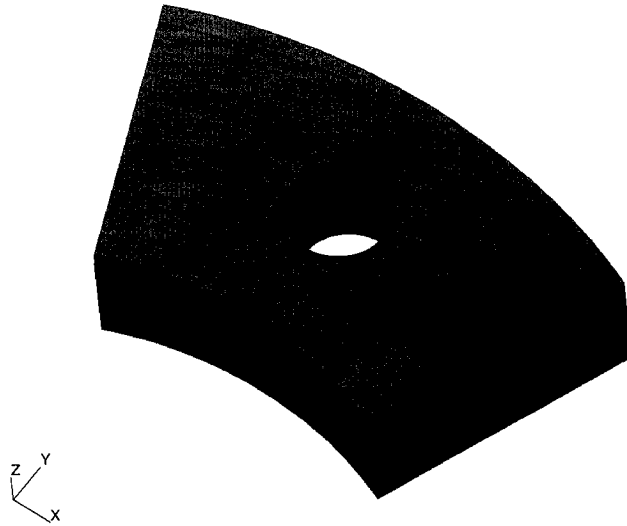


Figure 5.16: The FEM mesh with 7600 elements and 35514 nodes.

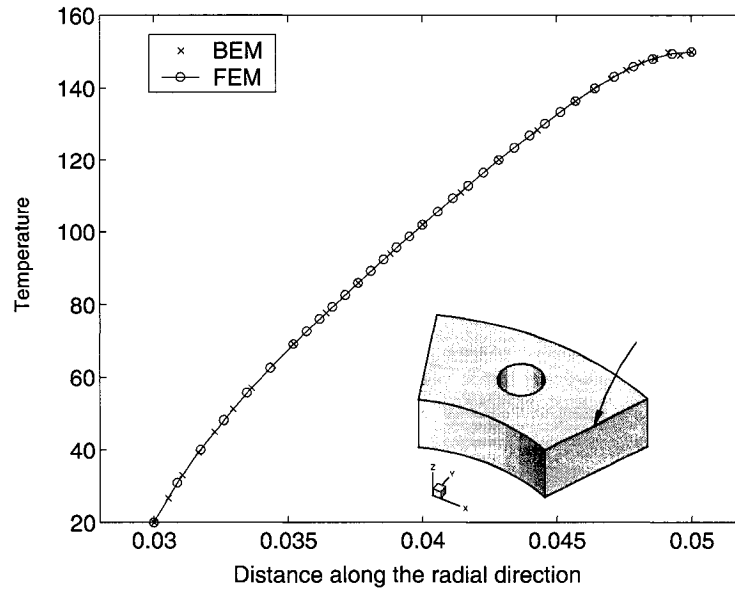


Figure 5.17: Temperature distribution along the right top edge (indicated by the arrow).

ation, the problem can be transformed to a modified Helmholtz equation; and for trigonometric variation, the problem can be transformed to a standard Helmholtz equation. By simple modification of the boundary conditions, standard codes for homogeneous material problems are used. A number of examples are presented to validate the methodology. This

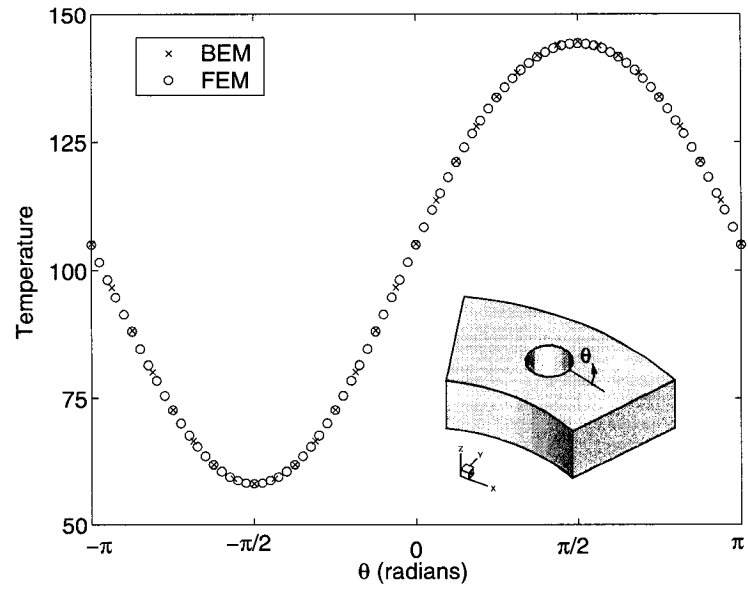


Figure 5.18: Temperature distribution along the circular contour on the top face.

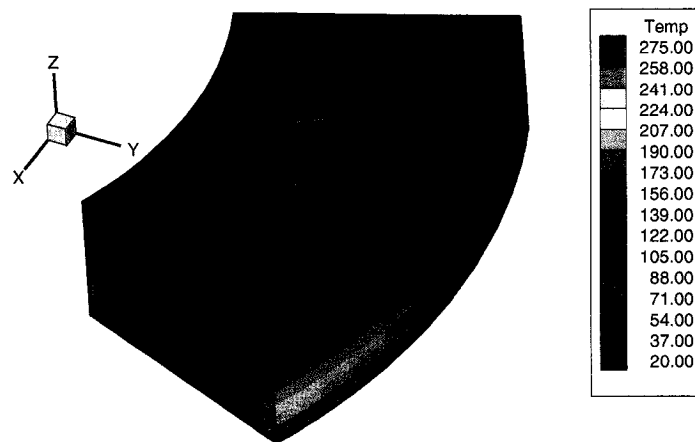


Figure 5.19: BEM contour plot of the temperature of the rotor.

implementation is carried out using the Galerkin BEM (non-symmetric), but the idea and development are applicable to collocation or other boundary element methods such as meshless or symmetric Galerkin BEM.

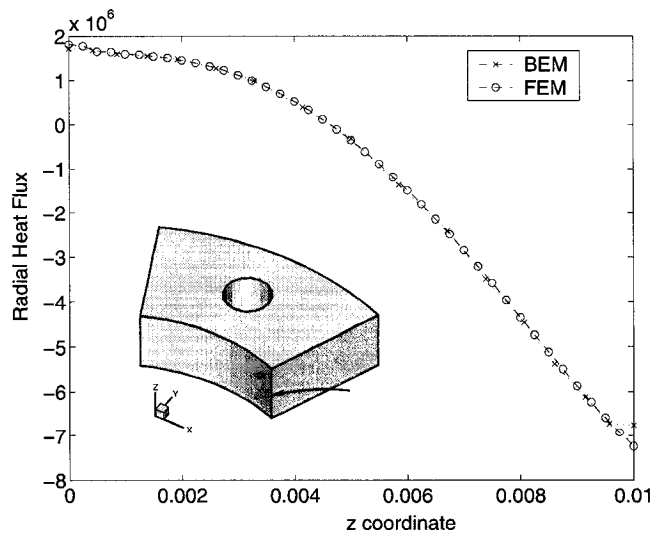


Figure 5.20: Radial heat flux along the interior edge (indicated by the arrow).

Chapter 6

Simple BEM for Transient heat conduction in FGMs

This chapter presents a “simple” boundary element method for transient heat conduction in functionally graded materials. For a broad range of functional material variation (quadratic, exponential and trigonometric) of thermal conductivity and specific heat, the nonhomogeneous problem can be transformed into the standard homogeneous diffusion problem. A three dimensional boundary element implementation, using the Laplace transform approach and the Galerkin approximation, is presented. The time dependence is restored by numerically inverting the Laplace transform by means of the Stehfest algorithm. A number of numerical examples demonstrate the efficiency of the method. The results of the test examples are in excellent agreement with analytical solutions and finite element simulation results.

This chapter is organized as follows. Section 6.1 gives an introduction to the problem and discusses about the variation of the thermal properties. The basic equations of the diffusion problem are described in Section 6.2. The Green’s function for the FGM diffusion equation is derived in Section 6.3. In Section 6.4, the Laplace Transform BEM formulation is presented. Section 6.5 discusses several aspects of the numerical implementation of the boundary integral analysis including the numerical inversion of the Laplace transform. Afterwards, some numerical examples are presented and verified in Section 6.6. Finally concluding remarks are provided in Section 6.7.

6.1 Introduction

FGMs consisting of heat-resisting ceramic and fracture-resisting metal can improve the properties of thermal barrier systems because cracking and delamination, which are often observed in conventional layered systems, are reduced by proper smooth transition of material prop-

erties. Ceramic based FGMs have also been used for thermal protection – see Carrillo-Heian *et al.*[23]. FGMs are being developed as thermal barrier materials for combustion chambers, gas vanes, air vanes, nose cones, fuel valve sheets and piston crowns which undergo high-temperature gradient and high-thermal cycles in addition to wear.

Steady state heat conduction in nonhomogeneous media has been addressed by a few BEM researchers. Bialecki and Kuhn [11] presented a multizone approach where the material property was modeled as constant in certain zones in the layered media. Divo and Kassab [50] introduced a technique for heat conduction problems in heterogeneous media based on a fundamental solution that is a locally radially symmetric response to non-symmetric forcing functions. Shaw and Manolis [157] employed a conformal mapping technique to solve heat conduction problems in graded materials. Tanaka *et al.*[178] derived a dual reciprocity BEM formulation for FGMs. Gray *et al.*[75] developed a Galerkin BEM formulation by deriving the Green's function for steady state heat conduction problem in exponentially graded materials.

Transient heat conduction problems are usually solved using either the time domain approach or the Laplace transform domain approach. In the *time domain approach*, a time marching scheme associated with the BEM solution at each time step is used, and solutions are found directly in the time domain. An alternative is to employ a *transform space approach* wherein the time dependent derivative is eliminated in favour of an algebraic transform variable. However, once the differential system is solved in transform space, inverse transform is required to reconstitute the solution in the time domain. A review of these techniques can be found in [188], [174] and the references therein.

Sutradhar *et al.*[174] extended the work of reference [75] to transient heat conduction for exponentially graded materials in three dimensions using the Laplace transform (LT) BEM. The implementation in reference [174] is a pure boundary-only formulation without any domain integral, however it relies on the actual Green's function (GF) associated with the function describing the material gradation. Recently, Sladek *et al.*[164, 163, 162] presented a meshless local boundary integral equation (LBIE) formulation for transient heat conduction considering exponential material variation. In the LBIE approach, the domain is divided into small circular sub-domains and on the surface of the sub-domains the LBIEs are written, resulting in a boundary-domain integral formulation. In each domain, the fundamental solution is related to the corresponding material constants. A different approach to treat transient heat conduction in nonhomogeneous materials can be found in the book by Divo and Kassab [50].

Recently, Sutradhar and Paulino [172] proposed a simple three dimensional (3D) BEM where nonhomogeneous problems can be transformed to known homogeneous problems for a class of variations (quadratic, exponential and trigonometric) of thermal conductivity.

The material property can have a functional variation in one, two or three dimensions. The present work extends the simple BEM concept of reference [172] to transient problems. In the present work, the material density (ρ) is considered constant, and the thermal conductivity and the specific heat have been chosen to have the same functional variation so that the thermal diffusivity κ^1 is constant, *i.e.*,

$$\kappa = \frac{k(x)}{\rho c(x)} \equiv \text{constant.} \quad (6.1)$$

This approach has been followed by Sladek *et al.*[164, 163, 162] in developing BEM formulation for transient thermal problems in FGMs. Carslaw and Jaeger [24] have also assumed the same material variation for both $k(\mathbf{x})$ and $c(\mathbf{x})$ by considering functions of the power type

$$k = k_0 x^n, \quad c = c_0 x^n, \quad (6.2)$$

and linear type

$$k = k_0(1 + \alpha x), \quad c = c_0(1 + \alpha x), \quad (6.3)$$

in which k_0 , c_0 and α are constants. An example of thermal properties for an actual FGM can be found in the experimental work by Khor and Gu [98], who investigated functionally graded yttria-stabilized ZrO₂/NiCoCrAlY coatings. For this specific material system, the thermal diffusivity is not a constant. However, the assumption of constant thermal diffusivity in FGMs leads to a class of solvable problems, which allow development of a boundary-only integral equation formulation without any domain discretization. Moreover, this method can provide benchmark solutions to other numerical methods (e.g. FEM, meshless, partition of unity) and can provide valuable insight into the thermal behavior of FGMs.

By using variable transformations, the transient heat equation for FGMs can be converted to the known standard diffusion equation for three different classes of material variations (quadratic, exponential and trigonometric). The variable transformation approach has been previously studied for potential problems by Cheng [34, 35], Shaw [154], Shaw and Gipson [155], Harrouni *et al.*[83, 84], and Li and Evan [110]. Based on these references, an alternative approach for the BEM formulation is the Green's function approach [174], where each different material variation requires a different fundamental solution. Thus, the kernels necessary for the BEM implementation for each case are different. As a result, separate computer codes are required to deal with individual functional variations. Moreover, if the treatment of singularity involves analytical integration, then the solution becomes more involved [176].

¹The symbols k and κ should not be confused. Note that k denoted thermal conductivity and κ denotes thermal diffusivity.

By means of the variable transformation approach, which consists of simple changes in the boundary conditions of existing homogeneous transient heat conduction computer codes, the solutions for nonhomogeneous media with quadratic, exponential and trigonometric material variations can be obtained.

Notice that our previous work [174] was based on the *GF approach* which could *only* handle exponentially graded materials with unidimensional material variation; while the present work is based on the *variable transform approach*, which can handle *three classes of material gradation (quadratic, exponential and trigonometric)* with multi-dimensional material variation. Moreover, since the diffusion equation for nonhomogeneous materials can be transformed to the diffusion equation for homogeneous materials by means of the simple BEM concept, standard available BEM codes can be used with elementary modifications. This nice feature was not possible with the former approach of reference [174]. The present chapter describes how to do the modifications, which lead to a straightforward numerical implementation.

6.2 Basic equations and the simple BEM concept

The governing differential equation for the transient heat conduction is given by

$$\nabla \cdot (k(x, y, z) \nabla \phi) = \rho c(x, y, z) \frac{\partial \phi}{\partial t} \quad (6.4)$$

where $\phi = \phi(x, y, z; t)$ is the temperature function, k is the thermal conductivity, c is the specific heat, and ρ is the density which is assumed to be constant. Two types of boundary conditions are prescribed. The Dirichlet condition for the unknown temperature ϕ is

$$\phi(x, y, z; t) = \bar{\phi}(x, y, z; t) \quad (6.5)$$

on boundary Σ_1 and the Neumann condition for its flux is

$$q(x, y, z; t) = -k(x, y, z) \frac{\partial \phi(x, y, z; t)}{\partial n} = \bar{q}(x, y, z; t) \quad (6.6)$$

on boundary Σ_2 , where \mathbf{n} is the unit outward normal to Σ_2 . Here a bar over the quantity of interest means that it assumes a prescribed value. For a well-posed problem $\Sigma_1 \cup \Sigma_2 = \Sigma$ with Σ being the entire boundary. As the problem is time dependent, in addition to these boundary conditions, an initial condition at a specific time t_0 must also be prescribed. For

simplicity, a zero initial temperature distribution has been considered, *i.e.*

$$\phi(x, y, z; t_0) = \phi_0(x, y, z) = 0. \quad (6.7)$$

A non-zero initial condition will introduce a domain integral in the formulation, which can be handled by domain integral techniques such as dual reciprocity method [187] or particular solution method [94].

By defining a variable

$$v(x, y, z) = \sqrt{k(x, y, z)} \phi(x, y, z), \quad (6.8)$$

Eq. (6.4) can be rewritten as

$$\nabla^2 v + \left(\frac{\nabla k(x, y, z) \cdot \nabla k(x, y, z)}{4k^2(x, y, z)} - \frac{\nabla^2 k(x, y, z)}{2k(x, y, z)} \right) v = \frac{\rho c(x, y, z)}{k(x, y, z)} \frac{\partial v}{\partial t} \quad (6.9)$$

or

$$\nabla^2 v + k'(x, y, z)v = \frac{\rho c(x, y, z)}{k(x, y, z)} \frac{\partial v}{\partial t} \quad (6.10)$$

where

$$k'(\cdot) = \frac{\nabla k(\cdot) \cdot \nabla k(\cdot)}{4k^2(\cdot)} - \frac{\nabla^2 k(\cdot)}{2k(\cdot)}. \quad (6.11)$$

If the heat conductivity and the specific heat have the same functional variation, say *e.g.*,

$$k(x, y, z) = k_0 f(x, y, z), \quad (6.12)$$

and

$$c(x, y, z) = c_0 f(x, y, z), \quad (6.13)$$

respectively then by substituting these material expressions into Eq. (6.10), one obtains

$$\nabla^2 v + k'(x, y, z)v = \frac{1}{\kappa} \frac{\partial v}{\partial t} \quad (6.14)$$

where the constant thermal diffusivity is given by

$$\kappa = \frac{k_0}{c_0 \rho}. \quad (6.15)$$

If k' is either zero or a constant, then by introducing another variable substitution

$$v = e^{k' \kappa t} u, \quad (6.16)$$

one gets from Eq. (6.14)

$$\nabla^2 u = \frac{1}{\kappa} \frac{\partial u}{\partial t}. \quad (6.17)$$

This is the standard diffusion equation for homogeneous materials. If a material variation makes $k'(x, y, z)$ in Eq. (6.10) zero or constant, then the FGM transient heat conduction, Eq. (6.4), can be transformed into the standard homogeneous case given by, Eq. (6.17).

6.2.1 Material variations

- If $k'(x, y, z) = 0$, then $k(x, y, z)$ can be determined according to Eq. (6.11), *i.e.*

$$\frac{\nabla k \cdot \nabla k}{4k^2} - \frac{\nabla^2 k}{2k} = 0. \quad (6.18)$$

In this case, if $k(\cdot)$ varies along the z direction only, then one gets

$$k(z) = k_0(c_1 + c_2 z)^2 \text{ (Quadratic)}, \quad (6.19)$$

where c_1 and c_2 are arbitrary constants and k_0 is a reference value for the function k .

- If $k'(x, y, z) = -\beta^2$, then $k(x, y, z)$ can be determined according to Eq. (6.11), *i.e.*

$$\frac{\nabla k \cdot \nabla k}{4k^2} - \frac{\nabla^2 k}{2k} = -\beta^2. \quad (6.20)$$

If $k(\cdot)$ varies only with z , then

$$k(z) = k_0(a_1 e^{\beta z} + a_2 e^{-\beta z})^2 \text{ (Exponential)}, \quad (6.21)$$

where a_1 and a_2 are arbitrary constants.

- If $k'(x, y, z) = \beta^2$, then $k(x, y, z)$ can be determined from Eq. (6.11), *i.e.*

$$\frac{\nabla k \cdot \nabla k}{4k^2} - \frac{\nabla^2 k}{2k} = \beta^2. \quad (6.22)$$

Again, for $k(\cdot)$ varying only with z ,

$$k(z) = k_0(a_1 \cos \beta z + a_2 \sin \beta z)^2 \text{ (Trigonometric)}, \quad (6.23)$$

where a_1 and a_2 are arbitrary constants.

Notice that for quadratic, exponential and trigonometric variations of both heat conductivity and specific heat, the FGM transient problem can be transformed into a standard diffusion equation.

6.2.2 Multi-dimensional material variation

Although in the above discussion, the material properties vary only in one coordinate, the technique can be applied to materials varying in two or three coordinates as well. For instance, the general expression for material property variation in three dimensions are given below.

- Quadratic

$$k(x, y, z) = k_0(a_1 + a_2x)^2(b_1 + b_2y)^2(c_1 + c_2z)^2 \quad (6.24)$$

$$\text{and } k_0(d_1 + d_2x + d_3y + d_4z + d_5xy + d_6yz + d_7zx + d_8xyz)^2. \quad (6.25)$$

Here $a_1, a_2, b_1, b_2, c_1, c_2$, and $d_i (i = 1..8)$ are arbitrary constants.

- Exponential

$$k(x, y, z) = k_0(a_1e^{\alpha x})^2(b_1e^{\beta y})^2(c_1e^{\gamma z})^2 \quad (6.26)$$

Here $a_1, b_1, c_1, \alpha, \beta$ and γ are arbitrary constants.

- Trigonometric

$$k(x, y, z) = k_0(a_1 \cos \alpha x + a_2 \sin \alpha x)^2(b_1 \cos \beta y + b_2 \sin \beta y)^2(c_1 \cos \gamma z + c_2 \sin \gamma z)^2 \quad (6.27)$$

Here $a_1, a_2, b_1, b_2, c_1, c_2, \alpha, \beta$ and γ are arbitrary constants. A numerical example with a 3D quadratic material variation is included in Section 6.

6.3 Green's function (GF)

The GF can be derived in closed form directly for the material property variations presented above because, by variable transformation the nonhomogeneous problem can be transformed into a homogeneous problem for which the Green's function is known. The GF for the nonhomogeneous problem is of great importance for a true boundary-only formulation.

The GF equation corresponding to Eq. (6.4) is

$$\nabla \cdot (k(x, y, z) \nabla G_{FGM}^*) - \rho c(x, y, z) \frac{\partial G_{FGM}^*}{\partial t} = -\delta(Q - P) \delta(t - t') \quad (6.28)$$

where G_{FGM}^* is the GF, $\delta(Q - P)$ is the Dirac delta function located at the source point $P(x_P, y_P, z_P)$, and $Q(x, y, z)$ is the field point. By defining the variable $v = \sqrt{k(x, y, z)} G_{FGM}^*$, and substituting in Eq. (6.28) one obtains

$$k^{1/2}(x, y, z) [\nabla^2 v + k'v] - \frac{\rho c(x, y, z)}{k^{1/2}(x, y, z)} \frac{\partial v}{\partial t} = -\delta(Q - P) \delta(t - t'). \quad (6.29)$$

After simplifying, one gets

$$\nabla^2 v + k'v - \frac{1}{\kappa} \frac{\partial v}{\partial t} = -\frac{\delta(Q - P) \delta(t - t')}{k^{1/2}(x_P, y_P, z_P)}. \quad (6.30)$$

where, due to the property of the Dirac delta function $\delta(Q - P)$, the independent variable of $k^{1/2}$ was changed from Q to P . If k' is either zero or a constant, then by defining another variable $u = e^{-k'\kappa t} v$ and using it in Eq. (6.30) we get

$$\nabla^2 u - \frac{1}{\kappa} \frac{\partial u}{\partial t} = -\frac{\delta(Q - P) \delta(t - t')}{k^{1/2}(x_P, y_P, z_P) e^{k'\kappa t}}. \quad (6.31)$$

Again, by the property of the Dirac Delta function $\delta(t - t')$, a change in the independent variable t to t' is permissible, so that

$$\nabla^2 u - \frac{1}{\kappa} \frac{\partial u}{\partial t} = -\frac{\delta(Q - P) \delta(t - t')}{k^{1/2}(x_P, y_P, z_P) e^{k'\kappa t'}}. \quad (6.32)$$

The solution of the GF of Eq. (6.32) can be readily obtained as

$$u(P, Q) = G_{hom}^*(P, Q) k^{-1/2}(x_P, y_P, z_P) e^{-k'\kappa t'}, \quad (6.33)$$

where $G_{hom}^*(P, Q)$ is the GF of the standard diffusion equation for the homogeneous problem. The GF corresponding to Eq. (6.30) is therefore,

$$v(P, Q) = e^{k'\kappa t} u(P, Q) = G_{hom}^*(P, Q) k^{-1/2}(x_P, y_P, z_P) e^{k'\kappa(t-t')}. \quad (6.34)$$

Similarly, the GF corresponding to Eq. (6.28) is

$$G_{FGM}^* = k^{-1/2}(x, y, z) v(P, Q) = G_{hom}^*(P, Q) k^{-1/2}(x, y, z) k^{-1/2}(x_P, y_P, z_P) e^{k'\kappa(t-t')}. \quad (6.35)$$

The time dependent fundamental solution or the GF for the homogeneous problem is [24]

$$G_{hom}^*(P, Q) = \frac{1}{[4\pi\kappa(t-t')]^{\frac{3}{2}}} e^{-\frac{r^2}{4\kappa(t-t')}}. \quad (6.36)$$

The GF represents the temperature field at time t produced by an instantaneous source of heat at point $P(x_P, y_P, z_P)$ at the time t' , r is the distance between the source point P and the field point Q . The GF for the nonhomogeneous material problem from Eq. (6.35) is therefore

$$G_{FGM}^*(P, Q) = \frac{e^{-\frac{r^2}{4\kappa(t-t')}}}{[4\pi\kappa(t-t')]^{\frac{3}{2}}} \frac{e^{k'\kappa(t-t')}}{k^{1/2}(x, y, z)k^{1/2}(x_P, y_P, z_P)}. \quad (6.37)$$

For the Laplace transform (LT) approach, the GF for the homogenous problem in the Laplace space is

$$G_{hom}^*(P, Q, s) = \frac{1}{4\pi r} e^{-\sqrt{\frac{s}{\kappa}} r}. \quad (6.38)$$

Following the above procedure by incorporating the variable transformations, the GF for the nonhomogeneous material problem in the LT space is derived as

$$G_{FGM}^*(P, Q, s) = \frac{1}{4\pi r} \frac{e^{-\sqrt{-k'+\frac{s}{\kappa}} r}}{k(x, y, z)^{1/2}k(x_P, y_P, z_P)^{1/2}}. \quad (6.39)$$

Note that by setting $k'(x, y, z) = 0, \beta^2$ and $-\beta^2$, a quadratic, trigonometric and exponential material variation, respectively, can be obtained (See Table 6.1).

Table 6.1: Variable transformation approach

k'	Material variation	1D Example
0	Quadratic	$k(z) = k_0(c_1 + c_2 z)^2$
β^2	Trigonometric	$k(z) = k_0(a_1 \cos \beta z + a_2 \sin \beta z)^2$
$-\beta^2$	Exponential	$k(z) = k_0(a_1 e^{\beta z} + a_2 e^{-\beta z})^2$

Although the GF for the FGM problem is given in this section, it is not used in the numerical implementation. Rather than using the GF for nonhomogeneous materials, we employ the simple boundary element method concept of reference [172] and extend the concept to the transient case which allows us to use the standard GF, (Eqs. (6.36) and (6.38)), for homogeneous materials.

6.4 Laplace transform BEM (LTBEM) formulation

In the present work, the transformed approach is chosen. As explained in the previous sections, two variable transformations are used to reduce the nonhomogeneous problem to the known standard diffusion problem. The first variable transformation involves only spatial variables (x, y, z) (from ϕ to v – see Eq. (6.8)) and the second variable transformation involves only the temporal variable t (from v to u – see Eq. (6.16)). Note that k' and κ are constants. The LTBEM formulation can be based on either variable u or variable v . In the following, the LTBEM formulations based on u and v are presented and their relative advantages and disadvantages are pointed out.

6.4.1 Approach 1: Formulation based on One-step Transformation

Let the Laplace transform (LT) of u be denoted by

$$\tilde{u}(Q, s) = \int_{\mathcal{R}} u(Q, t) e^{-st} dt. \quad (6.40)$$

Here a tilde over a quantity of interest means LT of the quantity of interest. Thus, in LT space, the differential equation (6.17) becomes

$$\nabla^2 \tilde{u} - \frac{s}{\kappa} \tilde{u} = 0, \quad (6.41)$$

where zero initial temperature ($u_0 = 0$ at $t = 0$) is considered for simplicity.

Following usual practice, the corresponding boundary integral statement can be obtained by ‘orthogonalizing’ this equation against an arbitrary (for now) function $f(x, y, z) = f(Q)$, and integrating over a bounded volume V

$$\int_V f(Q) \left(\nabla^2 \tilde{u} - \frac{s}{\kappa} \tilde{u} \right) dV_Q = 0. \quad (6.42)$$

According to Green’s second identity, if the two functions ψ and λ have continuous first and second derivatives in V , then

$$\int_V (\psi \nabla^2 \lambda - \lambda \nabla^2 \psi) dV = \int_{\Sigma} \left(\psi \frac{\partial \lambda}{\partial n} - \lambda \frac{\partial \psi}{\partial n} \right) dS. \quad (6.43)$$

Using this relation and denoting the boundary of V by Σ , we obtain the first term of

Eq. (6.42) as,

$$\int_V f(Q) \nabla^2 \tilde{u} dV_Q = \int_V \tilde{u}(Q) \nabla^2 f(Q) dV_Q + \int_\Sigma \left(f(Q) \frac{\partial \tilde{u}(Q)}{\partial n} - \tilde{u}(Q) \frac{\partial f(Q)}{\partial n} \right) dS_Q. \quad (6.44)$$

and using Eq. (6.43), we get,

$$0 = \int_\Sigma \left(f(Q) \frac{\partial \tilde{u}(Q)}{\partial n} - \tilde{u}(Q) \frac{\partial f(Q)}{\partial n} \right) dS_Q + \int_V \tilde{u}(Q) \left(\nabla^2 f(Q) - \frac{s}{\kappa} f(Q) \right) dV_Q \quad (6.45)$$

where $n(Q) = (n_x, n_y, n_z)$ is the unit outward normal on Σ .

If we select $f(Q) = G(P, Q, s)$ as a GF, then the GF equation is

$$\nabla^2 G(P, Q, s) - \frac{s}{\kappa} G(P, Q, s) = -\delta(Q - P), \quad (6.46)$$

where δ is the Dirac Delta function. Thus the source point volume integral in Eq. (6.45) becomes $-\tilde{u}(P)$. By means of Eq. (6.46), Eq. (6.45) can be rewritten as

$$\tilde{u}(P) + \int_\Sigma \left(\frac{\partial G(P, Q)}{\partial n} \right) \tilde{u}(Q) dS_Q = \int_\Sigma G(P, Q) \frac{\partial \tilde{u}(Q)}{\partial n} dS_Q. \quad (6.47)$$

Accordingly, the GF for the homogenous diffusion equation is given by Eq. (6.38) as

$$G(P, Q, s) = \frac{1}{4\pi r} e^{-\sqrt{(s/\kappa)} r}. \quad (6.48)$$

Boundary conditions: One-step Transformation

In order to solve the boundary value problem based on the modified variable u , the boundary conditions of the original problem should be incorporated in the modified boundary value problem. Thus, for the modified problem, the Dirichlet and the Neumann boundary conditions change to the following form, respectively:

$$\bar{u} = e^{-k'\kappa t} \bar{v} = e^{-k'\kappa t} \sqrt{k} \bar{\phi}(Q, t) \quad \text{on } \Sigma_1 \quad (6.49)$$

$$\frac{\partial \bar{u}}{\partial n} = \frac{1}{2k} \frac{\partial k}{\partial n} u - \frac{\bar{q}(Q, t)}{\sqrt{k}} e^{-k'\kappa t} \quad \text{on } \Sigma_2. \quad (6.50)$$

The boundary conditions must also be transformed into the Laplace space, *i.e.*

$$\tilde{u} = \sqrt{k} \int_{\mathcal{R}} \bar{\phi}(Q, t) e^{-k'\kappa t} e^{-st} dt, \quad (6.51)$$

$$\frac{\partial \tilde{u}}{\partial n} = \frac{1}{2k} \frac{\partial k}{\partial n} \tilde{u} - \frac{1}{\sqrt{k}} \int_{\mathcal{R}} \bar{q}(Q, t) e^{-k'\kappa t} e^{-st} dt. \quad (6.52)$$

6.4.2 Approach 2: Formulation Based on Two-step Transformation

Let the Laplace transform (LT) of v be denoted by

$$\tilde{v}(Q, s) = \int_{\mathcal{R}} v(Q, t) e^{-st} dt. \quad (6.53)$$

If the formulation is based on the modified variable v instead of u , then the differential equation for the formulation instead of (6.41) becomes

$$\nabla^2 \tilde{v} + k' \tilde{v} - \frac{s}{\kappa} \tilde{v} = 0. \quad (6.54)$$

Following the same steps as before, the final form of the boundary integral formulation becomes

$$\tilde{v}(P) + \int_{\Sigma} \left(\frac{\partial G(P, Q)}{\partial n} \right) \tilde{v}(Q) dS_Q = \int_{\Sigma} G(P, Q) \frac{\partial \tilde{v}(Q)}{\partial n} dS_Q. \quad (6.55)$$

Here, the GF in the 3D LT space is given by

$$G(P, Q, s) = \frac{1}{4\pi r} e^{-\sqrt{-k' + (s/\kappa)} r}. \quad (6.56)$$

Notice that the only difference between the formulations based on the variables u and v is in the Green's functions, Eq. (6.48) and Eq. (6.56), respectively. They differ in the exponential terms, *i.e.* $-\sqrt{-k' + s/\kappa}$ for the formulation based on v , and $-\sqrt{s/\kappa}$ for the formulation based on u . This change is very simple to implement numerically in order to extend the homogeneous code for FGM problems. The change in the treatment of the boundary conditions for the formulation based on v is discussed below, and is employed in the present work.

Boundary conditions: Two-step Transformation

The modified Dirichlet and Neumann boundary conditions for the modified variable v are

$$v = \sqrt{k} \bar{\phi}(Q, t) \quad \text{on } \Sigma_1 \quad (6.57)$$

and

$$\frac{\partial v}{\partial n} = \frac{1}{2k} \frac{\partial k}{\partial n} v - \frac{\bar{q}(Q, t)}{\sqrt{k}} \quad \text{on } \Sigma_2, \quad (6.58)$$

respectively. In the LT space they are transformed as

$$\tilde{v} = \sqrt{k} \tilde{\phi}(Q, s) \quad \text{on } \Sigma_1, \quad (6.59)$$

and

$$\frac{\partial \tilde{v}}{\partial n} = \frac{1}{2k} \frac{\partial k}{\partial n} \tilde{v} - \frac{\tilde{q}(Q, s)}{\sqrt{k}} \quad \text{on } \Sigma_2, \quad (6.60)$$

where

$$\tilde{\phi}(Q, s) = \int_{\mathcal{R}} \bar{\phi}(Q, t) e^{-st} dt, \quad \tilde{q}(Q, s) = \int_{\mathcal{R}} \bar{q}(Q, t) e^{-st} dt. \quad (6.61)$$

Compared to Eqs. (6.49)-(6.52), the changes herein do not involve an extra exponential function of t to deal with the Laplace transformation.

For constant values of $\bar{\phi}(Q, t)$ and $\bar{q}(Q, t)$, the expressions (6.59) and (6.60) becomes

$$\tilde{v} = \sqrt{k} \frac{\bar{\phi}(Q, t)}{s} \quad \text{on } \Sigma_1 \quad (6.62)$$

and

$$\frac{\partial \tilde{v}}{\partial n} = \frac{1}{2k} \frac{\partial k}{\partial n} \tilde{v} - \frac{\bar{q}(Q, s)}{s\sqrt{k}} \quad \text{on } \Sigma_2. \quad (6.63)$$

Notice that the Dirichlet boundary condition of the original problem is affected by the factor \sqrt{k} . Moreover, the Neumann boundary condition of the original problem changes to a mixed boundary condition or Robin boundary condition. This later modification is the only major change in the formulation.

Another common boundary condition of the original problem is a prescribed relationship between the potential and the flux (*e.g.* convective heat transfer problems). The boundary condition of this type is

$$q = \lambda_1 \phi + \lambda_2 \quad (\text{Robin type}). \quad (6.64)$$

The corresponding boundary condition for the modified problem is also a Robin boundary condition similar to Eq. (6.60), *i.e.*

$$\frac{\partial \tilde{v}}{\partial n} = \left(\frac{1}{2k} \frac{\partial k}{\partial n} - \lambda_1 \right) \tilde{v} - \frac{\tilde{\lambda}_2(Q, s)}{\sqrt{k}}. \quad (6.65)$$

6.4.3 Remarks

The formulation based on u uses the homogeneous GF, Eq. (6.48), but due to the exponential term $e^{-k'\kappa t}$, the modified boundary conditions in the LT space, Eqs. (6.51)-(6.52), include an exponential function of t in the Laplace transformation. On the other hand, the formulation based on v uses a slightly different Green's function (the exponential term changes from $-\sqrt{s/\kappa}$ to $-\sqrt{-k' + s/\kappa}$), but the treatment of the modified boundary condition does not involve the extra exponential term. For these reasons, we adopt the LT BEM formulation based on v for the numerical implementation. However, both formulations are equivalent.

6.5 Numerical implementation of the Galerkin LT BEM

The numerical methods employed in the current work use standard Galerkin techniques. A brief discussion of these techniques in the context of the BEM is presented below. It includes the development of the Galerkin boundary conditions (which is the main consideration in the simple BEM concept), selection of the boundary element type, treatment of singular integrals and corners, and numerical inversion of the Laplace transform in the LT BEM framework.

6.5.1 Galerkin boundary integral equation.

Define the collocation BIE as

$$\mathcal{B}(P) \equiv \tilde{v}(P) + \int_{\Sigma} \left(\frac{\partial G(P, Q, s)}{\partial n} \right) \tilde{v}(Q) dQ - \int_{\Sigma} G(P, Q, s) \frac{\partial \tilde{v}(Q)}{\partial n} dQ \quad (6.66)$$

and thus for an exact solution $\mathcal{B}(P) \equiv 0$.

In a Galerkin approximation, the error in the approximate solution is orthogonalized against the shape functions, *i.e.* the shape functions are the weighting functions and the condition $\mathcal{B}(P) = 0$ is enforced in the 'weak sense', *i.e.*

$$\int_{\Sigma} N_k(P) \mathcal{B}(P) dP = 0. \quad (6.67)$$

As a result the Galerkin technique possesses the important property of the *local support* (see Figure 6.1). The Galerkin technique is especially suitable to treat corners [137]. After replacing the boundary and the boundary functions by their interpolated approximations, a

set of linear algebraic equations emerges,

$$[\mathcal{H}]\{\tilde{v}\} = [\mathcal{G}] \left\{ \frac{\partial \tilde{v}}{\partial n} \right\}. \quad (6.68)$$

The matrix \mathcal{G} is symmetric because its coefficients depend only on the distance (r) between the source point (P) and the fields point (Q), but matrix \mathcal{H} is not symmetric because it depends on the normal vector of the field point point (Q). For Dirichlet problems, the Galerkin method gives rise to a symmetric system of equations.

After the boundary conditions of the problems are incorporated to the system, Eq. (6.68), the matrices can be reordered in the form

$$[\mathbf{A}]\{X\} = [\mathbf{B}], \quad (6.69)$$

where all the unknown quantities have been collected into the vector X . This system of equations can be solved by standard solution schemes for linear systems .

In the context of nonhomogeneous media a symmetric Galerkin boundary element method (SGBEM) has been presented recently by Sutradhar *et al.*[176]. Details of the symmetry property and numerical implementation can be found in references [85, 88, 13]. However, a non-symmetric Galerkin formulation, employing the singular Galerkin BIE, is adopted in the present work.

6.5.2 Treatment of boundary conditions

With respect to standard BEM codes the main modification in the implementation of the simple BEM is to incorporate the boundary conditions for the modified problem. In this section, the necessary modifications are described.

For the sake of illustration, let us assume three nodes, of which node 1 and node 3 have prescribed Neumann boundary condition, and node 2 has prescribed Dirichlet boundary condition, i.e.,

$$\begin{array}{lll} \bar{q}_1, & \bar{\phi}_2, & \bar{q}_3 \quad \text{known quantities} \\ \phi_1, & q_2, & \phi_3 \quad \text{unknown quantities.} \end{array}$$

These quantities are transformed into the Laplace space using Eq. (6.61). In the modified boundary value problem the variables are \tilde{v} and $\partial \tilde{v} / \partial n$. The system of algebraic equations

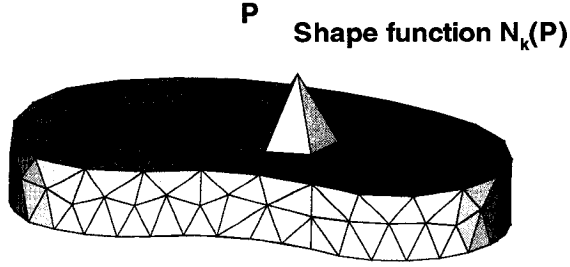


Figure 6.1: The local support of the Galerkin formulation at the source point P .

in the form of Eq. (6.68) emerges as,

$$\begin{bmatrix} H_{11} & H_{12} & H_{13} \\ H_{21} & H_{22} & H_{23} \\ H_{31} & H_{32} & H_{33} \end{bmatrix} \begin{Bmatrix} \tilde{v}_1 \\ \tilde{v}_2 \\ \tilde{v}_3 \end{Bmatrix} = \begin{bmatrix} G_{11} & G_{12} & G_{13} \\ G_{21} & G_{22} & G_{23} \\ G_{31} & G_{32} & G_{33} \end{bmatrix} \begin{Bmatrix} \partial\tilde{v}_1/\partial n \\ \partial\tilde{v}_2/\partial n \\ \partial\tilde{v}_3/\partial n \end{Bmatrix}. \quad (6.70)$$

By rearranging the equations so that the unknowns are passed to the left-hand side, we can rewrite the linear system as follows

$$\begin{bmatrix} H_{11} & -G_{12} & H_{13} \\ H_{21} & -G_{22} & H_{23} \\ H_{31} & -G_{32} & H_{33} \end{bmatrix} \begin{Bmatrix} \tilde{v}_1 \\ \partial\tilde{v}_2/\partial n \\ \tilde{v}_3 \end{Bmatrix} = \begin{bmatrix} G_{11} & -H_{12} & G_{13} \\ G_{21} & -H_{22} & G_{23} \\ G_{31} & -H_{32} & G_{33} \end{bmatrix} \begin{Bmatrix} \partial\tilde{v}_1/\partial n \\ \tilde{v}_2 \\ \partial\tilde{v}_3/\partial n \end{Bmatrix}. \quad (6.71)$$

Using Eq. (6.59) and Eq. (6.60), we obtain the final form of the set of equations,

$$\begin{bmatrix} \left(H_{11} - \frac{G_{11}}{2k} \frac{\partial k}{\partial n}\right) & -G_{12} & \left(H_{13} - \frac{G_{13}}{2k} \frac{\partial k}{\partial n}\right) \\ \left(H_{21} - \frac{G_{21}}{2k} \frac{\partial k}{\partial n}\right) & -G_{22} & \left(H_{23} - \frac{G_{23}}{2k} \frac{\partial k}{\partial n}\right) \\ \left(H_{31} - \frac{G_{31}}{2k} \frac{\partial k}{\partial n}\right) & -G_{32} & \left(H_{33} - \frac{G_{33}}{2k} \frac{\partial k}{\partial n}\right) \end{bmatrix} \begin{Bmatrix} \tilde{v}_1 \\ \partial\tilde{v}_2/\partial n \\ \tilde{v}_3 \end{Bmatrix} = \begin{bmatrix} G_{11} & -H_{12} & G_{13} \\ G_{21} & -H_{22} & G_{23} \\ G_{31} & -H_{32} & G_{33} \end{bmatrix} \begin{Bmatrix} -\tilde{q}_1(s)/\sqrt{k} \\ \tilde{\phi}_2(s)\sqrt{k} \\ -\tilde{q}_3(s)/\sqrt{k} \end{Bmatrix}, \quad (6.72)$$

which is in the form of Eq. (6.69). We solve these equations for \tilde{v}_1 , $\partial\tilde{v}_2/\partial n$, and \tilde{v}_3 ; and

finally, by using Eq. (6.59) and Eq. (6.60), we obtain

$$\begin{aligned}\tilde{\phi}_1(s) &= \tilde{v}_1/\sqrt{k}, \\ \tilde{q}_2(s) &= -\sqrt{k} \left\{ \frac{\partial \tilde{v}_2}{\partial n} - \frac{1}{2k} \frac{\partial k}{\partial n} \tilde{v}_2 \right\}, \\ \tilde{\phi}_3(s) &= \tilde{v}_3/\sqrt{k}.\end{aligned}\tag{6.73}$$

These quantities are the solutions in the transform space. The final step is to invert these quantities back to the time domain by using numerical inverse Laplace transform technique.

6.5.3 Boundary elements

The surface of the solution domain is divided into a number of connected elements. Over each element, the variation of the geometry and the variables (potential and flux) is approximated by simple functions. Six noded isoparametric quadratic triangular elements are used (see Figure 6.2).

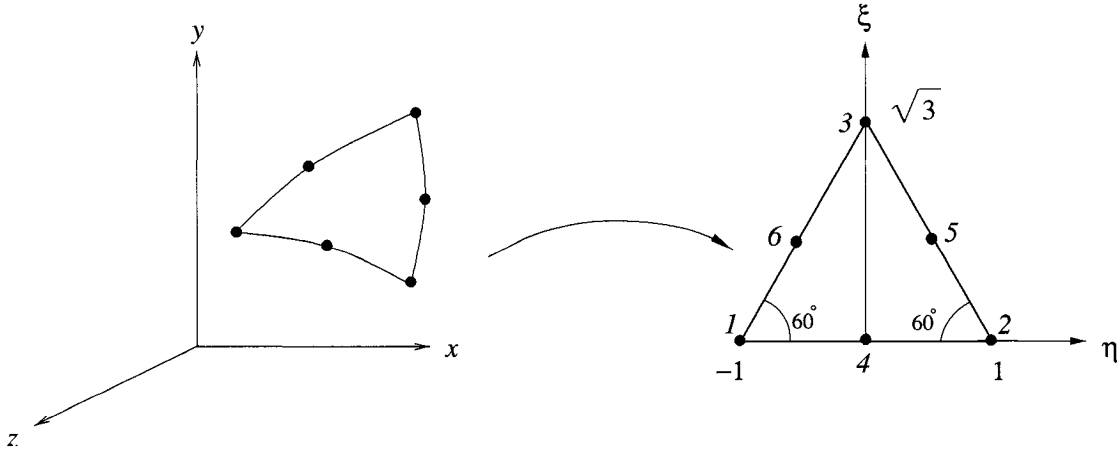


Figure 6.2: A triangle in the 3D space is mapped to an equilateral triangular quadratic element in $\{\eta, \xi\}$ space, where $-1 \leq \eta \leq 1$, $0 \leq \xi \leq \sqrt{3}(1 - |\eta|)$.

The geometry of an element can be defined by the coordinates of its six nodes using appropriate quadratic shape functions as follows

$$x_i(\eta, \xi) = \sum_{j=1}^6 N_j(\eta, \xi)(x_i)_j.\tag{6.74}$$

By means of an isoparametric approximation, the same shape functions are used for the

solution variables (both potential and flux), as follows:

$$\begin{aligned}\phi_i(\eta, \xi) &= \sum_{j=1}^6 N_j(\eta, \xi)(\phi_i)_j, \\ q_i(\eta, \xi) &= \sum_{j=1}^6 N_j(\eta, \xi)(q_i)_j.\end{aligned}\tag{6.75}$$

The shape functions can be explicitly written in terms of intrinsic coordinates ξ and η as (see Figure 6.2):

$$\begin{aligned}N_1(\eta, \xi) &= (\xi + \sqrt{3}\eta - \sqrt{3})(\xi + \sqrt{3}\eta)/6 & N_4(\eta, \xi) &= (\xi + \sqrt{3}\eta - \sqrt{3})(\xi - \sqrt{3}\eta - \sqrt{3})/3 \\ N_2(\eta, \xi) &= (\xi - \sqrt{3}\eta - \sqrt{3})(\xi - \sqrt{3}\eta)/6 & N_5(\eta, \xi) &= -2\xi(\xi - \sqrt{3}\eta - \sqrt{3})/3 \\ N_3(\eta, \xi) &= \xi(2\xi - \sqrt{3})/3 & N_6(\eta, \xi) &= -2\xi(\xi + \sqrt{3}\eta - \sqrt{3})/3\end{aligned}\tag{6.76}$$

The intrinsic coordinate space is the equilateral triangle with $-1 \leq \eta \leq 1$, $0 \leq \xi \leq \sqrt{3}(1 - |\eta|)$.

6.5.4 Singular integrals

For three dimensional problems, there are four typical configurations for the two elements containing the source point P and the field point Q (see Figure 6.3), and thus four distinct situations regarding the singularity must be considered:

- *Non-singular case*, when the source point P and the field point Q lie on distinct elements, that do not share a common vertex or edge.
- *Coincident case*, when the source point P and the field point Q lie in the same element;
- *Edge adjacent case*, when two elements share a common edge; and
- *Vertex adjacent case*, when a vertex is the only common node between the two elements.

A hybrid analytical/numerical approach using the “limit to the boundary” approach has been adopted to treat the singular integrals. Details of this technique can be found in the papers by Gray *et al.*[74, 73] and Sutradhar *et al.*[176].

6.5.5 Corners

The treatment of corners in the Galerkin BEM is simple and elegant due to the flexibility in choosing the weight function for the Galerkin approximation. Corners are represented by

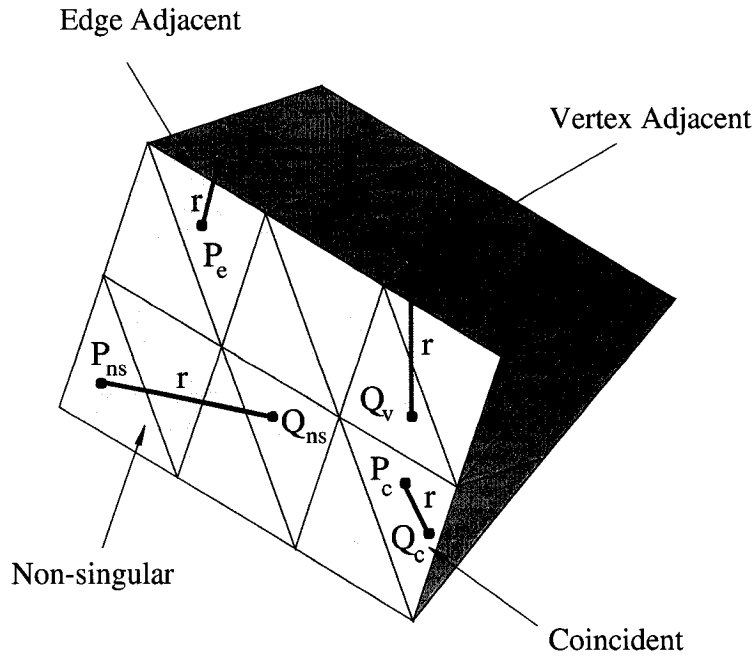


Figure 6.3: Four different cases considered for integration: (a) non-singular; (b) coincident; (c) edge adjacent; and (d) vertex adjacent.

multiple nodes, and on each side different weight functions are used (see Figure 6.4). For a mixed corner (flux is unknown in one side of the corner, potential is known), a non zero weight function is assigned only on the side where flux is unknown. For a Neumann corner (flux specified on both sides of the corner, potential is the unknown), the weight functions are combined together. On a Dirichlet corner (unknowns are flux on each sides, potential is known) the usual weight functions are assigned on both sides of the corners.

6.5.6 Numerical inversion of the Laplace transform

In the LT-BEM approach, the numerical inversion of the LT is an important issue. For the present implementation the Stehfest's algorithm [167, 168] has been employed for this purpose. During the inversion process, the sign of the expression under the square root in Eq. (6.56) *i.e.*, $-\sqrt{-k' + s/\kappa}$ should not become negative. A few comments on this issue are in order. For the parabolic material variation $k' = 0$, and for the exponential material variation $k' = -\beta^2$. As a result for these two cases, the sign of the expression is always

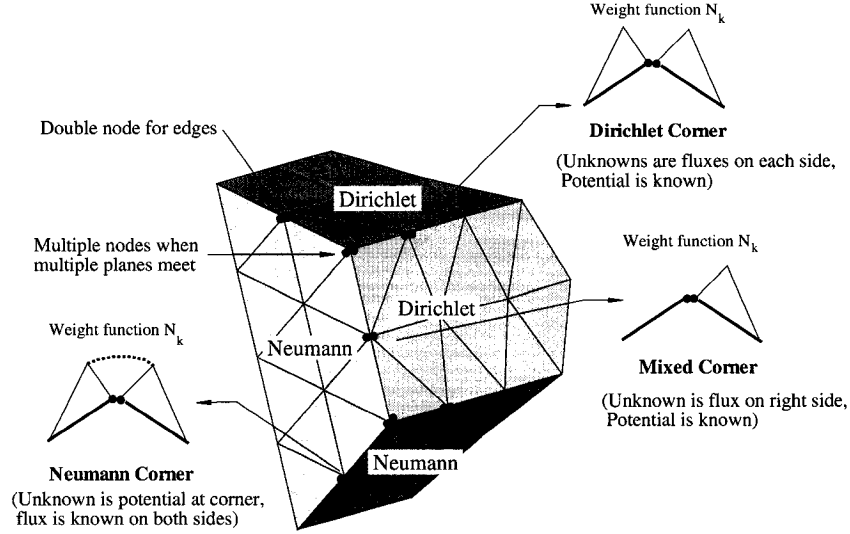


Figure 6.4: Corner treatment in the Galerkin BEM.

positive. However, for the trigonometric material variation, if $k' = \beta^2$ is greater than s/κ , then the sign can be negative, but it will depend on a few parameters. Since in the inversion process the Laplace parameter

$$s = \frac{\ln 2}{T} i, \quad (6.77)$$

where T is the specific time for which the solution is sought, there exists a criterion when the sign can be negative. The critical criterion can be written as

$$T > \frac{\ln 2}{\kappa \beta^2}, \quad (6.78)$$

which occurs for $i = 1$. The criterion depends on the relative magnitudes of the nonhomogeneity parameter β , the specific time for solution T and the diffusivity κ .

6.6 Examples

In this section, a number of test examples are reported, demonstrating the implementation of the above techniques. To validate the numerical implementation, the following examples are presented:

(1) Cube problem

- material gradation along the z -axis,
- 3D material gradation,

(2) Rotor problem

The first example is a cube with constant temperatures in two sides and insulated in all the other sides. Two different cases are studied for this example by changing the material variation and changing the boundary conditions. For this problem, all the three kinds of material variation, *i.e.* quadratic, exponential and trigonometric, are prescribed. This is a verification problem, in which the numerical solutions are compared against analytical solutions. The other example is a rotor problem, which is of engineering significance in the field of functionally graded materials.

6.6.1 Cube problem

Material gradation along the z -axis.

A unit cube ($L = 1$) with prescribed constant temperature on two sides is considered. The problem of interest and corresponding BEM mesh is shown in Figure 6.5. The top surface of the cube at $[z = 1]$ is maintained at the temperature $T = 100$, while the bottom at $[z = 0]$ has $T = 0$. The remaining four faces are insulated (zero normal flux). The initial temperature is zero. Three different classes of variations are considered. Analytical solutions for the three cases are derived by using the method of separation of variables.

Analytical solutions

- *Quadratic material gradation*

Let the quadratic variation of thermal conductivity $k(x, y, z)$ and specific heat $c(x, y, z)$ be defined as

$$k(x, y, z) = k(z) = k_0(1 + \beta z)^2 = 5(1 + 2z)^2, \quad (6.79)$$

and

$$c(x, y, z) = c(z) = c_0(1 + \beta z)^2 = 1(1 + 2z)^2, \quad (6.80)$$

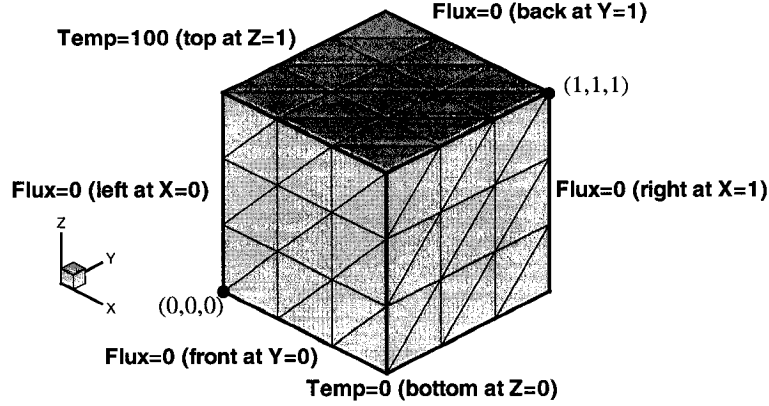


Figure 6.5: Geometry and boundary conditions of the FGM unit cube problem with constant temperature on two planes. The BEM mesh consists of 294 nodes and 108 quadratic triangular elements.

respectively, in which β is the nonhomogeneity parameter. The analytical solution for temperature is

$$\phi(x, y, z; t) = \frac{T_1 z}{\sqrt{k}L} + \frac{2T_1}{\sqrt{k}} \sum_{n=1}^{\infty} \frac{\cos n\pi}{n\pi} \sin \frac{n\pi z}{L} e^{-\left(\frac{n^2\pi^2}{L^2} \kappa t\right)}, \quad (6.81)$$

where L is the dimension of the cube (in the z -direction) and

$$T_1 = \sqrt{k_0}(1 + \beta L)T. \quad (6.82)$$

The analytical solution for flux is

$$\begin{aligned} q(x, y, z; t) &= -k(x, y, z) \frac{\partial \phi}{\partial z} \\ &= -k(x, y, z) \left[\frac{(1 + \beta L)T}{(1 + \beta z)^2 L} + \frac{2T_1}{\sqrt{k}} \sum_{n=1}^{\infty} \frac{\cos n\pi}{n\pi} \sin \frac{n\pi z}{L} e^{-\left(\frac{n^2\pi^2}{L^2} \kappa t\right)} \right. \\ &\quad \left. \times \left(\cos \left(\frac{n\pi z}{L} \right) \frac{n\pi}{L} - \sin \left(\frac{n\pi z}{L} \right) \frac{\beta}{(1 + \beta z)} \right) \right]. \end{aligned} \quad (6.83)$$

- *Exponential material gradation*

Let the exponential variation of thermal conductivity $k(x, y, z)$ and specific heat $c(x, y, z)$ be defined as

$$k(x, y, z) = k(z) = k_0 e^{2\beta z} = 5e^{2z}, \quad (6.84)$$

and

$$c(x, y, z) = c(z) = c_0 e^{2\beta z} = 1e^{2z}, \quad (6.85)$$

respectively, where β is the nonhomogeneity parameter. The analytical solution for temperature is

$$\phi(x, y, z; t) = T \frac{1 - e^{-2\beta z}}{1 - e^{-2\beta L}} + \sum_{n=1}^{\infty} \frac{2T e^{\beta L} n\pi \cos n\pi}{\beta^2 L^2 + n^2 \pi^2} \sin \frac{n\pi z}{L} e^{-\beta z} e^{-\left(\frac{n^2 \pi^2}{L^2} + \beta^2\right) \kappa t} \quad (6.86)$$

where L is the dimension of the cube (in the z -direction). The analytical solution for flux is

$$\begin{aligned} q(x, y, z; t) &= -k(x, y, z) \frac{\partial \phi}{\partial z} \\ &= -k(x, y, z) \left[\frac{2\beta T e^{-2\beta z}}{1 - e^{-2\beta L}} + \sum_{n=1}^{\infty} \frac{2T e^{\beta L} n\pi \cos n\pi}{\beta^2 L^2 + n^2 \pi^2} e^{-\beta z} e^{-\left(\frac{n^2 \pi^2}{L^2} + \beta^2\right) \kappa t} \right. \\ &\quad \left. \times \left(\frac{n\pi}{L} \cos \frac{n\pi z}{L} - \beta \sin \frac{n\pi z}{L} \right) \right] \end{aligned} \quad (6.87)$$

- *Trigonometric material gradation*

Let the trigonometric variation of the thermal conductivity $k(x, y, z)$ and specific heat $c(x, y, z)$ be defined as

$$k(z) = k_0 (a_1 \cos \beta z + a_2 \sin \beta z)^2 = 5(\cos(0.2z) + 2 \sin(0.2z))^2, \quad (6.88)$$

and

$$c(z) = c_0 (a_1 \cos \beta z + a_2 \sin \beta z)^2 = 1(\cos(0.2z) + 2 \sin(0.2z))^2, \quad (6.89)$$

respectively, where β is the nonhomogeneity parameter and a_1 and a_2 are constants.

The analytical solution for temperature is

$$\phi(x, y, z; t) = \frac{T_1 \sin \beta z}{\sqrt{k} \sin \beta L} + \frac{2T_1}{\sqrt{k}} \sum_{n=1}^{\infty} \frac{n\pi \cos n\pi}{n^2\pi^2 - \beta^2 L^2} \sin \frac{n\pi z}{L} e^{-\left(\frac{n^2\pi^2}{L^2} - \beta^2\right)\kappa t} \quad (6.90)$$

where L is the dimension of the cube (in the z -direction) and

$$T_1 = \sqrt{k_0} (\cos \beta L + 2 \sin \beta L) T. \quad (6.91)$$

The analytical solution for flux is

$$\begin{aligned} q(x, y, z; t) &= -k(x, y, z) \frac{\partial \phi}{\partial z} \\ &= -k(x, y, z) \left[-\frac{(\cot \beta L + 2) T \beta}{3 \cos^2 \beta z - 4 \cos \beta z \sin \beta z - 4} \right. \\ &\quad + \frac{2T_1}{\sqrt{k}} \sum_{n=1}^{\infty} \frac{n\pi \cos n\pi}{n^2\pi^2 - \beta^2 L^2} e^{-\left(\frac{n^2\pi^2}{L^2} - \beta^2\right)\kappa t} \\ &\quad \times \left. \left(\cos \left(\frac{n\pi z}{L} \right) \frac{n\pi}{L} - \sin \left(\frac{n\pi z}{L} \right) \frac{\beta(-\sin \beta z + 2 \cos \beta z)}{(\cos \beta z + 2 \sin \beta z)} \right) \right] \quad (6.92) \end{aligned}$$

Results

The cube is discretized with 294 nodes and 108 quadratic triangular elements as illustrated by Figure 6.5. The profiles of the thermal conductivity $k(z)$ of the three cases are illustrated in Figure 6.6. The temperature profile along the z axis is plotted at different times for the quadratic, exponential and trigonometric material variations, and compared with the analytical solutions in Figures 6.7, 6.8 and 6.9 respectively. The variation of flux at the $z = 0$ surface with respect to time is plotted in Figure 6.10 for the three material variations. The variation of flux at the $z = 1$ surface is plotted in Figure 6.11. The numerical and analytical results are in excellent agreement.

Cube with three dimensional material gradation.

The three dimensional variation of the thermal conductivity and the specific heat are

$$k(x, y, z) = (5 + 0.2x + 0.4y + 0.6z + 0.1xy + 0.2yz + 0.3zx + 0.7xyz)^2, \quad (6.93)$$

and

$$c(x, y, z) = 0.2(5 + 0.2x + 0.4y + 0.6z + 0.1xy + 0.2yz + 0.3zx + 0.7xyz)^2, \quad (6.94)$$

respectively. Figure 6.12 illustrates the iso-surfaces of the three dimensional variation of the thermal conductivity. The BEM mesh and the boundary conditions are shown in Figure 6.13.

The initial temperature of the cube is kept as zero. The mixed boundary conditions at the six faces of the cube are prescribed as follows

$$\begin{aligned}
 \phi(0, y, z) &= 0 \\
 \bar{q}(1, y, z) = -k(1, y, z) \frac{\partial \phi(x, y, z)}{\partial x} &= -0.2zy(25 + 2y + 3z + zy) \\
 \phi(x, 0, z) &= 0 \\
 \bar{q}(x, 1, z) = -k(x, 1, z) \frac{\partial \phi(x, y, z)}{\partial y} &= -0.1xz(50 + 2x + 6z + 3xz) \\
 \phi(x, y, 0) &= 0 \\
 \bar{q}(x, y, 1) = -k(x, y, 1) \frac{\partial \phi(x, y, z)}{\partial z} &= -0.1xy(50 + 2x + 4y + xy).
 \end{aligned} \tag{6.95}$$

The cube is discretized with 294 nodes and 108 quadratic triangular elements. For validation purposes, the BEM result is compared with the finite element simulation performed by the commercially available software ABAQUS. In the FEM simulation 4961 nodes and 1000 20-noded brick elements were used. The temperatures at (1, 1, 1) and (0.5, 1, 0.5) (center of the $Y = 1$ plane) are plotted against time and compared in Figure 6.14. The results show good agreement. Note that the point of interest at (1, 1, 1) is a corner node with Neumann boundary condition in all three associated planes and only 3 elements are used in each directions in the cube. Flux values at (0.5, 0, 0.5) (center of the $X = 0$ plane) are plotted against time and compared with the corresponding FEM solution in Figure 6.15. These results are also in very good agreement.

In general, conventional FEM software (including ABAQUS [1]) use homogeneous elements with constant material properties at the element level. In order to incorporate the functional variation of the material at the finite element level, a user subroutine UMATHT [172] was developed for ABAQUS [1]. By means of this subroutine, functional variations of thermal conductivity and specific heat can be included within an element by sampling the material property at each Gauss point. Graded elements approximate the material gradient better than conventional homogeneous elements and provide a smoother transition at element boundaries. Further investigations on graded elements can be found in the papers by Santare and Lambros [148] and Kim and Paulino [99] for 2D problems, and in the paper by Walters *et al.*[180] for 3D problems.

6.6.2 Rotor problem

The last numerical example is an FGM rotor with eight mounting holes having an eight-fold symmetry. Due to the symmetry, only one-eighth of the rotor is analysed. The top view of the rotor, the analysis region, and the geometry of the region are illustrated in Figure 6.16. The grading direction for the rotor is parallel to its line of symmetry, which is taken as the z -axis. The thermal conductivity and the specific heat for the rotor vary quadratically according to,

$$k(z) = 20(1 + 420.7z)^2, \quad (6.96)$$

and

$$c(z) = 5(1 + 420.7z)^2, \quad (6.97)$$

respectively.

The profile of the thermal conductivity $k(z)$ and the specific heat $c(z)$ of the variations are illustrated in Figure 6.17. The temperature is specified along the inner radius as $T_{inner} = 20 + 1.25 \times 10^6(z - 0.01)^2$ and outer radius as $T_{outer} = 150 + 1.25 \times 10^6(z - 0.01)^2$. A uniform heat flux of 5×10^5 is added on the bottom surface where $z = 0$, and all the other surfaces are insulated. The BEM mesh employs 1584 elements and 3492 nodes. A schematic for the thermal boundary conditions and the BEM mesh employed is shown in Figure 6.18. Here the solution of the problem is verified with the commercially available software ABAQUS using the user-defined subroutine UMATHT of reference [172]. The FEM mesh consists of 7600 20-noded brick elements (quadratic) and 35,514 nodes. The mesh discretization is summarized in Table 6.2.

Table 6.2: Mesh discretization by means of BEM and FEM for the rotor problem.

Method	Nodes	Elements	Element type
BEM	3,492	1,584	T6
FEM	35,514	7,600	B20

The FEM mesh is shown in Figure 6.19, which is intended simply to provide a reference solution against which the BEM results can be compared to. The temperature along the radial direction at the straight edge located at $z = 0.01$ is plotted and compared with the FEM results at different times in Figure 6.20. Figure 6.21 shows the comparison of the BEM and FEM results for the temperature around the hole at different times. Contour plots of the temperature distribution at different time levels are shown in Figure 6.22. The radial heat flux at the right interior corner is plotted at various times in Figure 6.23. All the results

obtained with BEM and the FEM are in good agreement.

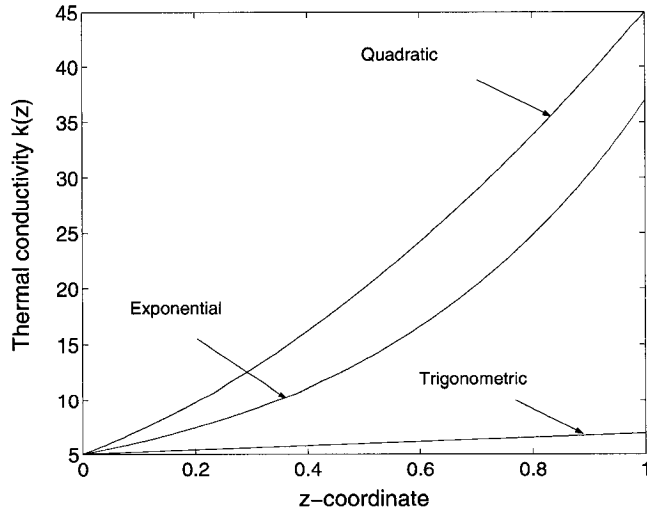


Figure 6.6: Thermal conductivity variation along the z direction. The quadratic variation is $k(z) = 5(1 + 2z)^2$, the exponential variation is $k(z) = 5e^{2z}$ and the trigonometric variation is $k(z) = 5[\cos(0.2z) + 2\sin(0.2z)]^2$.

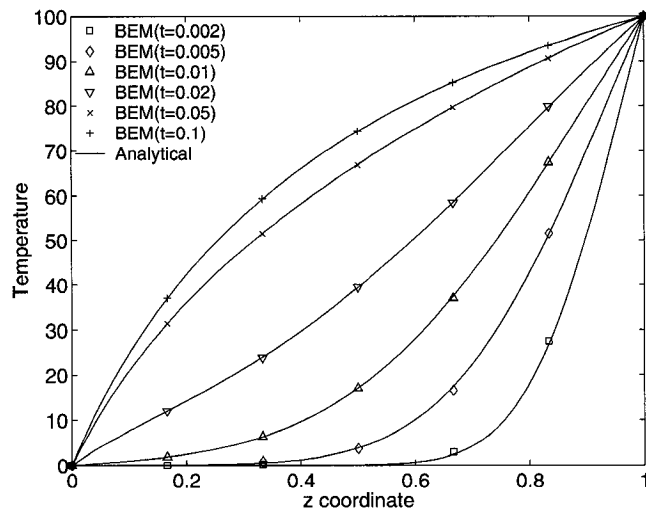


Figure 6.7: Temperature profile in the z direction for different time levels for the FGM cube problem with quadratic material variation.

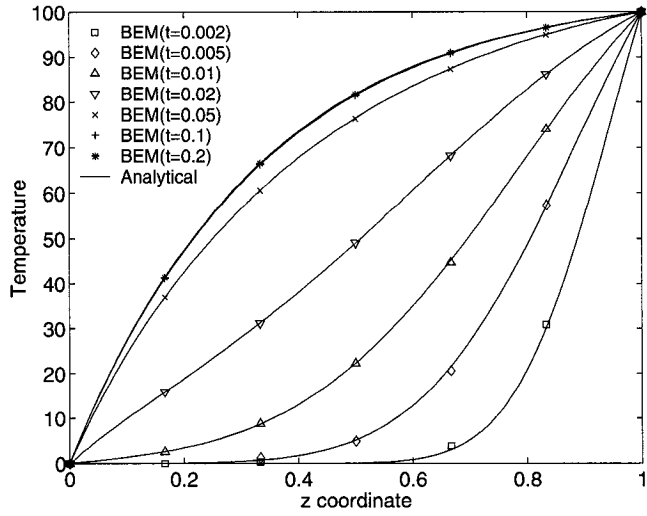


Figure 6.8: Temperature profile in the z direction for different time levels for the FGM cube problem with exponential material variation.

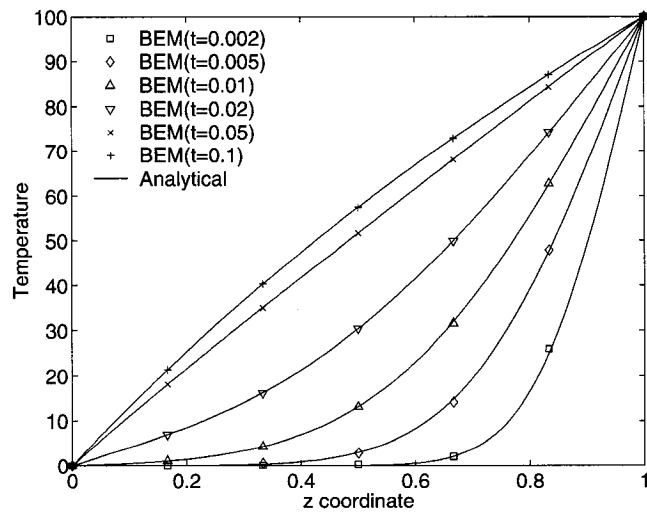


Figure 6.9: Temperature profile in the z direction for different time levels for the FGM cube problem with trigonometric material variation.

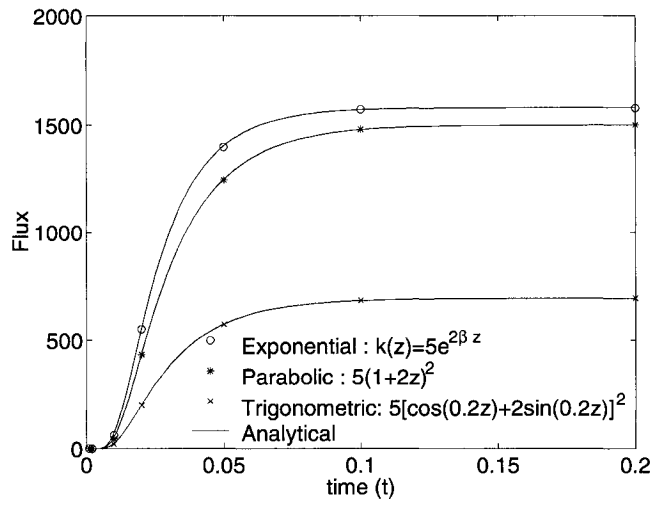


Figure 6.10: Variation of flux at $z = 0$ surface with time for the three variations.

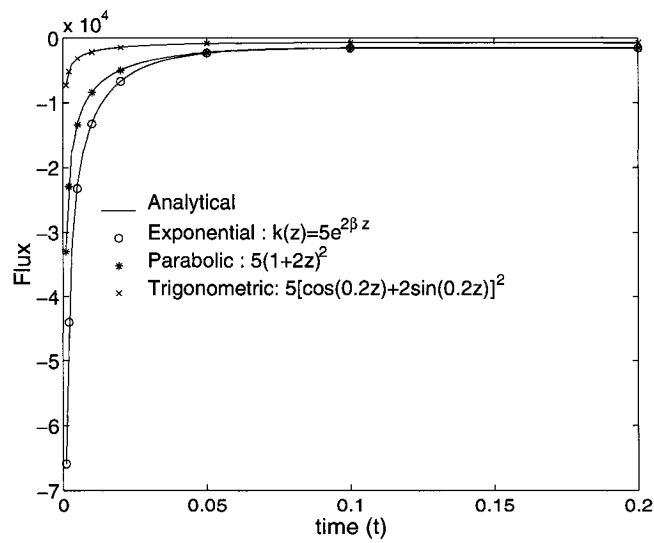


Figure 6.11: Variation of flux at $z = 1$ surface with time for three types of material gradation.

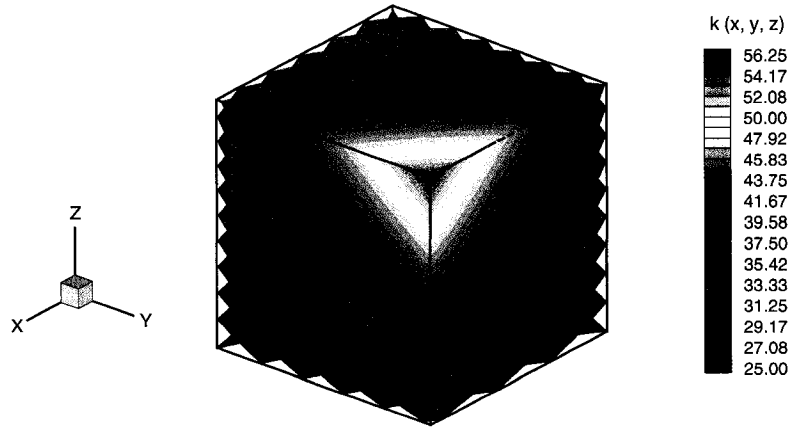


Figure 6.12: Representation of iso-surfaces for the three dimensional variation of thermal conductivity $k \equiv k(x, y, z)$.

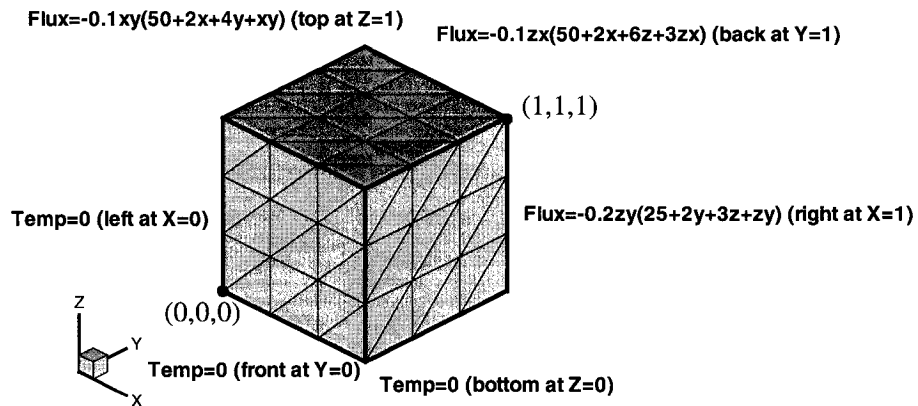


Figure 6.13: The geometry, boundary conditions and the BEM mesh of the FGM unit cube problem with 3D material variation.

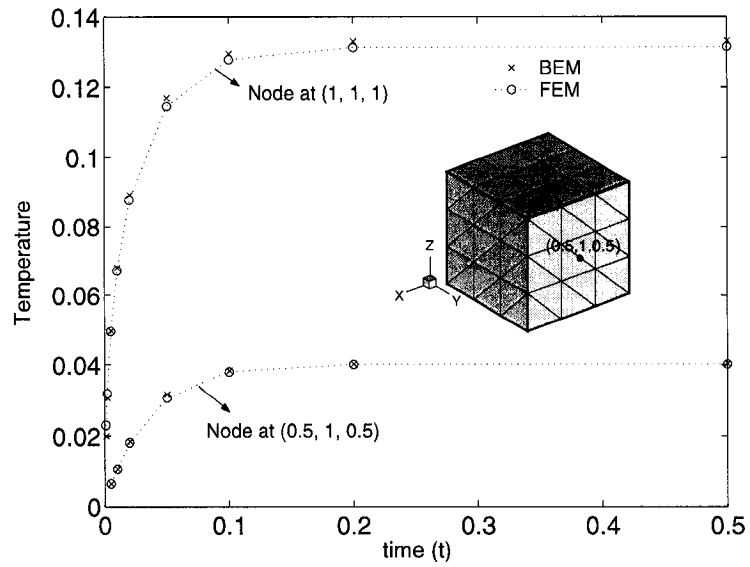


Figure 6.14: Variation of temperature with time at (1, 1, 1) and (0.5, 1, 0.5).

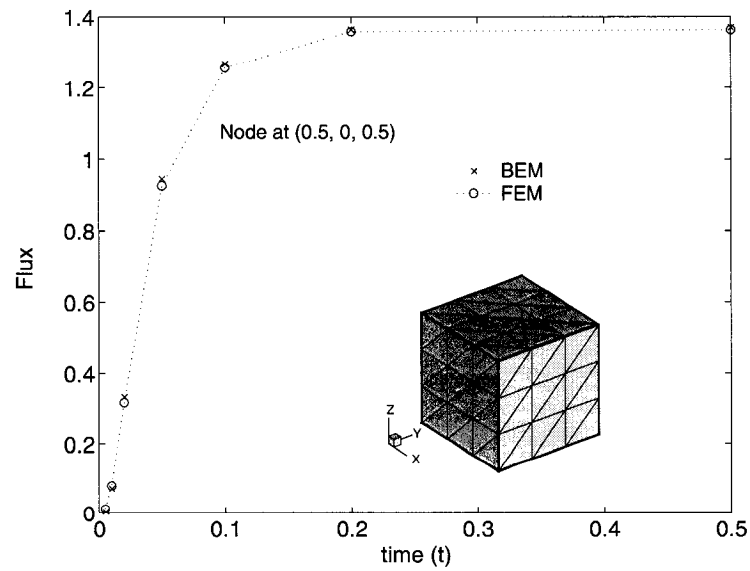


Figure 6.15: Variation of flux with time at (0.5, 0, 0.5).

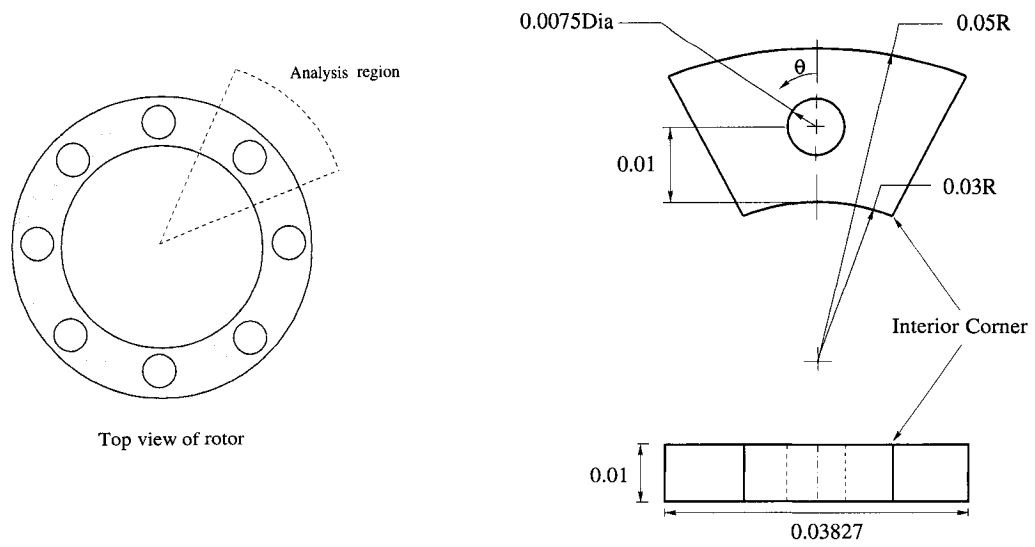


Figure 6.16: Geometry of the functionally graded rotor with 8-fold symmetry.

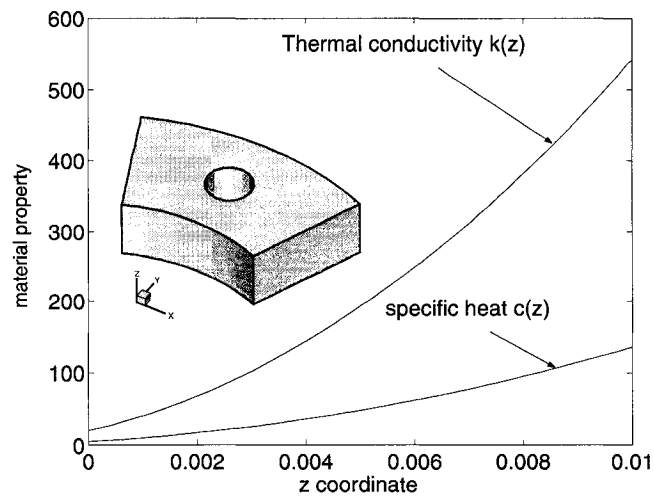


Figure 6.17: Profile of thermal conductivity and specific heat along z direction. The quadratic variation of the thermal conductivity and specific heat are $k(z) = 20(1 + 420.7z)^2$ and $c(z) = 5(1 + 420.7z)^2$, respectively.

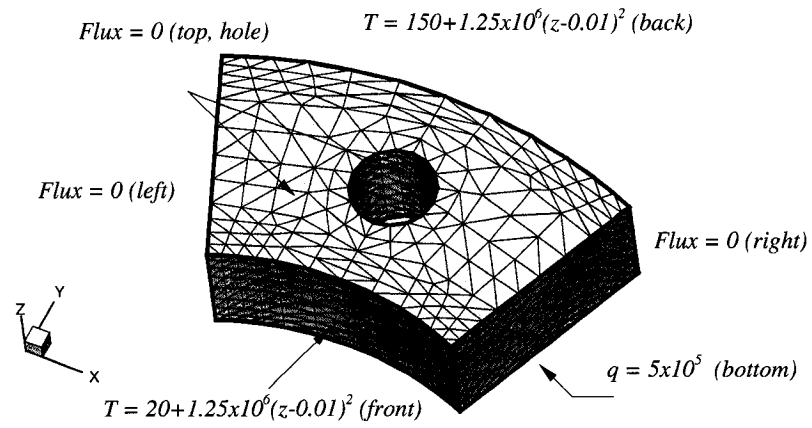


Figure 6.18: Thermal boundary conditions and the BEM mesh on the rotor.

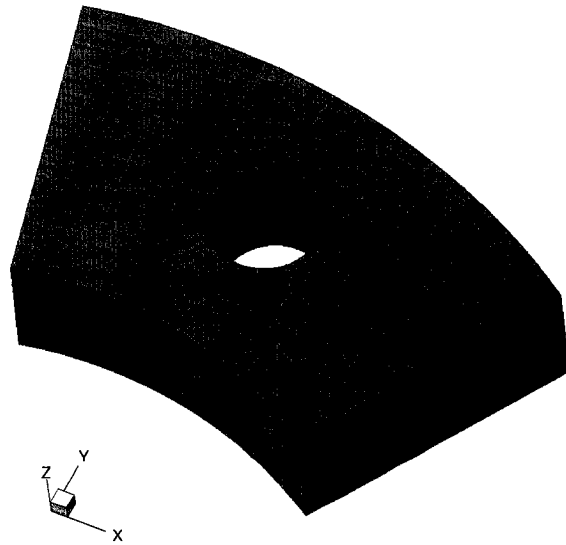


Figure 6.19: The FEM mesh with 7600 20-noded brick elements and 35514 nodes.

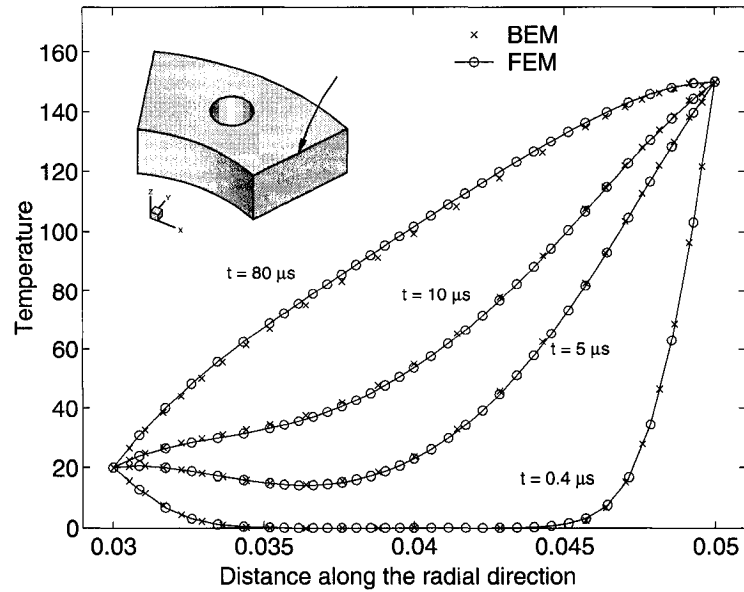


Figure 6.20: Temperature distribution along the right top edge (indicated by the arrow).

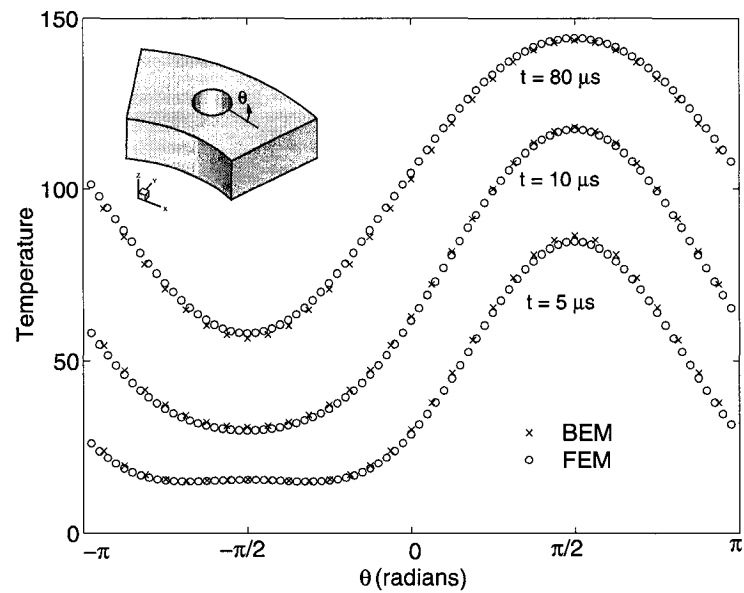


Figure 6.21: Temperature distribution along the circular contour around the hole on the top face.

6.7 Concluding Remarks

By means of a simple variable transformation, transient heat conduction problems in functionally graded materials for three different classes of material variation (quadratic, exponen-

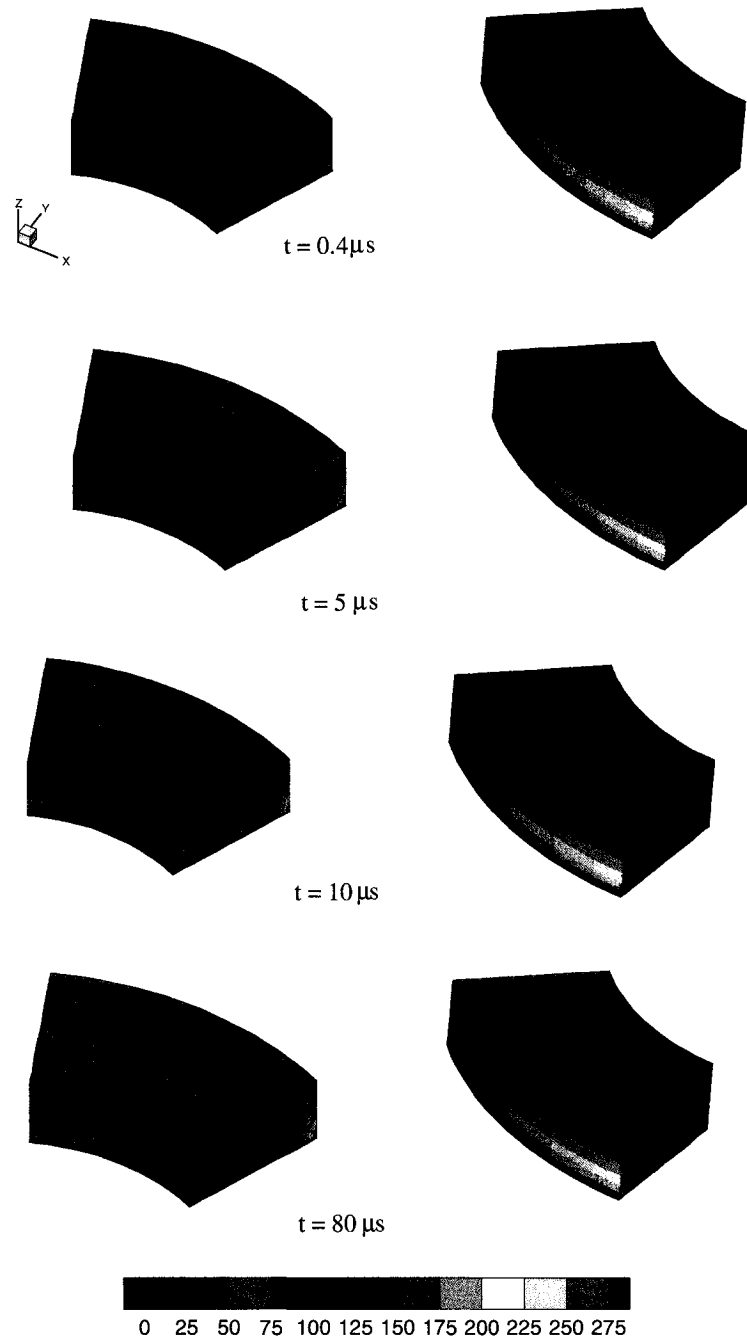


Figure 6.22: BEM contour plot of the temperature of the rotor at different time levels.

tial, trigonometric) can be transformed into the homogeneous diffusion problem. Moreover, the material variation can be in one, two or three dimensions. With easy changes in an existing BEM code for homogeneous materials, the FGM transient heat conduction problem

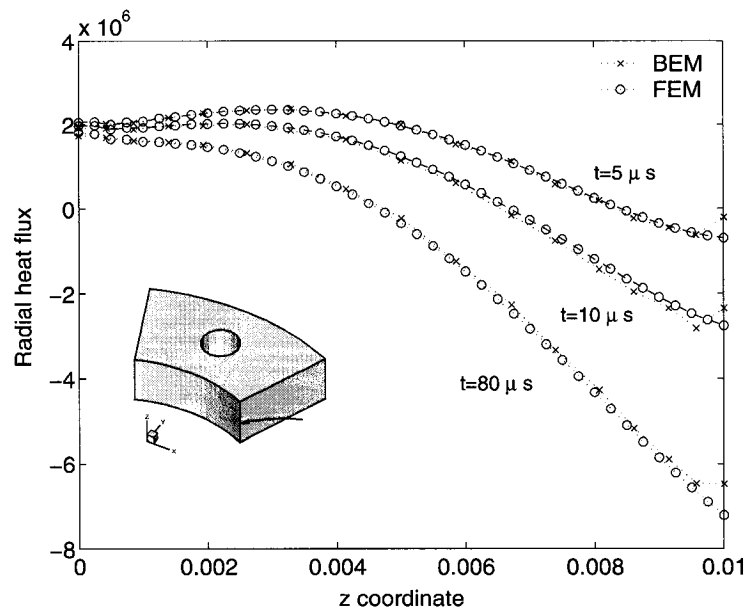


Figure 6.23: Radial heat flux along the interior edge (indicated by the arrow).

with constant diffusivity can be solved. A Laplace transform Galerkin BEM formulation has been presented in order to implement the methodology, however, the idea is also applicable to collocation BEM, symmetric Galerkin BEM or meshless BEM. The results of the present BEM numerical simulations show excellent agreement with analytical solutions and FEM simulations. The numerical inversion of the Laplace transform using Stehfest algorithm yield accurate results.

Chapter 7

Simple BEM for multiple cracks in FGMs

The simple boundary element method consists of recycling existing codes for homogeneous media to solve problems in nonhomogeneous media while maintaining a purely boundary-only formulation. Within this scope, this chapter presents a “simple” Galerkin boundary element method for multiple cracks in problems governed by potential theory in functionally graded media. Steady state heat conduction is investigated for thermal conductivity varying either parabolically, exponentially, or trigonometrically in one or more coordinates. A three dimensional implementation which merges the dual boundary integral equation technique with the Galerkin approach is presented. Special emphasis is given to the treatment of crack surfaces and boundary conditions. The test examples simulated with the present method are verified with finite element results using graded finite elements. The numerical examples demonstrate the accuracy and efficiency of the present method especially when multiple interacting cracks are involved.

The chapter is organized as follows. Section 7.1 gives a brief introduction on crack problems in BEM for nonhomogeneous media. The simple BEM concept is presented in Section 7.2. Section 7.3 describes the fracture algorithm for crack analysis. It is shown that the standard displacement discontinuity approach is not suitable to solve the fracture problem using the “simple BEM”, and thus the dual BIE approach is used to circumvent this situation. Section 7.4 briefly discusses various aspects of the numerical implementation including treatment of boundary conditions, singularity, and corners. Section 7.5 demonstrates, by means of numerical examples, that the methodology works and is efficient. Section 7.6 contains some concluding remarks.

7.1 Introduction

Fracture geometries arise in important technological applications in which the governing relation is governed by potential theory. Modeling of subsurface flow often deal with fractures in the rock [121, 152, 149] or soil systems having embedded thin layers of different permeability [169]. Simulation of an electroplating process provides an important industrial application [70, 72]. Moreover, moving boundary problems, such as crack propagation, is an area in which the boundary element method (BEM) is best suited. Remeshing an evolving geometry for crack propagation problems is much simpler with boundary element analysis than with a domain-based analysis such as the finite element method (FEM), especially if multiple interacting cracks are involved.

In this chapter, crack problems in functionally graded media are investigated. Such media correspond to those in which the volume fraction of the constituents varies gradually leading to a non-uniform microstructure with continuously graded macro properties, e.g. thermal conductivity, density and specific heat. For instance, for problems governed by potential theory, e.g. steady state heat transfer, the thermal conductivity is a function of position, i.e. $k \equiv k(\mathbf{x})$. For further literature regarding functionally graded materials (FGMs), the reader is referred to the books by Suresh and Mortensen [171] and Miyamoto *et al.*[122], to the special issue of the Materials Science and Engineering journal which contains papers from the German Priority Programme (FGMs) [91], and to the review chapter by Paulino *et al.*[138].

This chapter describes a “simple BEM” for crack geometries which merges the dual boundary integral equation approach with the Galerkin approximation. In the BEM literature, most implementations have been developed for non-crack problems in nonhomogeneous media. In the context of BEM, problems of potential in nonhomogeneous media have been previously studied by Cheng [34, 35], Ang *et al.*[5], Shaw and Makris [156], Shaw [154], Harrouni *et al.*[83, 84], Divo and Kassab [50, 48], Bansal and Pindera [6] and recently by Gray *et al.*[75] and Dumont *et al.*[55]. The majority of these works have emphasized on obtaining the Green’s function.

In recent years, the Galerkin boundary element method (GBEM) has emerged as a powerful numerical method in computational mechanics [13]. To solve crack problems by the collocation BEM, higher order interpolation using Hermite element or Overhauser element, which possesses C^1 smoothness, is required [79]. For three dimensional implementations, such higher order elements involve tremendous complexity. An alternative approach consists of using non-conforming elements. Unlike collocation, the Galerkin formulation does not require C^1 interpolation. The Galerkin formulation involves an additional integration over the

boundary, that balances out the extra derivative in the hypersingular equation, and thus a C^0 interpolation suffices [71]. Moreover, this technique allows a natural treatment of corners [137] as discussed later on this chapter.

Recently, Sutradhar and Paulino [172] presented a *transformation approach*, called the “simple BEM,” for potential theory problems in nonhomogeneous media where nonhomogeneous problems are transformed into known problems in homogeneous media. The method leads to a pure boundary-only formulation. This idea has been successfully implemented in three dimensions for steady state [172] and also for transient heat conduction [173] problems where the material property varies in one, two and three dimensions. However, no crack problems were addressed in previous works. Thus, the present work extends the simple BEM concept for multiple interacting crack problems governed by potential theory.

7.2 On the simple BEM concept

The idea of the “simple BEM” consists of transforming problems in nonhomogeneous media to known problems in homogeneous media such that existing codes for homogeneous media can be recycled with simple modifications. By means of the variable transformation approach, which consists of simple changes in the boundary conditions of existing homogeneous heat conduction computer codes, the solutions for nonhomogeneous media with quadratic, exponential and trigonometric material variations can be readily obtained.

7.2.1 Governing Equation

For problems governed by potential theory, the governing differential equation for a potential function ϕ defined on a region Ω bounded by a surface Γ , with an outward normal \mathbf{n} (see Figure 7.1), can be written as

$$\nabla \cdot (k(x, y, z) \nabla \phi) = 0 \quad (7.1)$$

where $k(x, y, z)$ is a position-dependent material function and the dot represents the inner product. Equation (7.1) is the field equation for a wide range of problems in physics and engineering such as heat transfer, fluid flow motion, flow in porous media, electrostatics and magnetostatics [96]. The boundary conditions of the problem can be of the Dirichlet or Neumann type:

$$\phi = \bar{\phi} \quad \text{on } \Gamma_1 \quad (7.2)$$

$$q = -k(x, y, z) \frac{\partial \bar{\phi}}{\partial \mathbf{n}} = \bar{q} \quad \text{on } \Gamma_2 \quad (7.3)$$

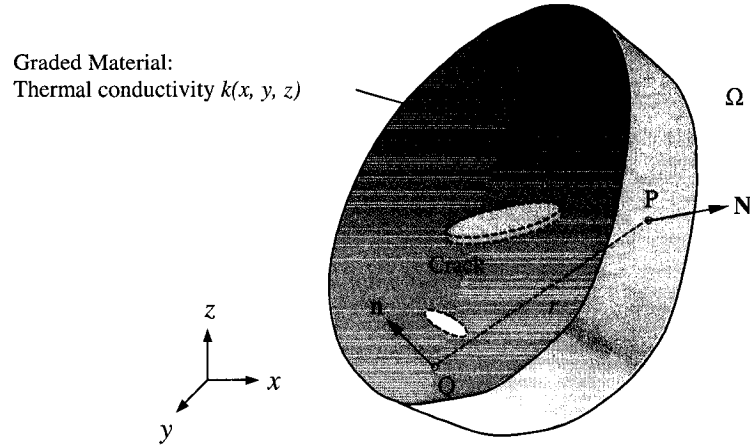


Figure 7.1: Definition of the boundary value problem with boundary Γ (including crack surfaces and outer boundary) and interior domain Ω .

respectively, with $\Gamma = \Gamma_1 + \Gamma_2$ for a well-posed problem. The boundary value problem is a Dirichlet problem if the potential is known on the whole boundary, whereas it is a Neumann problem if the flux is known on the whole boundary. Mixed boundary conditions are also frequently encountered: flux is prescribed over some portion of the boundary and potential is prescribed over the complementary portion of the boundary [172]. Handling of all those boundary conditions in the context of the “simple BEM” is described in Section 7.2.3.

7.2.2 Variable Transformation Approach

By defining the variable [65]

$$v(x, y, z) = \sqrt{k(x, y, z)} \phi(x, y, z), \quad (7.4)$$

one rewrites Eq. (7.1) as

$$\nabla^2 v + \left(\frac{\nabla k \cdot \nabla k}{4k^2} - \frac{\nabla^2 k}{2k} \right) v = 0 \quad (7.5)$$

or, alternatively

$$\nabla^2 v + k'(x, y, z)v = 0 \quad (7.6)$$

where

$$k' = \frac{\nabla k \cdot \nabla k}{4k^2} - \frac{\nabla^2 k}{2k}. \quad (7.7)$$

By setting $k'(x, y, z) = 0, +\beta^2$ and $-\beta^2$, three classical homogeneous equations namely, the Laplace, standard Helmholtz and the modified Helmholtz can be obtained, respectively. From these cases, a family of variations of $k(x, y, z)$ can be generated, as shown in Table 7.1.

Table 7.1: Family of material variations: transformation approach

k'	Equation	Material variation	$k(x, y, z)$
0	Laplace: $\nabla^2 v = 0$	Quadratic	$k_0(a_1 + a_2 x)^2(b_1 + b_2 y)^2(c_1 + c_2 z)^2$
β^2	Helmholtz: $\nabla^2 v + \beta^2 v = 0$	Trigonometric	$k_0(a_1 \cos \alpha x + a_2 \sin \alpha x)^2(b_1 \cos \mu y + b_2 \sin \mu y)^2$ $\times (c_1 \cos \gamma z + c_2 \sin \gamma z)^2$
$-\beta^2$	Modified Helmholtz: $\nabla^2 v - \beta^2 v = 0$	Exponential	$k_0(a_1 e^{\alpha x} + a_2 e^{-\alpha x})^2(b_1 e^{\mu y} + b_2 e^{-\mu y})^2$ $\times (c_1 e^{\gamma z} + c_2 e^{-\gamma z})^2$

In this paper we focus on variations which depend only on one cartesian coordinate, namely z . From an engineering point of view (for applications such as FGMs), material variation in one coordinate is of practical importance as described in references [138, 101].

7.2.3 Boundary conditions

In order to solve the boundary value problem based on the modified variable v , the boundary conditions of the original problem have to be incorporated in the modified boundary value problem. Thus for the modified problem, the Dirichlet and the Neumann boundary conditions given by Eq. (7.2) and Eq. (7.3) respectively, change as follows:

$$v = \sqrt{k} \bar{\phi} \quad \text{on } \Gamma_1 \quad (7.8)$$

$$\frac{\partial v}{\partial \mathbf{n}} = \frac{1}{2k} \frac{\partial k}{\partial \mathbf{n}} v - \frac{\bar{q}}{\sqrt{k}} \quad \text{on } \Gamma_2 \quad (7.9)$$

Notice that the Dirichlet boundary condition of the original problem is affected by the factor \sqrt{k} . Moreover, the Neumann boundary condition of the original problem changes to a mixed boundary condition (Robin boundary condition). This later modification is the only major change on the boundary value problem.

Another common boundary condition of the original problem is a prescribed relationship between the potential and the flux (e.g. convective heat transfer problems) i.e. Robin type:

$$q = \lambda_1 \phi + \lambda_2 \quad (7.10)$$

The corresponding boundary condition for the modified problem is also a Robin boundary

condition, which is given by

$$\frac{\partial v}{\partial \mathbf{n}} = \left(\frac{1}{2k} \frac{\partial k}{\partial \mathbf{n}} - \lambda_1 \right) v - \frac{\lambda_2}{\sqrt{k}} \quad (7.11)$$

7.3 Crack Analysis

Consider a body of arbitrary shape which contains a crack, as shown in Figure 7.2. The boundary Γ of the body B is composed of non-crack boundary Γ_b and the crack surface Γ_c . The portion of the boundary Γ_b with prescribed potential is denoted by $\Gamma_{b(\phi)}$, and the portion with prescribed flux boundary is denoted by $\Gamma_{b(q)}$. The crack surface Γ_c consists of two coincident surfaces Γ_c^+ and Γ_c^- , representing the upper and lower crack surfaces respectively. The outward normals to the crack surfaces, designated by n_c^+ and n_c^- are oriented in opposite directions and at any point on the crack surfaces, $n_c^- = -n_c^+$ (see Figure 7.2). The dual equation Galerkin approximation for a fracture geometry can be written in terms of a 3x3 block matrix. Specifically, the first block row will represent the outer, or non-crack, boundary equations, and the equation for a particular node, as per the usual Galerkin procedure, is chosen according to the prescribed boundary data. In accordance with the dual BEM approach [141, 4], the second and third rows will denote, respectively, the hypersingular and standard equations written on the crack surface. With these definitions, the equations take the abbreviated form

$$\begin{pmatrix} h_{11} & h_{12} & h_{13} \\ h_{21} & h_{22} & h_{23} \\ h_{31} & h_{32} & h_{33} \end{pmatrix} \begin{pmatrix} \Omega_1 \\ V_2 \\ V_3 \end{pmatrix} = \begin{pmatrix} g_{11} & g_{12} & g_{13} \\ g_{21} & g_{22} & g_{23} \\ g_{31} & g_{32} & g_{33} \end{pmatrix} \begin{pmatrix} \hat{\Omega}_1 \\ V_2^{\mathbf{n}} \\ V_3^{\mathbf{n}} \end{pmatrix} \quad (7.12)$$

The vector of unknowns on the non-crack boundary can be a mixture of potential and flux, and is therefore denoted by Ω_1 . The corresponding vector of prescribed boundary values is indicated by $\hat{\Omega}_1$. On the fracture, V represents the vector of unknown potential values, $V^{\mathbf{n}}$ the specified flux, and the subscripts $\{2, 3\}$ label the two sides of the crack. The matrix \mathcal{H} on the left therefore multiplies the vector of unknowns, and the right hand side consists of known quantities.

7.3.1 Displacement discontinuity approach

The displacement discontinuity approach has been extensively used to solve fracture problems [41, 42]. Notice that, the only difference between the two coincident crack surfaces is the orientation of the normals ($n_c^- = -n_c^+$) and, as a result, $h_{13} = -h_{12}$ and $h_{23} = -h_{22}$.

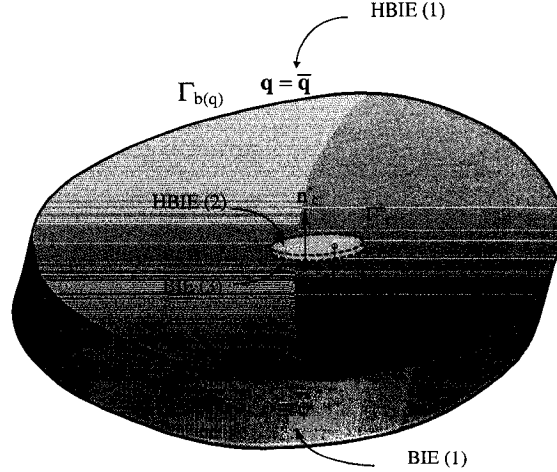


Figure 7.2: Fracture scheme using the dual BEM approach.

These relationships between the second and third columns are a consequence of the integration over the two sides of the fracture differing by a sign. The usual boundary condition is the derivative quantity (e.g. flux, traction) and thus only the hypersingular equation should be employed.

$$\left(\begin{array}{cc|c} h_{11} & h_{12} & -h_{12} \\ h_{21} & h_{22} & -h_{22} \\ h_{31} & h_{32} & -h_{32} \end{array} \right) \begin{pmatrix} \Omega_1 \\ V_2 \\ V_3 \end{pmatrix} = \left(\begin{array}{cc|c} g_{11} & g_{12} & g_{12} \\ g_{21} & g_{22} & g_{22} \\ g_{31} & g_{32} & g_{32} \end{array} \right) \begin{pmatrix} \hat{\Omega}_1 \\ V_2^n \\ V_3^n \end{pmatrix} \quad (7.13)$$

It is convenient to replace the potential V_2 and V_3 by a single jump in potential

$$\Delta V = V_2 - V_3$$

Similarly on the right-hand side the flux V_2^n and V_3^n is replaced by the flux summation

$$\Sigma V^n = V_2^n + V_3^n$$

Thus the system of equations can be rewritten as

$$\left(\begin{array}{cc|c} h_{11} & h_{12} & 0 \\ h_{21} & h_{22} & 0 \\ h_{31} & h_{32} & 0 \end{array} \right) \begin{pmatrix} \Omega_1 \\ \Delta V \\ 0 \end{pmatrix} = \left(\begin{array}{cc|c} g_{11} & g_{12} & 0 \\ g_{21} & g_{22} & 0 \\ g_{31} & g_{32} & 0 \end{array} \right) \begin{pmatrix} \hat{\Omega}_1 \\ \Sigma V^n \\ 0 \end{pmatrix} \quad (7.14)$$

It therefore suffices to solve the smaller 2×2 block system for the unknowns $(\Omega_1, \Delta V)$.

In the simple BEM approach, as explained earlier, the boundary conditions of the origi-

nal problem have to be incorporated in the modified boundary value problem. As shown in Section 7.2.3, the Neumann boundary condition of the original problem changes to a Robin boundary condition. Typically the crack surfaces are subjected to Neumann boundary conditions. If the known flux on the two crack surfaces is denoted by \bar{q}_2 and \bar{q}_3 then, according to Eq. (7.9), ΣV^n in Eq. (7.14) changes to

$$\Sigma V^n = \frac{1}{2k} \frac{\partial k}{\partial \mathbf{n}} (V_2 + V_3) - \frac{\bar{q}_2 + \bar{q}_3}{\sqrt{k}} \quad (7.15)$$

Therefore Eq. (7.14) is rewritten as

$$\left(\begin{array}{cc|c} h_{11} & h_{12} & 0 \\ h_{21} & h_{22} & 0 \\ h_{31} & h_{32} & 0 \end{array} \right) \left(\begin{array}{c} \Omega_1 \\ V_2 - V_3 \\ 0 \end{array} \right) = \left(\begin{array}{cc|c} g_{11} & g_{12} & 0 \\ g_{21} & g_{22} & 0 \\ g_{31} & g_{32} & 0 \end{array} \right) \left(\begin{array}{c} \hat{\Omega}_1 \\ \frac{1}{2k} \frac{\partial k}{\partial \mathbf{n}} (V_2 + V_3) - \frac{\bar{q}_2 + \bar{q}_3}{\sqrt{k}} \\ 0 \end{array} \right) \quad (7.16)$$

Due to this change in the system of equations it is apparent from Eq. (7.16) that the unknown variable can no longer be the jump in potential $\Delta V = V_2 - V_3$. As a result, the standard displacement discontinuity approach is not directly suitable as a fracture algorithm for the simple BEM technique.

7.3.2 The Dual BEM approach

The Dual BEM approach is the method of choice to solve fracture problems in this work. In this technique, Eq. (7.13) is used after modifying the boundary conditions. This is suitable for problems in potential because for these problems the variable of interest is the potential distribution on the crack surfaces. In the Dual BEM approach, the potentials are calculated directly during the solution process. On the contrary, in the displacement discontinuity approach, the variable that is obtained from the system of equations is the jump in potential. As a consequence, postprocessing and assembling the h_{31} and h_{32} are required. The system of equations (before incorporating the treatment of boundary conditions) is

$$\left(\begin{array}{ccc} h_{11} & h_{12} & -h_{12} \\ h_{21} & h_{22} & -h_{22} \\ h_{31} & h_{32} & -h_{32} \end{array} \right) \left(\begin{array}{c} \Omega_1 \\ V_2 \\ V_3 \end{array} \right) = \left(\begin{array}{ccc} g_{11} & g_{12} & g_{12} \\ g_{21} & g_{22} & g_{22} \\ g_{31} & g_{32} & g_{32} \end{array} \right) \left(\begin{array}{c} \hat{\Omega}_1 \\ V_2^n \\ V_3^n \end{array} \right) \quad (7.17)$$

Note the relationship between the columns 2 and 3 of the matrix. As a result, only the upper (or lower) crack surface needs to be discretized and corresponding kernels need to be calculated. Finally, during the solution phase, the system of equations is assembled by

including the kernels corresponding to the other crack surface.

Remark. Note that, for the non-crack boundary the BIE can be employed instead of the HBIE. The reason behind choosing the HBIE over the BIE is that the present code is written in such a way that while solving homogeneous problems the code works as a symmetric Galerkin BEM [13] for which the HBIE is applied to the surface with Neumann boundary conditions.

7.4 Numerical Implementation

Numerical implementation for specific cases using the variations of $k(x, y, z)$ in one coordinate are presented. In the present paper only parabolic k -variation has been considered although exponential and trigonometric material variation can be dealt with in similar fashion [172]. The numerical methods employed in the current work use Galerkin techniques for the BIE and HBIEs. A brief discussion of these techniques in the context of the BEM is presented below. It also includes the development of the Galerkin boundary conditions, selection of the boundary element type, treatment of singular integrals and corners.

7.4.1 Galerkin Boundary Integral Equation.

Define the collocation BIE as

$$\mathcal{B}(P) \equiv v(P) + \int_{\Sigma} \left(\frac{\partial}{\partial \mathbf{n}} G(P, Q) \right) v(Q) dQ - \int_{\Sigma} G(P, Q) \frac{\partial v}{\partial \mathbf{n}}(Q) dQ \quad (7.18)$$

and thus for an exact solution $\mathcal{B}(P) \equiv 0$.

In a Galerkin approximation, these shape functions are employed as weighting functions for enforcing the integral equations, and Eq. (7.18) takes the form (see Figure 7.3)

$$\int_{\Sigma} \psi_k(P) \mathcal{B}(P) dP = 0 \quad (7.19)$$

7.4.2 Galerkin Hypersingular Boundary Integral Equation.

The hypersingular boundary integral equation for the Laplace equation $\nabla^2 v = 0$ is an expression for the surface flux $\partial v / \partial \mathbf{n} = \nabla v \cdot \mathbf{n}$, usually written in the form

$$\frac{\partial v}{\partial \mathbf{N}}(P) + \int_{\Sigma} v(Q) \frac{\partial^2 G}{\partial \mathbf{N} \partial \mathbf{n}}(P, Q) dQ - \int_{\Sigma} \frac{\partial G}{\partial \mathbf{N}}(P, Q) \frac{\partial v}{\partial \mathbf{n}}(Q) dQ = 0. \quad (7.20)$$

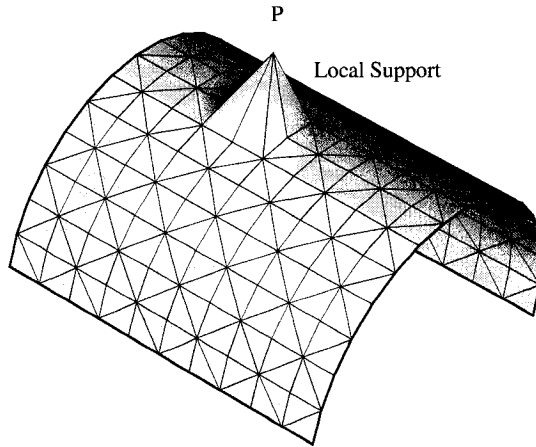


Figure 7.3: Local support for the Galerkin BEM.

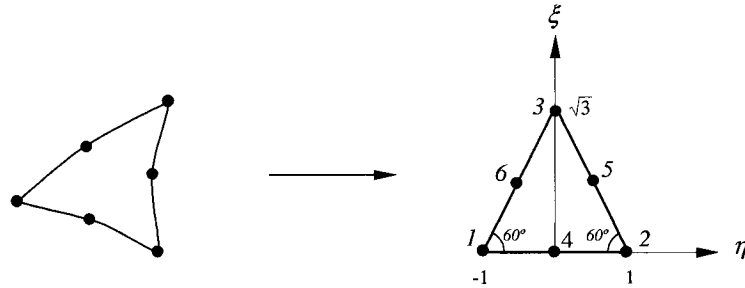


Figure 7.4: A triangle in the 3D space is mapped to an equilateral triangular quadratic element in $\{\eta, \xi\}$ space.

Here $\mathbf{n} = \mathbf{n}(Q)$, $\mathbf{N} = \mathbf{N}(P)$ denote the unit outward normal on the boundary surface Σ , and P and Q are points on Σ (see Figure 7.1). The fundamental solution $G(P, Q)$ is usually taken as the point source potential (for homogeneous media):

$$G(P, Q) = \frac{1}{4\pi r}, \quad (7.21)$$

where $\mathbf{R} = \mathbf{Q} - \mathbf{P}$ and $r = \|\mathbf{R}\|$ is the distance between points P and Q . The hypersingular kernel is therefore given by

$$\frac{\partial^2 G}{\partial \mathbf{N} \partial \mathbf{n}}(P, Q) = \frac{1}{4\pi} \left(\frac{\mathbf{n} \cdot \mathbf{N}}{r^3} - 3 \frac{(\mathbf{n} \cdot \mathbf{R})(\mathbf{N} \cdot \mathbf{R})}{r^5} \right). \quad (7.22)$$

It is important to note that Eq. (7.20) is formally obtained by differentiating the standard BIE for surface potential, and then interchanging the derivative with the integral. As there are no singularities, the interchange is permitted, and the limit as P returns to the boundary can then be considered. This limit process will be employed below. A side benefit of the direct limit procedure is that, if the limit is taken with the source point P approaching the boundary from *outside* the domain, then the ‘free term’ $\partial v(P)/\partial \mathbf{N}$ from Eq. (7.20) is not present. Define the hypersingular BIE (flux BIE) as

$$\mathcal{F}(P) \equiv \int_{\Sigma} v(Q) \frac{\partial^2 G}{\partial \mathbf{N} \partial \mathbf{n}}(P, Q) \, dQ - \int_{\Sigma} \frac{\partial G}{\partial \mathbf{N}}(P, Q) \frac{\partial v}{\partial \mathbf{n}}(Q) \, dQ . \quad (7.23)$$

Thus Eq. (7.20) takes the form

$$\mathcal{F}(P) = 0, \quad (7.24)$$

with the free term automatically incorporated in the *exterior limit* evaluation of the second integral in this Eq. (7.23).

Following the Galerkin approximation, the flux BIE, Eq. (7.20), takes the form

$$\int_{\Sigma} \psi_k(P) \mathcal{F}(P) \, dP = 0, \quad (7.25)$$

As a result the Galerkin technique possesses the important property of the *local support* (see Figure 7.3).

7.4.3 Interpolation of physical variables

Following standard practice, the boundary potential and flux are approximated in terms of values at element nodes Q_j and shape functions $\psi_j(Q)$, *i.e.*,

$$v(Q) = \sum_j v(Q_j) \psi_j(Q) \quad (7.26)$$

$$\frac{\partial v}{\partial \mathbf{n}}(Q) = \sum_j \frac{\partial v}{\partial \mathbf{n}}(Q_j) \psi_j(Q) \quad (7.27)$$

Notice that the same shape functions are used to define both potential and flux.

7.4.4 Boundary elements

The surface of the solution domain is divided into a number of connected elements. Over each element, the variation of the geometry and the variables (potential and flux) is approximated

by polynomial functions. Six noded isoparametric quadratic triangular elements are used in the present work (see Figure 7.4).

The geometry of an element can be defined by the coordinates of its six nodes using appropriate quadratic shape functions as follows

$$x_i(\eta, \xi) = \sum_{j=1}^6 N_j(\eta, \xi)(x_i)_j. \quad (7.28)$$

By means of an isoparametric approximation, the same shape functions are used for the solution variables (both potential and flux), as follows:

$$v_i(\eta, \xi) = \sum_{j=1}^6 N_j(\eta, \xi)(v_i)_j, \quad (7.29)$$

$$\frac{\partial v_i}{\partial \mathbf{n}}(\eta, \xi) = \sum_{j=1}^6 N_j(\eta, \xi) \left(\frac{\partial v_i}{\partial \mathbf{n}} \right)_j. \quad (7.30)$$

The shape functions can be explicitly written in terms of intrinsic coordinates ξ and η as (see Figure 7.4):

$$\begin{aligned} N_1(\eta, \xi) &= (\xi + \sqrt{3}\eta - \sqrt{3})(\xi + \sqrt{3}\eta)/6 & N_4(\eta, \xi) &= (\xi + \sqrt{3}\eta - \sqrt{3})(\xi - \sqrt{3}\eta - \sqrt{3})/3 \\ N_2(\eta, \xi) &= (\xi - \sqrt{3}\eta - \sqrt{3})(\xi - \sqrt{3}\eta)/6 & N_5(\eta, \xi) &= -2\xi(\xi - \sqrt{3}\eta - \sqrt{3})/3 \\ N_3(\eta, \xi) &= \xi(2\xi - \sqrt{3})/3 & N_6(\eta, \xi) &= -2\xi(\xi + \sqrt{3}\eta - \sqrt{3})/3 \end{aligned} \quad (7.31)$$

The intrinsic coordinate space is the equilateral triangle with $-1 \leq \eta \leq 1$, $0 \leq \xi \leq \sqrt{3}(1 - |\eta|)$. The range of coordinates has been chosen for the sake of ease of computational implementation when dealing with singular integration [176].

7.4.5 Treatment of boundary conditions

With respect to standard BEM codes the main modification in the implementation of the simple BEM consists of incorporating the boundary conditions for the modified problem. In this section, the necessary modifications are described.

For the sake of illustration, let us assume three nodes, of which node 1 and node 3 have prescribed Neumann boundary condition, and node 2 has prescribed Dirichlet boundary

condition, i.e.,

$$\begin{aligned} \overline{q_1}, \quad \overline{\phi_2}, \quad \overline{q_3} & \text{ known quantities} \\ \phi_1, \quad q_2, \quad \phi_3 & \text{ unknown quantities.} \end{aligned}$$

In the modified boundary value problem the variables are v and $\partial v/\partial \mathbf{n}$ (see Eq. (7.8) and Eq. (7.9), respectively). The system of algebraic equations emerges as,

$$\begin{bmatrix} H_{11} & H_{12} & H_{13} \\ H_{21} & H_{22} & H_{23} \\ H_{31} & H_{32} & H_{33} \end{bmatrix} \begin{Bmatrix} v_1 \\ v_2 \\ v_3 \end{Bmatrix} = \begin{bmatrix} G_{11} & G_{12} & G_{13} \\ G_{21} & G_{22} & G_{23} \\ G_{31} & G_{32} & G_{33} \end{bmatrix} \begin{Bmatrix} \partial v_1/\partial \mathbf{n} \\ \partial v_2/\partial \mathbf{n} \\ \partial v_3/\partial \mathbf{n} \end{Bmatrix}. \quad (7.32)$$

By rearranging the equations so that the unknowns are passed to the left-hand side, we rewrite the linear system as follows

$$\begin{bmatrix} H_{11} & -G_{12} & H_{13} \\ H_{21} & -G_{22} & H_{23} \\ H_{31} & -G_{32} & H_{33} \end{bmatrix} \begin{Bmatrix} v_1 \\ \partial v_2/\partial \mathbf{n} \\ v_3 \end{Bmatrix} = \begin{bmatrix} G_{11} & -H_{12} & G_{13} \\ G_{21} & -H_{22} & G_{23} \\ G_{31} & -H_{32} & G_{33} \end{bmatrix} \begin{Bmatrix} \partial v_1/\partial \mathbf{n} \\ v_2 \\ \partial v_3/\partial \mathbf{n} \end{Bmatrix}. \quad (7.33)$$

Using Eq. (7.8) and Eq. (7.9), we obtain the final form of the system of equations,

$$\begin{bmatrix} \left(H_{11} - \frac{G_{11}}{2k} \frac{\partial k}{\partial \mathbf{n}} \right) & -G_{12} & \left(H_{13} - \frac{G_{13}}{2k} \frac{\partial k}{\partial \mathbf{n}} \right) \\ \left(H_{21} - \frac{G_{21}}{2k} \frac{\partial k}{\partial \mathbf{n}} \right) & -G_{22} & \left(H_{23} - \frac{G_{23}}{2k} \frac{\partial k}{\partial \mathbf{n}} \right) \\ \left(H_{31} - \frac{G_{31}}{2k} \frac{\partial k}{\partial \mathbf{n}} \right) & -G_{32} & \left(H_{33} - \frac{G_{33}}{2k} \frac{\partial k}{\partial \mathbf{n}} \right) \end{bmatrix} \begin{Bmatrix} v_1 \\ \partial v_2/\partial \mathbf{n} \\ v_3 \end{Bmatrix} = \begin{bmatrix} G_{11} & -H_{12} & G_{13} \\ G_{21} & -H_{22} & G_{23} \\ G_{31} & -H_{32} & G_{33} \end{bmatrix} \begin{Bmatrix} -\overline{q_1}/\sqrt{k} \\ \overline{\phi_2}\sqrt{k} \\ -\overline{q_3}/\sqrt{k} \end{Bmatrix}, \quad (7.34)$$

We solve these equations for v_1 , $\partial v_2/\partial \mathbf{n}$, and v_3 ; and finally, by using Eq. (7.8) and Eq. (7.9), we obtain

$$\begin{aligned} \phi_1 & = v_1/\sqrt{k}, \\ q_2 & = -\sqrt{k} \left\{ \frac{\partial v_2}{\partial \mathbf{n}} - \frac{1}{2k} \frac{\partial k}{\partial \mathbf{n}} v_2 \right\}, \\ \phi_3 & = v_3/\sqrt{k}. \end{aligned} \quad (7.35)$$

7.4.6 Singular integrals

In a Galerkin approximation, the integration is carried out with respect to both the field point Q and the source point P (see Figure 7.1). In the numerical implementation, the integrals are evaluated for every pair of elements. Singular integrals take place as the Green's function

and its derivatives diverge when the field point approaches the source point. An integral is therefore singular if the elements are *coincident*, or are *adjacent*, sharing either an edge or a vertex. Thus, for three dimensional problems, there are four typical configurations for the two elements containing the source point P and the field point Q (see Figure 7.5), and thus four distinct situations regarding the singularity must be considered:

- *Non-singular case*, when the source point P and the field point Q lie on distinct elements, that do not share a common vertex or edge.
- *Coincident case*, when the source point P and the field point Q lie in the same element;
- *Edge adjacent case*, when two elements share a common edge; and
- *Vertex adjacent case*, when a vertex is the only common node between the two elements.

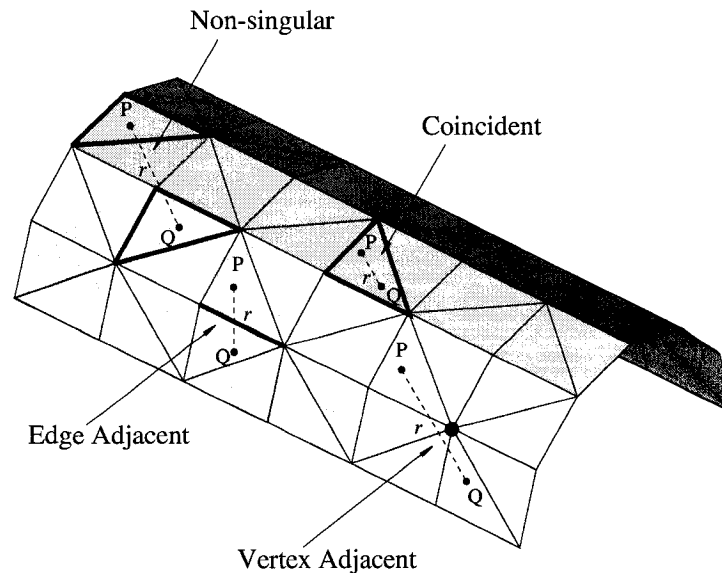


Figure 7.5: Four different cases considered for integration: (a) non-singular; (b) coincident; (c) edge adjacent; and (d) vertex adjacent.

A hybrid analytical/numerical approach using the “limit to the boundary” approach is adopted to treat the singular integrals. The non-singular integrals can be evaluated using standard Gaussian quadrature formulas. In the “limit to the boundary” approach for evaluating the singular integrals, the integrals for the coincident and the edge-adjacent cases are forced to be finite by moving the source P off the boundary in the direction \mathbf{N} at a

distance ϵ . The next step is to employ polar coordinate transformations and then integrate analytically with a *fixed distance from the singularity*. After the exact integration, the limit $\epsilon \rightarrow 0$ is considered. The coincident and the edge-adjacent hypersingular integrals are separately divergent, producing terms of the form $\log(\epsilon)$. However, the divergent terms from the coincident case cancels out with the divergent terms from the edge-adjacent case, and therefore the divergent terms are removed exactly in this approach. Taking the limit $\epsilon \rightarrow 0$ back to the boundary results in finite expressions, thus giving a well behaved integral. Once the divergent terms have been identified and removed, the remaining terms of the integral can be evaluated using standard numerical quadrature. Details of this technique can be found in the papers by Gray *et al.*[74, 73] and Sutradhar *et al.*[176].

7.4.7 Corners

The treatment of corners in the Galerkin BEM is simple and elegant due to the flexibility in choosing the weight function for the Galerkin approximation [137]. Corners are represented by multiple nodes [76], and on each side different weight functions are used (see Figure 7.6) [137]. Figure 7.6 shows an assembly of six planes with different orientation of the normals where, each plane has been prescribed with either Dirichlet or Neumann boundary conditions. Consequently at the intersection of two planes double nodes are applied. For a mixed corner (flux is unknown in one side of the corner, potential is known), a non zero weight function is assigned only on the side where flux is unknown. For a Neumann corner (flux specified on both sides of the corner, potential is the unknown), the weight functions are combined together. On a Dirichlet corner (unknowns are flux on each sides, potential is known) the usual weight functions are assigned on both sides of the corners.

7.5 Numerical Examples

In this section, a number of numerical problems are reported to demonstrate the implementation of the techniques described above. To verify the numerical implementation, the following three examples are presented

- (1) A penny shaped crack inside a cylinder,
- (2) Three parallel penny shaped crack inside a cylinder,
- (3) Multiple random cracks inside a cube with 3D material variation.

The first problem is a penny shaped crack inside a cylinder with constant temperature on two sides and insulated on the wall. The material property varies quadratically only in

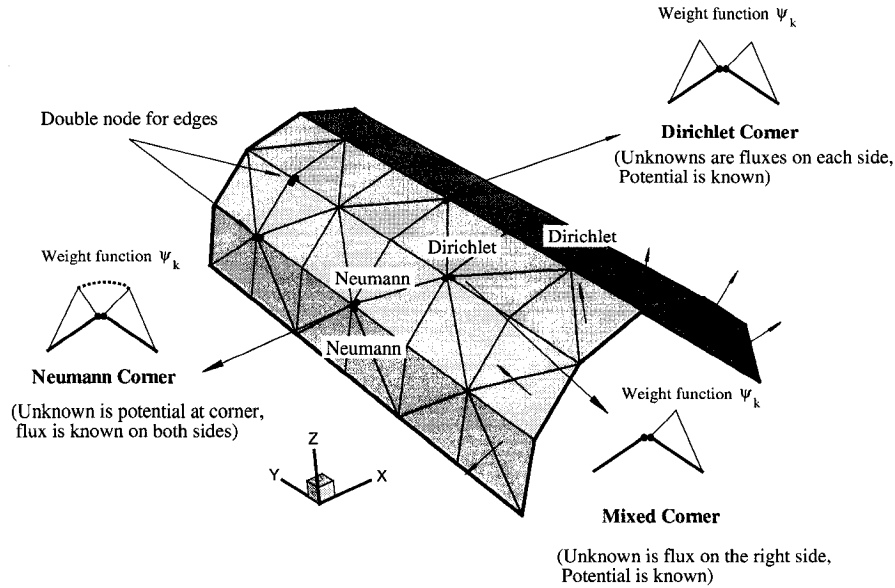


Figure 7.6: Corner treatment in the Galerkin BEM. Notice that the 6 normal vectors in the figure define the 6 planes that compose the semi-cylindrical geometry (with axis along the y -direction).

the z direction. The second problem has three parallel penny shaped cracks inside a cylinder with same outer boundary conditions and gradation. The last example is a complicated 3D problem with multiple random cracks inside a cube. This example demonstrates the efficiency and robustness of the BEM formulation and the code. The conductivity varies gradually along the z -direction. Other material property variations can be considered by using the present methodology to handle cracks in the simple BEM (see sections 2 to 4) and reference [172].

7.5.1 Penny shaped crack inside a cylinder

A cylinder with dimensions of (radius=1.476, height=3) is considered as shown in Figure 7.7. The radius of the penny shaped crack is 0.5 unit. The top surface of the cylinder at $[z = 1]$ is maintained at a temperature of $T = 100$ while the bottom is maintained at $T = 0$. The cylindrical wall is insulated. The quadratic variation of the thermal conductivity $k(x, y, z)$ is defined as (see Table 7.1)

$$k(x, y, z) = k(z) = k_0(a_1 + \beta z)^2 = 5(1 + \beta z)^2, \quad (7.36)$$

in which β is the nonhomogeneity parameter and a_1 is a constant. Notice that β has units of $1/[\text{Length}]$, and this $1/\beta$ represents the length scale of material nonhomogeneity. The BEM results are compared with results from finite element simulations. The BEM mesh consisting of 1,752 elements and 3,502 nodes is shown in Figure 7.8. The FEM mesh consisting of 6,680 brick and tetrahedral crack-tip elements, and 27,310 nodes is shown in Figure 7.9. In the present work, in order to incorporate the functional variation of the material at the finite element level, the user subroutine UMATHT developed for the FEM software ABAQUS [1] is used [172]. By means of this subroutine, any functional variation can be included within an element by sampling the material property at each Gauss point. The temperature distribution along the radial distance from the center of the crack for both the upper and the lower crack surfaces for different values of β , for the BEM simulations are shown in Figures 7.10 to 7.12. The BEM and FEM results match very well. A contour plot of the temperature for the upper crack surface comparing the BEM and the FEM results in Figure 7.13. Finally, Figure 7.14 depicts a contour plot showing the temperature distribution on the clipped cylindrical wall.

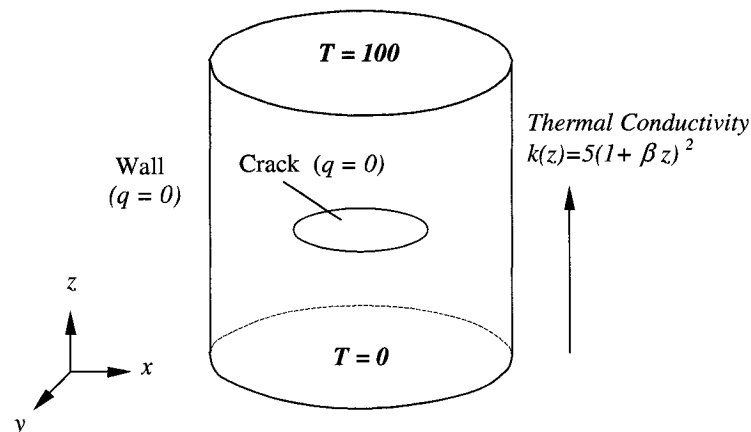


Figure 7.7: Geometry and boundary condition for penny shaped crack inside a cylinder.

7.5.2 Three parallel penny shaped cracks inside a cylinder

The cylinder of the previous example is considered again, but now there are three parallel cracks (radius of each crack = 0.5 unit) as shown in Figure 7.15. The outer boundary conditions and the material gradation are the same as in the previous example. The crack surfaces are insulated. The BEM mesh consisting of 5,180 elements and 7,752 nodes is illustrated in Figure 7.16. Again, for this example, the BEM results are compared with results from finite element simulations. The FEM mesh consisting of 16,080 brick and tetrahedral

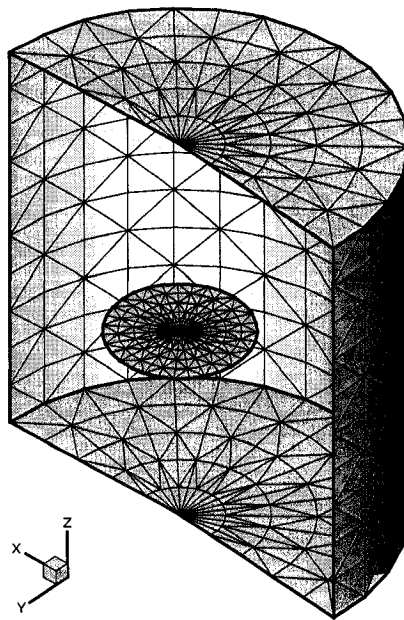


Figure 7.8: Illustration of the BEM mesh for penny shaped crack inside a cylinder (1752 elements and 3502 nodes). The cylinder is clipped for visualization purpose.

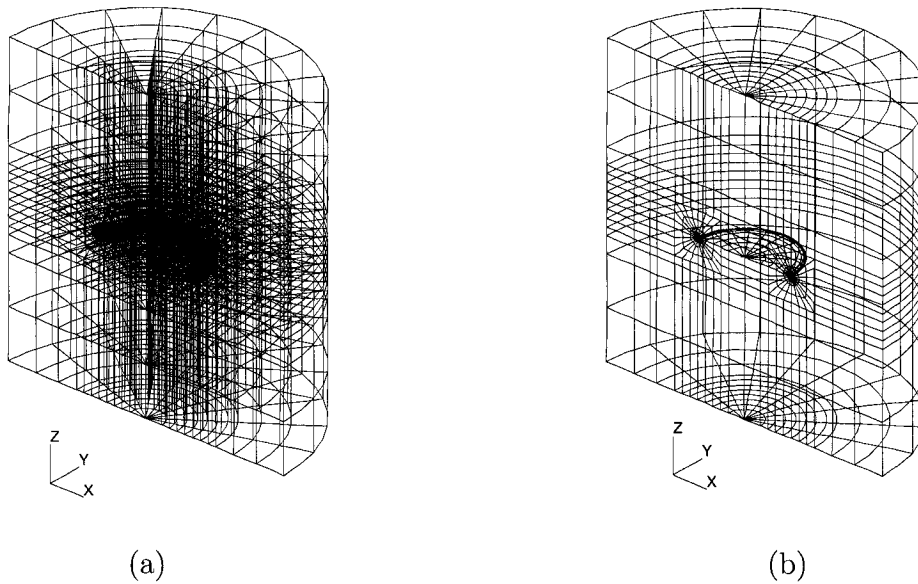


Figure 7.9: Illustration of FEM mesh for penny shaped crack inside a cylinder (6,680 elements and 27,310 nodes); (a) half mesh; (b) surface-only display.

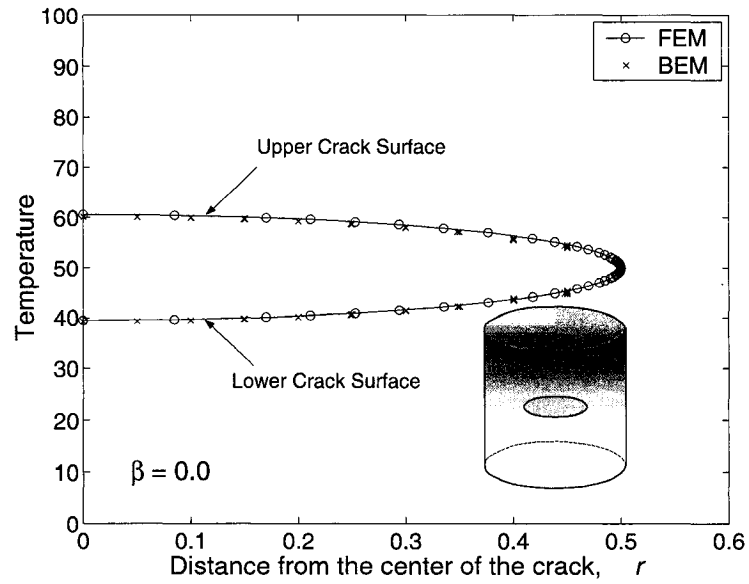


Figure 7.10: Temperature along radial distance from the center of the crack for $\beta = 0.0$ (homogeneous media).

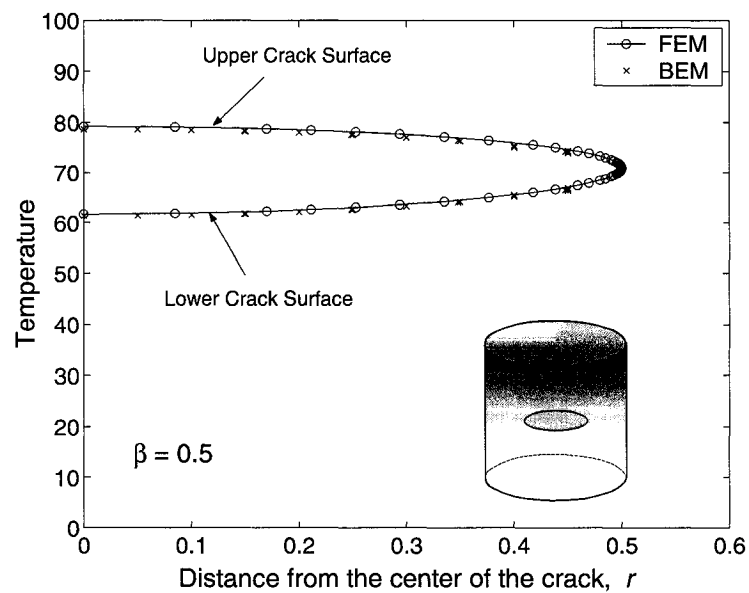


Figure 7.11: Temperature along radial distance from the center of the crack for $\beta = 0.5$ (graded medium).

crack-tip elements and 64,732 nodes is shown in Figure 7.17(a). Figure 7.17(b) shows the overall FEM mesh which depicts the complexity of the meshing effort. A section thru the

crack front is taken in Figure 7.17(c) in order to show the finer mesh distribution along the crack front. The temperature distribution along the radial distance from the center of the crack for both the upper and the lower crack surfaces, for different values of β , are shown in Figures 7.18 to 7.20. The BEM and FEM results match very well for this multiple crack problem in a finite geometry. Contour plots of the temperature distribution on both the upper and the lower crack surfaces for the top, middle and the bottom cracks considering $\beta = 1.0$, are shown in Figure 7.21, which illustrates the spatial distribution of temperature.

7.5.3 Multiple random cracks inside a cube

In this example, eleven cracks of circular and elliptical shapes are randomly oriented inside a cube. The thermal conductivity variation is

$$k(x, y, z) = 5(1 + 1.5z)^2, \quad (7.37)$$

The boundary conditions prescribed for this problem is similar to the previous examples i.e., the top surface of the cube at $[z = 1]$ is maintained at a temperature of $T = 100$ while the bottom is maintained at $T = 0$, and the remaining four walls are insulated. The outer cube geometry and the BEM mesh on the cracks are shown in Figure 7.22. The BEM mesh consists of only 900 elements and 2,033 nodes. Contour plots showing usage of clippers for visualizing the upper temperature of the crack surfaces are shown in Figure 7.23(a)-(c). The flux distribution for the upper $[z = 1]$ and the lower $[z = 0]$ plane of the cube is shown in Figure 7.24, which shows the presence of the multiple cracks influences the resulting flux on these planes. A complicated problem such as this would be very tedious to mesh using three-dimensional finite elements. This problem demonstrates the robustness of the present simulation. The code can handle any number of cracks of different sizes and shapes.

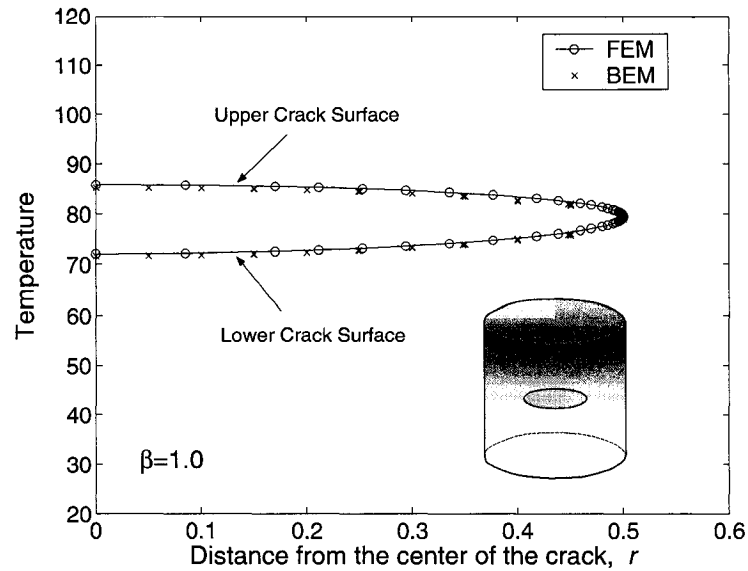


Figure 7.12: Temperature along radial distance from the center of the crack for $\beta = 1.0$ (graded medium).

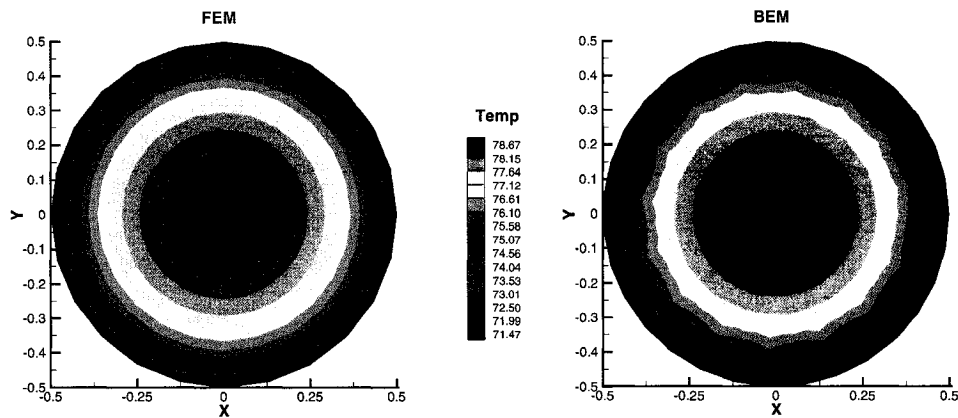


Figure 7.13: Comparison of contour plots of temperature for the FEM and BEM results for the lower crack surface for $\beta = 1.0$.

7.6 Concluding Remarks

The “simple BEM” consists of transforming problems in nonhomogeneous media to known problems in homogeneous media such that existing codes (for homogeneous media) can be reused with straightforward modifications. A “simple BEM” for solving multiple cracks in problems governed by potential theory is presented herein. Steady state heat conduction

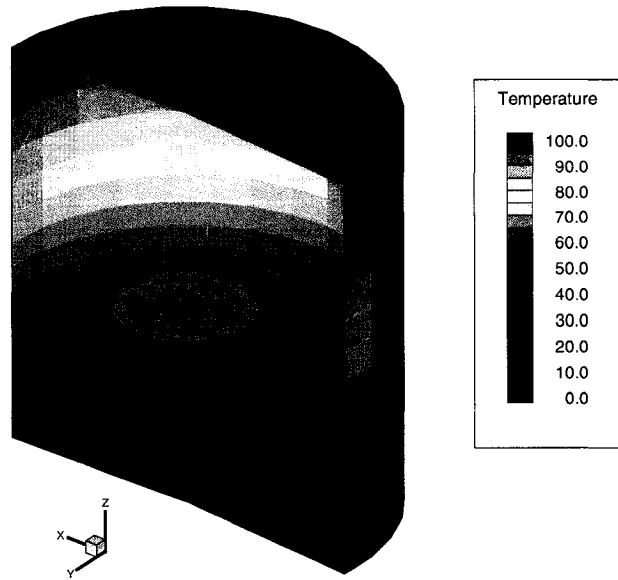


Figure 7.14: A contour plot showing the temperature distribution obtained from BEM on the wall and on the crack surface for $\beta = 0.5$.

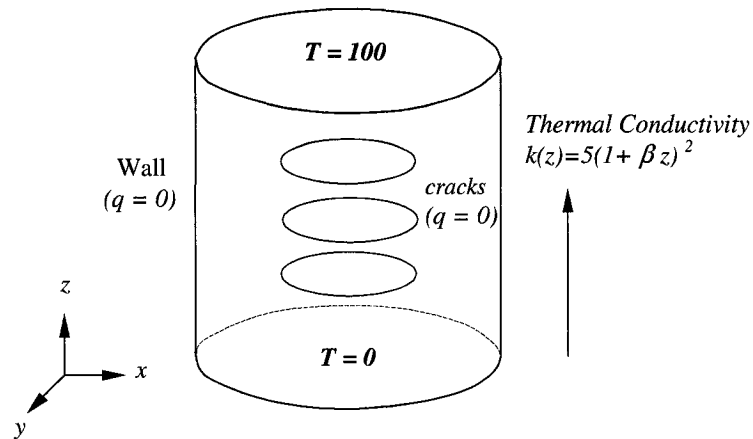


Figure 7.15: Geometry and boundary condition of three penny shaped cracks inside a cylinder.

problems with functionally graded thermal conductivity are investigated. Numerical problems with single and interacting cracks are solved and verified by the means of the FEM. A numerical example consisting of several random cracks of various sizes and shapes is pre-

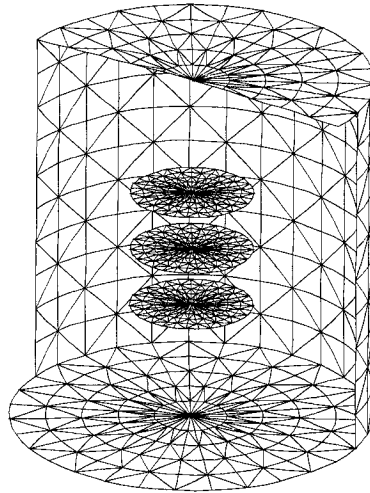


Figure 7.16: BEM mesh for three penny shaped crack inside a cylinder with 5,180 elements and 7,752 nodes. The cylinder is clipped for visualization purpose.

sented to demonstrate the robustness of the present BEM formulation and implementation. A quadratic variation of thermal conductivity was considered in the examples, however, other gradations, such as trigonometric and exponential, can be readily solved by employing the present “simple BEM” technique (for crack problems). From the formulation point of view, a key observation is that if the jump in potential is used as the primary variable on the crack surface, then the displacement discontinuity approach is not directly applicable. The dual boundary element method, which employs the potential as the primary variable on the crack surfaces, is shown to be more suitable to treat the fracture problem.

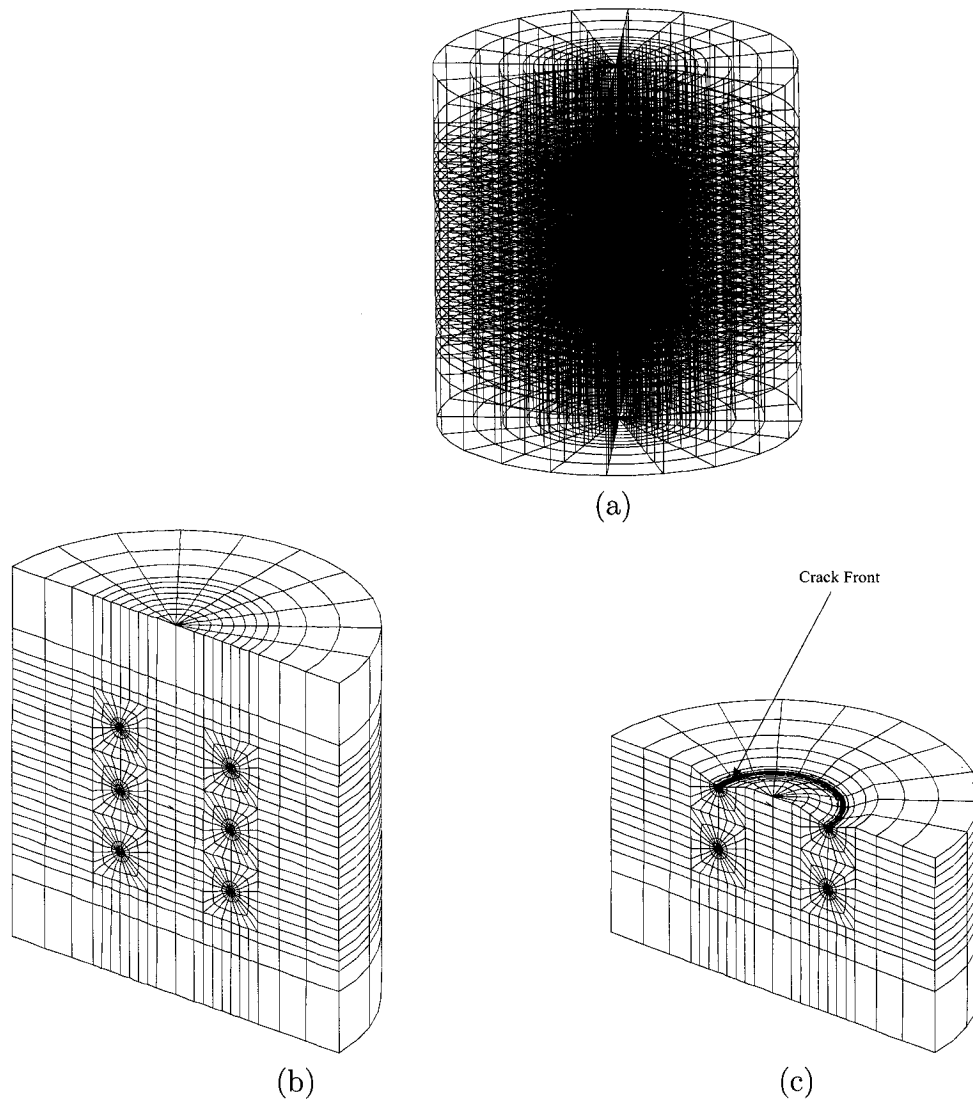


Figure 7.17: The FEM mesh for three penny shaped cracks inside a cylinder (16,080 elements and 28,732 nodes); (a) mesh discretization; (b) Section through the middle of the FEM mesh only showing the surface of the elements; (c) Section through the crack plane showing the mesh around the crack front.

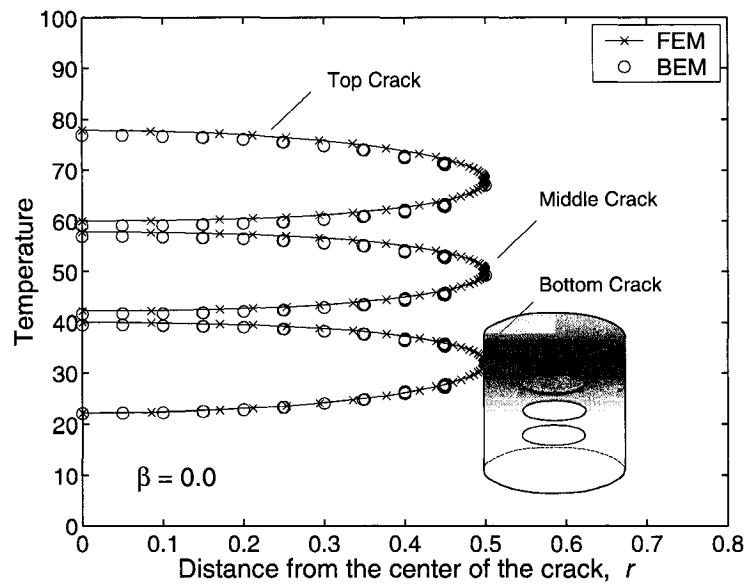


Figure 7.18: Temperature distribution along radial distance from the center for $\beta = 0.0$ on the three cracks inside a cylinder.

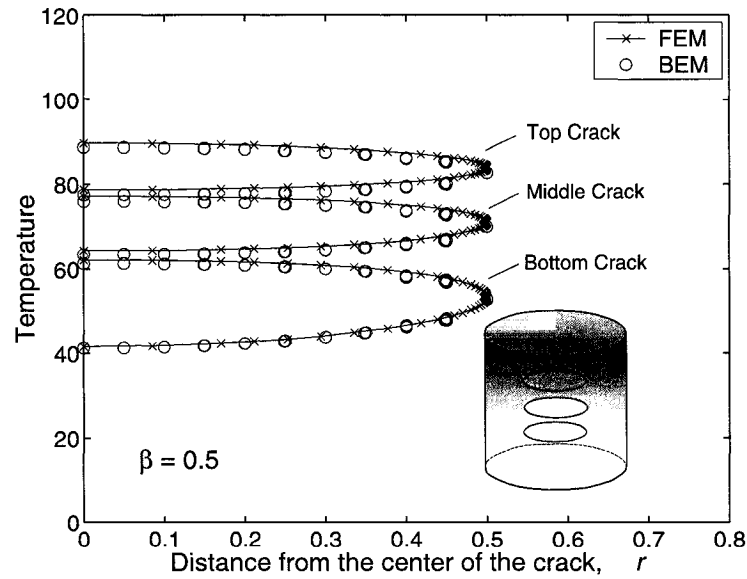


Figure 7.19: Temperature distribution along radial distance from the center for $\beta = 0.5$ on the three cracks inside a cylinder.

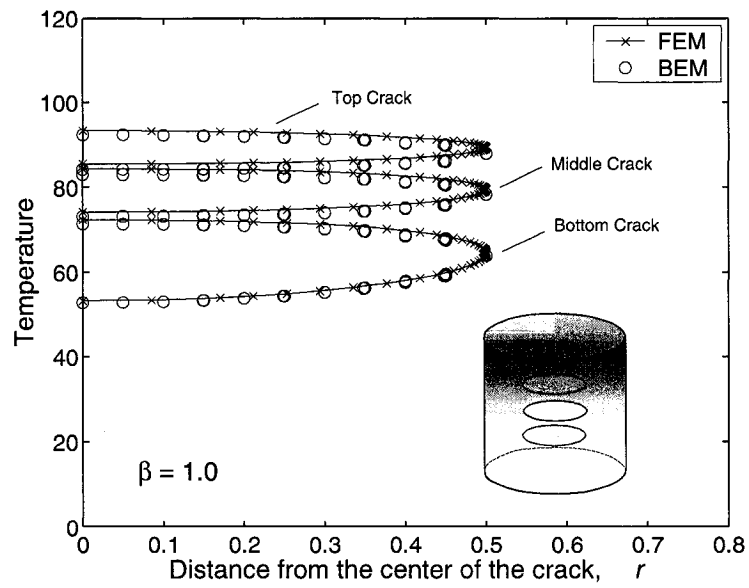


Figure 7.20: Temperature distribution along radial distance from the center for $\beta = 1.0$ on the three cracks inside a cylinder.

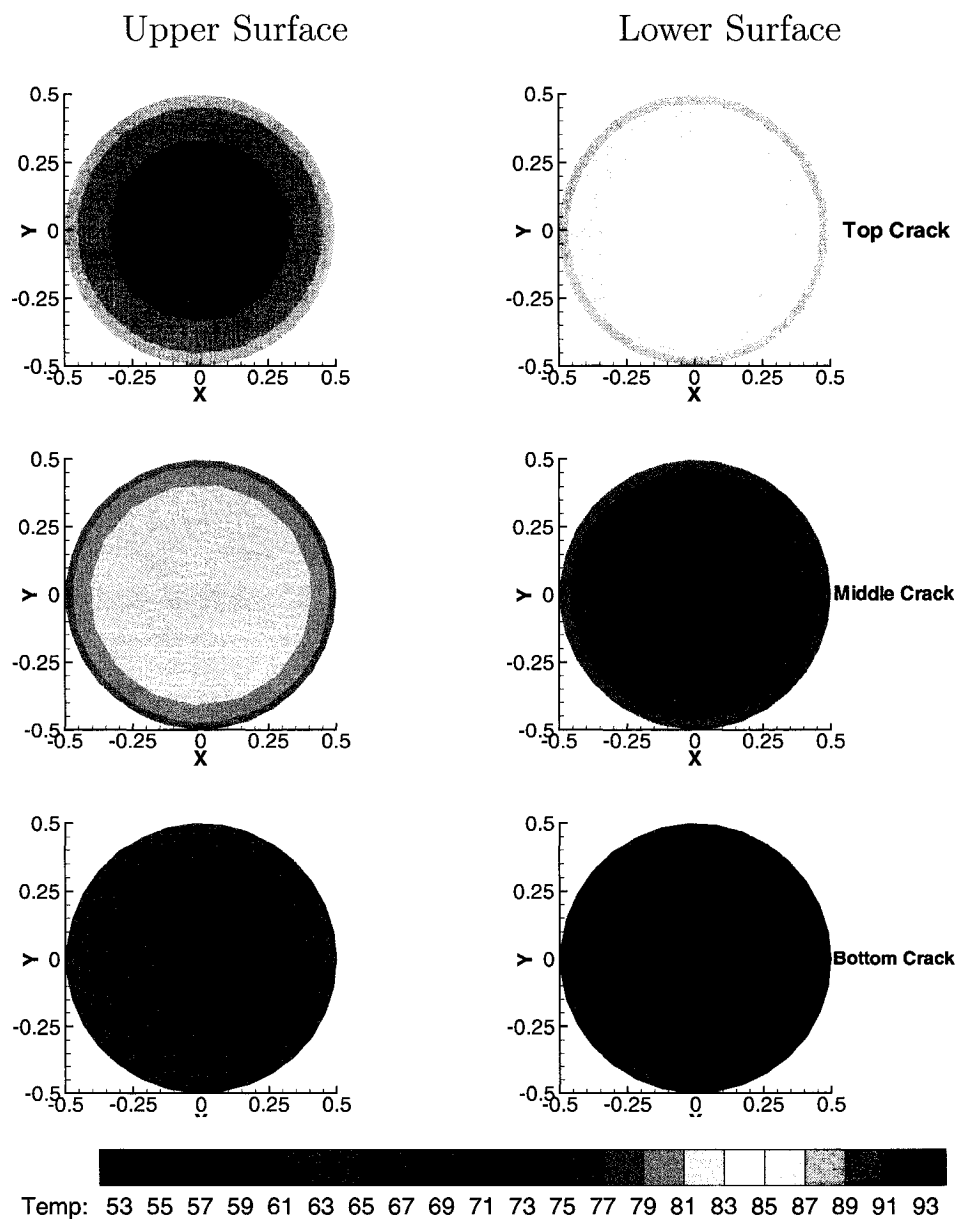


Figure 7.21: BEM temperature distribution on the upper (left) and lower (right) crack surfaces for the top, middle and bottom crack. The material nonhomogeneity parameter $\beta = 1.0$.

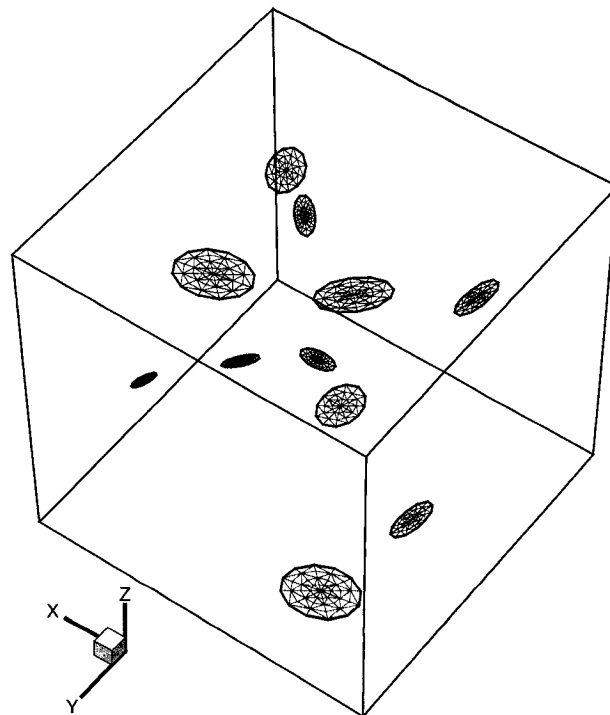


Figure 7.22: Multiple cracks inside a cube. The complete BEM mesh consists of 900 elements and 2,033 nodes.

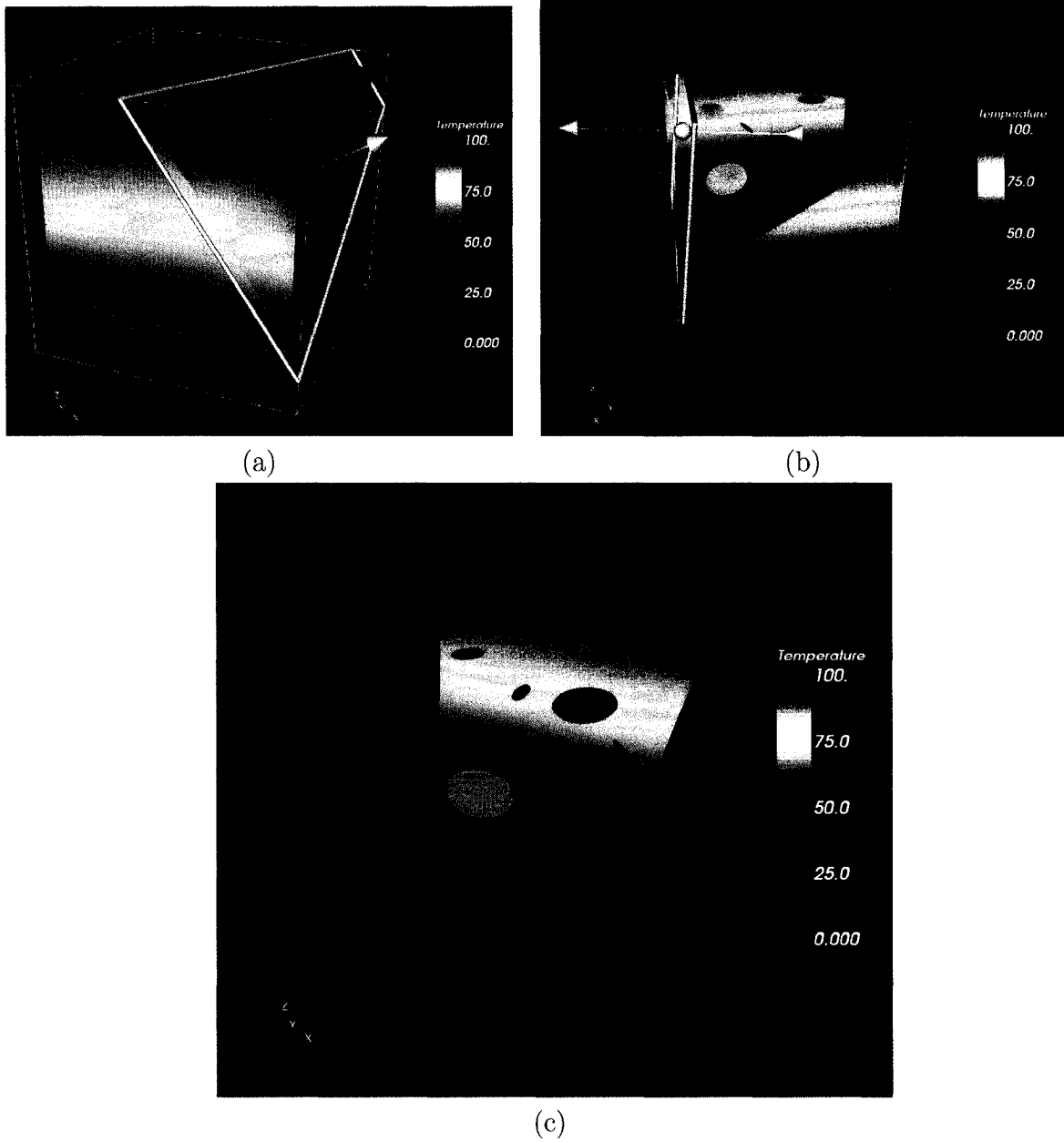
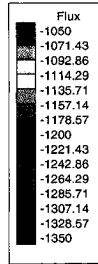
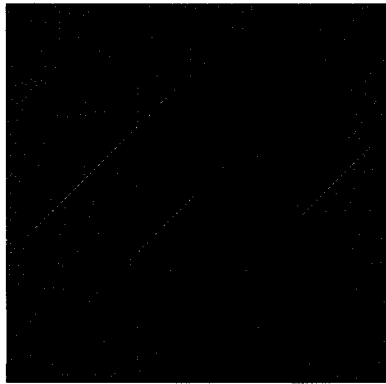


Figure 7.23: (a) Temperature distribution on the wall with a clip plane applied. (b) Clipped cube. (c) Clipped cube showing the temperature distribution of the upper crack surfaces and walls. is shown.

$z = 1$ plane



$z = 0$ plane

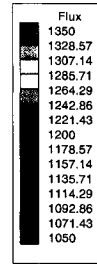
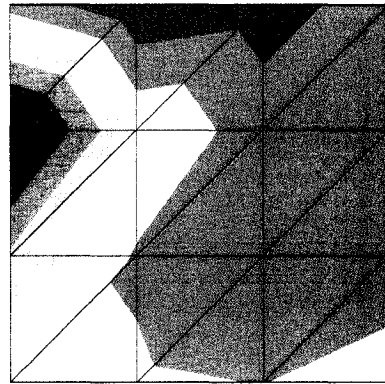


Figure 7.24: BEM flux distribution on the $z = 1$ (left) and $z = 0$ (right) plane of the cube.

Chapter 8

Scientific Visualization with BEM

Scientific visualization aids the scientists by representing the data in its entirety. Representing the data in visual form is much easier for human brains to interpret than raw data. In this way scientists are able to capture the characteristics of the data and explain unrecognized phenomena easily. Animations created from time varying data presents the events naturally. Applying virtual reality techniques, data can be viewed as well as manipulated in a true three dimensional immersive environment. This chapter is structured as follows. An introduction to scientific visualization is given in section 8.1. Section 8.2 introduces a few basics of the visualization process and reviews available visualization techniques. A brief description of visualization softwares and frameworks is given in Section 8.3. Section 8.4 details the characteristics, algorithm, techniques of BEM visualization and presents our work on the topic. A virtual reality based visualization tool named ‘MechVR’, developed in our research group to visualize FEM and BEM data is presented in Section 8.5. Section 8.6 discusses web-based data visualization using the VRML. Finally, the chapter concludes with a few remarks followed by a brief discussion on new ideas and promising directions for future research.

8.1 Introduction

Scientific visualization is an integral part of computational mechanics research. The purpose of scientific visualization is to facilitate scientists to observe, gain insight, and better understand their experiments or numerical simulation data [120]. Advances in scientific computing facilities have tremendously enhanced the ability to generate and collect large scale datasets allowing the mathematical models and numerical simulations to be more complex. Often direct inspection of the data is not easy to comprehend due to the size and complexity of the data. Additionally, if the data is generated at several different times during the experiment

or simulation, understanding how the data varies with time may be complicated.

Another excellent feature that scientific visualization has been able to offer is interaction with the data during the computations. Often, researchers and scientists would want to change certain representation or parameters during the simulations to dynamically verify its impact in the simulation results. In order to convey and interact with information of huge data sets, scientific visualization is an effective tool. Other potential usage of visualization is in calibrating and debugging of large scale simulations. Inconsistencies present in large data sets can be detected and identified very easily, which otherwise may be hard to determine from data files alone. Missing data can be interpolated. Efficient and creative use of color, texture, and opacity facilitate the study of true three dimensional characteristics of complex physical phenomena.

Virtual Reality (VR) is a newly emerging tool for scientific visualization that makes possible multisensory, three-dimensional modeling of scientific data [20, 158]. While the emphasis is on visualization, the other senses are added to enhance what the scientist can visualize. Also, sharing data and visualization with other scientists are integral part of the growing collaboration and connection among researchers. Providing results using a new type of visualization based on VRML gives the opportunity for researchers to navigate the visualization in an interactive 3D virtual environment over the internet [97]. It is a new interface paradigm that uses computers and human-computer interfaces to create the effect of a three-dimensional world in which the user interacts directly with virtual objects [20]. The three-dimensional display and interaction capabilities of VR allow for significantly enhanced three-dimensional perception and interaction over three-dimensional computer graphics. In order to understand complex phenomena from a time-dependent data set in a complicated three-dimensional structure, VR allows rapid and intuitive exploration of the volume containing the data, enabling the phenomena at various places in the volume to be explored, as well as provide simple control to manipulate and interact through interfaces integrated into the environment. In recent years, there has been much excitement about Virtual Reality (VR) [10]. From its beginning in the field of scientific simulation [69], VR has gradually grown into a new phase [68] and has become a distinct field in computing. It has already been researched and used in such diverse areas as car design [151], robot design [166], medicine [95], chemistry, biology and education, as well as in building design and construction [131].

Scientific visualization has been successfully used many areas such as, computational fluid dynamics, electronic design automation, medical imaging, geospatial, propagation, meteorology, hydrology, data fusion, ground water modeling, oil and gas exploration, and data mining. Until recently the power of visualization has not been used much in computational mechanics. A typical visualization algorithm works by computing sample positions, evaluat-

ing the value of the field variable at those positions, and creating a geometric representation for those values and positions. Since each computational method has its own characteristics in data structure and dimension, it is necessary to design visualization technique best suited for that method. Among the methods in computational mechanics, visualization for the finite element method and finite difference method have been explored and researched tremendously. In the BEM literature, there has been very limited publications on visualization, mostly limited to two dimensions [130]. This work attempts to deal with the visualization of 3D BEM data wholly starting from viewing boundary and domain results by means of modern visualization techniques such as point based isosurfacing and volume rendering to virtual reality based visualization and finally concluding with modern web based interactive visualization.

8.2 Visualization process and techniques

The visualization process consists basically of transforming data into images that convey information correctly and efficiently. In general, the visualization consists of four essential steps [150, 183]. In the first step, the raw numerical data is filtered in order to select data that we want to see or process. In the second step, the selected data is transformed into forms that can be displayed by the graphics systems. In the third step the transformed data is mapped to 3D geometric primitives. Finally in the fourth step the resulting geometry is displayed. For example, if we have a set of scattered point, we would like to read the data set (*source*), create a polygonal mesh (*filtering*), then use surfaces on it (*mapping*) and finally display (*rendering*). This model is termed as the visualization pipeline or visualization network. Figure 8.1 shows the four steps of the visualization process. This approach is typical of many commercial visualization systems.

Some of the visualization techniques that are available based on the type of the attribute data are:

Visualization of Scalar Fields: color mapping, isosurface, volume rendering, cutting plane contour etc.

Visualization of Vector Fields: streamlines, vector glyphs, warping, displacement plot etc.

Visualization of Tensor Fields: glyphs, hyperstreamlines, tensor ellipsoids, tensor lines etc.

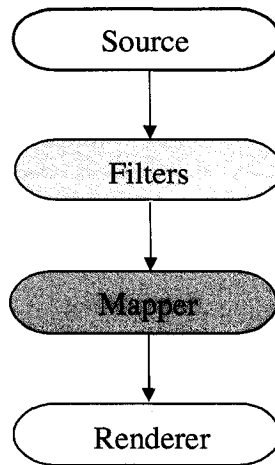


Figure 8.1: Visualization pipeline: Steps of the visualization process.

8.3 Visualization: Softwares and frameworks

With rapid advances in visualization research, a number of excellent visualization software has been created. Visualization systems fall into two main categories, *turnkey* and *modular visualization environments* (MVE) [184]. Turnkey systems, in general, have fixed functionality and present options to the user through a simple pull down menu type interface. The advantage of a turnkey system is its ease of use for the novice user. MVEs offer much richer functionality with the possibility of user extension. AVS, IBM's Data explorer (renamed as OpenDX), NAG explorer, Templated Graphic's Amira and Visualization toolkit (VTK) are examples of some of the visualization systems. In order to select a suitable visualization software some of our key considerations were:

- free
- open-source
- multi-platform (e.g. Windows, Unix, IRIX, SGI)
- simple to use
- extensibility

- scalability
- modular architecture.

The VTK and its *turnkey* version ParaView turn out to be the most suitable for the present purposes. The Visualization ToolKit (VTK) is an open source, freely available software system for 3D computer graphics, image processing, and visualization [150]. It consists of a C++ class library, and several interpreted interface layers including Tcl/Tk, Java, and Python. VTK supports a wide variety of visualization algorithms including scalar, vector, tensor, texture, and volumetric methods; and advanced modeling techniques such as implicit modelling, polygon reduction, mesh smoothing, cutting, contouring, and Delaunay triangulation. ParaView is a *turn-key* visualization system build on top of VTK, and it makes VTK easier to use with an interactive, point and click interface [87]. ParaView also supports supercomputing applications, including tiled display and distributed parallel processing. ParaView has an excellent professional support provided by Kitware, Inc (<http://www.kitware.com>). ParaView supports a huge array of data file formats i.e., vtk, EnSight, HDF5, VRML, Protein data bank, XMol Molecule, Plot3D, Stereo Lithography, BYU, Gaussian cube, Raw binary files, XDMF, AVS, Meta Image files, polygonal PLY files, Exodus files and SAF files. One of the best features of ParaView is, by writing XML files new data readers, writers, sources and filters can be written and incorporated into it. In this regards, we include the BEM visualization into ParaView.

We also investigated the Rocketeer and Voyager (its parallel version) [58] developed at University of Illinois Center for Simulation of Advanced rockets (CSAR). Rocketeer is a powerful interactive 3D visualization but it only takes the NCSA HDF format as the input file, while Voyager works only in Solarix and Linux only.

8.4 Visualization of BEM Data

8.4.1 Basic Data representation

In order to create useful visualization models and efficient visualization system, the characteristics of the data needs to be analysed. A structure or object is often represented by a mesh. A mesh is a collection of volumetric (in 3D) or surface (in 2D) elements called cells. The cells are defined over a set of points often called vertices. Geometry and topology define a mesh. The geometry describes the layout of vertices in space. The topology connects vertices to form cells. For instance, a simpler element which is a triangle specifies its topology and the endpoints coordinates specify its geometry. In the dataset, the cells specify the

topology and the points specify the geometry.

The characteristics of data, in general, refer to the discrete nature of the data, i.e. if it is regular or irregular, structured or unstructured and also the topological dimension. Regular or structured data are those where there exists an inherent relationship between the points. Typically if the dataset has equally spaced points then storing all the points coordinates is unnecessary, rather only the beginning point, the interval and the total number of the points are necessary [150]. For simulations in computational methods normally we have densely populated points where there are sharp changes in results, and less dense where the change is not much. Figure 8.2 depicts uniform, rectilinear, structured and unstructured mesh.

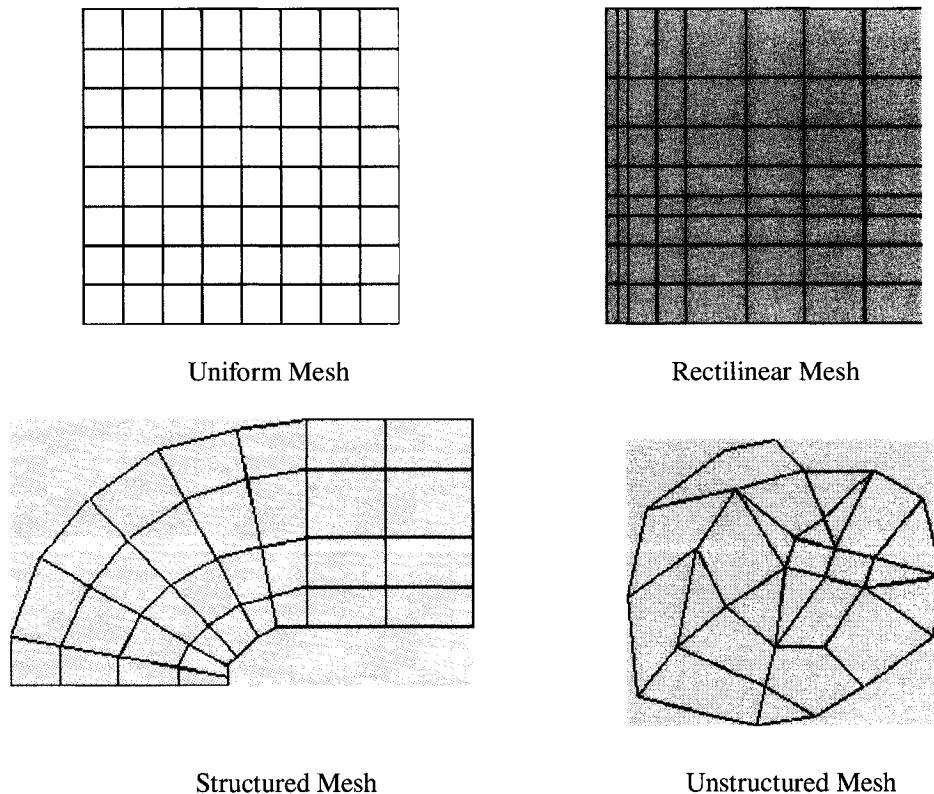


Figure 8.2: Different types of dataset

BEM data consists of mesh information of the boundary and field variable data (scalar, vector, tensor) on the boundary. The data is discrete since we have information from a finite number of points. In the BEM data, the boundary data has both the topology and the geometry information, but the topology is unknown for the results inside the domain

or interior. The boundary data are datasets with either regular or irregular topology, and irregular geometry, so it can be classified as *structured or unstructured grid dataset*. For a three-dimensional analysis surface mesh information of the boundary is available. The results of the interior points are obtained by postprocessing using collocation type techniques.

Visualizing the boundary data is simple and straight-forward. Visualizing the interior data from the BEM requires a few steps of filtering and processing before the mapping. Before discussing about the details and issues of interior visualization, first we look at boundary data visualization.

8.4.2 Visualizing the boundary results

Visualizing the boundary data is simpler than interior data because it has both the geometry and topology defined. In this section we first include a new file extension `.bem` for BEM files in `ParaView` and then we explore some of the visualization techniques that can be applied to visualize the boundary data.

BEM data files with `.bem` extension

`ParaView` supports a wide range of file formats. Typically, the BEM format file is not supported by `ParaView`. One approach is to convert the BEM data files to a format that `ParaView` can read. The other approach is to write a new data file reader. We chose to write our own reader and propose a BEM file format with (`.bem`) extension. The reader operates within the standard VTK pipeline. `ParaView` uses VTK (which is written in C++), and the user interface and the server manager are created by parsing XML files [87]. Figure 8.3 shows the interface of the `ParaView` with a `.bem` file data. This problem is analysed in Chapter 5, a parallelepiped with a cylindrical cavity. The exterior surfaces of the cube and the cylindrical wall are the boundary where the results are known. The boundary is colormapped with the flux results and the opacity is reduced in order to show the interior cylindrical cavity.

Visualization techniques: Scalars

Scalar data consists of single data associated with each location in the dataset.

- Color Mapping

This is a common scalar visualization technique that maps scalar data to colors and displays the colors. The scalar mapping is implemented by indexing into a color lookup table. Figure 8.3 is an example of color mapping.

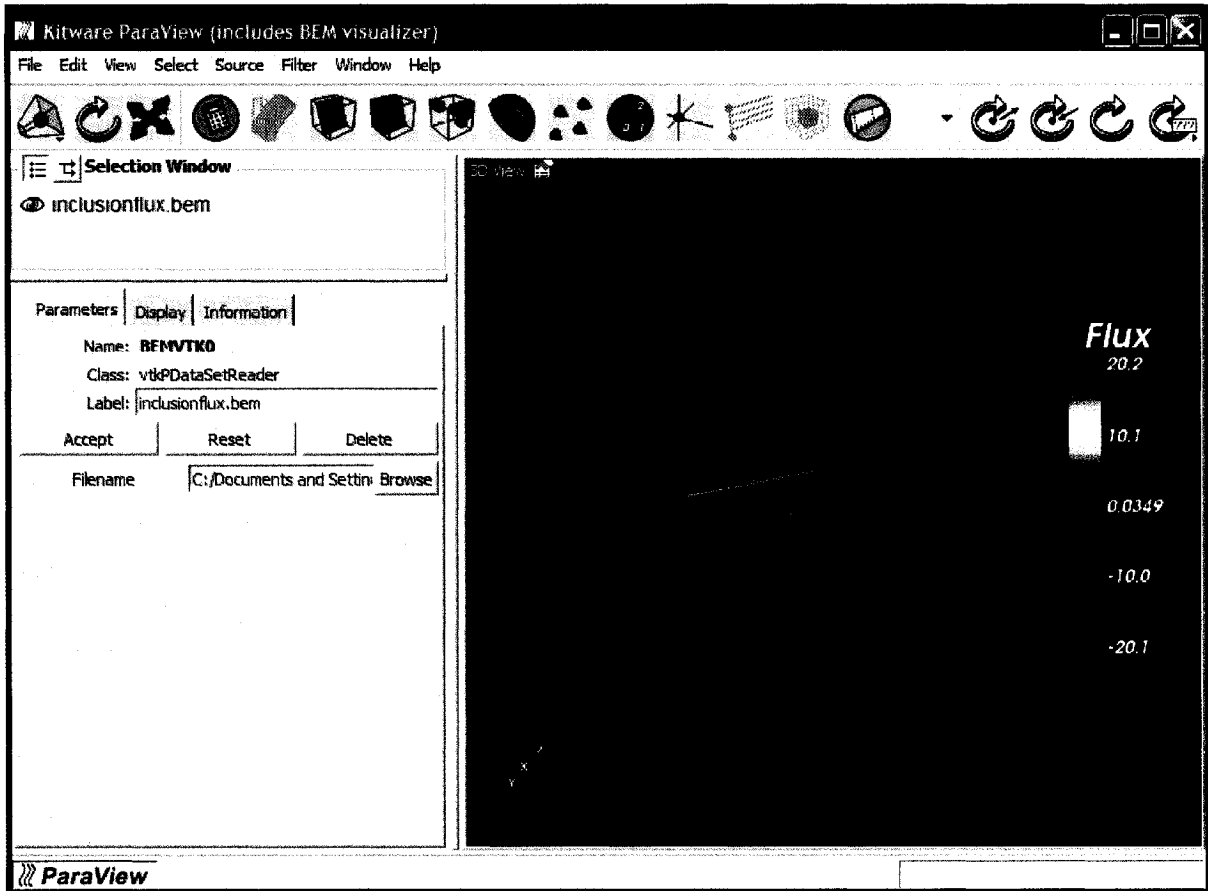


Figure 8.3: ParaView: Flux results of a parallelepiped with a cylindrical cavity (from Chapter 5)

- Contouring

Contours are surfaces/lines of constant scalar values. We can either set up contour for specific value or specify a scalar range and the number of contours to be generated in the range. Figure 8.4 shows contours of the temperature on the boundary.

- Glyphing

Glyphing is a visualization technique that represents data by using symbols, or glyphs. The symbols may be a cone, a sphere or multivariated glyphs which can be scaled, colored and oriented along a direction. The glyphs are copied at each point of the input dataset. Figure 8.5 shows the temperatures represented as glyphs.

- Clipping

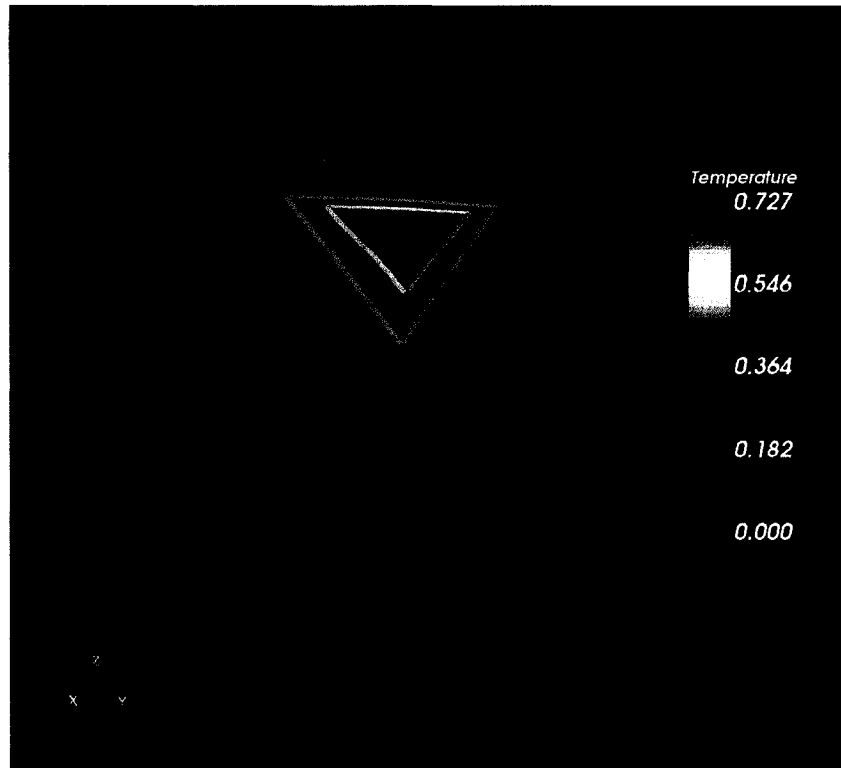


Figure 8.4: Contours: A scalar range and number of contours are specified for temperature profile.

Clipping can be used to visualize the details of interior of a body. For example, the contour plot of the flux on the surface of the cavity can be visualized clearly if it is clipped using a plane. Figure 8.6(a) depicts the contours without the clipper and Figure 8.6(b) demonstrates clipping the model with a plane. Also multiple clippers can be used too. Figure 8.7(a) and 8.7(b) show the two clippers that were used to generate Figure 8.8. By using the clippers, the interior results of temperature and also the temperature on the crack surfaces can be conveniently visualized.

8.4.3 Visualizing BEM Interior Data

Visualizing the interior results of BEM is a challenge. The BEM results in the interior of the domain are obtained by defining coordinates of points and collocating the boundary integral equation at those point. So the dataset that we obtain is basically the coordinates of the set of points and their attributed field value. This type of data have different names e.g., 'point cloud', 'scattered data' or 'unstructured points'. Unstructured points are irregularly located in space [123]. Unlike structured grids or unstructured grids, unstructured point dataset

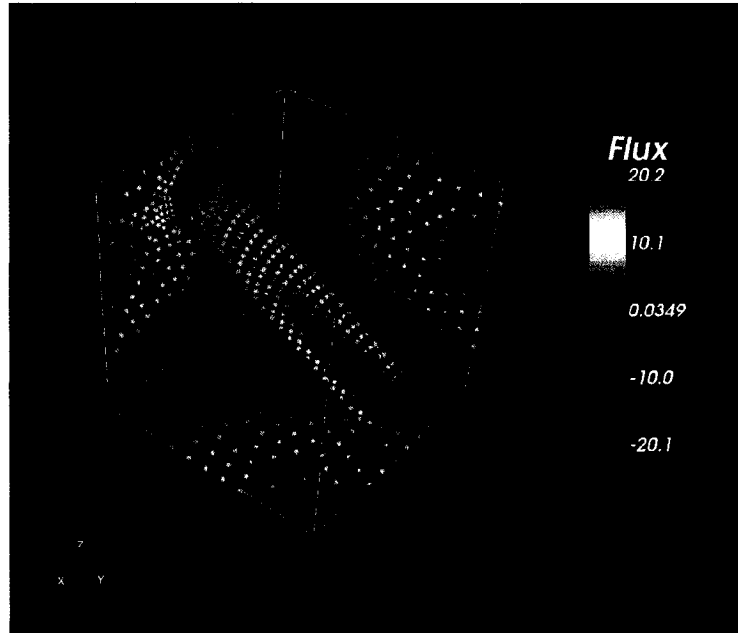


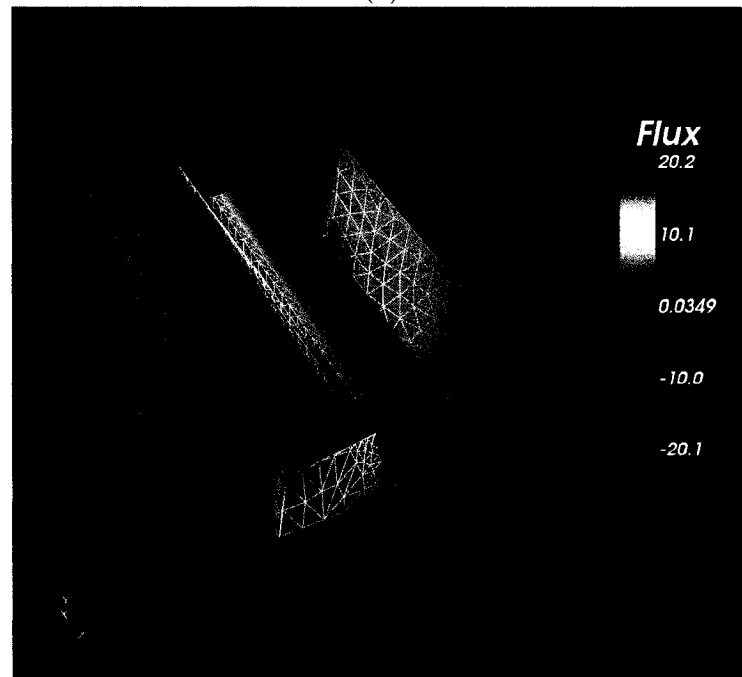
Figure 8.5: Glyphs representing the flux for the parallelepiped with cavity.

have no topological component relating one point to another. Unstructured points are easy to represent but difficult to visualize [150]. Most scientific visualization techniques require data to include connectivity information, which is not provided by the data set. It is difficult because there is no inherent structure to which the library of visualization techniques can be applied. ‘Point-cloud’ or ‘scattered-data’ visualization is becoming increasingly important in new emerging scientific applications [82]. One goal is to produce visualizations of the monitored variables - but rendered as smoothly varying variables over the particular region of interest. Advances in meshless methods are producing more and more data at random points in space and time that must be processed to make possible meaningful three-dimensional visualization, possibly changing with time depending on the specific phenomenon being monitored. This problem is still an ongoing research topic among leading visualization scientists.

There are couple of approaches available to build topological structures from a random set of points. One of the main approaches available are sampling the points into a data set often called field reconstruction method and visualize the data using standard volume or surface based rendering techniques. The other approach is to perform a 3D triangulation to create the topological structure from the unstructured points.



(a)



(b)

Figure 8.6: Flux results of: (a) Model without using the clipper. (b) Model after clipping with a plane through the cavity.

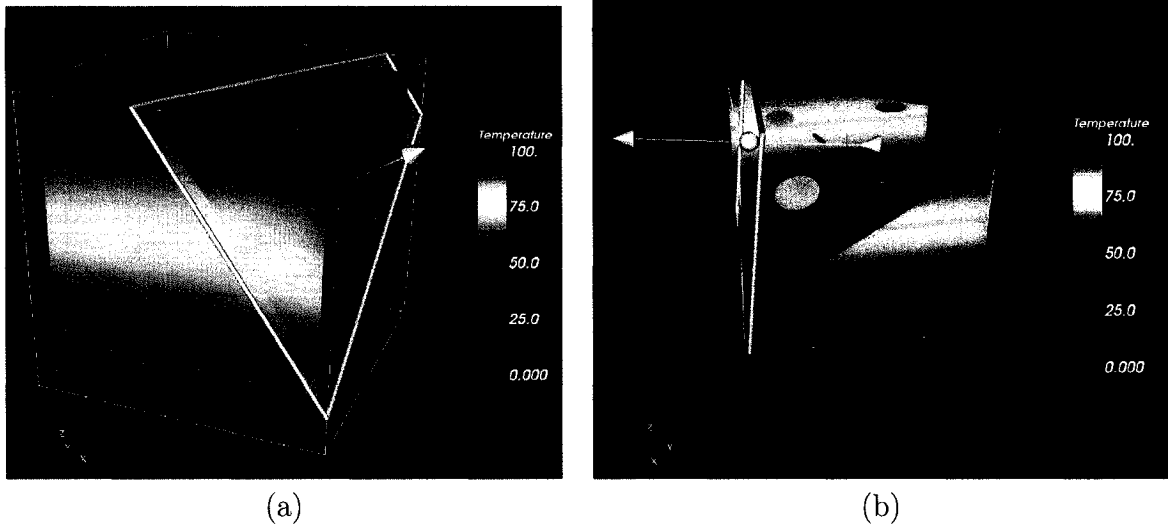


Figure 8.7: Clippers

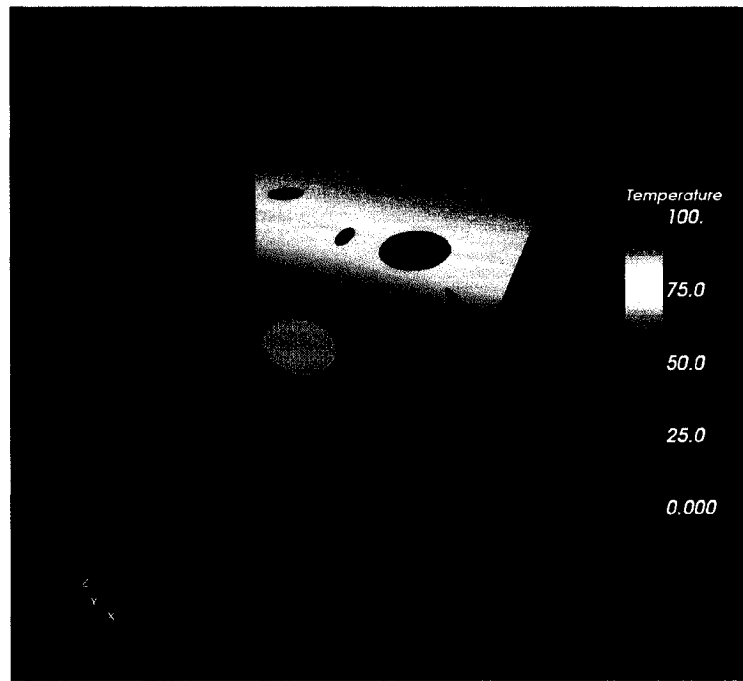


Figure 8.8: Visualizing the results on the crack surfaces using the two clippers.

Splatting Techniques

Techniques used to deal with unconnected data include the use of field reconstruction methods producing an analytical definition that is then resampled to a standard grid format supported by standard visualization methods, such as volume rendering and isosurfacing [82]. While these methods work well for offline analysis, they are less practical for real-

time visualization and become even less effective as the data size increases. Highly efficient schemes, operating directly on raw scattered data, are necessary. Splatting is a volume rendering method that distributes volume data values across a region on the rendered image in terms of a distribution function [150]. Typically the distribution functions are Gaussian functions.

Isosurface extraction is an important technique for visualizing three-dimensional scalar fields. By exposing contours of constant value, isosurfaces provide a mechanism for understanding the structure of scalar data. Isosurface extraction poses a unique challenge in that no geometry exists before the user provides an isovalue [115]. Furthermore, the user may change the isovalue often, and any geometry extracted based on the previous isovalue should be discarded.

Recently, a number of researchers have proposed and developed methods for the direct rendering of scattered data, which involves using different building blocks to construct high-quality data visualization. For instance, the construction of isosurfaces typically is done by extracting isotriangles from some spatial grid structure [82]. Isosurfaces can also be constructed directly by merely using point primitives, given in space with associated function value but no connectivity information [36]. In this work, prototypes have been developed for the rendering of scattered data sets using point primitives directly, without performing any meshing steps. The method is called ‘iso-splatting’, and it is a powerful alternative to traditional extraction-based iso surface visualization.

The `vtkGaussian` splatting filter available in VTK build topological structure by sampling the points into the image dataset. The sampling is performed by creating some kind of influence or splatting that distribute the data value of each unstructured points over the surrounding region. `vtkGaussian` splatter can take the polydata as input. This class is typically used to convert point-valued distributions into a volume representation. The volume is then usually iso-surfaced or volume rendered to generate visualization [150].

Delaunay Triangulation Techniques

For unstructured mesh generation, Delaunay-based algorithms have become popular [52, 181, 63, 159]. For such algorithms, the input data are often given in a discrete formulation of the domain boundary which, in the three dimensional space, may represent a surface triangulation of the boundary. Delaunay-based methods usually first produce an initial triangulation that forms the convex hull of the boundary points which may not match with the prescribed boundary surface, that is, the triangulation may not satisfy the constraints (edges and faces in 3D) imposed by the surface triangulation. This leads to the problem of

recovering the boundary geometric constraints from the initially constructed triangulation, or simply, the problem of boundary recovery. Such problems have been successfully resolved in 2D spaces [14], while they are still under active investigation in 3D [51, 160].

Delaunay triangulation in 3D creates tetrahedrons from the unstructured points. It is numerically sensitive but enough for the purpose of visualization. Some issues related to this technique are uniqueness and degeneracy. Creating triangles with poor aspect ratio cause the algorithm to break. By randomizing the point order, better triangles with aspect ratios can be generated [150]. In this work, we use the Delaunay triangulation technique. We included the `vtkDelaunay3D` filter in the ParaView writing XML codes [87] (see Figure 8.9). Three parameters can be adjusted, namely, tolerance, alpha and the offset, as explained below.

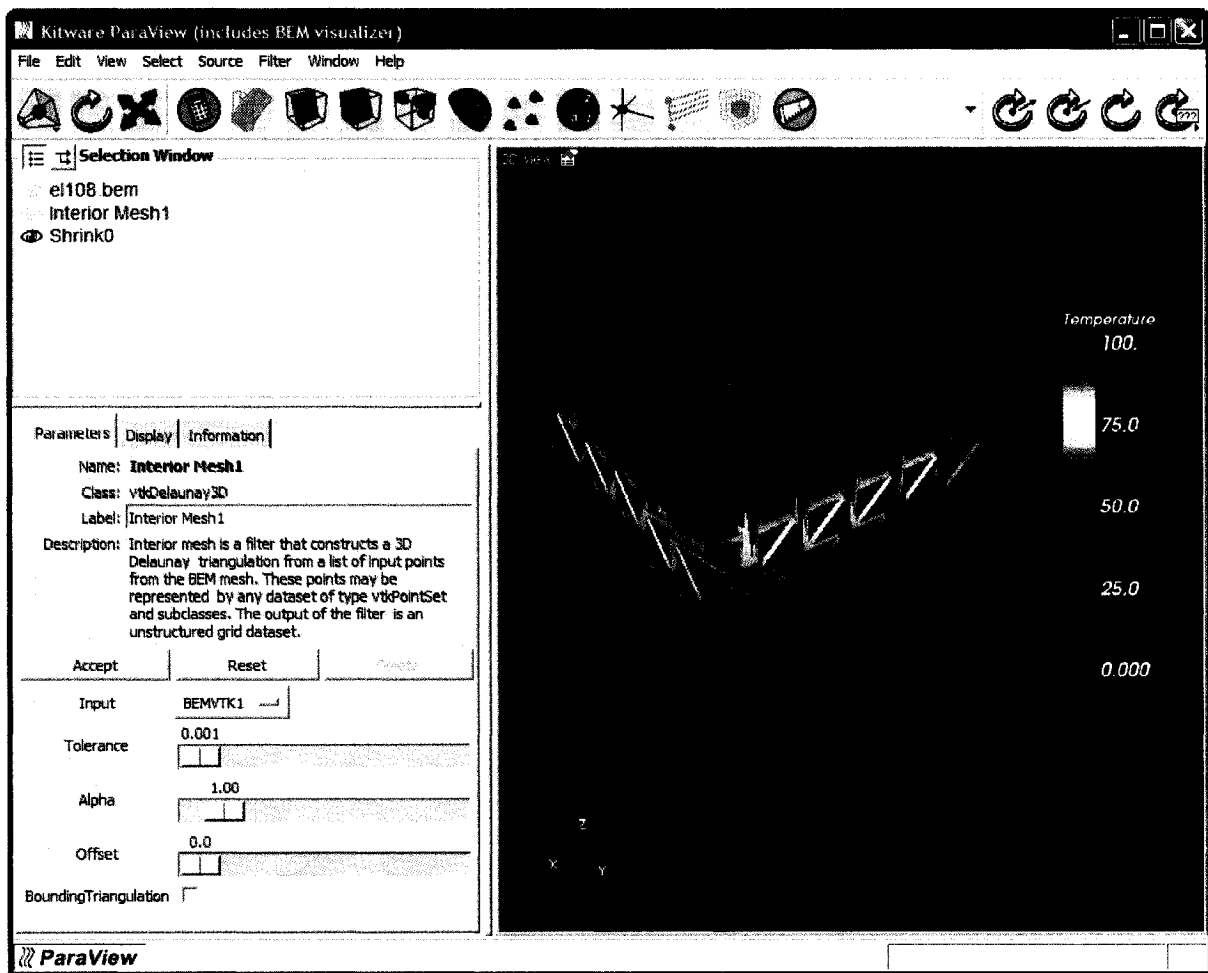


Figure 8.9: ParaView: Shrunked surfaces of the tetrahedrons created using Delaunay 3D.

A tolerance can be specified to control discarding of closely spaced points. This tolerance is specified as a fraction of the diagonal length of the bounding box of the point. An alpha

(or distance) value can be specified to control output of this filter. For a non-zero alpha value, only edges, faces, or tetra contained within the circumsphere (of radius alpha) will be output. Otherwise, only tetrahedra will be output. Finally an offset to specify a multiplier to control the size of the initial, bounding Delaunay triangulation can be provided. Also more points can be inserted in order to have a better mesh. With the advent of new and effective Delaunay algorithms, this capability should be included in **ParaView** soon.

Alternative techniques

Surface reconstruction and tetrahedralizing unstructured points are a thriving research area [160]. Besides the techniques described above, some other simple steps can be taken for the purpose. One approach is to remesh the interior using freely available powerful 3D mesh generators e.g. NETGEN, GMSH, which can take boundary mesh as an input. Although this may seem to go against the basic flavour of BEM, the meshing effort is for the sake of visualization only. This means that the quality of the mesh is not important, any automatic 3D mesh generator should serve the purpose. In this approach, when the analyst creates the BEM mesh, a corresponding FEM-type mesh can also be created for visualization purpose only.

Instead of meshing the structure, interior BEM results can be obtained on points of a known probing plane. By calculating the results on the probing plane either a priori or in real-time, the interior can be visualized.

Visualizing Scalars

Once the topology of the interior data is available, different visualization techniques can be applied. Some techniques, which can be used to visualize interior results, are shown next.

- **Cutting Planes and Clipping**

By cutting (often called slicing) a dataset entails creating a cross-section. Normally a plane is used to have a planar cut. The cutting surface interpolates the data as it cuts, which can then be visualized. By making a series of slices and varying the opacity, a pseudo-volume rendering can also be done. Figure 8.10 shows five slices through the cube (of Chapter 5) and in Figure 8.11, a clipper is used to show that interior results can be visualized and clipped.

- **Isosurfaces**

Isosurfaces represent 3-D scalar fields by drawing surfaces representing constant function values. Isosurface generating software packages allow more than one isosurface

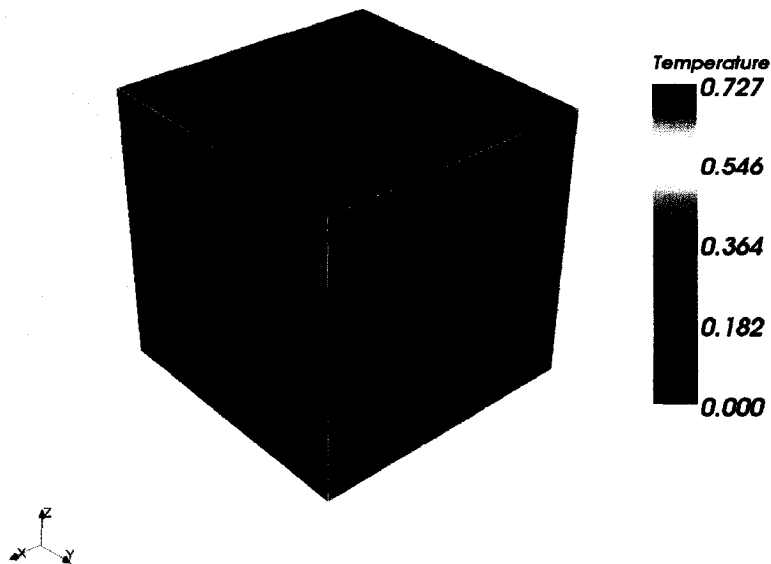


Figure 8.10: Slices of the interior of the cube

to be generated and rendered with varying levels of opacity and color. A legend can be drawn to show the range of values that each color represents. Figure 8.12 shows isosurfaces of the temperature distribution on the rotor.

- **Thresholding**

A threshold filter can be used to filter out the the scalar values which lie below, above, or between a threshold range. Figure 8.13 shows a temperature plot of the FGM rotor problem where the range of the threshold for temperature is set between 100 and 160 units.

8.5 MechVR: A Virtual Reality-Based Scientific Visualization Tool

8.5.1 CAVE: Cave Automatic Virtual Environment

The Cave Automatic Virtual Environment (CAVE) is an immersive virtual reality facility designed for the exploration of and interaction with spatially engaging environments. A

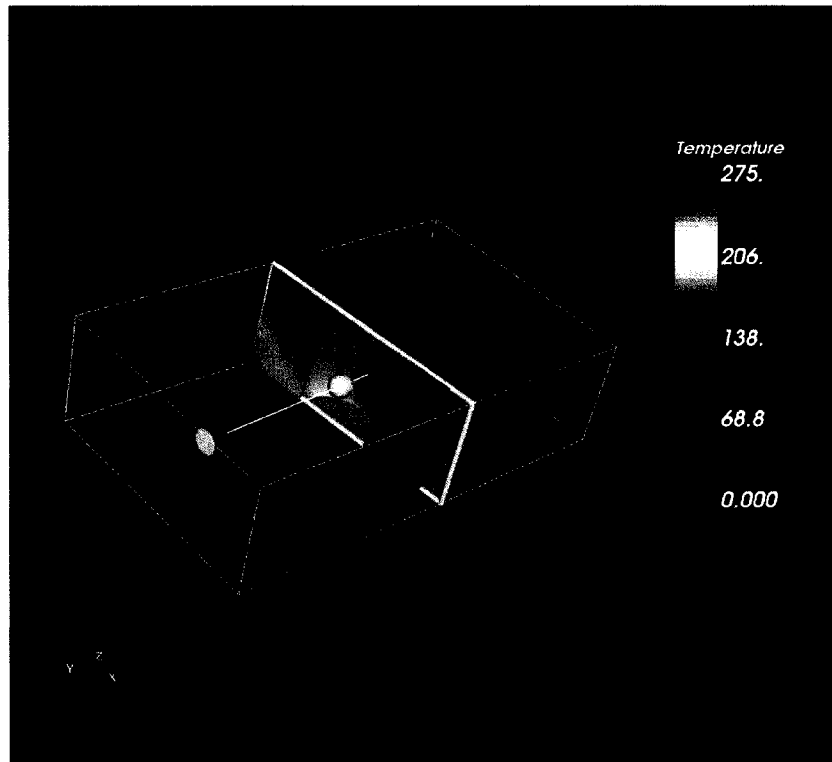


Figure 8.11: Clipper to show that interior results are obtained for the FGM rotor.

virtual environment constructed in the CAVE places the user inside the simulation and thereby provides the level of understanding necessary to accurately assess the design of the system being modeled [16]. The CAVE is a projection-based VR system that surrounds the viewer with 4 screens. The screens are arranged in a cube made up of three rear-projection screens for walls and a down-projection screen for the floor; that is, a projector overhead points to a mirror, which reflects the images onto the floor (see Figure 8.14). A viewer wears stereo shutter glasses and a six-degrees-of-freedom head-tracking device. As the viewer moves inside the CAVE, the correct stereoscopic perspective projections are calculated for each wall. A second sensor and buttons in a wand held by the viewer provide interaction with the virtual environment. The current implementation of the CAVE at NCSA uses three walls and the floor. The projected images are controlled by an SGI Onyx with two Infinite Reality graphics pipelines, each split into two channels. For testing, one can run the CAVE using any number of walls simultaneously. The number of CAVE walls used does not change the program. Audio system components are provided using an Indy workstation, speakers, a MIDI interface, and synthesizer. The Indy functions as a 'sound server' for the CAVE. Commands are sent to the workstation over the network, and it then either generates sounds internally, or controls the synthesizer.

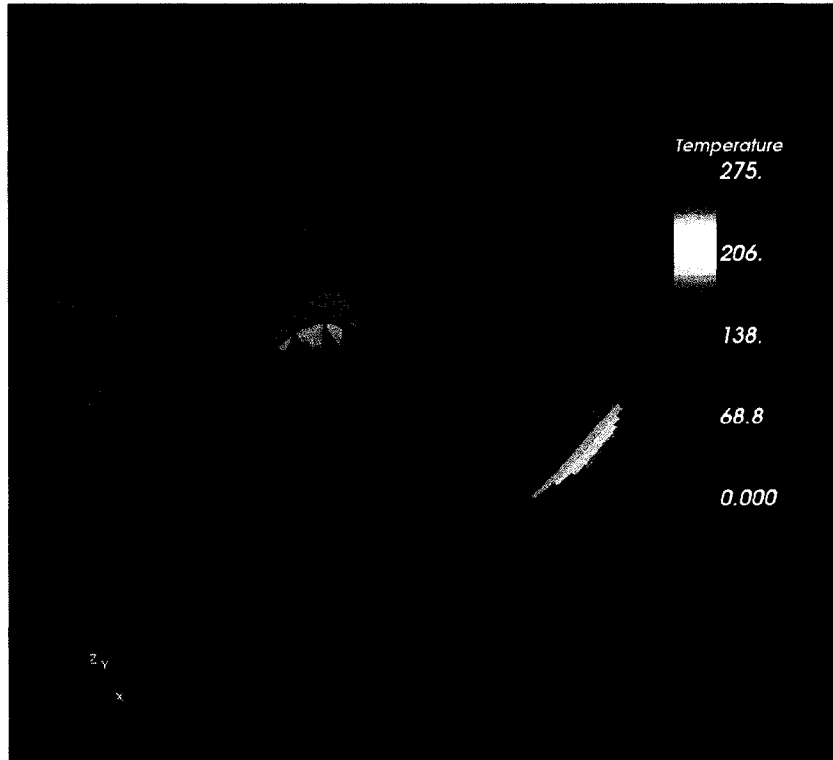


Figure 8.12: Isosurface generated for the temperature for the FGM rotor problem.

A diagram of the CAVE environment is shown in Figure 8.14.

8.5.2 The MechVR

MechVR (Mechanics Virtual Reality) is a preliminary VR application software, which was developed in our research group. It can visualize FEM and BEM data in the CAVE. It is preferable to visualize such data in a 3D interactive environment and allow the other researchers to share information in an effective and easy way. In this application, data sets obtained from mechanics computation, are taken as data source, and by using VTK the data is processed and rendered in the CAVE.

Programming Steps

The CAVE programming is done in C++ using VTK and the CAVE library functions, and the graphics is displayed using Performer. The VTK takes various types of data and produces final images depending on which pipelines the data go through. The flowchart followed in this application can be shown in a simple way in Figure 8.15. In this project, isosurface and slice are used to visualize individual stress component, and hyperstreamline is used to

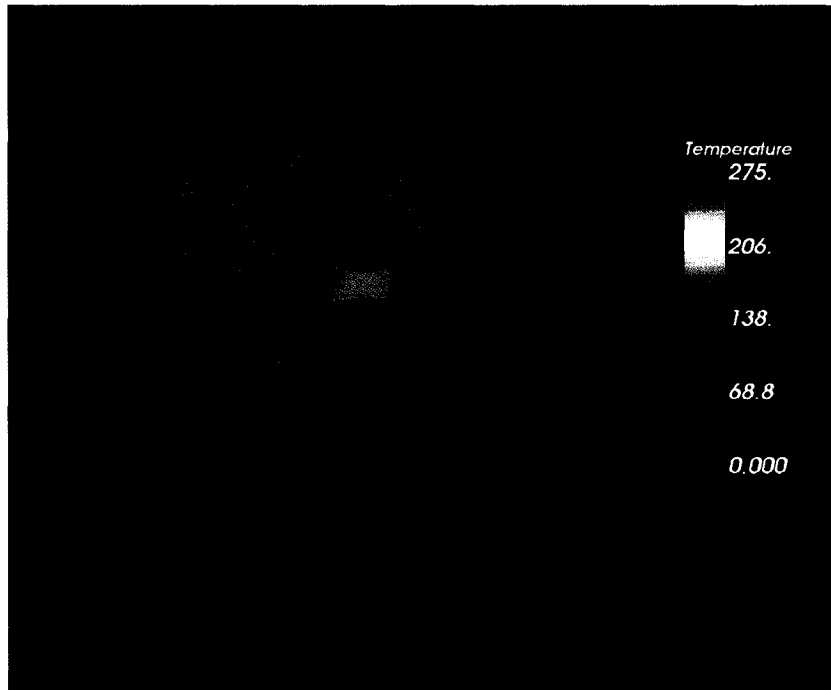


Figure 8.13: Thresholding the temperature from 100 to 160 units for the FGM rotor problem.

visualize stress tensors.

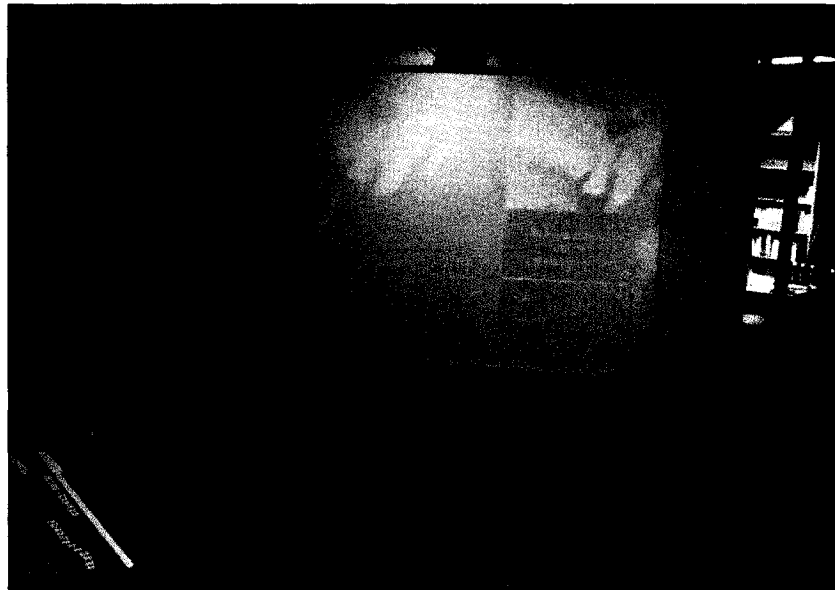
Figure 8.16 (a)-(c) show the isosurfaces, slices and the hyperstreamline of a cube subjected to point forces.

Application functionality and interaction

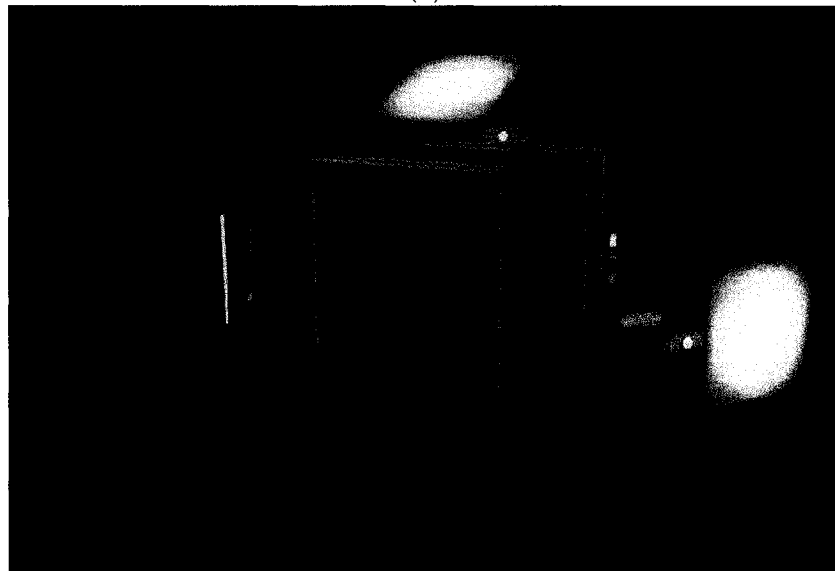
MechVR gives users the ability to create and modify a set of visualization tools for exploring the stress field from a given dataset. They also have the ability to change their viewpoint in the virtual environment, manipulate the dataset. Isosurfaces, slices, and hyperstreamlines are generated to represent certain stress component and stress tensors. An user interface is provided in the CAVE environment to allow new images being generated according to user-defined parameters.

Creation and manipulation

At present, MechVR provides three visualization tools; isosurfaces, slices and hyperstreamlines for stress components and tensors. Once the application is invoked, it reads the dataset and generate isosurfaces. In order to interact and manipulate, a user interface is provided, which is controlled by the wand with a pointer emanating from the wand in virtual reality.



(a)



(b)

Figure 8.14: NCSA CAVE: (a) Schematic Illustration (b) A cartoon model showing the projectors and the overall assembly.

By simply moving the pointer and pushing the buttons and sliders, the user is able to interact. Allowing the user to interact with data is essential in the VR application. In this project, we provide a preliminary user interface that consists of 6 buttons and 4 sliders to let the user adjust the viewing process. The design of the interface is illustrated in Figure 8.17. The buttons work in the following way: At the same time, only one of the three 'Isosurface',

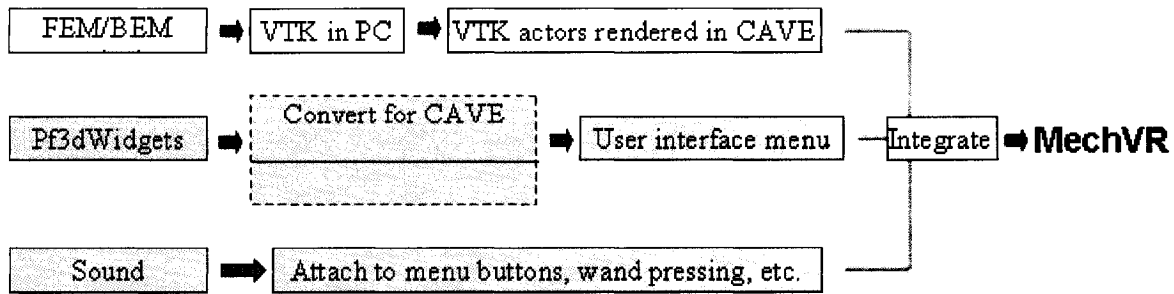


Figure 8.15: The simplified flowchart of MechVR.

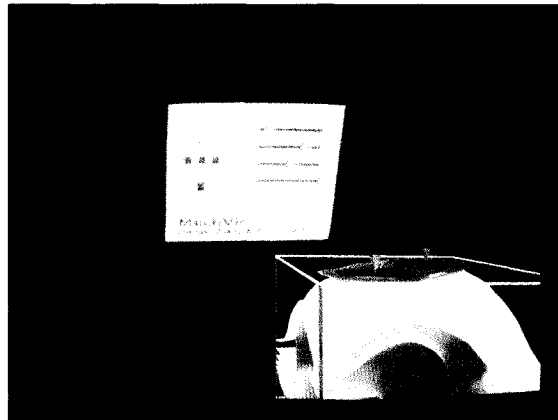
'Slice' and 'Hyperstreamline' buttons shall be active. The 'x', 'y' and 'z' buttons are attached to the 'Slice' button, so they can only be activated when the 'Slice' button is active. When the isosurface is activated then the sliders allow the user to specify the number of isosurfaces to be generated, the value ranges of isosurfaces, as well as the opacity of the rendering. The first two sliders named 'value 1' and 'value 2' give the value ranges when the isosurface button is active. The 'n layers' slider controls the number of isosurfaces to be generated. When the slice is activated the first two sliders give location ranges of the slice planes. The 'n layers' slider controls the number of slices to be generated.

Hyperstreamline

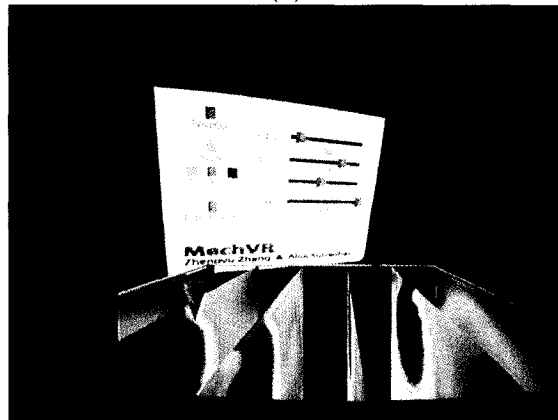
For the hyperstreamline feature, only the opacity can be controlled. Vector fields can be visualized effectively using streamlines, which represent the trajectory path of a particle in a flow field. Hyperstreamlines, an extension of the concept of streamlines to second-order tensor fields, provide the user with a continuous representation of the tensor field along a three dimensional path. Hyperstreamlines are defined by a trajectory path and a cross-sectional geometry at each point in that path [86]. The trajectory path of a hyperstreamline is essentially a streamline computed from one of the eigenvector fields. The cross-sectional geometry of a hyperstreamline is determined by the two remaining eigenvector fields and can either be an ellipse, a circle (if the eigenvectors are 'degenerate', or equal to each other), or a cross. Connecting these cross-sectional geometries along the trajectory path results in a hyperstreamline that either looks like a tube (elliptical/circular geometry) or a helix (cross geometry).

Sound effect

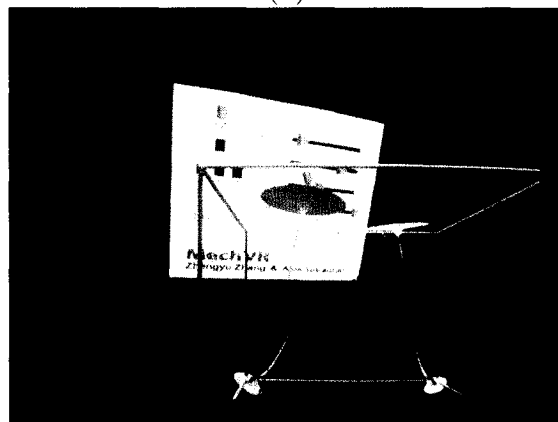
Sound effects are attached to the user interface, so that the scene becomes more dynamic and the user is notified about the undergoing process. Since the data is large, it takes a while



(a)



(b)



(c)

Figure 8.16: MechVR on the CAVE: (a) Isosurface (b) Slices and (c) hyperstreamlines.

for the computer to initialize the scene. Therefore a welcome message and a piece of music is provided. The sound effects are mainly bound with the button click, so that whenever a button is pressed, a corresponding voice text will notify the user of the current image shown.

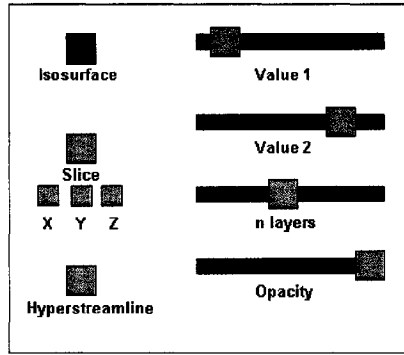


Figure 8.17: Preliminary user interface of MechVR

Moreover, when the update sign is given (pressing both wand buttons 1 and 2), the user is also notified about the process. Since the time taken to generate new images vary according to the parameters given, it may be desirable to have music tracks of different lengths to be sued accordingly. A text to speech reader software was used in order to generate the voice-sounds.

User Evaluation and future works

Figure 8.18 shows the author using the MechVR inside the CAVE at NCSA. Users provide constructive criticism for improvement [15, 108]. From an interactive perspective, a majority of users found the interface easy to use. The sliders and the manipulation seem effective. A significant amount of work remains to be done in order to make the application robust.

8.6 Web Visualization using VRML

The web has tremendously increased our ability to share information quickly and efficiently. Sharing data and visualization with other scientists are integral part of growing collaboration and connection among researchers. Previously either static pictures or pre-recorded visualization were available. This would not allow other researchers to interact with the visualization. There was no way to look from a different angle or change the parameters of the visualization. This problem has been circumvented by development of interactive 3D virtual environment over the internet. A 3D environment allows the user to navigate a scene, observe and manipulate an object.

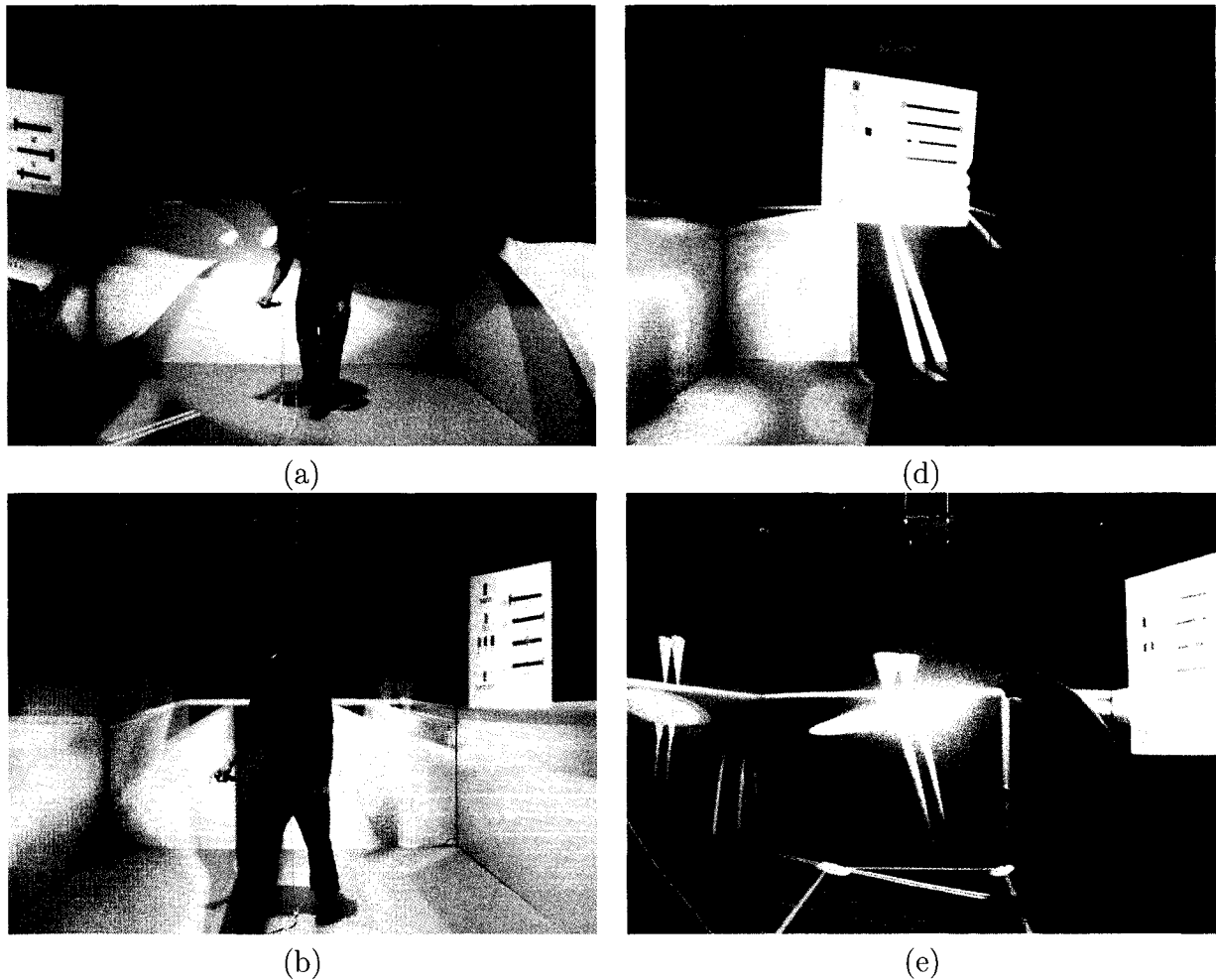


Figure 8.18: Demonstration of MechVR inside CAVE

8.6.1 Virtual Reality Modeling Language (VRML) visualization

Because of the need for interaction, a new type of visualization has appeared, which is referred as Virtual Reality Modeling Language (VRML) [7]. It is a platform independent modeling language use for creating three-dimensional virtual worlds and objects that can be displayed on the Internet. Using VRML, visualizations can be created in three-dimensional space. With the introduction of VRML 2.0, and later VRML 97 [39], it is now possible to build dynamic, interactive worlds where objects can be animated [128]. In addition, users can also interact with the objects. Using external authoring interface (EAI), users can also interact with VRML objects in the scene externally via JavaScript or java applet.

For better integration with the next-generation web technologies, which is expected to rely heavily on XML, the W3C is also working on X3D [40]. X3D is the new open standard

for 3D content on the web and it is designed to be compatible with existing VRML browsers and tools.

VRML is chosen for this project as it is a web standard and Plugins are readily available for major web browsers. In addition, it does not require expensive hardware or software, thus it can reach out to a wider audience. X3D is a new technology with great potential. However, it is still a relatively new technology and a suitable Plugin are not widely available and thoroughly evaluated.

VRML world files have the file extension .wrl (or .wrz for gzip compressed files) and require either a stand-alone application or web browser plug-in to be viewed. It is versatile, compact, extensible and constantly evolving. VRML is generally viewed within a Web browser like Netscape Navigator or Microsoft Internet Explorer. These browsers don't support VRML natively and thus a plug-in is required to view VRML content. VRML plug-ins are available for most platforms, the two most popular being: Cosmo Player, (for Windows, Mac, IRIX), Cortona (for Windows 9x/NT Mac, Windows CE).

8.6.2 Creating and viewing VRML models

In order to view VRML models in web browsers Cortona VRML Client may be used. Cortona VRML Client is a fast and highly interactive Web3D viewer. It works as a VRML plug-in for popular Internet browsers (Internet Explorer, Netscape Navigator, Mozilla, etc.) and office applications (Microsoft PowerPoint, Microsoft Word, etc).

In order to create VRML models, VTK has a filter called `vtkVRMLExporter` which is capable of exporting the scene to a VRML model. We modified the `ParaView` and included an option in the 'File' menu to save the data as a VRML output.

Figure 8.19 show screen shots of the VRML option in `ParaView` that we have created.

Figure 8.20 show screen shots of the a VRML model that we have generated of the mesh of the crack problem inside a cylinder (from chapter 7).

8.7 Remarks

In this chapter we have explored the techniques that can be used to visualize simulation results from computational methods, especially the BEM. For large scale datasets visualization is extremely important to process the results. We plan to introduce more visualization tools, functionalities, voice activated commands in the `MechVR` application. Also the Virtual Reality and the VRML visualization have also been investigated.

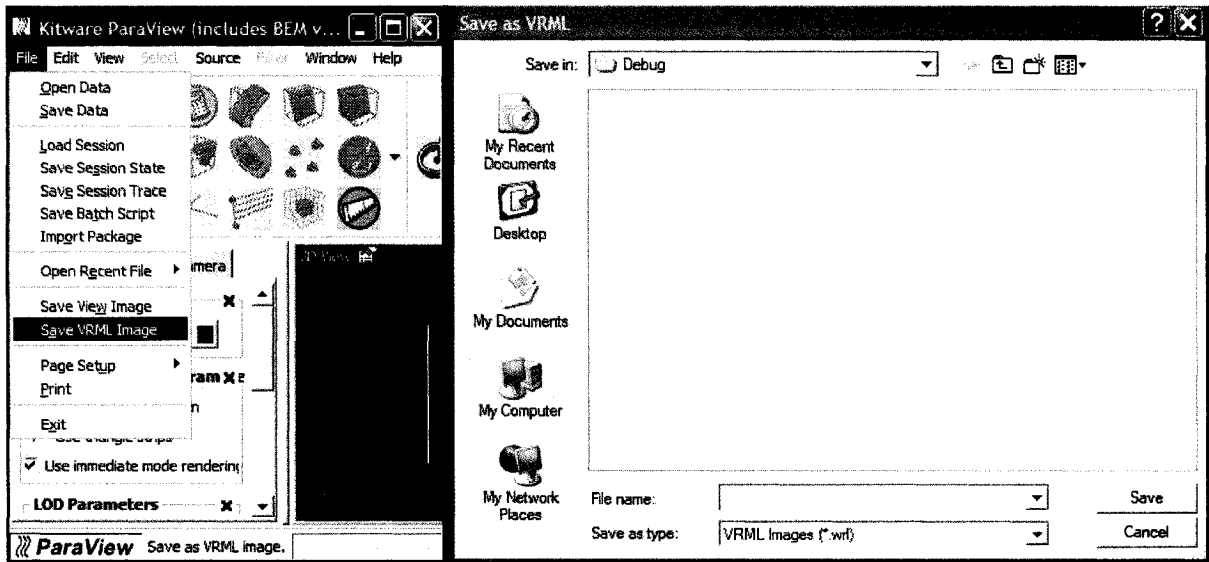


Figure 8.19: Screen shots of the VRML option in ParaView

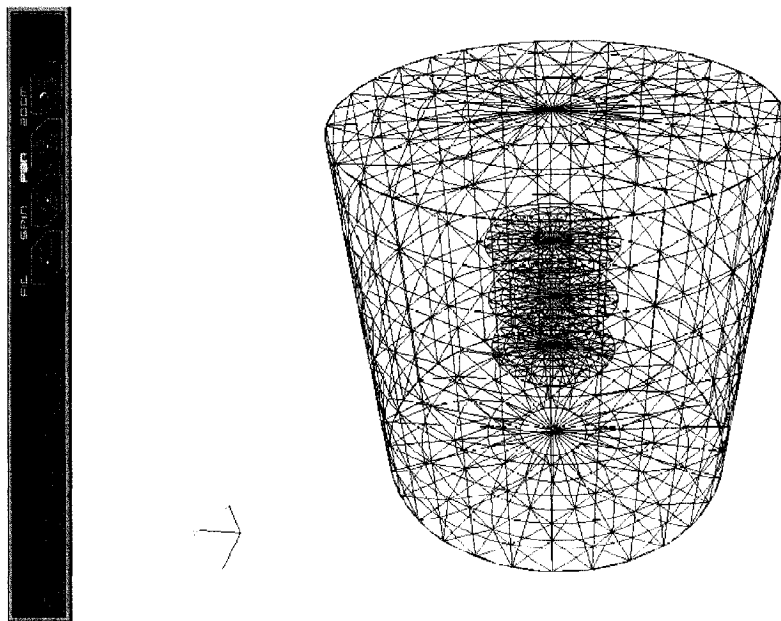


Figure 8.20: VRML model showing the mesh of the three crack problem (Chapter 7)

Chapter 9

Conclusions and Future Work

In this chapter a brief summary of the content and contribution of the study is presented followed by a number of suggestions for future work.

9.1 Concluding Remarks

Boundary element analysis has, for the most part, been limited to homogeneous or piecewise homogeneous media. In this work it was shown that BEM can be successfully applied to analyze heat transfer problems in functionally graded materials using a boundary-only formulation. In the Green's function approach, the Green's function is required to derive. But in this approach for each different variation different formulations are necessary. An exponential thermal conductivity variation was explored in this regards using the elegant symmetric Galerkin BEM. In Galerkin BEM evaluating the hypersingular integrals is one of the challenges. A simple direct 'limit to the boundary' algorithm using a hybrid analytical/numerical approach is presented. The same approach is used for evaluating less singular integrals as well. The proposed 'simple' boundary element method is an efficient technique because it can handle different classes of material variation. Moreover, it uses the standard homogeneous codes with simple changes. The presented numerical results based upon these formulation, were implemented in a Galerkin BEM framework. All the implementations presented are pure boundary-only formulations without any domain integral. The numerical studies agreed extremely well with available analytical solutions and finite element simulations. The investigation included steady state heat conduction, transient heat conduction and also crack problems. A Laplace transform Galerkin boundary element formulation was implemented in the the transient heat conduction problem. The principal computational difficulty with the LTBEM is the numerical inversion of the transform, which was handled accurately and efficiently by Stehfest's algorithm. BEM is best suited for crack problems

specially is 3D. The modeling becomes more efficient than finite element methods when multiple cracks are present. A ‘simple’ BEM for solving cracks in problems governed by the potential theory using the dual BEM technique is presented which can handle functional variation of thermal conductivity and several random cracks of various sizes and shapes. The implementation is carried out using the Galerkin BEM (non-symmetric), but the idea and development are applicable to collocation or other boundary element methods such as meshless or symmetric Galerkin BEM.

The contributions of this study are:

- A direct treatment of the hypersingular double integrals using a hybrid analytical/numerical approach applied to the hypersingular integrals that arise in the SGBEM formulation for heat conduction in an exponentially graded material is presented. The procedure for treating the hypersingular integral are applicable to other less singular integrals. The direct “limit to the boundary” approach for evaluation of the singular integrals is suitable for handling complicated Green’s function such as those obtained in FGM problems.
- A symmetric Galerkin boundary element analysis using the Green’s function approach is carried out for heat conduction problem on exponentially graded FGMs.
- The Green’s function for three-dimensional transient heat conduction (diffusion equation) for functionally graded materials (FGMs) is derived. The thermal conductivity and heat capacitance both vary exponentially in one coordinate. In the process of solving this diffusion problem numerically, a Laplace transform approach is used to eliminate the dependence on time. The fundamental solution in Laplace space is derived and the boundary integral equation formulation for the Laplace Transform Boundary Element Method (LTBEM) is obtained. The numerical implementation is performed using a Galerkin approximation, and the time-dependence is restored by numerical inversion of the Laplace transform.
- A novel simple boundary element technique to address problems of potential flow for nonhomogeneous media is presented. It is shown that for quadratic material variation, the nonhomogeneous problem can be transformed to a Laplace problem; for exponential variation, the problem can be transformed to a modified Helmholtz equation; and for trigonometric variation, the problem can be transformed to a standard Helmholtz equation. By simple modification of the boundary conditions, standard codes for homogeneous material problems are used.

- By simple variable transformation, transient heat conduction problems in functionally graded materials for three different classes of material variation (quadratic, exponential, trigonometric) can be transformed into the homogeneous diffusion problem. Moreover, the material variation can be in one, two or three dimensions. With easy changes in an existing BEM code for homogeneous materials, the FGM transient heat conduction problem with constant diffusivity can be solved. A Laplace transform Galerkin BEM formulation has been presented here in order to implement the methodology.
- A “simple BEM” for solving multiple cracks in problems governed by potential theory is presented. Steady state heat conduction problems with functionally graded thermal conductivity are investigated. Numerical problems with single and interacting cracks are solved and verified by the means of the FEM. A numerical example consisting of several random cracks of various sizes and shapes is presented to demonstrate the robustness of the present BEM formulation and implementation. A quadratic variation of thermal conductivity was considered in the examples, however, other gradations, such as trigonometric and exponential, can be readily solved by employing the present “simple BEM” technique (for crack problems). From the formulation point of view, a key observation is that if the jump in potential is used as the primary variable on the crack surface, then the displacement discontinuity approach is not directly applicable. The dual boundary element method, which employs the potential as the primary variable on the crack surfaces, is shown to be more suitable to treat the fracture problem.
- Visualization is an integral part of computational research. State of art visualization techniques and how they can be used for visualizing BEM results has been studied and explored. A virtual reality toolkit (MechVR) has been developed to visualize simulation results in CAVE. Some useful modules and extensions to the turnkey software ParaView has been proposed.

9.2 Suggestions for Future Works

Having the boundary integral representation for thermal analysis opens the possibility of developing efficient tools for optimization of FGM parameters (*e.g.*, material constants and geometry) and sensitivity analysis [139]. These topics are important for design and application of these new materials.

The present “simple BEM” leads naturally to several extensions. Although only interior problems were addressed, exterior problems can be treated on a similar fashion [17]. In

addition, fracture problems involving transient heat conduction with constant diffusivity can be easily solved by employing the Laplace transform technique of Sutradhar and Paulino [173]. The present formulation also offers room for extension to graded orthotropic media [9, 45].

Appendix A

A.1 Maple codes for analytical integration

The following codes were implemented with Maple 7.0. Only a few basic Maple operations, integration and substitution, are employed, and thus it is likely that, with relatively minor changes, these scripts would work with other symbolic computation systems. The code shows the analytical integration to extract the divergent terms for the coincident case and the edge adjacent case. The naming of variables follows the notation in this paper fairly closely, and it is therefore hoped that the codes are mostly self-explanatory. For convenience, references to the equations in the paper corresponding to the code are provided. However a few comment lines, which begin with the pound sign(`#`), are also included.

A.1.1 Analytical integration for coincident case

```
# This Maple file shows the analytical integration to extract divergent terms
# for the coincident case.

> restart;
> with(linalg):
> with(codegen,fortran);

# Initialize arrays
> phi:=array(0..2,0..1);
> Lterm:=array(0..3,0..1);
> phi_h:=array(0..3,0..1);
> jnp:=array(0..3);
```



```

# P --> P+ eps N
# Eq.(2.30)
> rh:=(eps^2+a^2*rho^2)^(1/2);
> jnr:=-eps*jp;

# Kernels
> ker:=3*jnr^2/rh^5-jp^2/rh^3+3*b00*jnr^2/rh^4+b00^2*jnr^2/rh^3
      -b00*jp^2/rh^2-b00^2*jnp[3]^2/rh;
# Eq.(2.26)

# Taylor expansion
> expo1:=b00*(-rh+alpha*rho);
> exp1:=1+expo1;
# Eq.(2.36)

# integrand
> ker:=ker*exp1;

# Loop for m=0 and m=1
> for j from 0 to 1 do

# first analytical integration
> zz:=int(rho^(j+1)*ker,rho=0..QR);
# Eq.(2.37)

# Simplification
> zz:=expand(zz);
> zz := subs((eps^2)^(5/2)=eps^5,1/(eps^2)^(5/2)=1/eps^5,
sqrt(a^2)=a,1/sqrt(a^2)=1/a,sqrt(eps^2)=eps,1/sqrt(eps^2)=1/eps,zz);
> zz:=expand(zz);
> zz:= subs(ln(eps^2)=2*log_e,zz);

# log_e term which are not the real divergent term
> zz:= collect(zz,log_e);
> zz_log_koef:=coeff(zz,log_e,1);
> zz_log_koef:=simplify(zz_log_koef);

```

```

> zz_log_koef:=simplify(subs(eps=0,zz_log_koef));
> zz:=coeff(zz,loge,0);

# second polar transformation
> zz := subs(QR=Lambda,zz);
> zz := zz*sp;
> zz := expand(zz);
> zz := normal(zz);
> zz:=expand(zz);
> zz:=simplify(zz);
> zz:=subs(ln(a*Lambda+sqrt(eps^2+a^2*Lambda^2))=ln(2*a*Lambda),zz);
> zz:=subs(arctan(a*Lambda/eps)=Pi/2,zz);
> zz:=subs(ln(eps^2+a^2*Lambda^2)=2*ln(a*Lambda),zz);
> zz:=expand(zz);

# Second Taylor expansion
> expo2:=b00*(2*zz2*Lambda);
> exp2:=1+expo2+expo2^2/2;
# Eq. (2.51)
> zz:=zz*exp2;

# Second analytical integration
# Loop for s=0,1,2

> for k from 0 to 2 do
> phi[k,j]:= int(Lambda^k*zz,Lambda=0..QL);
# Eq. (2.52)
> phi[k,j]:= subs((eps^2)^(5/2)=eps^5,1/(eps^2)^(5/2)=1/eps^5,
                (eps^2)^(3/2)=eps^3,1/(eps^2)^(3/2)=1/eps^3,sqrt(a^2)=a,1/sqrt(a^2)=1/a,
                sqrt(eps^2)=eps,1/sqrt(eps^2)=1/eps,phi[k,j]);
> phi[k,j]:=subs(sqrt(eps^2+a^2*QL^2)=a*QL,1/sqrt(eps^2+a^2*QL^2)
                =1/(a*QL),phi[k,j]);
> phi[k,j]:=subs(arctan(a*QL/eps)=pi/2,phi[k,j]);
> phi[k,j]:= subs(ln((eps^2+a^2*QL^2)/eps^2)=ln(eps^2+a^2*QL^2)-ln(eps^2),phi[k,j]);
> phi[k,j]:= subs(ln(eps^2)=2*log_e,phi[k,j]);
> phi[k,j]:= expand(phi[k,j]);

```

```

> Lterm[k,j] := coeff(phi[k,j],loge);
> Lterm[k,j] := subs(eps=0,Lterm[k,j]);
# Eq.(2.55)
> phi[k,j] := coeff(phi[k,j],loge,0);
> phi[k,j] := collect(phi[k,j],eps);

# set eps ---> 0
> phi[k,j] := subs(eps=0,phi[k,j]);
> phi[k,j] := normal(expand(phi[k,j]));
> phi[k,j]:=subs(ln(a^2*QL^2)=2*ln(a*QL),1/(a^2*QL^2)^(3/2)=1/(a^3*QL^3),
(a^2*QL^2)^(3/2)=(a^3*QL^3),phi[k,j]);
> phi[k,j] := expand(phi[k,j]);

# check with Laplace equation for homogenous material
# b00:=0;
> phi_h[k,j] := simplify(subs(b00=0,phi[k,j]));
> Lterm[k,j] ;
> od;
> od;

# print results
# m=0
> for k from 0 to 2 do
> phi[k,0];
> phi_h[k,0];
> Lterm[k,0];
> od;

# m=1
> for k from 0 to 2 do
> phi[k,1];
> phi_h[k,1];
> Lterm[k,1];
> od;

# Convert to Fortran

```

```
> fortran(phi);
> fortran(Lterm);
```

A.1.2 Analytical integration for edge adjacent case

```
# This Maple file shows the analytical integration to extract divergent terms
# for the edge adjacent case.
```

```
> restart;
> with(linalg):
> with(codegen,fortran):
```

```
# Initialize arrays
```

```
> jnp:=array(1..3);
> jnq:=array(1..3);
> phi := array(0..2);
> sng := array(0..2);
```

```
# P --> P+ eps N
```

```
> rh := (eps^2 + eps*a1*Lambda + a2*Lambda^2)^(1/2);
```

```
# Eq. (2.65)
```

```
> ##
```

```
> ## kernel
```

```
> ## Note: cos(psi) factor from jacobian product omitted
```

```
> ##
```

```
> jNR:=(j1p*Lambda-jnpL*eps);
```

```
> jnR:=j1q*Lambda-jnqL*eps;
```

```
> nz:=jnq[3];
```

```
> Nz:=jnp[3];
```

```
# Kernels
```

```
# Eq. (2.26)
```

```
> hyp:=3*jnR*jNR/rh^5+3*b00*jnR*jNR/rh^4+(b00^2*jnR*jNR-b00*(Nz*jnR-nz*jNR)
      -ndN)/rh^3-b00*((b00*(Nz*jnR-nz*jNR)+ndN)/rh^2)-b00^2*Nz*nz/rh;
```

```
> hyp:=Lambda^2*hyp;
```

```

# Taylor expansion
> exp_term:=1;
# Eq.(2.67)

# integrand
> exp_hyp:=exp_term*hyp;

# Loop for s=0,1,2
> ## powers from shape function product
> for ll from 0 to 2 do
> phi[ll]:= Lambda^ll*exp_hyp;

# Analytical integration
> phi[ll] := int(phi[ll],Lambda=0..QL);
# Eq.(2.63)

# Simplification
> phi[ll] := subs((eps^2)^(5/2)=eps^5,ln((eps*a1+2*eps*sqrt(a2))/a2^(1/2))
                =loge+ln(a1/a2^(1/2)+2),
> sqrt(eps^2*a1^2-4*a2*eps^2)=eps*sqrt(a1^2-4*a2),ln(eps^2)=2*loge,
> arctanh(eps*a1/(eps^2*a1^2-4*a2*eps^2)^(1/2))=arctanh(a1/(a1^2-4*a2)^(1/2)),
> arctanh((2*a2*QL+eps*a1)/(eps^2*a1^2-4*a2*eps^2)^(1/2))=1/2*ln(2*a2*QL)
                -1/2*ln(-2*a2*QL),
> 1/(eps^2)^(5/2)=1/eps^5,1/sqrt(eps^2*a1^2-4*a2*eps^2)=1/(eps*sqrt(a1^2-4*a2))
,ln((eps*a1+2*sqrt(eps^2)*sqrt(a2))/a2^(1/2)) = loge+ln(a1/a2^(1/2)+2),
(eps^2)^(3/2)=eps^3,1/(eps^2)^(3/2)=1/eps^3
> ,phi[ll]);
> phi[ll] := expand(phi[ll]);

# set eps ---> 0
> phi[ll] := subs(eps=0,phi[ll]);
> sng[ll] := normal(coeff(phi[ll],loge,1));
# Eq.(2.68)
> phi[ll] := normal(coeff(phi[ll],loge,0));
> phi[ll]:=expand(phi[ll]);

```

```

> phi[11]:=simplify(phi[11]);
> end do;
# Convert to Fortran
> fortran(phi);

```

A.2 Analytical solution of the FGM cube problem (Example 3 of Section 4.7)

The problem described in Section 4.7.3 is one dimensional in nature. The governing differential equation is,

$$\frac{\partial^2 u}{\partial x^2} + 2\beta \frac{\partial u}{\partial x} = \frac{1}{\alpha} \frac{\partial u}{\partial t} \quad (\text{A.1})$$

The thermal conductivity and the specific heat are taken to be

$$\begin{aligned} k(x) &= k_0 e^{2\beta x} \\ c(x) &= c_0 e^{2\beta x} \end{aligned}$$

and the boundary conditions and initial condition are

$$\begin{aligned} u(0, t) &= 0 \\ u(L, t) &= T \\ u(x, 0) &= 0 \end{aligned} \quad (\text{A.2})$$

Since the boundary condition of this problem is inhomogeneous and the problem is transient, it is better to express the temperature as the sum of two distributions. One will represent the steady state distribution (independent of t) and the other will represent the transient response. The transient response approaches zero as t increases indefinitely.

$$u(x, t) = u_s(x) + v_t(x, t) \quad (\text{A.3})$$

The steady state solution is

$$u_s(x) = T \frac{1 - e^{-2\beta x}}{1 - e^{-2\beta L}} \quad (\text{A.4})$$

and the transient solution is,

$$v_t(x, t) = u(x, t) - T \frac{1 - e^{-2\beta x}}{1 - e^{-2\beta L}} \quad (\text{A.5})$$

This solution will hold for homogeneous boundary conditions. So the modified problem is,

$$\frac{\partial^2 v}{\partial x^2} + 2\beta \frac{\partial v}{\partial x} = \frac{1}{\alpha} \frac{\partial v}{\partial t} \quad (\text{A.6})$$

$$v(0, t) = 0$$

$$v(L, t) = 0$$

$$v(x, 0) = -T \frac{1 - e^{-2\beta x}}{1 - e^{-2\beta L}} \quad (\text{A.7})$$

To solve the problem we use the separation of variables, i.e.

$$v(x, t) = X(x)T(t) \quad (\text{A.8})$$

Substituting this assumed form and separating the variables we get,

$$\frac{\frac{\partial^2 X}{\partial x^2} + 2\beta \frac{\partial X}{\partial x}}{X} = \frac{\frac{1}{\alpha} \frac{\partial T}{\partial t}}{T} \quad (\text{A.9})$$

Thus setting each side of the above equation equal to $-\lambda^2$ leads to,

$$\frac{\partial^2 X}{\partial x^2} + 2\beta \frac{\partial X}{\partial x} + \lambda^2 X = 0 \quad (\text{A.10})$$

$$\frac{1}{\alpha} \frac{\partial T}{\partial t} + \lambda^2 T = 0 \quad (\text{A.11})$$

Now let $X = e^{sx}$ be the solution, for which the associated characteristic equation is,

$$s^2 + 2\beta s + \lambda^2 = 0 \quad (\text{A.12})$$

with,

$$s = -\beta \pm i\sqrt{\lambda^2 - \beta^2} \quad (\text{A.13})$$

Substituting the value of s we get the general solution,

$$X = e^{-\beta x} \left(A_1 e^{i\sqrt{\lambda^2 - \beta^2} x} + A_2 e^{-i\sqrt{\lambda^2 - \beta^2} x} \right) \quad (\text{A.14})$$

The term in parenthesis can be rewritten in terms of trigonometric functions, i.e.

$$X(x) = e^{-\beta x} \left(B_1 \cos \sqrt{\lambda^2 - \beta^2} x + B_2 \sin \sqrt{\lambda^2 - \beta^2} x \right) \quad (\text{A.15})$$

From Eq. (A.8), we get the general solution,

$$T(t) = C e^{-\alpha \lambda^2 t} \quad (\text{A.16})$$

Hence, we obtain

$$v(x, t) = e^{-\beta x} \left(A \cos \sqrt{\lambda^2 - \beta^2} x + B \sin \sqrt{\lambda^2 - \beta^2} x \right) e^{-\alpha \lambda^2 t} \quad (\text{A.17})$$

To satisfy the boundary condition at $x = 0$,

$$v(0, t) = 0 = A e^{-\alpha \lambda^2 t} \quad (\text{A.18})$$

and therefore A must be zero. To satisfy the boundary condition at $x = L$,

$$v(L, t) = 0 = e^{-\beta L} B \sin \left(\sqrt{\lambda^2 - \beta^2} L \right) e^{-\alpha \lambda^2 t} \quad (\text{A.19})$$

and since $B \neq 0$, we obtain the following equality

$$\sin \sqrt{\lambda^2 - \beta^2} L = 0$$

This implies,

$$\sqrt{\lambda^2 - \beta^2} L = n\pi$$

or

$$\lambda^2 = \frac{n^2 \pi^2}{L^2} + \beta^2 \quad (\text{A.20})$$

where $n = 1, 2, 3, \dots$, so these are the eigenvalues and the associated eigenfunction is

$$v_n = B_n \sin \frac{n\pi x}{L} e^{-\beta x} e^{-\left(\frac{n^2 \pi^2}{L^2} + \beta^2\right) \alpha t} \quad (\text{A.21})$$

Now by the superposition principle the function v is

$$v(x, t) = \sum_{n=1}^{\infty} B_n \sin \frac{n\pi x}{L} e^{-\beta x} e^{-\left(\frac{n^2\pi^2}{L^2} + \beta^2\right)\alpha t} \quad (\text{A.22})$$

and B_n will be selected such that it satisfies the initial condition. At $t = 0$, the above expression becomes

$$-T \frac{1 - e^{-2\beta x}}{1 - e^{-2\beta L}} = \sum_{n=1}^{\infty} B_n \sin \frac{n\pi x}{L} e^{-\beta x} \quad (\text{A.23})$$

Recognizing this expression as a half-range expansion of a Fourier sine series we get

$$\begin{aligned} B_n &= -\frac{2T}{L(1 - e^{-2\beta L})} \int_0^L (e^{\beta x} - e^{-\beta x}) \sin \frac{n\pi x}{L} dx \\ &= -\frac{2Te^{\beta L}}{\beta^2 L^2 + n^2\pi^2} \left[\beta L \sin n\pi \frac{1 + e^{-2\beta L}}{1 - e^{-2\beta L}} - n\pi \cos n\pi \right]. \end{aligned} \quad (\text{A.24})$$

Hence the analytical solution to this problem is

$$u(x, t) = u_s(x) + v_t(x, t) \quad (\text{A.25})$$

$$= T \frac{1 - e^{-2\beta x}}{1 - e^{-2\beta L}} + \sum_{n=1}^{\infty} B_n \sin \frac{n\pi x}{L} e^{-\beta x} e^{-\left(\frac{n^2\pi^2}{L^2} + \beta^2\right)\alpha t} \quad (\text{A.26})$$

and thus the flux is

$$\begin{aligned} q(x, t) &= -k(x) \frac{\partial u}{\partial x} \\ &= -k(x) \left[\frac{2\beta T e^{-2\beta x}}{1 - e^{-2\beta L}} + \sum_{n=1}^{\infty} B_n e^{-\beta x} e^{-\left(\frac{n^2\pi^2}{L^2} + \beta^2\right)\alpha t} \left(\frac{n\pi}{L} \cos \frac{n\pi x}{L} - \beta \sin \frac{n\pi x}{L} \right) \right] \end{aligned} \quad (\text{A.27})$$

where

$$B_n = -\frac{2Te^{\beta L}}{\beta^2 L^2 + n^2\pi^2} \left[\beta L \sin n\pi \frac{1 + e^{-2\beta L}}{1 - e^{-2\beta L}} - n\pi \cos n\pi \right]. \quad (\text{A.28})$$

A.3 ABAQUS user subroutine

The ABAQUS user subroutine UMATHT for graded elements with variable conductivity is presented here. It is written in Fortran language.

```
c      ABAQUS  User subroutine umatht
c      This user subroutine implements graded elements with variable
c      conductivity in ABAQUS. It can incorporate any functional
```

```

c variation of heat conductivity and specific heat.

      subroutine umatht(u,dudt,dudg,flux,dfdt,dfdg,statev,temp,
$      dtemp,dtemdx,time,dtime,predef,dpred,cmname,ntgrd,nstatv,
$      props,nprops,coords,pnewdt,noel,npt,layer,kspt,kstep,kinc)
c
      include 'aba_param.inc'
      character*80 cmname
      dimension dudg(ntgrd),flux(ntgrd),dfdt(ntgrd),
$      dfdg(ntgrd,ntgrd),statev(nstatv),dtemdx(ntgrd),time(2),
$      predef(1),dpred(1),props(nprops),coords(3)
c
      read in properties
c
      exponential
c
      beta = 1.5
c
      cond=5.0*exp(2.0*beta*coords(3))
c
      trigonometric
c
      cond=5.0*(cos(coords(3))+4.68392*sin(coords(3)))**2.d0
c
      quadratic
      cond=20*(1+420.7*coords(3))**2.0
      specht = 0.0
c
      input specific heat
      dudt = specht
      deltu = dudt*dtemp
      u = u+deltu
c
      input flux = -[k]*{dtemdx}
      do i=1, ntgrd
         flux(i) = -cond*dtemdx(i)
      end do
c
      input isotropic conductivity
      do i=1, ntgrd
         dfdg(i,i) = -cond
      end do
      return
      end

```

References

- [1] ABAQUS Version 6.2. Hibbitt, Karlsson and Sorensen, Inc., 2002.
- [2] S. Ahmad and P. K. Banerjee. Free vibration analysis of BEM using particular integrals. *Journal of Engineering Mechanics*, 112:682–695, 1986.
- [3] A. Aimi and M. Diligenti. Hypersingular kernel integration in 3D Galerkin boundary element method. *Journal of Computational and Applied Mathematics*, 138:51–72, 2002.
- [4] M. H. Aliabadi. Dual boundary element method for three-dimensional fracture mechanics analysis. *Engineering Analysis with boundary elements*, 10:161–171, 1992.
- [5] W. T. Ang, J. Kusuma, and D. L. Clements. A boundary element method for a second order elliptic partial differential equation with variable coefficients. *Engineering Analysis with Boundary Elements*, 18:311–316, 1996.
- [6] Y. Bansal and M. J. Pindera. Efficient reformulation of HOTFGM: Heat conduction with variable thermal conductivity. Technical Report NASA CR 211910, NASA-Glenn Research Center, Cleveland, OH, 2002, 1992.
- [7] K.-P. Beier. Web-based virtual reality in design and manufacturing applications. In *Proceedings of COMPIT'2000*, pages 45–55, 2000.
- [8] U. A. Benz and J. J. Rencis. Coupling two-dimensional and axisymmetric boundary element zones for transient heat transfer applications. *Engineering Analysis with Boundary Elements*, 26(5):455–467, 2002.
- [9] J. R. Berger, P. A. Martin, V. Mantic, and L. J. Gray. Fundamental solutions for steady-state heat transfer in an exponentially-graded anisotropic material. *Zeitschrift fr Angewandte Mathematik und Physik*, 2004. (in press).

- [10] F. F. Bernardon, C. A. Pagot, J.L.D. Comba, and C.T. Silva. The use of virtual reality in interactive finite element analysis- a state of the art report. Technical Report 01:8, Department of Structural Mechanics, Chalmers University of Technology, Gteborg, Sweden, 2002.
- [11] R. Bialecki and G. Kuhn. Boundary element solution of heat conduction problems in multizone bodies of nonlinear materials. *International Journal for Numerical Methods in Engineering*, 36:799–809, 1993.
- [12] M. Bonnet. *Boundary Integral Equation Methods for Solids and Fluids*. Wiley and Sons, England, 1995.
- [13] M. Bonnet, G. Maier, and C. Polizzotto. Symmetric Galerkin boundary element method. *ASME Applied Mechanics Review*, 51(11):669–704, 1998.
- [14] H. Borouchaki and P. L. George. Aspects of 2-D Delaunay mesh generation. *International Journal for Numerical Methods in Engineering*, 40:1957–1975, 1998.
- [15] D. Bowman, E. Kruijff, J. LaViola, and I. Poupyrev. *3D User Interfaces: Theory and Practice*. Addison-Wesley, 2004.
- [16] S. Bradshaw, T. Canfield, and J. Kokinis and T. Disz. An interactive virtual environment for finite element analysis. In *Proceedings of High Performance Computing '95*, 1995.
- [17] C. A. Brebbia and J. Dominguez. *Boundary Elements: An Introductory Course*. WIT Press, Boston, Southampton, 1992.
- [18] C. A. Brebbia, J. C. F. Telles, and L. C. Wrobel. *Boundary Element Techniques*. Springer-Verlag, Berlin and New York, 1984.
- [19] J. C. Bruch and G. Zyvoloski. Transient two dimensional heat conduction problems solved by the finite element method. *International Journal for Numerical Methods in Engineering*, 8:481–494, 1974.
- [20] S. Bryson. Virtual reality in scientific visualization. *Commun. ACM*, 39(5):62–71, 1996.
- [21] A. Carini, M. Diligenti, P. Maranesi, and M. Zanella. Analytical integrations for two dimensional elastic analysis by the symmetric Galerkin boundary element method. *Computational Mechanics*, 23:308–323, 1999.

- [22] Angelo Carini and Alberto Salvadori. Analytical integrations 3D BEM. *Computational Mechanics*, 28:177–185, 2002.
- [23] E. M. Carrillo-Heian, C. Unuvar, J. C. Gibeling, G. H. Paulino, and Z. A. Munir. Simultaneous synthesis and densification of niobium silicide/niobium composites. *Scripta Materialia*, 45:405–412, 2001.
- [24] H. Carslaw and J. Jaeger. *Conduction of heat in Solids*. Oxford University Press, London, 2nd edition, 1959.
- [25] U. Chang, C. S. Kang, and D. J. Chen. The use of fundamental Green’s functions for the solution of problems of heat conduction in anisotropic media. *International Journal of Heat and Mass*, 16:1905–1918, 1973.
- [26] M.K. Chati and S. Mukherjee. Evaluation of gradients on the boundary using fully regularized hypersingular boundary integral equations. 135:41–45, 1999.
- [27] M.K Chati and S. Mukherjee. The boundary node method for three-dimensional problems in potential theory. 47:1523–1547, 2000.
- [28] S. Mukherjee, M. K. Chati and Y.X. Mukherjee. The boundary node method for three-dimensional linear elasticity. 46:1163–1184, 1999.
- [29] S. Mukherjee, M. K. Chati and G.H. Paulino. The meshless hypersingular boundary node method for three-dimensional potential theory and linear elasticity problems. 25:639–653, 2001.
- [30] G. H. Paulino, M. K. Chati and S. Mukherjee. The meshless standard and hypersingular boundary node methods - applications to error estimation and adaptivity in three-dimensional problems. 50:2233–2269, 2001.
- [31] H. T. Chen and C. K. Chen. Hybrid Laplace transform/finite difference method for transient heat conduction problems. *International Journal for Numerical Methods in Engineering*, 26:1433–1447, 1988.
- [32] H. T. Chen and J.-Y. Lin. Application of the Laplace transform to non-linear transient problems. *Applied Mathematical Modeling*, 15:144–151, 1991.
- [33] A-H. D. Cheng, Y. Abousleiman, and T. Badmus. A Laplace transform bem for axysymmetric diffusion utilizing pre-tabulated Green’s function. *Engineering Analysis with Boundary Elements*, 9:39–46, 1992.

- [34] A.H.-D. Cheng. Darcy's flow with variable permeability: a boundary integral solution. *Water Resources Research*, 20:980–984, 1984.
- [35] A.H.-D. Cheng. Heterogeneities in flows through porous media by the boundary element method. In C.A. Brebbia, editor, *Topics in Boundary Element Research, Vol. 4: Applications in Geomechanics*, chapter 6, pages 129–144. Springer-Verlag, 1987.
- [36] C. S. Co, B. Hamann, and K. I. Joy. Iso-splatting: A Point-based Alternative to Isosurface Visualization. In J. Rokne, W. Wang, and R. Klein, editors, *Proceedings of Pacific Graphics 2003*, pages 325–334, October 8–10 2003.
- [37] H. B. Coda and W. S. Venturini. Further improvements on 3-D treatment bem elastodynamic analysis. *Engineering Analysis with Boundary Elements*, 17:231–243, 1996.
- [38] H. B. Coda and W. S. Venturini. A simple comparison between two 3D time domain elastodynamic boundary element formulations. *Engineering Analysis with Boundary Elements*, 17:33–44, 1996.
- [39] The VRML Consortium. The virtual reality modeling language, 1997.
- [40] The Web3D Consortium. Extensible 3d (x3d 8482;) graphics, 2003.
- [41] S. L. Crouch. Solution of plane elasticity problems by the displacement discontinuity method. *International Journal for Numerical Methods in Engineering*, 10:301–343, 1976.
- [42] S. L. Crouch and A. M. Starfield. *Boundary Element Methods in Solid Mechanics*. George Allen and Unwin, London, 1983.
- [43] K. S. Crump. Numerical inversion of Laplace transforms using a Fourier series approximation. *Journal of the Association for Computing Machinery*, 23:89–96, 1974.
- [44] D. A. S. Curran, M Cross, and B A Lewis. A preliminary analysis of boundary element methods applied to parabolic differential equations. In C. A. Brebbia, editor, *New Developments in boundary element methods*, pages 179–190. Computational Mechanics Publications, Southampton, 1980.
- [45] W. S. Budhi D. L. Clements DL. A boundary element method of the solution of a class of steady-state problems for anisotropic media. *Journal of Heat Transfer*, 19:462–465, 1999.

- [46] L. D'Amore, G. Laccetti, and A. Murli. An implementation of a Fourier series method for the numerical inversion of the Laplace transform. *ACM Transactions on Mathematical Software*, 25:279–305, 1999.
- [47] B. Davies and B. Martin. Numerical inversion of the Laplace transform: A survey and comparison of methods. *Journal of Computational Physics*, 33:1–32, 1979.
- [48] E. Divo and A. J. Kassab. Generalized boundary integral equation for heat conduction in non-homogeneous media: recent developments on the sifting property. *Engineering Analysis with Boundary Elements*, 22:221–234, 1998.
- [49] E. Divo and A. J. Kassab. A generalized bem for steady and transient heat conduction in media with spatially varying thermal conductivity. In M. Goldberg, editor, *Boundary Integral Methods: Numerical and Mathematical Aspects*, pages 37–76. Computational Mechanics Publications, 1999.
- [50] E. Divo and A. J. Kassab. *Boundary Element Method for Heat Conduction: with Applications in Non-Homogeneous Media, Topics in Engineering Series Vol. 44*. WIT Press, Billerica, MA, 2002.
- [51] Q. Du and D. Wang. Tetrahedral mesh generation and optimization based on centroidal Voronoi tessellation. *International Journal for Numerical Methods in Engineering*, 56:1355–1373, 2003.
- [52] Q. Du and D. Wang. Constrained boundary recovery for three dimensional Delaunay triangulations. *International Journal for Numerical Methods in Engineering*, 61:1471–1500, 2004.
- [53] H. Dubner and J. Abate. Numerical inversions of Laplace transforms by relating them to the finite Fourier cosine transform. *Journal of the Association for Computing Machinery*, 15:115–223, 1968.
- [54] D. G. Duffy. On the numerical inversion of Laplace transforms: Comparison of three new methods on characteristic problems from applications. *ACM Transactions on Mathematical Software*, 19:333–359, 1993.
- [55] N. A. Dumont, R. A. P. Chaves, and G. H. Paulino. The hybrid boundary element method applied to functionally graded materials. In C. A. Brebbia, A. Tadeu, and V. Popov, editors, *Boundary Elements XXIV, Series: Advances in Boundary Elements*, volume 1, pages 267–276, Southampton, 2002. Computational Mechanics Publication.

- [56] F. Durbin. Numerical inversion of Laplace transforms: Efficient improvement to Dubner and Abate's method. *Journal of the Association for Computing Machinery*, 17:371–376, 1974.
- [57] V. J. Ervin and E. P. Stephan. A boundary element Galerkin method for a hypersingular integral equation on open surfaces. *Math. Meth. Appl. Sci.*, 13:281–289, 1990.
- [58] R. Fiedler and J. Norris. Massively parallel visualization on linux clusters with Rocketeer Voyager. In *Proceedings of Linux Clusters: the HPC Revolution*, 2001.
- [59] A. Frangi. Regularization of boundary element formulations by the derivative transfer method. In V. Sladek and J. Sladek, editors, *Singular Integrals in the Boundary Element Method*, Advances in Boundary Elements, chapter 4, pages 125–164. Computational Mechanics Publishers, 1998.
- [60] A. Frangi. Fracture propagation in 3D by the symmetric Galerkin boundary element method. *International Journal of Fracture*, 116:313–330, 2002.
- [61] A. Frangi and G. Novati. Symmetric BE method in two-dimensional elasticity: evaluation of double integrals for curved elements. *Computational Mechanics*, 19:58–68, 1996.
- [62] A. Frangi, G. Novati, R. Springhetti, and M. Rovizzi. 3D fracture analysis by the symmetric Galerkin BEM. *Computational Mechanics*, 28:220–232, 2002.
- [63] P. J. Frey, H. Borouchaki, and P. L. George. 3d Delaunay mesh generation coupled with an advancing-front approach. *Computer Methods in Applied Mechanics and Engineering*, 157:115–131, 1998.
- [64] D. P. Gaver. Observing stochastic processes, and approximate transform inversion. *Operational Research*, 14:444–459, 1966.
- [65] St. I. Georghitza. On the plane steady flow of water through inhomogeneous porous media. In *First symposium on the Fundamentals of Transport Phenomena in Porous media*, Haifa, Israel, 1969. International Association for Hydraulics Research.
- [66] M. A. Golberg, C. S. Chen, H. Bowman, and H. Power. Some comments on the use of radial basis functions in the dual reciprocity method. *Computational Mechanics*, 23:141–148, 1998.

- [67] M. A. Goldberg and C. S. Chen. The method of fundamental solutions for potential, helmholtz and diffusion problems. In M. A. Goldberg, editor, *Boundary Integral Methods: Numerical and Mathematical Aspects*, pages 103–176. Pineridge Press, Southampton, Boston, 1999.
- [68] B. Goldiez, R. Rogers, and P. Woodard. Projects in VR: Real-time visual simulation on pcs. In *IEEE Computer Graphics and Applications*, 1999.
- [69] M. Grave. *Visualization in Scientific Computing*. Springer-Verlag, 1994.
- [70] L. J. Gray. Boundary element method for regions with thin internal cavities. *Engineering Analysis with Boundary Elements*, 6:180–184, 1989.
- [71] L. J. Gray, C. Balakrishna, and J. H. Kane. Symmetric Galerkin boundary integral fracture analysis. *Engineering Analysis with Boundary Elements*, 15:103–109, 1995.
- [72] L. J. Gray, G. E. Giles, and M. W. Wendel. Boundary element method for regions with thin internal cavities II. *Engineering Analysis with Boundary Elements*, 8:81–88, 1991.
- [73] L. J. Gray, J. Glaeser, and T. Kaplan. Direct evaluation of hypersingular Galerkin surface integrals. *SIAM Journal on Scientific Computing*, 25:1534–1556, 2002.
- [74] L. J. Gray and T. Kaplan. 3D Galerkin integration without Stokes’ Theorem. *Engineering Analysis with Boundary Elements*, 25:289–295, 2001.
- [75] L. J. Gray, T. Kaplan, J. D. Richardson, and G. H. Paulino. Green’s functions and boundary integral analysis for exponentially graded materials: heat conduction. *ASME Journal of Applied Mechanics*, 70:543–549, 2003.
- [76] L. J. Gray and E. D. Lutz. On the treatment of corners in the boundary element method. *Journal of Computational and Applied Mathematics*, 32:369–386, 1990.
- [77] L. J. Gray and G. H. Paulino. Symmetric Galerkin boundary integral formulation for interface and multi-zone problems. *International Journal for Numerical Methods in Engineering*, 40(16):3085–3101, 1997.
- [78] L. J. Gray and G. H. Paulino. Crack tip interpolation, revisited. *SIAM J. Applied Mathematics*, 58:428–455, 1998.

- [79] L. J. Gray and C. San Soucie. Hermite interpolation algorithm for hypersingular boundary integrals. *International Journal for Numerical Methods in Engineering*, 36:2357–2367, 1993.
- [80] A. S. Gullerud, K. C. Koppenhoefer, A. Roy, and R. H. Dodds Jr. WARP3D-Release 13.18 manual. Technical Report UILU-ENG-95-2012, University of Illinois at Urbana-Champaign, Urbana, IL,, 2000.
- [81] J. Hadamard. *Lectures on Cauchy's Problem in Linear Partial Differential Equations*. Dover Publications, 1952.
- [82] B. Hamann and K. Joy. Visualization methods for point data in space. Citris technical report, University of California, Davis, 2004.
- [83] K. E. Harrouni, D. Quazar, L. C. Wrobel, and C. A. Brebbia. Dual reciprocity boundary element method for heterogeneous porous media. In C.A. Brebbia and M. S. Ingber, editors, *Boundary element technology VII*, pages 151–159. Computational Mechanics Publication and Elsevier Applied Science, 1992.
- [84] K. E. Harrouni, D. Quazar, L. C. Wrobel, and A. H.-D. Cheng. Global interpolation function based DRBEM applied to darcy's flow in heterogenous media. *Engineering Analysis with Boundary Elements*, 16:281–285, 1995.
- [85] F. Hartmann, C. Katz, and B. Protopsaltis. Boundary elements and symmetry. *Ingenieur-Archiv*, 55:440–449, 1985.
- [86] J. L. Helman and L. Hesselink. Representation and display of vector field topology in fluid flow data sets. *Computer*, 22:27–36, 1989.
- [87] Amy Henderson. *The Paraview Guide: A Parallel Visualization Approach*. Kitware, Inc., 2004.
- [88] S. M. Hölzer. The symmetric Galerkin BEM for plane elasticity: scope and applications. In C. Hirsch, editor, *Numerical Methods in Engineering '92*. Elsevier, 1992.
- [89] S. M. Hölzer. How to deal with hypersingular integrals in the symmetric BEM. *Communications in Numerical Methods in Engineering*, 9:219–232, 1993.
- [90] M. Ikeuchi and K. Onishi. Boundary elements in transient convective diffusive problems. In C. A. Brebbia, T. Futagami, and M. Tanaka, editors, *Boundary Elements V*, pages 275–282. Springer, Berlin, 1983.

- [91] M. Ikeuchi and K. Onishi. Special issue: Papers from the German priority programme (functionally graded materials). In C. A. Brebbia, T. Futagami, and M. Tanaka, editors, *Materials Science and Engineering A*, volume 362, pages 1–331. Springer, Berlin, 2003.
- [92] M. S. Ingber, A. A. Mammoli, and M. J. Brown. A comparison of domain integral evaluation techniques for boundary element methods. *International Journal for Numerical Methods in Engineering*, 52:417–432, 2001.
- [93] M. S. Ingber and M. J. Martinez. Groundwater flow in heterogeneous media. Technical Report WERC-01-4-23194, Waste-Management Education and Research Consortium(WERC), 1994.
- [94] Marc S. Ingber, Andrea A. Mammoli, and Mary J. Brown. A comparison of domain integral evaluation techniques for boundary element methods. *International Journal for Numerical Methods in Engineering*, 52:417–432, 2001.
- [95] M. Joseph, H. Soltanian, J. R. Richard, and R. L. Donald. Evolution of virtual reality: from planning to performing surgery. In *IEEE Engineering in medicine and biology*, pages 16–22, 1996.
- [96] O. D. Kellogg. *Foundations of Potential Theory*. Dover Publications, New York, 1953.
- [97] D. R. Khattab, A. H. A. Aziz, and A. S. Hussein. An enhanced www-based scientific data visualization service using VRML. In *VRCAI '04: Proceedings of the 2004 ACM SIGGRAPH international conference on Virtual Reality continuum and its applications in industry*, pages 134–140. ACM Press, 2004.
- [98] K. A. Khor and Y. W. Gu. Thermal properties of plasma-sprayed functionally graded thermal barrier coatings. *Thin Solid Films*, 372:104–113, 2000.
- [99] J.-H. Kim and G. H. Paulino. Isoparametric graded finite elements for nonhomogeneous isotropic and orthotropic materials. *ASME Journal of Applied Mechanics*, 69:502–514, 2002.
- [100] P. Knupp and K. Salari. *Verification of computer codes in computational science and engineering*. CRC Press LLC, Boca Raton, FL, USA, 2002.
- [101] N. Konda and F. Erdogan. The mixed mode crack problem in a nonhomogeneous elastic medium. *Engineering Fracture Mechanics*, 47:533–545, 1994.

- [102] S. Mukherjee, V. S. Kothnur and Y.X. Mukherjee. Two dimensional linear elasticity by the boundary node method. 36(4):1129–1147, 1999.
- [103] L. Nicolazzi, C. A. Duarte, E. Fancello, and C. Barcellos. Hp-clouds - a meshless method in boundary elements. part I: Formulation. *Boundary Element Communications*, 8:8082, 1997.
- [104] L. Nicolazzi, C. A. Duarte, E. Fancello, and C. Barcellos. Hp-clouds - a meshless method in boundary elements. part II: Implementation. *Boundary Element Communications*, 8:8385, 1997.
- [105] L. A. De Lacerda, L. C. Wrobel, and W. J. Mansur. Boundary integral formulation for two-dimensional acoustic radiation in a subsonic uniform flow. *Journal of Acoustic Society of America*, 100:98–107, 1996.
- [106] O. E. Lafe and A. H.-D. Cheng. A pertubation boundary element code for steady state groundwater flow in heterogeneous aquifers. *Water Resources Research*, 23:1079–1084, 1987.
- [107] O. E. Lafe, J. A. Liggett, and P. L.-F. Liu. BIEM solutions to combination of leaky, layered, confined, unconfined, nonisotropic acquifers. *Water Resources Research*, 17:1431–1444, 1981.
- [108] J. LaViola. Msvt: A virtual reality-based multimodal scientific visualization tool. In *Proceedings of the Third IASTED International Conference on Computer Graphics and Imaging*, pages 1–7, 2000.
- [109] D. Lesnic, L. Elliott, and DB Ingham. Treatment of singularities in time-dependent problems using boundary element method. *Engineering Analysis with Boundary Elements*, 16:65–70, 1995.
- [110] B. Q. Li and J. W. Evans. Boundary element solution of heat convection-diffusion problems. *Journal of Computational Physics*, 93:255–272, 1991.
- [111] G. Li and N.R. Aluru. Boundary cloud method: a combined scattered point/boundary integral approach for boundary-only analysis. *Computer Methods in Applied Mechanics and Engineering*, 191:2337–2370, 2002.
- [112] S. Li, M. E. Mear, and L. Xiao. Symmetric weak form integral equation method for three-dimensional fracture analysis. *Computer Methods in Applied Mechanics and Engineering*, 151:435–459, 1998.

- [113] J. A. Liggett and P. L. F. Liu. Unsteady flow in confined aquifers: A comparison of boundary integral methods. *Water Resources Research*, 15:861–866, 1979.
- [114] G.R. Liu. *Mesh-free methods: moving beyond the finite element method*. CRC Press, Boca Raton, FL, 2002.
- [115] Y. Livnat and X. Tricoche. Interactive point based isosurface extraction. In *Proceeding of IEEE Visualization 2004*, pages 457–464, 2004.
- [116] E. D. Lutz and L. J. Gray. Exact evaluation of singular boundary integrals without CPV. *Communications in Numerical Methods in Engineering*, 9:909–915, 1993.
- [117] M. K. Singh and M. Tanaka. On exponential variable transformation based boundary element formulation for advection-diffusion problems. *Engineering Analysis with Boundary Elements*, 24:225–235, 2000.
- [118] G. Kuhn M. Haas. A symmetric Galerkin BEM implementation for 3D elastostatic problems with an extension to curved elements. *Computational Mechanics*, 28:250–259, 2002.
- [119] D. Maillat, S. Andre, J. C. Batsale, A. Degiovanni, and C. Moyne. *Numerical Fracture Mechanics*. Thermal Quadrupoles Solving the Heat Equation through Integral Transforms, John Wiley and Sons, 2000.
- [120] B. H. McCormick, T. A. DeFanti, and M. D. Brown. Visualization in Scientific Computing. *Computer Graphics*, 21(6), 1987.
- [121] D. E. Medina and J. A. Liggett. Three dimensional boundary element computation of potential flow in fractured rock. *International Journal for Numerical Methods in Engineering*, 26:2319–2330, 1988.
- [122] Y. Miyamoto, W. A. Kaysser, B. H. Rabin, A. Kawasaki, and R. G. Ford. *Functionally Graded Materials: Design, Processing and Applications*. Kluwer Academic Publishers, Dordrecht, 1999.
- [123] K. Moreland and E. Angel. A fast high accuracy volume renderer for unstructured data. In *Proceedings of IEEE Symposium on Volume Visualization and Graphics 2004*, pages 9–16, 2004.
- [124] G. J. Moridis and D. L. Reddell. The Laplace transform boundary element (LTBE) method for the solution of diffusion-type equations. In C. A. Brebbia and G. S. Gipson, editors, *BEM XIII*, pages 83–97. Computational Mechanics Publications, 1991.

- [125] M. S. Ingber MS and N. Phan-Thien. A boundary element approach for parabolic equations using a class of particular solutions. *Applied Mathematical Modelling*, 16:124–132, 1992.
- [126] Y.X. Mukherjee and S. Mukherjee. The boundary node method for potential problems. *International Journal for Numerical Methods in Engineering*, 40:797–815, 1997.
- [127] D. Nardini and C. A. Brebbia. A new approach to free vibration analysis using boundary elements. In C. A. Brebbia, editor, *Boundary Element Methods in Engineering*, pages 312–326. Springer, Berlin, 1982.
- [128] Ker Sin Neo, Qingping Lin, and Robert K. L. Gay. A web-based system for interactive visualization of scientific concepts. In *VRCAI '04: Proceedings of the 2004 ACM SIGGRAPH international conference on Virtual Reality continuum and its applications in industry*, pages 155–158. ACM Press, 2004.
- [129] N. Noda. Thermal stresses in functionally graded material. *Journal of Thermal Stresses*, 22:477–512, 1999.
- [130] M. A. M. Noronha and A. M. B. Pereira. A new algorithm for visualization of domain results in analysis with the boundary element method. In *Boundary Element Technology XV*, 2003.
- [131] S. North. Toward a 3d visualization framework for construction planning with procession. In *Proceedings IEEE International Conference on Information Visualization*, pages 577–582, 2000.
- [132] A. J. Nowak. The multiple reciprocity method of solving transient heat conduction problems. In C. A. Brebbia and J. J. Connor, editors, *BEM XI*, pages 81–95. Computational Mechanics Publications, Springer-Verlag, 1989.
- [133] A.J. Nowak and C.A. Brebbia. The Multiple Reciprocity Method - a new approach for transforming BEM domain integrals to the boundary. *Engineering Analysis with Boundary Elements*, 6:164–167, 1989.
- [134] F. París and J. Cañas. *Boundary Element Method*. Oxford University Press Inc., New York, 1997.
- [135] P. W. Partridge, C. A. Brebbia, and L. C. Wrobel. *The Dual Reciprocity Boundary Element Method*. Computational Mechanics Publications, Southampton and Boston, 1992.

- [136] R. Pasquetti, A. Caruso, and Wrobel LC. Transient problems using time-dependent fundamental solutions. In L. C. Wrobel and C. A. Brebbia, editors, *Boundary Element Methods in Heat transfer*, pages 33–62. Computational Mechanics Publications, Southampton Boston, 1992.
- [137] G. H. Paulino and L. J. Gray. Galerkin residuals for error estimation and adaptivity in the symmetric Galerkin boundary integral method. *ASCE Engineering Mechanics*, 125(5):575–585, 1999.
- [138] G. H. Paulino, Z. H. Jin, and R. H. Dodds. Failure of functionally graded materials. In B. Karihaloo and W. G. Knauss, editors, *Comprehensive Structural Integrity*, volume 2, chapter 13, pages 607–644. Elsevier Science, 2003.
- [139] G. H. Paulino, F. Shi, S. Mukherjee, and P. Ramesh. Nodal sensitivities as error estimates in computational mechanics. *Acta Mechanica*, 121:191–213, 1997.
- [140] G. H. Paulino, A. Sutradhar, and L. J. Gray. Boundary element methods for functionally graded materials. In C. A. Brebbia, C. Y. Cha, and R. E. Dippery, editors, *Boundary Element Technology XV*. WIT press, 2003. .
- [141] A. Portela, M. H. Aliabadi, and D. P. Rooke. The dual boundary element method: efficient implementation for cracked problems. *International Journal for Numerical Methods in Engineering*, 33:1269–1287, 1992.
- [142] H. Power. A complete multiple reciprocity approximation for the non-permanent stokes flow. In C. A. Brebbia and A. J. Kassab, editors, *Boundary Element Technology*, volume IX, pages 127–137. Computational Mechanics Publications, Southampton, 1994.
- [143] Pasquetti A. Caruso R. Boundary element approach for transient and non-linear thermal diffusion. *Numerical Heat Transfer, PartB*, 17:83–99, 1990.
- [144] P. A. Ramachandran. *Boundary element methods in transport phenomena*. Elsevier, London, 1994.
- [145] F. Rizzo and D. J. A. Shippy. Method of solution for certain problems of transient heat conduction. *AIAA Journal*, 8:2004–2009, 1970.
- [146] Alberto Salvadori. Analytical integrations of hypersingular kernel in 3D BEM problems. *Computer Methods in Applied Mechanics and Engineering*, 190:3957–3975, 2001.

- [147] Alberto Salvadori. Analytical integrations in 2D BEM elasticity. *International Journal for Numerical Methods in Engineering*, 53:1695–1719, 2002.
- [148] M. H. Santare and J. Lambros. Use of graded finite elements to model the behavior of nonhomogeneous materials. *ASME Journal of Applied Mechanics*, 67:819–822, 2000.
- [149] A. A. Savitski and E. Detournay. Propagation of a penny-shaped fluid-driven fracture in an impermeable rock: asymptotic solutions. *International Journal of Solids and Structures*, 39:6311–6337, 2002.
- [150] W. Schroeder, K. Martin, and W. Lorensen. *The Visualization Toolkit: An Object Oriented Approach to 3D Graphics*, 3rd Edition. Kitware, Inc., 2003.
- [151] M. Schulz, T. Reuding, and T. Ertl. Analyzing engineering simulation in a virtual environment. In *IEEE Virtual Reality*, pages 46–52, 1998.
- [152] Allen M. Shapiro and Johan Andersson. Steady state fluid response in fractured rock: a boundary element solution for a coupled, discrete fracture continuum model. *Water Resources Research*, 19:959–969, 1983.
- [153] R. Shaw. An integral equation approach to diffusion. *International Journal of Heat and Mass transfer*, 17:693–699, 1974.
- [154] R. P. Shaw. Green’s functions for heterogeneous media potential problems. *Engineering Analysis with Boundary Elements*, 13:219–221, 1994.
- [155] R. P. Shaw and G. S. Gipson. Interrelated fundamental solutions for various heterogeneous potential, wave and advective-diffusive problems. *Engineering Analysis with Boundary Elements*, 16:29–34, 1995.
- [156] R. P. Shaw and N. Makris. Green’s functions for Helmholtz and Laplace equations in heterogeneous media. *Engineering Analysis with Boundary Elements*, 10:179–183, 1992.
- [157] R. P. Shaw and G. D. Manolis. Two dimensional heat conduction in graded materials using conformal mapping. *Communications in Numerical Methods in Engineering*, 19:215–221, 2003.
- [158] W. R. Sherman and A. B. Craig. *Understanding Virtual Reality: Interface, Application and Design*. Morgan Kaufmann, 2003.

- [159] J. Shewchuk. Delaunay refinement mesh generation. Technical report, Carnegie Mellon University, 1997. Ph.D. Thesis.
- [160] J. Shewchuk. Constrained Delaunay tetrahedralization and provably good boundary recovery. In *Proceedings of the 11th International Meshing Roundtable 2002*, pages 193–204, 2002.
- [161] S. Sirtori, G. Maier, G. Novati, and S. Miccoli. A Galerkin symmetric boundary element method in elasticity: formulation and implementation. *International Journal for Numerical Methods in Engineering*, 35:255–282, 1992.
- [162] J. Sladek, V. Sladek, J. Krivacek, and Ch. Zhang. Local BIEM for transient heat conduction analysis in 3-d axisymmetric functionally graded solids. *Computational Mechanics*, 32:169–176, 2003.
- [163] J. Sladek, V. Sladek, and Ch. Zhang. Transient heat conduction analysis in functionally graded materials by the meshless local boundary integral equation method. *Computational Materials Science*, 28:494–504, 2003.
- [164] J. Sladek, V. Sladek, and Ch. Zhang. A local BIEM for analysis of transient heat conduction with nonlinear source terms in fgms. *Engineering Analysis with Boundary Elements*, 28:1–11, 2004.
- [165] V. Sladek, J. Sladek, and S.N. Atluri. Local boundary integral equation (LBIE) method for solving problems of elasticity with nonhomogeneous material properties. 24:456–462, 2000.
- [166] G. T. Spyros and S. T. Costas. Virtual reality in telerobotics: The state-of-the-art. In *IEEE ISIE99-Bled*, pages 280–286, 1999.
- [167] H. Stehfest. Algorithm 368: Numerical inversion of Laplace transform. *Communications of the Association for Computing Machinery*, 13:47–19, 1970.
- [168] H. Stehfest. Remarks on algorithm 368: Numerical inversion of Laplace transform. *Communications of the Association for Computing Machinery*, 13:624, 1970.
- [169] O. D. L. Strack. Flow in aquifers with clay laminae 1. The comprehensive potential. *Water Resources Research*, 17:985–992, 1981.
- [170] E. A. Sudicky. The Laplace transform Galerkin technique: a time-continuous finite element theory and application to mass transport in groundwater. *Water Resources Research*, 25:1833–1846, 1989.

- [171] S. Suresh and A. Mortensen. *Fundamentals of Functionally Graded Materials*. The Institute of Materials, IOM Communications Ltd., London, 1998.
- [172] A. Sutradhar and G. H. Paulino. A simple boundary element method for problems of potential in nonhomogeneous media. *International Journal for Numerical Methods in Engineering*, 60:2203–2230, 2004.
- [173] A. Sutradhar and G. H. Paulino. A simple boundary element method for transient heat conduction in functionally graded materials. *Computer Methods in applied mechanics and engineering*, 193:4511–4539, 2004.
- [174] A. Sutradhar, G. H. Paulino, and L. J. Gray. Transient heat conduction in homogeneous and nonhomogeneous materials by the Laplace transform Galerkin boundary element method. *Engineering Analysis with Boundary Elements*, 26:119–132, 2002.
- [175] A. Sutradhar, G. H. Paulino, and L. J. Gray. Erratum to ‘transient heat conduction in homogeneous and non-homogeneous materials by the Laplace transform Galerkin boundary element method’. *Engineering Analysis with Boundary Elements*, 27:639, 2003.
- [176] A. Sutradhar, G. H. Paulino, and L. J. Gray. On hypersingular surface integrals in the symmetric galerkin boundary element method: Application to heat conduction in exponentially graded materials. *International Journal for Numerical Methods in Engineering*, 62:122–157, 2005.
- [177] A. Talbot. The accurate numerical inversion of Laplace transforms. *Journal of the Institute of Mathematics and Its Applications*, 23:97–120, 1979.
- [178] M. Tanaka, T. Matsumoto, and Y. Suda. A dual reciprocity boundary element method applied to the steady-state heat conduction problem of functionally gradient materials. *Electronic Journal of Boundary Elements*, BETEQ 2001, No. 1:128–135, 2002.
- [179] Y. Tanigawa. Some basic thermoelastic problems for nonhomogeneous structural materials. *Applied Mechanics Reviews*, 48:287–300, 1995.
- [180] M. C. Walters, G. H. Paulino, and R. H. Dodds Jr. Stress intensity factors for surface cracks in functionally graded materials under mode I thermomechanical loading. *International Journal of Solids and Structures*, 41:1081–1118, 2004.

- [181] N. Weatherill and O. Hassan. Efficient three dimensional Delaunay triangulation with automatic point creation and imposed boundary constraints. *International Journal for Numerical Methods in Engineering*, 37:2005–2039, 1994.
- [182] W. T. Weeks. Numerical inversion of Laplace transforms using laguerre functions. *Journal of the Association for Computing Machinery*, 13:419–429, 1966.
- [183] D.M. Weinstein, S.G. Parker, J. Simpson, K. Zimmerman, and G. Jones. Visualization in the SCIRUN problem-solving environment. In C.D. Hansen and C.R. Johnson, editors, *The Visualization Handbook*, pages 615–632. Elsevier, 2005.
- [184] J. Wood, H. Wright, and K. Brodlie. Collaborative visualization. In R. Yagel and H. Hagen, editors, *Proceedings of Visualization '97*, pages 253–259. IEEE Computer Society Press, 1997.
- [185] L. C. Wrobel and C. A. Brebbia. The boundary element for steady state and transient heat conduction. In R. W. Lewis and K. Morgan, editors, *Numerical Methods in thermal problems*, pages 58–73. Pineridge Press, Swansea, 1979.
- [186] L. C. Wrobel and C. A. Brebbia. The dual reciprocity boundary element formulation for non-linear diffusion problems. *Computer Methods in Applied Mechanics and Engineering*, 65:147–164, 1987.
- [187] L. C. Wrobel, C. A. Brebbia, and N. Nardini. The dual reciprocity boundary element formulation for transient heat conduction. *Finite elements in Water Resources V*, 1986.
- [188] L. C. Wrobel and C.A. Brebbia, editors. *Boundary element methods in heat transfer*. Computational Mechanics Publication and Elsevier Applied Science, 1992.
- [189] T. W. Wu and L. Lee. A direct boundary integral formulation for acoustic radiation in a subsonic uniform flow. *Journal of Sound and Vibration*, 175:51–63, 1994.
- [190] S. P. Zhu. Time-dependent reaction diffusion problems and the LTDRM approach. In M. A. Goldberg, editor, *Boundary Integral Methods: Numerical and Mathematical Aspects*, pages 1–35. Pineridge Press, Southampton, Boston, 1999.
- [191] S. P. Zhu and P. Satravaha. An efficient computational method for nonlinear transient heat conduction problems. *Applied Mathematical Modeling*, 20:513–522, 1996.

- [192] S. P. Zhu, P. Satravaha, and X. Lu. Solving linear diffusion equations with the dual reciprocity method in Laplace space. *Engineering Analysis with Boundary Elements*, 13:1–10, 1994.
- [193] Zhang J-D. Zhu, T. and S.N. Atluri. A local boundary integral equation (LBIE) method in computational mechanics, and a meshless discretization approach. 21:223–235, 1998.

Author's biography

Alok Sutradhar was born to Sunil and Binapani Sutradhar in Dhaka, Bangladesh on October 27th, 1971. Since his childhood, he began to grow interest in science partly due to the inspiration of his father Sunil, who has been an accomplished civil engineer and writer, and his mother Binapani, who has been a high school science teacher. He followed his father to pursue undergraduate studies in civil engineering in Bangladesh University of Engineering and Technology (BUET). During his undergraduate study two books, one by Igor Popov titled, 'Mechanics of Solids' and the other by Timoshenko and Goodier titled, 'Theory of Elasticity' inspired him to work in the field of mechanics. After graduating and being ranked 2nd in his undergrad class, he joined the structural engineering division as a lecturer in his Alma Mater. Simultaneously, he started his graduate studies and worked on his thesis in finite element methods under the guidance of Professor Sohrabuddin Ahmad who was a former PhD student of O. C. Zienkiewicz.

In 1999, Alok came to UIUC to pursue his doctorate degree in civil engineering and in Spring 2000, he joined the functionally graded materials group led by Professor Glaucio H. Paulino. He took the challenge to work in mesh reduction techniques like boundary element method and meshless methods. In two summers (2000-2001) he spent as a summer intern in the computer science and mathematics division at the Oak Ridge National Laboratory. In 2002, He was awarded the Computational Science and Engineering Fellowship to carry out his research. While pursuing the PhD in computational mechanics he concurrently started to do a minor in Computational Science and Engineering. Taking couple of courses in computer graphics, he got interested in the scientific visualization and later joined the Visualization and Virtual Environment group at NCSA as a research assistant. Recently, he won the best student paper award (2nd place) for writing and presenting his paper in boundary element method in the International Association for Boundary element methods conference (2004).

Alok is extremely passionate about teaching. He has thoroughly enjoyed his teaching experience at BUET as a lecturer and at UIUC as a TA. He graduates in May 2005. After graduation, he plans to go into academia and continue his research and teaching. His latest interests are in the field of bioengineering especially in biomechanics and cell mechanics.